5-2009

Synthesis and characterization of nanostructured materials

Kate Labelle Klein
University of Tennessee

To the Graduate Council:

I am submitting herewith a dissertation written by Kate Labelle Klein entitled "Synthesis and characterization of nanostructured materials." I have examined the final electronic copy of this dissertation for form and content and recommend that it be accepted in partial fulfillment of the requirements for the degree of Doctor of Philosophy, with a major in Materials Science and Engineering.

Michael L. Simpson, Major Professor

We have read this dissertation and recommend its acceptance:

Accepted for the Council:

Carolyn R. Hodges

Vice Provost and Dean of the Graduate School

(Original signatures are on file with official student records.)

To the Graduate Council:

I am submitting herewith a dissertation written by Kate Labelle Klein entitled "Synthesis and Characterization of Nanostructured Materials." I have examined the final electronic copy of this dissertation for form and content and recommend that it be accepted in partial fulfillment of the requirements for the degree of Doctor of Philosophy, with a major in Materials Science and Engineering.

Michael L. Simpson, Major Professor

We have read this dissertation and
recommend its acceptance:

Philip D. Rack

David C. Joy

Easo P. George

Accepted for the Council:

Carolyn R. Hodges, Vice Provost and
Dean of the Graduate School

(Original signatures are on file with official student records.)

Synthesis and Characterization of Nanostructured Materials

A Dissertation

Presented for the

Doctor of Philosophy

Degree

The University of Tennessee, Knoxville

Kate Labelle Klein

May 2009

Dedication

To my mother who has always been a strong role model for her daughters and has supported me in all of my endeavors; and to my husband who has challenged me in so many ways and encouraged me to finish this chapter in my life.

Acknowledgements

There are many people and organizations to whom I am tremendously appreciative for making this dissertation research possible. First of all, I would like extend my gratitude to my committee members for all their time and patience throughout this process. I cannot thank enough my advisor, Dr. Michael Simpson, who has unwaveringly provided guidance and support while at the same time has allowed me the freedom to explore new research opportunities and experience both failure and success. Over the years he has helped to keep me grounded and maintain perspective on the big picture. I am also indebted to Anatoli (Tolik) Melechko, who has essentially been my mentor for the technical aspects of this research, a great sounding board for ideas, and someone I truly could rely on in times of need.

Next I would like to acknowledge the members of the Molecular-scale Engineering and Nanoscale Technologies (MENT) research group who have provided invaluable support and camaraderie from the onset. I especially want to thank close collaborators Philip Rack, Jason Fowlkes, Steven Randolph, Dale Hensley, and Igor Merkulov for the rewarding work we accomplished together. I would also like to recognize Vladimir Merkulov and Tim McKnight for the visionary direction of our group's research—where would we be without carbon nanofibers and impalefection? Additional assistance with sample preparation was provided by Pam Fleming, Teri Subich, Darrell Thomas, and Ryan Rucker. Special appreciation also goes to Gayle Jones and Carla Lawrence for administrative support and to Laura Edwards for manuscript editing and chocolate. There are also previous graduate students to whom I owe my gratitude. These include Michael Guillorn, Lan Zhang, Derek Austin, Xiaojing Yang, Steven Randolph, David Mann, and Ben Fletcher, who led the way before me and set the bar high. Classmates Steven Randolph, Ben Fletcher, and Roy Dar have suffered along with me through the trials of graduate school with late night study sessions and I am grateful for their feedback, moral support, and friendship. While Michael Guillorn may have been my reason for coming, the people of MENT were my reason for staying.

Several other collaborators at Oak Ridge National Laboratory also deserve particular thanks, including Larry Allard, Joe Horton, David Joy, and Ian Anderson for

their invaluable assistance with transmission electron microscopy and data interpretation. Auger analysis and discussions with Harry Meyer were also influential in this research. I would like to acknowledge Korey Sorge from Florida Atlantic University who performed magnetic measurements and offered meaningful interpretation. Additionally, I am thankful to Dmitri Golberg who hosted me for a summer research experience in Japan and graciously provided equipment and facilities at the National Institute of Materials Science (NIMS). Pedro Costa also lent a great deal of his time and expertise toward making the collaboration a success. Support for this travel was supplied by the National Science Foundation (NSF) and the Japan Society for the Promotion of Science (JSPS) under the East Asian Pacific Summer Institute (EAPSI) Program.

I am also grateful to the Center for Nanophase Materials Sciences (CNMS), which is sponsored at ORNL by the DOE's Division of Scientific User Facilities, for their support through the Research Scholars Program. The CNMS has afforded me a first-class environment to conduct research, establish collaborations, and compose this dissertation. Additional support for this research was provided by the Materials Sciences and Engineering Division Program of the DOE Office of Science.

Furthermore, I owe much gratitude to my undergraduate and lifelong mentors and role models, Christine Broadbridge and Ann Lehman. In my first year as an undergrad, these two professors opened by eyes to the world of materials research and electron microscopy and they continued to believed in my abilities as a researcher and inspired me to pursue a career in science. And last but not least, I would like to sincerely thank my family and friends who have stuck by me through the ups and downs and supplied a much-needed diversion from the stresses of graduate study.

Abstract

In addition to technological motivations, nanomaterials are interesting for basic scientific investigation because their properties reside in the largely unexplored realm between molecules and bulk solids. The controlled synthesis of these materials, by methods that permit their assembly into functional nanoscale structures, lies at the core of nanoscience and nanotechnology. Here, controlled synthesis refers to a process of collective nanostructure growth where the pertinent attributes such as location, size, orientation, and composition as well as the electrical, mechanical, and chemical properties of the individual elements can be predetermined by the choice of the growth conditions and the preparation of the growth substrate. This dissertation work furthers the understanding of the mechanisms by which synthesis conditions affect the morphology, composition, and crystal structure of nanostructured materials with the objective of achieving greater control over the synthesis process. Three types of systems are investigated in depth: vertically aligned carbon nanofibers (grown by plasma-enhanced chemical vapor deposition), catalytic alloy nanoparticles (sputter-deposited, carbon-encapsulated), and tungsten nanowires (grown by electron-beam-induced deposition). The effects of growth parameters on the resulting nanostructure properties are characterized by methods including high-resolution transmission electron microscopy, electron diffraction, and chemical spectroscopy.

Table of Contents

List of Figures

List of Symbols and Variables

a	lattice parameter of a cubic unit cell
α	alpha, graphitic cone angle in carbon nanostructures *or* designation for the primary thermodynamic phase
Å	angstrom, 10^{-10} meters
β	beta, designation for secondary thermodynamic phase
c	speed of light *or* camera calibration constant
d	*d*-spacing, distance between atomic planes in a crystal
D	diameter (e.g. of a nanoparticle, nanofiber, or nanowire)
E	energy
F	total gas flow
f(θ)	atomic scattering factor
F(θ)	structure factor
hkl	generic plane Miller indices for cubic systems
H	applied magnetic field
H_c	coercive field, coercivity
k_B	Boltzmann constant
λ	lambda, wavelength
m	total sample magnetic moment
M	sample magnetization (m normalized by volume)
M_s	saturation magnetization
μm	micron, 10^{-6} meters
μ	mu, particle magnetic moment
μ_B	Bohr magneton, physical constant of magnetic moment
n	whole number (e.g. wavelengths)
Ω	ohms (unit of resistance)
P	total pressure
r	radius *or* measured distance from origin to diffraction spot
R	carbon source gas to etchant gas flow ratio

t	film thickness
T	temperature
T_e	eutectic temperature, depressed melting point by the formation of an alloy
T_m	melting point of an elemental solid
θ	theta, the scattering angle *or* designation for the angle between the *r*-axis and the normal growth velocity of the CNP-G interface
θ_B	Bragg angle
v_n	normal growth velocity
v_t	tangential growth velocity
ω	x-ray grazing incidence angle relative to the specimen surface
x	atomic concentration
z	growth axis direction
Z	atomic number

List of Abbreviations and Units

A	ampere (unit of current)
AES	Auger electron spectrometer/spectroscopy
AC	alternating current
AFM	atomic force microscope/microscopy
at. %	atomic percent (composition)
BCC	body centered cubic (lattice)
BF	bright field (TEM imaging mode)
BSE	backscattered electron
CNF	carbon nanofiber
CNP-G	catalyst nanoparticle-graphite interface
CNT	carbon nanotube
CVD	chemical vapor deposition
DC	direct current
DC-PECVD	direct current plasma-enhanced chemical vapor deposition
DF	dark field (TEM imaging mode)
EBID	electron-beam-induced deposition
emu	electromagnetic units
eV	electron volts (unit of energy)
FCC	face centered cubic (lattice)
FFT	fast Fourier transform
FIB	focused ion beam (milling)
FM	ferromagnetic
HAADF	high angle annular dark field (detector)
HCP	hexagonal close packed (lattice)
HOPG	highly oriented pyrolytic graphite
HRTEM	high-resolution transmission electron microscopy
Hz	hertz (unit of frequency)
ICP	inductively coupled plasma
K	degrees Kelvin

MWCNT	multiwalled carbon nanotube
nm	nanometer, 10^{-9} meters
OIM	orientation imaging microscope/microscopy
Oe	oersted (unit of magnetizing field)
Pa	pascal (unit of pressure)
PECVD	plasma-enhanced chemical vapor deposition
PM	paramagnetic
ppm	parts per million
PVD	physical vapor deposition
px	pixels
QD	quantum dot
RF	radio frequency
RIE	reactive ion etch
SAD	selected area diffraction
sccm	standard cubic centimeter per minute (unit of gas flow)
SE	secondary electron
SAM	scanning Auger microprobe
SEM	scanning electron microscope/microscopy
SPM	superparamagnetic
SPR	surface plasmon resonance
SQUID	superconducting quantum interference device (magnetometer)
STEM	scanning transmission electron microscope/microscopy
SWCNT	single-walled carbon nanotube
T	tesla (unit of magnetic flux density)
TEM	transmission electron microscope/microscopy
Torr	torr (unit of pressure)
V	volt (unit of electromotive force)
VACNF	vertically aligned carbon nanofiber
VLS	vapor-liquid-solid (catalytic growth mechanism)
VSS	vapor-solid-solid (catalytic growth mechanism)
W	watt (unit of power)

wt. %	weight percent (composition)
XEDS	x-ray energy-dispersive spectroscopy (a.k.a. EDX, EDS)
XRD	x-ray diffraction
1D	one-dimensional
2D	two-dimensional
3D	three-dimensional

1. Introduction

1.1 Introduction to Nanomaterials

Nanostructured materials or *nanomaterials* are conventionally defined as materials having a characteristic length scale of less than ~100 nm. This characteristic length could represent a range of aspects from a particle diameter, grain size or feature size, to a layer thickness. In this domain, phenomena length scales become comparable to the size of the structure, imparting new properties. Common discrete nanostructures include quantum dots, nanoparticles, nanowires, and nanotubes, while the collection of these structures can form arrays, assemblies, metamaterials, and superlattices. Nanostructures can be found in both natural systems and artificial materials.

Mother Nature has been creating nanosized structures for billions of years—the components of a cell, precipitates in magnetotactic bacteria, scales on a butterfly wing, diatom structures, etc. As a result, it has become popular to utilize bio-templates for making nanomaterials, since biological nanomaterials can serve as a model system for efficient architectures and synthesis methods. For instance, the cavities of proteins can be used as nucleation sites for nanoparticles, inherently limiting their size.[1] Ideal candidates for three-dimensional (3D) templates are plant viruses, which assemble protein shells with precise 3D structures. These nanoscale architectures are highly homogeneous, can be produced in large quantities, and are amenable to genetic and chemical modification.[2] A method has also been demonstrated that converts whole nano/mesoscale diatom structures from silica into different inorganic materials while maintaining the intricate details of the original organism.[3]

Contrary to popular belief, man-made nanomaterials are not solely a modern phenomenon, as colloidal gold nanoparticles and carbon nanotubes have been around for centuries. Historically, nanosized gold has been found in the decorative stained glass windows of European cathedrals[4] and was used for coloring Chinese vases and ornaments since the Middle Ages.[5] Nanogold was often employed unwittingly because of its vivid

ruby red color. Isolated artifacts from even earlier time periods have also been found including the Lycurgus Cup from the 4th century, which is made of impressive dichroic glass containing colloidal gold and silver.[6] Recently, it was discovered that the steel of Damascus sword blades may owe its rare strength, sharpness, and beautiful patterned texture to nanostructured materials.[7] The lost recipe for Damascus steels, forged in the ovens of the Middle East and India, had mysteriously incorporated carbon nanotubes and iron carbide nanowires more than 400 years ago. While carbon nanostructures can occur randomly in ordinary combustion processes and have been found in household soot,[8] they require a great deal of technological effort to be produced as useful structural materials; hence the fortuitous recipe used for damascened steel has been unable to be replicated to this day.

Actual scientific study of what are regarded as nanomaterials, in retrospect, can be traced to 150 years ago with the British physicist Michael Faraday's colloid experiments,[9] a subject later studied by Zsigmondy, Maxwell, and Einstein, among others. In a colloid, nanoparticles, because of their small size, intriguingly stay in a suspended homogeneous mixture, unable to be separated by gravity or filtration methods. Faraday discovered that the optical properties of gold colloids differed from those of bulk gold and indicated that the variation in the size of the particles seemed to cause the visible color change. Although the specific reason was not well understood, this was likely the first reported observation of quantum effects and thereby could be considered the "birth of nanoscience". Continued research on nanomaterials has been stimulated by technological applications and the belief that the ability to control the nanoscale building blocks of materials can result in enhanced properties at the macroscale, such as increased hardness, ductility, magnetic coupling, catalytic enhancement, selective absorption, or higher efficiency electronic or optical behavior.[10] The first modern technological uses of nanomaterials were as catalysts[11,12] and pigments.[13]

The only aspect tying the vast scope of nanomaterials together comes down to one thing: their size. So, what is so important about size? The ability to construct structures and control processes on the nanoscale opens a whole new realm of possibilities from biology and medicine to technology. Synthetic nanoscale structures offer a particularly suitable means of interfacing with biological systems because they intervene at the scale

where life processes proceed—the molecular level. Likewise, the push in the microelectronics industry for faster switching times and greater integration has lead to a reduction in the size of the components. For an ideal efficiency, the switch action would occur with the movement of only a single electron, which would require molecular components. In 1959 Richard Feynman realized these possibilities in his landmark speech at Caltech entitled, "There's plenty of room at the bottom".[14] In this lecture Feynman posed a set of challenges—for instance to write in text 1/25,000 times smaller (such that the entire 24 volumes of the Encyclopedia Britannica could fit on the head of a pin), to record a bit of information using just 100 atoms, and also to be able to read and resolve these nanoscale structures by increasing the resolving power of electron microscopes to the sub-angstrom level. Thus Feynman recognized that there were two important aspects to increased miniaturization, which he saw as essential to progress: the ability to make things smaller, as well as to see what has been made.[15]

The next few decades after Feynman's lecture saw the "discovery" of novel nanomaterials and processes with milestones such as the atomic layer deposition patent in 1974,[16] birth of cluster science[17] and quantum dots[18] in the 1980's, buckyballs in 1985,[19] and carbon nanotubes in 1991.[20] By the late 1990's there was an evident need to create an infrastructure for science, technology, facilities, and human resources in the field of nanotechnology. A few years later, the National Nanotechnology Initiative (NNI, 2001) was launched with $422 million in funds during the Clinton administration. Since 2001, government agencies participating in the NNI have funded more than 60 facilities, centers, and networks to advance nanotech research for economic growth and public benefit.[21] Earlier, in 1997 it was estimated that all U.S. agencies together were spending approximately $115 million per year for nanotech research,[10] whereas today the proposed NNI budget for 2009 is over $1.5 billion,[22] reflecting major investment growth in nanotechnology research and development over the past decade.

1.2 Why Nanomaterials are Different

Nanomaterials are a special class of materials because their properties are different from and often extend beyond those achievable in bulk materials. While bulk materials should have constant properties regardless of size, this is frequently not the case at the nanoscale. There are several interrelated aspects that make nanomaterial properties so different, namely the scaling laws of size, surface properties, as well as the electronic, magnetic, and crystallographic restructuring that result from both diminished volume and increased surface area. It should also be noted that nanostructures present an extraordinary opportunity for meaningful computer simulation and modeling since their size is accessible with the methods at hand, such as electronic structure calculations and molecular dynamics. First-principles electronic structure calculations can realistically only be performed on clusters less than several hundred atoms since the time required increases with the number of atoms in the cluster. Calculations on larger clusters are usually performed using approximate techniques such as the embedded atom method (EAM)[23] for metallic systems and modified embedded atom method (MEAM) for covalent systems.

Feynman incisively noted that as materials approach the nanometer level, scaling issues would arise from the changing magnitude of various physical phenomena—gravity would become more trivial while surface tension and van der Waals attractions become more significant.[14] For instance, suspensions of nanoparticles (colloids) are only possible because the interaction of the particle surface with the solvent is strong enough to overcome differences in density, which generally result in the material either sinking or floating in the liquid.

For bulk materials larger than one micrometer the percentage of atoms at the surface is minute relative to the total number of atoms in the material. However, as demonstrated in from Figure 1.1 below, the number of surface atoms reaches quite a significant proportion in particles less than ~10 nm. Crystalline materials with grain sizes on this scale are referred to as nanocrystalline. Due to increased surface area, nanocrystalline materials contain a higher fraction of grain boundary volume. These

boundaries act as sources and sinks for dislocations thereby facilitating stress-relief mechanisms such as grain boundary sliding,[24] resulting in exceptional mechanical strength and hardness. Thus the interesting and sometimes unexpected properties of nanomaterials are partly due to aspects of the material's surface dominating in lieu of the bulk properties.

It is well known that surface properties often vary substantially from the bulk material properties due to a difference in physical structure and chemistry. Moreover, the surface is a dynamic system which interacts with the environment, a characteristic that can be exploited for many applications. The surfaces of nanostructured materials are of special significance because of their enhanced role in determining functional properties – a phenomenon that becomes more pronounced as the surface to volume ratio increases. The large surface to volume ratio of nanomaterials increases their chemical activity, which can be problematic due to rapid surface oxidation[25] but advantageous for such purposes as catalysis. In fact, one of the most remarkable differences in bulk properties compared to those of the surface occurs in gold. Gold is normally viewed as an inert metal as exemplified by Figure 1.2(a), which displays the trend in transition metals to bind oxygen. Gold is the only metal with an endothermic chemisorption energy, implying that it does not oxidize. Yet, gold nanoparticles less than 3-5 nm in diameter are quite catalytically active for several reactions.[26] Figure 1.2(b) shows the activity of Au particles as a function of their size, exhibiting a $1/D^3$ relationship. Interestingly from the calculation of the fractions of atoms at the surfaces, edges, and corners of the Au particle [Figure 1.2(c)], a similar $1/D^3$ trend is seen with respect to the corner atoms. This demonstrates that the activity of gold catalysts is approximately proportional to the number of low-coordinated atoms at the corners of the gold particles.[26]

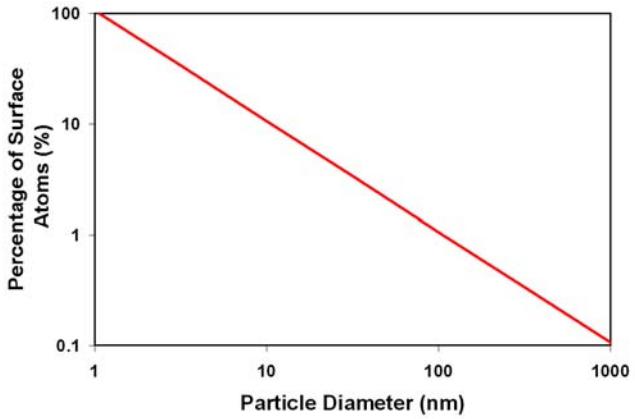

Figure 1.1 The percentage of atoms at the surface as a function of the particle diameter.

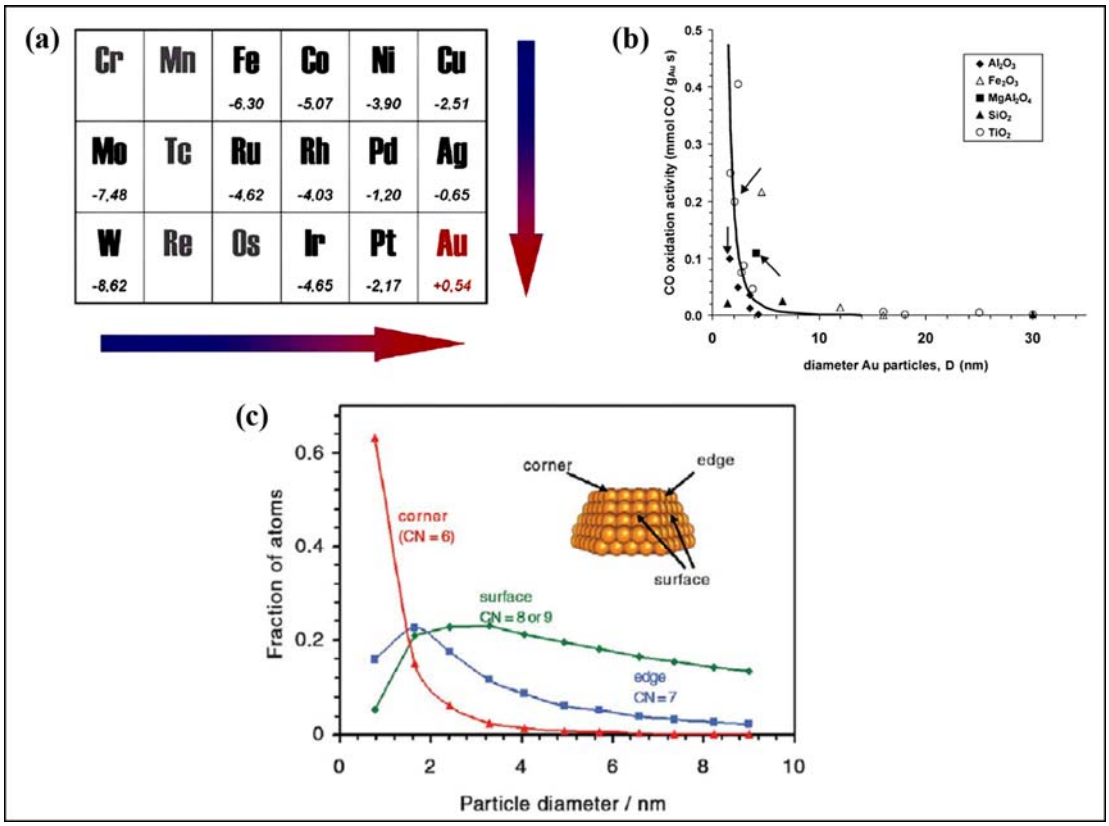

Figure 1.2 Reactivity of gold. (a) The dissociative chemisorption energies for oxygen on transition metal surfaces with respect to a molecule in vacuum, calculated by density functional theory.[27] (b) Reported catalytic activities for CO oxidation at 273 K as a function in gold particle size, with various supports indicated in corner.[26] (c) Calculated fractions of Au atoms at corners (red), edges (blue), and crystal faces (green) as a function of particle size where particle consists of the top half of a truncated octahedron as pictured. Adapted from [[27]].

At the nanoscale, deviations from bulk behavior also include a reduction in plasticity temperature and melting point (T_m) due to increased surface energy per area at high curvatures.[17,28,29] Accordingly, dewetting and sintering processes also take place at lower temperatures and over shorter time scales than for larger particles. Exploration of new phase diagrams has shown particle size dependent behavior until a critical size is reached where the particles behave essentially as bulk matter. Figure 1.3 shows that as the diameter of gold particles decrease, the melting point drastically falls with a diameter of less than ~20 nm.

In addition, at small particle sizes there is a contraction of the lattice parameter related to high surface stress, as illustrated in Figure 1.4.[30] Below a diameter of ~20 nm a significant decrease in the lattice parameter is found, amounting to about 1.5% for a 6 nm diameter particle. These effects are a direct result of a decrease in the coordination of the surfaces atoms coupled with an increase in surface to volume ratio of the material.[31]

Nanoparticles often have unexpected optical properties because they are small enough to confine their electrons and produce quantum effects. Mie Theory calculations for the scattering of light by spherical particles predict size-dependent behavior at the nanoscale. Intense color can be produced from the quantum confinement effect on an electron in a semiconductor nanocrystal, whose dimensions are less than the Bohr radius of the exciton. Thus, smaller particle size results in a blue-shift and larger particle size results in a red-shift in the emission spectrum (discussed further in the Nanoparticles Section 1.3.2).

Another electronic structure quantum effect, called surface plasmon resonance (SPR), is observed in noble metal nanoparticles.[32] As the metal particles are reduced in size down to tens of nanometers, a particularly strong absorption effect is observed where the electrons in the conduction band collectively oscillate from one surface of the particle to the other.[5] For Au, Ag, and Cu, surface plasmons resonate when excited by visible light; this is why, for example, gold nanoparticles appear deep red to black in solution. As was mentioned earlier, this strong absorption that gives rise to characteristic color has been both observed and used for centuries but not understood until recently.

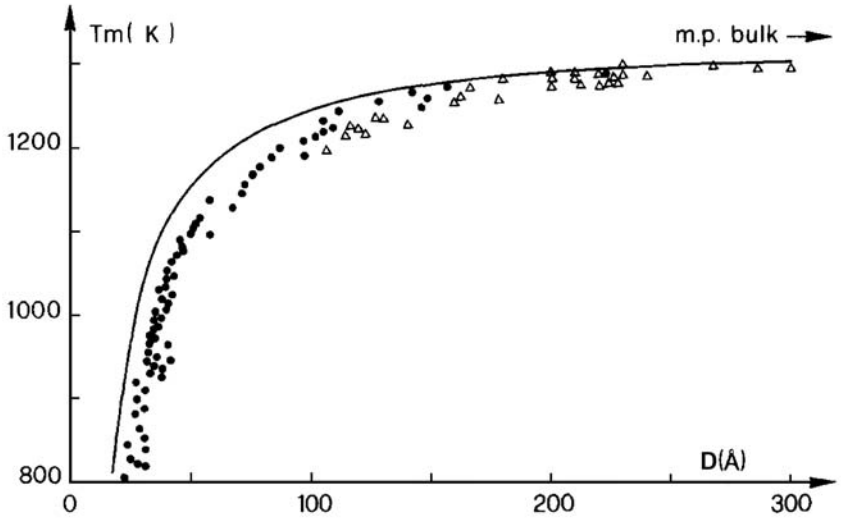

Figure 1.3 Melting of small gold particles: (Δ) Sambles experiment; (•) Buffat experiment; solid line, the Pawlow first order theory. Adapted from [17].

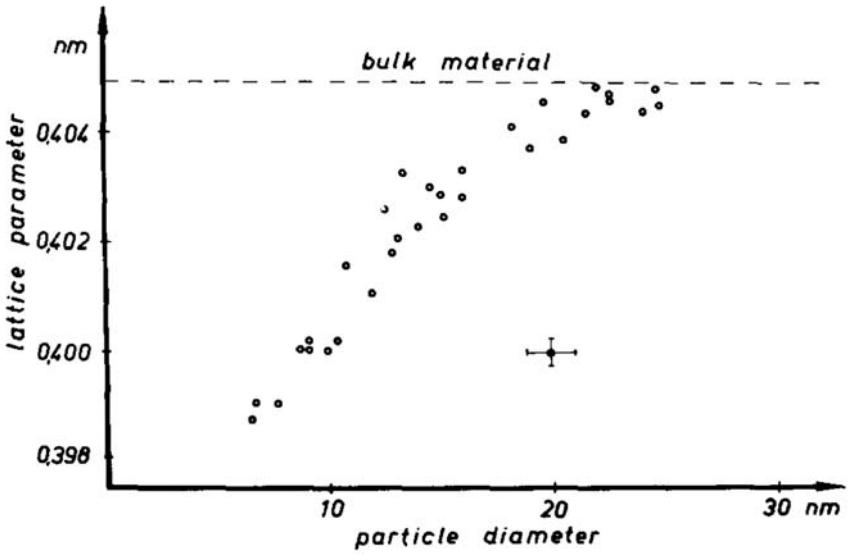

Figure 1.4 Dependence of lattice parameter on particles size (aluminum nanoparticles on MgO substrate, as measured by the moiré fringe method). Adapted from [30].

Novel magnetic quantum mechanical behavior has been found in multiphase nanostructured materials resulting from the diminished size of each phase. In 1988 it was discovered that thin multilayers of Fe and Cr can create giant magnetoresistance (GMR).[33] The GMR effect is utilized today in hard drive disk read heads, which consist of a sensing layer (often made of Ni-Fe alloy), a spacer made of nonmagnetic material (often Cu), a pinned magnetic layer (typically Co), and an exchange layer (usually Fe and Mn) that couples to the pinned layer. As the head moves across a bit, the electrons in the sensing layer rotate, increasing the resistance of the overall structure. However, it should be cautioned that ferromagnetic materials much smaller than 10 nm can switch their magnetization direction using room temperature thermal energy (superparamagnetic behavior), rendering them useless for memory storage.

Lastly, as a result of diminished volume and large surfaces areas, it should also be noted that the energy landscapes of nanomaterials are significantly affected, which in turn disrupts the atomic arrangements stable in bulk forms. Nanoscale particles in a variety of systems can exhibit crystallographic structures prohibited by translational symmetry rules, such as those with fivefold symmetry.[34,35] On this scale, growth processes are controlled by kinetic rather than energetic factors, thus a system can easily find a metastable state or local potential energy minimum via irreversible processes.[34-36] It is a challenging task to explore how the structure of nanoparticles evolves on a thermodynamic diagram with respect to their size, and many attempts have been made to observe size dependent phase transitions.[34,37,38]

1.3 Overview of Nanostructured Materials

While established technologies such as catalysis, glass making, and film photography have been employing nanomaterials for years, the capability to synthesize, organize, and tailor materials at the nanoscale is a recent phenomenon. Over the past two decades we have observed rapid advances in our ability to construct matter at the nanoscale with sufficient control over the material size, shape, composition, and morphology.[5] Of the plethora of nanomaterials types ranging from fullerenes to oxide

heterostructure superlattices to macromolecular complexes, this section will focus on introducing three kinds of structures that are central to this dissertation: carbon nanostructures, nanoparticles, and inorganic nanowires.

1.3.1 Nanostructured Carbons*

Among the multitude of nanomaterials, carbon nanostructures hold a special place due to their mechanical strength and chemical stability. In addition, the covalent chemistry of carbon with oxygen, hydrogen, and nitrogen, provides facile routes for functionalization of carbon surfaces with organic or biological molecules. In elemental form, carbon constructs allotropes with different kinds of carbon-carbon bonds, such as in sp^3-based diamond [Figure 1.5(a)] and sp^2-based graphite [Figure 1.5(b)], resulting from the variety of covalent bonding arrangements provided by orbital hybridization.[40]

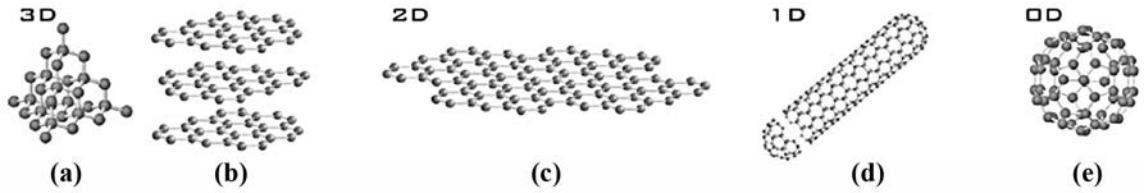

Figure 1.5 Crystal structures of the different allotropes of carbon: three-dimensional diamond (a) and graphite (b); two-dimensional graphene (c); one-dimensional nanotubes (d); and zero-dimensional C_{60} buckyballs (e). Adapted from [41].

* This section contains lightly revised passages from [39].

In its simplest form, a hexagonal network of carbon atoms is represented by a graphene sheet,[41] as in Figure 1.5(c). However, a small piece of graphene, unless it is terminated by hydrogen atoms, would have many carbon atoms located at the edge or surface that are unstable because of dangling bonds. The solution to this energetic instability is to create curved structures, known as fullerenes, including nanotubes [Figure 1.5(d)] and buckyballs [Figure 1.5(e)]. The introduction of five and seven member rings into the graphene [Figure 1.6(a)], allows for high curvature such as in the formation of buckyballs[19] and nanocones[42] [Figure 1.6(b)]. A carbon nanotube (CNT),[20] more specifically a single-walled carbon nanotube (SWCNT), can then be considered as a graphene sheet rolled into a cylinder, where multiple concentric sheets create a multiwalled carbon nanotube [MWCNT, Figure 1.6(c)]. Carbon nanofibers (CNFs) are a class of fullerenes that consist of curved graphene layers or nanocones stacked to form a quasi one-dimensional (1D) filament,[43] whose internal structure can be characterized by the angle α between the graphene layers and the fiber axis [Figure 1.6(d)].[44] Thus in the case of a true carbon nanotube, α is zero.

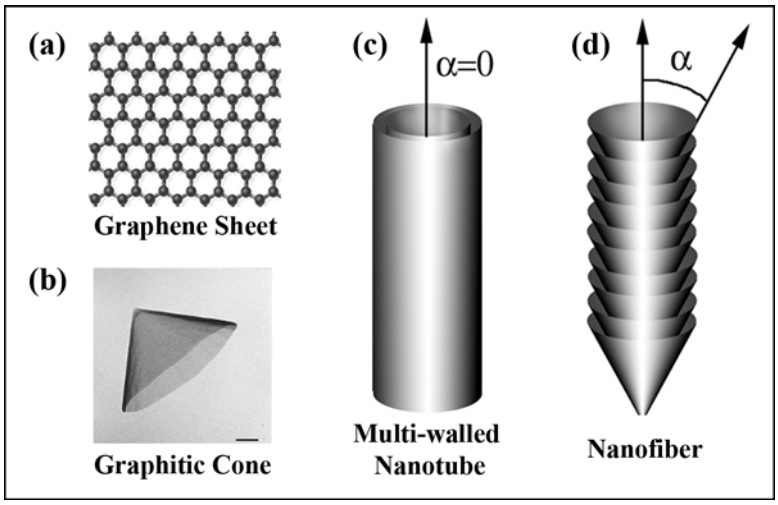

Figure 1.6 Illustration of carbon nanostructures: (a) hexagonal network of carbon (graphene), (b) TEM image of curved graphitic cone, (c) multiwalled carbon nanotube consisting of concentric graphene sheets, and (d) carbon nanofiber composed of stacked graphitic cones at an angle alpha with respect to the axis of the fiber. Adapted from [42,44].

Carbon nanotubes can be metallic or semiconducting, depending on how the graphene sheet is wrapped; there are three main types: zig-zag, armchair, and helical structures.[45] Figure 1.7 shows the electronic structure of a metallic armchair nanotube and a semiconducting chiral nanotube.[46] The calculated density of electronic states at the Fermi energy is finite for a metallic tube but zero for a semiconducting tube. The gap for the semiconducting nanotube is roughly 0.7 eV. At higher energies, sharp Van Hove singularities appear in the density of states for both the semiconducting and metallic nanotubes. While CNTs possess exceptional electrical and mechanical properties and are beginning to be produced in mass quantities, several obstacles for their widespread application remain, such as their alignment and the ability to grow selectively specific tube chiralities.

Carbon nanofibers are often called nanotubes, as they can display similar morphology despite distinct differences in their internal structures. Their physical and chemical properties, however, are quite different. While nanotubes are reported to display ballistic electron transport[47] and have the highest known tensile strength along their axis,[48] nanofibers have proven their robustness as individual, freestanding structures with superior chemical reactivity and electron transport across their sidewalls relevant to functionalization strategies and electrochemical applications, respectively.

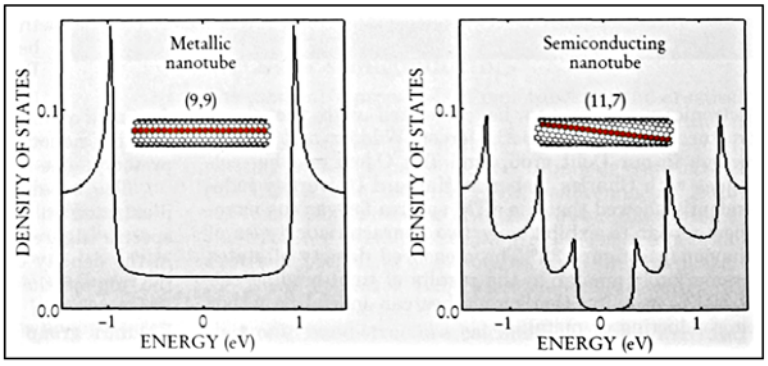

Figure 1.7 The calculated density of states for SWCNTs with metallic armchair structure (left) and semiconducting chiral structure (right). Adapted from [46].

1.3.2 Nanoparticles

Research has shown that the size, shape, surface chemistry, and optical properties of nanoparticles are all parameters which can be controlled, resulting in some very unique and fascinating capabilities. The unique properties of nanoparticles include particle size dependant luminescence from quantum dots (QDs), superparamagnetism in magnetic materials, and new and unusual crystal structures. Today we have the ability to design nanoparticle biological probes that meet specific challenges. Systematic characterization of the effect of size, morphology, charge, surface composition and other factors on the mobility (uptake/clearance) of these nanoparticles is critical for the design of nanoparticle probes as molecular *in vivo* imaging and therapeutic agents.

Semiconductor nanocrystals posses a narrow yet strong emission range that covers almost the entire UV-Vis-NIR spectral region depending on the particle size and composition. Metal and metal oxide nanocrystals also possess desirable optical properties and some also have an added magnetic component. These nanoparticles can be applied as thin films, in a polymer matrix or as colloidal photonic crystals for applications in light-emitting diodes, solar cells, or biolabels. Biolabeling is the addition of a marking substance, or label, to a biological sample. This biolabel can then be detected and information learned about the local biochemical environment and processes. For instance, nanoparticles can selectively bind to single receptors on cell surfaces for tracking applications or sense analytes and report on concentrations of species that are important for following pathways and monitoring microenvironments. In the past, fluorophores have been commonly used for this purpose, however labeling with nanoparticles has several advantages. Quantum dots are notably chemically and photochemically stable, delivering the same intensity signal in harsh environments and long periods of irradiation. In addition, nanoparticles can achieve quantum yields comparable to the brightest traditional dyes available while absorbing up to 1000 times more light, with a combined result of the single brightest class of fluorescence materials. This superior stability and brightness enables the observation of rare molecules that are unobservable by conventional methods. Lastly, the emission spectrum from quantum

dots is narrow and symmetric, which means spectral overlap with other colors is minimized. Cadmium selenide (CdSe) quantum dots, shown in Figure 1.8, are synthesized by a solution precipitation method. These QD nanoparticles produce photoluminescence due to radiative recombination of electron-hole pairs. As can be seen in the figure, quantum confinement of the exciton in all three dimensions leads to an increase in the effective band gap of the material with decreasing crystallite size, resulting in a shift of both the optical absorption and emission of QDs to the blue (higher energies) as the particle size decreases.[49]

Recently it has similarly been demonstrated that gold nanoparticles have polarized emission, can radiate more efficiently than single molecules, and are photostable under hours of continuous excitation.[50] These observations suggest that noble metal nanoparticles are a viable alternative to dyes or even semiconductor nanoparticles for biological labeling and imaging.

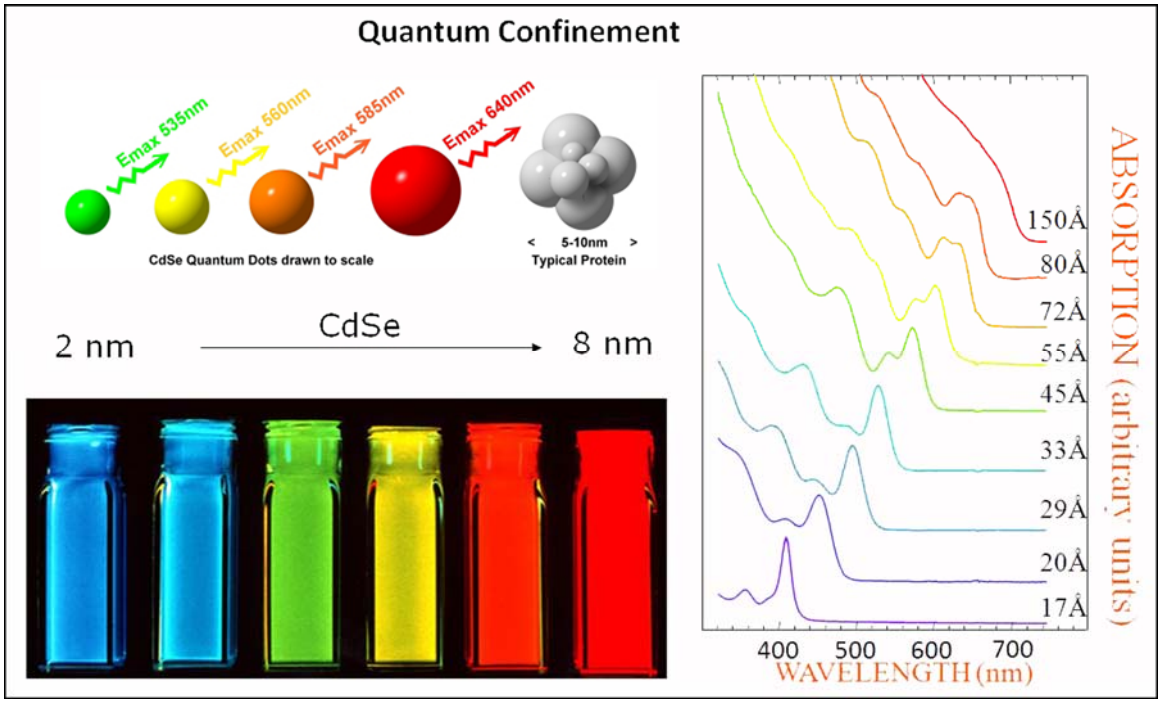

Figure 1.8 Size dependent florescence spectrum of CdSe QDs (upper left), a fluorescence image of the QDs as a function of size (lower left), and their absorbance spectrum as a function of size. Adapted from [49].

Gold particles have an especially great potential for cancer diagnosis and treatment due to SPR enhanced light scattering and absorption.[51] The shape and composition of gold nanoparticles tunes the SPR to the near-infrared range for *in vivo* imaging and photothermal therapy of cancer. Imaging and detection of cancer is attained through conjugation of gold nanoparticles to ligands that are targeted for biomarkers on cancer cells. The second functionality of the nanoparticles includes selective laser photothermal therapy in which they efficiently convert adsorbed light into localized heat.

Unlike conventional dyes, this tuning of the optical absorbance and scattering properties of noble nanometals is achieved by changing the size, shape, and composition of colloidal particles. As can be seen in Figure 1.9(a,d), increasing the concentration of Au in AuAg alloy particles results in a red-shift in the emission. Elongated nanoparticles, such as the gold nanorods in Figure 1.9(b,e), display two distinct plasmon bands related to transverse and longitudinal electron oscillations. The longitudinal oscillation is ultra sensitive to the particle's aspect ratio, such that minute deviation from spherical geometry can lead to impressive color changes.[32] Likewise, reports of asymmetric shapes such as silver nanoprism particles are also showing interesting optical trends [Figure 1.9(c,f)].

While many nanoparticles will assemble into continuous films or ordered arrays, dip pen lithography methods offer a viable way to locally pattern magnetic nanoparticles on a substrate.[52,53] Magnetic nanoparticles show a variety of unusual magnetic behaviors when compared to the bulk materials, mostly due to surface/interface effects, including symmetry breaking, electronic environment/charge transfer, and magnetic interactions. Core/shell magnetic nanoparticles morphologies have been reported.[54,55] Interestingly, when a sample containing a ferromagnet/antiferromagnet interface is cooled in a magnetic field, magnetic coupling at the interface may result in additional unidirectional anisotropy.[56] This phenomenon has been explored in colloidal ~8 nm Co nanoparticles at three stages in oxidation: native sample with a ~1 nm CoO shell, a partially oxidized sample with a thicker ~3.2 nm shell, and a fully oxidized sample.[55] It was reported that the partially oxidized nanoparticles exhibited exchange biasing while the native and fully oxidized samples did not, showing that this effect depends on a finite-thickness antiferromagnetic shell coupled to a finite-size ferromagnetic core.

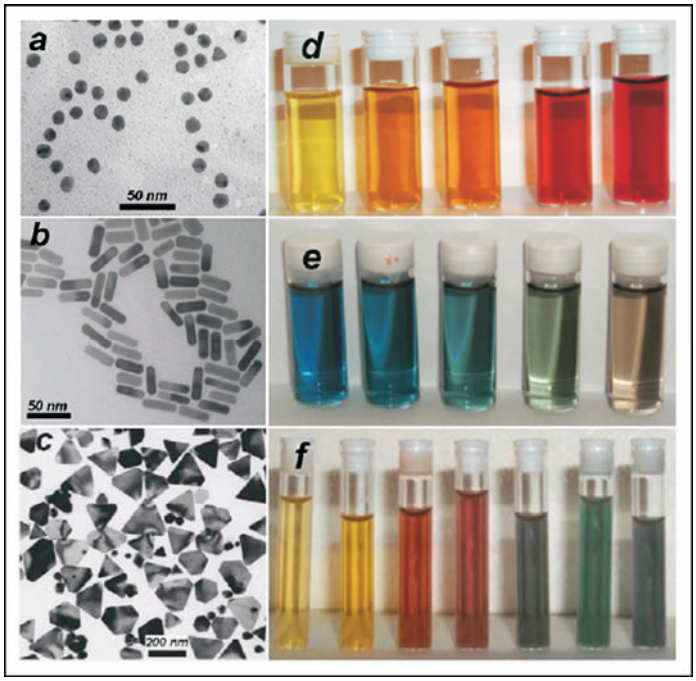

Figure 1.9 Optical properties of noble metal nanoparticles. Left: Transmission electron micrographs of Au nanospheres and nanorods (a,b) and Ag nanoprisms (c, mostly truncated triangles) formed using citrate reduction, seeded growth, and DMF reduction, respectively. Right: Photographs of colloidal dispersions of AuAg alloy nanoparticles with increasing Au concentration (d), Au nanorods of increasing aspect ratio (e), and Ag nanoprisms with increasing lateral size (f). Adapted from [32].

Magnetic nanoparticles are also finding an increasing number of bio-related applications. For instance, technologies utilizing patented thermo-responsive magnetic nanoparticles for cell isolation or biomolecule purification have been developed.[57] In this method, cell sorting by magnetic separation is achieved through the binding of magnetic beads to specific ligands on the surface of a cell and the bound cells are subsequently isolated with a magnet. Another example is the use of binary alloy nanoparticles, composed of a ferromagnetic metal and a non-magnetic material (eg. CuNi), for the self-regulating magnetic hyperthermia of cancer cells. Such promising binary alloys show lowered magnetic phase transition in the temperature range for inducing hyperthermia in cancer cells (314-319 K).[58]

1.3.3 Nanowires

Nanowires represent an important and diverse class of one-dimensional nanostructures at the forefront of nanomaterials research today, spanning such applications as nanoelectronics, nano-optoelectronics, nanosensors, nanobiotechnology, scanning probe tips, composite materials, and energy harvesting. 1D systems are the smallest dimension structures that can be exploited for the efficient transport of electrons and optical excitations, and therefore are considered to be critical to the operation of many nanoscale devices.[59] Both nanowires and nanotubes can carry charge and excitons efficiently,[46,59] making them ideal building blocks for nanoscale electronics and optoelectronics. CNTs have already been demonstrated as elements in devices such as field-effect and single-electron transistors;[60,61] however, to date the practical utility of nanotube components in electronic circuitry is limited, as it is still not possible to selectively grow semiconducting or metallic nanotubes. Nanowires, on the other hand, have delivered results, with highly controllable electrical properties achieved via selective doping.[62]

Typically, nanowires are high aspect ratio, single-crystal, highly anisotropic, semiconducting, insulating, or metallic nanostructures that result from rapid growth along one direction.[63] Depending on the crystal structure, the nanowire cross section is cylindrical, hexagonal, square, or triangular. Strategies for rational design and synthesis of nanowires have been developed with predictable control over important structural, chemical, and dimensional attributes. Over the past several years, the most prevalent synthesis techniques utilizes a catalyst or "seed" to define the wire diameter and location as well as confine the crystal growth to one dimension during vapor-liquid-solid (VLS) growth [Figure 1.10(a)], discussed further in Section 2.1.2. Modulated heterostructures of varied composition or doping [Figure 1.10(b)] can easily be formed with this method simply by changing the reactant supply during growth.[63] In addition, during VLS growth the crystallographic orientation of the nanowire is determined by the surface lattice of the substrate. This epitaxial aspect can be exploited for the assembly of branched structures [Figure 1.10(c)].[64] By decorating a nanowire with additional seed particles, epitaxial branches can then be grown forming 3D networks or junction arrays.

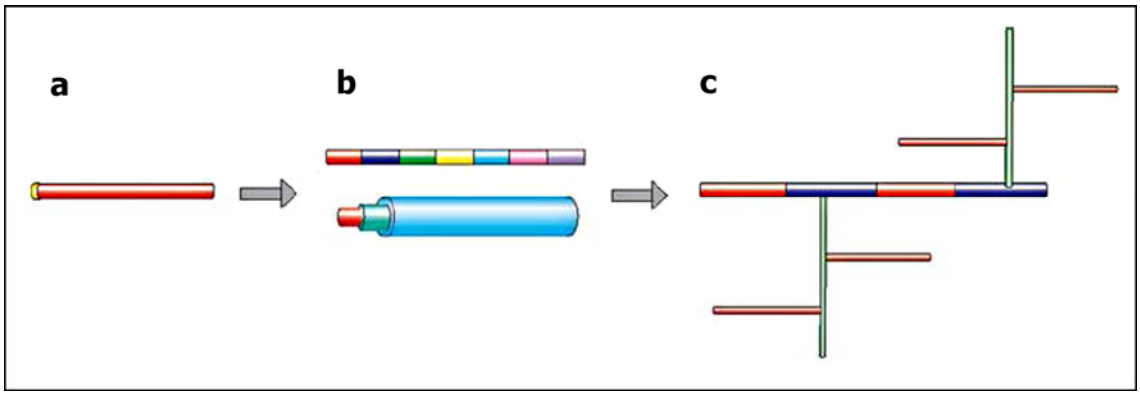

Figure 1.10 Illustration of the evolution of nanowire structural and compositional complexity enabled today through controlled synthesis, from (a) homogeneous materials to (b) axial and radial heterostructures and (c) branched heterostructures, where the colors indicate regions with distinct chemical composition or doping. Adapted from [[63].

Many types of semiconductor nanowires (III-V, IV) are commonly synthesized with gold nanoparticle catalysts. Indium phosphide nanowires [Figure 1.11(a)], for example, are particularly attractive because of their directly tunable band gap. The gate-voltage-dependent transport measurements displayed in Figure 1.11(b,c), illustrate that the nanowires can be predictably synthesized as either n- or p-type by selective doping with Te or Zn. In addition, the nanowires can be aligned by electric-field-directed assembly using an applied bias of ~100 V while suspended in solution, Figure 1.11(d). The individual doped nanowires function as nanoscale field-effect transistors and they exhibit rectifying behavior when assembled into crossed-wire p-n junctions [Figure 1.11(e)]. These junctions emit light strongly and are perhaps the smallest examples of light-emitting diodes that have yet been made.[62]

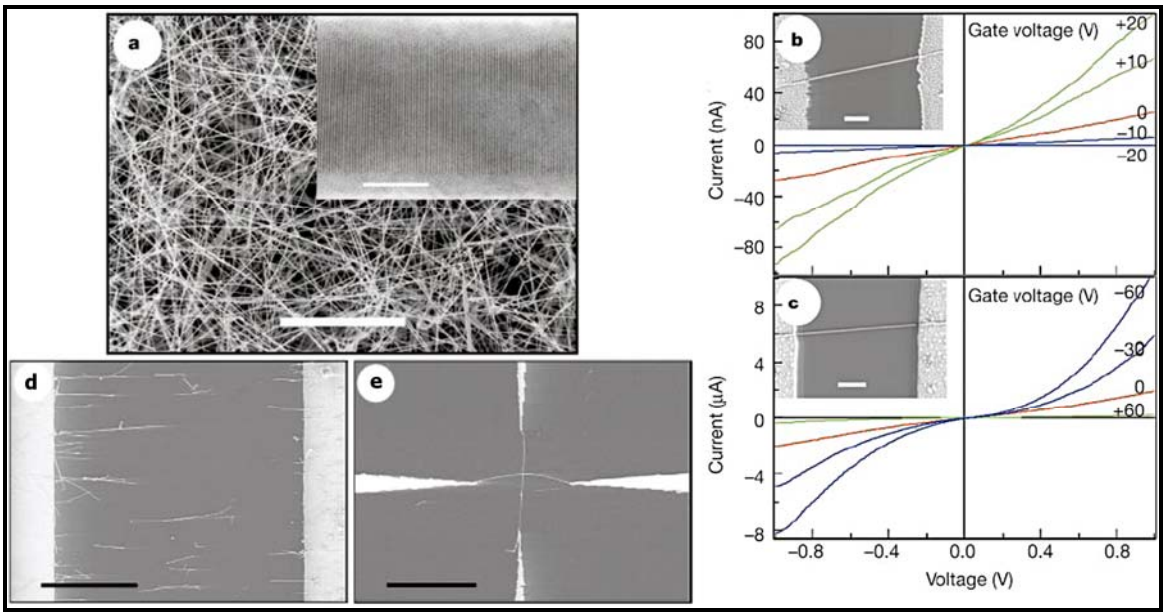

Figure 1.11 InP nanowires. (a) Typical SEM image (scale bar 10 mm) with inset displaying a lattice resolved TEM image of a 26 nm diameter Zn-doped nanowire (scale bar 10 nm). The (111) lattice planes are visible perpendicular to the wire axis. (b,c) Gate-dependent I-V behavior for Te- and Zn-doped InP nanowires, respectively. Insets show the nanowire measured with two-terminal Ni/In/Au contact electrodes (scale bars 1mm). Data were recorded at room temperature. (d) Parallel array of nanowires aligned between two parallel electrodes. (e) Crossed nanowire junction obtained using layer-by-layer alignment with the electric field applied in orthogonal directions in the two assembly steps. The applied bias in both steps was 80 V. Scale bars in (d,e) are 10mm. Adapted from [62].

Recent studies on the electrical and magnetic properties of metal nanowires have disclosed an assortment of fascinating properties. For instance, researchers have shown that the shot noise in metal nanowires may be suppressed[65] and the thermoelectric figure of merit greatly enhanced.[66] However, when a nanowire becomes smaller than the mean free path of an electron, depending on the grain size, it can exhibit a depressed conductivity caused by classical boundary scattering.[67] In addition, the quantized conduction of gold and copper nanowires immersed in liquids is reduced by the presence in the liquid of adsorbates such as adenine,[68,69] suggesting the application of metal nanowires as chemical sensors. A simple method has been described for depositing metallic nanowires (Mo, Cu, Ni, Au, and Pd) laterally on highly oriented pyrolytic graphite (HOPG) surfaces.[70] Nanowires were formed by selectively electrodepositing

either a metal or metal oxide at the step edges present on the basal plane of the HOPG electrode. The resulting nanowires were organized in parallel arrays of 100-1000 wires that were also "portable". After embedding the nanowires in a polymer film, arrays of nanowires could be lifted off the graphite surface, thereby enabling integration of the arrays into devices.[70]

As a final example, nanowires have been alternatively utilized as templated precursors for nanoparticle synthesis. It was discovered that fragmentation of copper nanowires into nanospheres takes place as a function of temperature well below the bulk melting point, driven by Rayleigh instability. This instability originates from atomic surface diffusion in conjunction with periodic variations in wire diameter. This type of experiment not only reveals the thermal stability limits of nanostructured materials to be used in devices but the resulting “string of nanospheres” could also find applications in nanophotonics, since it may be used to guide light below the diffraction limit via coherent coupling of surface plasmon polaritons.[71]

1.4 Challenges in Controlled Synthesis

As we have seen, the properties of nanomaterials can vary considerably from the bulk, exhibiting exciting new nanoscale phenomena. The controlled synthesis of these materials, by methods that permit their assembly into functional nanoscale structures, lies at the core of nanoscience and nanotechnology. By controlled synthesis, we refer to a process of collective nanostructure growth where the pertinent attributes such as location, size, orientation, composition, as well as electrical, mechanical, and thermal properties, of the individual elements can be selected *a priori* by the choice of the growth conditions and the preparation of the growth substrate. The research presented in this dissertation promotes understanding of the mechanisms by which synthesis conditions affect the morphology, composition, and crystal structure of nanostructured materials with the objective of achieving complete control over the synthesis process. Three types of systems are explored in depth: vertically aligned carbon nanofibers, catalytic alloy nanoparticles, and tungsten nanowires.

Carbon nanofibers are high aspect ratio, graphitic materials that have been considered for numerous applications due to their unique physical properties. Vertically aligned carbon nanofibers (VACNFs) are freestanding structures grown by catalytic plasma-enhanced chemical vapor deposition (PECVD) that are highly compatible with microfabrication, thereby facilitating their incorporation as functional nanostructured components a wide variety of devices.[72-86] These diverse applications are made possible by the *nearly* deterministic synthesis process of catalytic PECVD, which offers substantial control over geometrical characteristics such as location, length, diameter, and alignment.[44] However, deterministic synthesis also implies control over the nanofiber's internal graphitic structure, an aspect that remains elusive due to lack of a fundamental understanding of the processes that drive structure determination. This dissertation explores the intimate relationship between the catalyst and the growing nanofiber to answer the most fundamental of questions: how can graphitic structure be controlled? Experimental findings on the influence of the catalyst composition, crystal structure and orientation, as well as growth conditions on the internal structure of VACNFs will be elucidated.

Remarkably, as most of the catalyst metals used in carbon nanostructure synthesis are well known ferromagnets, encapsulation of this metal presents a unique opportunity to study the fundamental aspects magnetism under nanoscale confinement. In addition, the ability to encapsulate various metals within these carbon nanostructures is increasingly recognized as an opportunity to study the physical properties of these metals and metallurgical processes at the nanoscale.[87-91] In this dissertation research, the properties of bimetallic alloy systems Cu-Ni, Fe-Co, and Fe-Ni are studied throughout their evolution from thin films to encapsulated catalyst particles.

Lastly, electron-beam-induced deposition (EBID) is a promising nanoscale directed assembly technique capable of 3D, 2D, and 1D growth of a variety of dielectric, semiconductor, and metallic materials.[92] Metallic nanowires offer promise for a number of applications, including high-brightness field emission electron sources,[93-96] scanning probe tips,[97,98] mask repair,[99] and nanoscale electrical contacts.[94] In addition, higher growth rates actually occur at room temperature[100] and therefore EBID has an added advantage over traditional vapor-liquid-solid methods that require elevated substrate

temperatures. The EBID process, however, has been limited in many cases because precursor by-products [typically from organic precursors like $W(CO)_6$] do not completely desorb during growth and are incorporated into the nanoscale feature resulting in contaminated and amorphous structures.[101] To gain more control over the EBID process, this dissertation investigates the structural and compositional characteristics of EBID tungsten grown under various deposition conditions. The effects of growth parameters (namely beam energy, current, precursor pressure, and scan mode) on the deposit quality are characterized in depth by high-resolution electron microscopy, electron diffraction, and electron and x-ray spectroscopies.

1.5 Scope of Dissertation

The Chapter 1 introduction provides the reader with background on nanomaterials research, motivations for why nanomaterials are interesting to investigate, as well as a taste of the vast applications and emerging functionalities of nanomaterials to date. In addition, it sets forth the research challenges for the particular material systems investigated in this work. Chapter 2 supplies additional background on both the synthesis and characterization methods specific to the research presented in this dissertation. Chapter 3 centers on VACNFs, establishing the concept of co-synthesis and presenting new methods for internal graphitic structure control. Chapter 4 presents studies exploring the phase diagrams of binary alloy systems and the link between composition and suitability for VACNF catalysis. The structure, phase, and magnetic properties of the alloy nanoparticles are also characterized. Chapter 5 includes characterization results of novel tungsten nanowire structures deposited by electron-beam-induced deposition and correlates how the nanowire purity, crystal structure, and crystal orientation vary with the electron beam scanning conditions. Finally, concluding remarks and suggestions for future direction are given in Chapter 6.

2. Methods and Instrumentation

2.1 Synthesis Methods

Nanoscale materials can be synthesized, shaped, and assembled via a variety of techniques. These strategies utilize precursors from liquid, solid, or gas phase and often employ physical or chemical deposition approaches. This section will describe several methods and processes used to synthesize nanostructured materials in this dissertation research. These techniques include catalytic vapor-liquid-solid or vapor-solid-solid, physical vapor deposition, chemical vapor deposition, plasma-enhanced chemical vapor deposition, and electron-beam-induced deposition.

2.1.1 Overview of Approaches

There are two philosophically distinct approaches when it comes to nanostructured materials synthesis: “top-down” and "bottom-up", depicted in Figure 2.1. The top-down approach begins with a suitable starting material and then "sculpts" functionality from this starting material, whereas the bottom-up approach forms nanostructured “building blocks” from atoms or molecules and guides the assembly of these building blocks into the final material.

In general, the top-down method uses techniques such as lithography, writing, and stamping essentially to impose a structure or pattern on the substrate. Ball milling could also be considered a top-down technique, in which nanostructures are formed through controlled, mechanical attrition of bulk powder material. Unlike solidification methods such as physical vapor deposition, mechanical attrition produces nanostructures not by cluster assembly, but by structural decomposition of coarse-grained materials through severe plastic deformation.[102] The nanoparticles formed by ball milling are then subsequently compacted into a new bulk material.

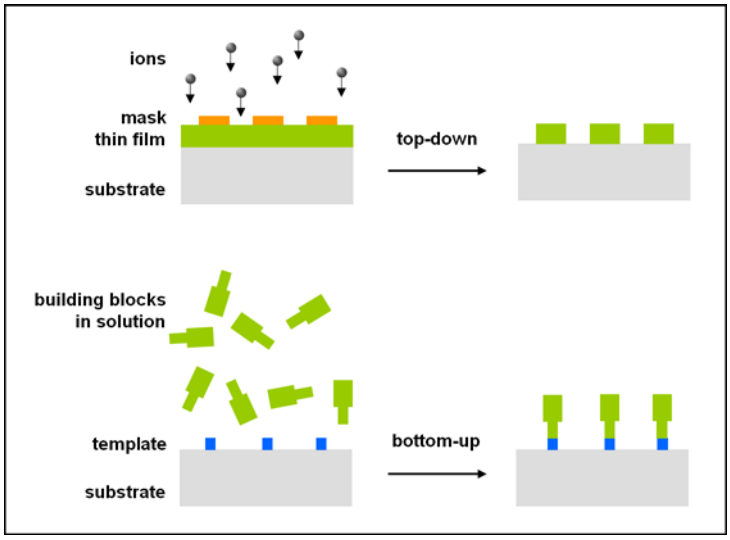

Figure 2.1 Schematic of top-down and bottom-up approaches. In the top-down method material is removed by ion etching from around a lithographically-defined mask, resulting in nanostructure. In the bottom-up approach building blocks in solution assemble on a templated surface to form nanostructure.

Often, the top-down approach implies "extreme miniaturization" of components, as proposed in Feynman's lecture.[14] This concept has been employed for many years by the semiconductor industry to fabricate microelectronic devices out of a silicon substrate. In general, small features are patterned in bulk materials by a combination of lithography, etching, and deposition to form functional devices. These processes today have the necessary spatial resolution to routinely create structures at the nanoscale; however, even though developments continue to push the resolution limits of the top-down approach, the improvements in resolution incur a near exponential increase in the cost associated with each new generation of manufacturing facilities.[63] Thus economic factors as well as other scientific challenges associated with the top-down approach, such as making nanostructures with atomic precision, have stimulated scientists worldwide to search for new synthesis strategies.

The latest groundbreaking nanotechnology approach is to build upward from molecules and nanoparticles, in the so-called bottom-up or building blocks approach. This approach presents a powerful alternative to conventional top-down methods because it parallels nature's practice of utilizing proteins and other macromolecules to construct

complex biological architectures. In fact, many current strategies for material synthesis integrate both synthesis and assembly into a single process to create superstructure. These strategies include self assembly[103] and directed assembly[44,63] techniques that are increasingly employed for nanostructure synthesis. It is likely that the bottom-up approach may enable novel device concepts by, for example, seamlessly combining chemically distinct nanoscale building blocks (unable to be integrated by traditional top-down processing) to create unique functional nanosystems.[63] For the most part, the methods utilized in this dissertation for materials deposition and growth can be considered controlled synthesis and directed assembly processes where materials are created from the bottom up with an advanced level of control over the material location and structure by altering parameters during the synthesis process.

2.1.2 Catalytic Synthesis of Nanostructures

A catalyst is a chemical substance that is used to increase the rate of a chemical reaction. However, unlike other reagents that participate in the chemical reaction, a catalyst is not consumed by the reaction itself. In general, a catalyzed reaction has a lower rate-limiting change in free energy to the transition state (i.e. lower activation energy) than the corresponding uncatalyzed reaction, which results in a larger reaction rate occurring at a lower temperature. Catalysts can be used to facilitate the growth of nanostructures by converting vapor precursors into solid material via either the vapor-liquid-solid (VLS) or vapor-solid-solid (VSS) growth mechanisms.

The VLS mechanism was first defined by Wagner and Ellis in 1964 to describe the growth of single-crystal silicon "whiskers" from gold impurities.[104] VLS refers to a deposition route involving the condensation of vapor species into a miscible liquid catalyst, followed by the supersaturation of species, and subsequent precipitation, producing the solid phase. In this process, the role of the catalyst is to form a liquid alloy with the vapor material with a *depressed* melting temperature, T_e, due to eutectic composition as demonstrated by step (I) in Figure 2.2. The liquid droplet is a preferred site for catalytic adsorption of the vapor, causing the liquid to become supersaturated

with the vapor material, which is the driving force for crystal nucleation, step (II). In this way, 1D single-crystal nanowires[63,105] (see Section 1.3.3) are commonly grown with catalyst riding atop the growing nanowire, as in step (III). It can be seen that temperature and partial pressure of the gaseous precursor (in this case, Ge) are key to the progression of nanowire growth.

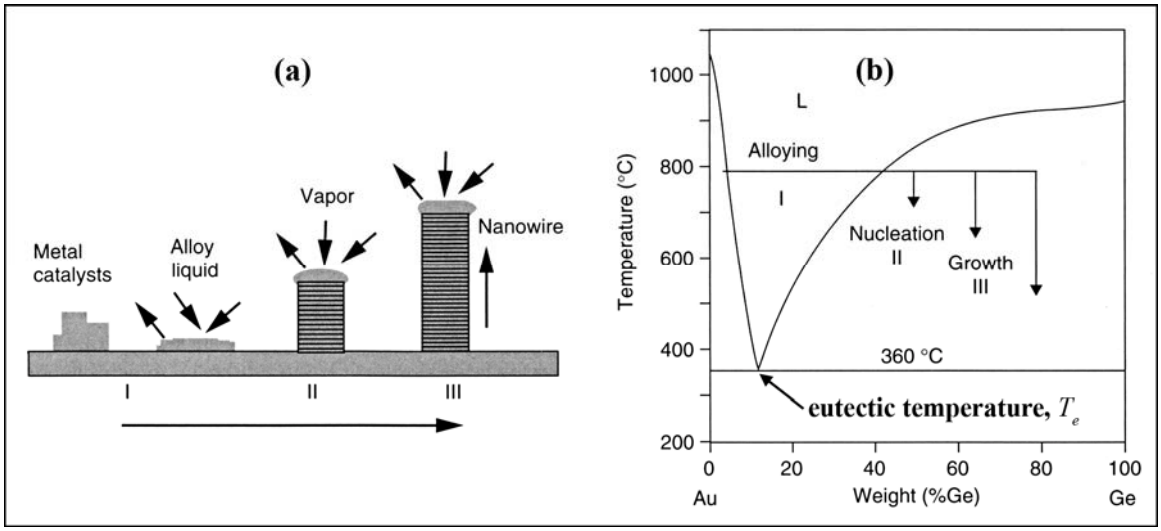

Figure 2.2 Schematic of the VLS growth process (a) and binary Au–Ge phase diagram (b) with the labeled zones responsible for alloying, nucleation, and growth. Adapted from [105].

Though VLS is the more commonly assumed route for nanowire growth, there have been a number or reports for the formation of nanowires on catalyst particles at temperatures well below the T_e,[106,107] which can only be explained by two reasons: either the diameters of the catalyst particles are small enough (< 20 nm, Figure 1.3)[17] that the melting temperature is significantly depressed, or that the catalyst remains solid and growth proceeds by the VSS mechanism. Using *in situ* TEM Persson *et al.* demonstrated that the VSS mechanism is in fact operative for GaAs nanowire growth from Au catalysts and that the nanowire elemental species are transported by solid-state diffusion.[107] The crystallinity of the nanoparticle was verified by diffraction patterns from the nanowire catalysts heated above the growth temperature (540°C), which is strong evidence that the catalyst remains solid during growth. Changes in the shape of the heated nanoparticle were attributed to enhanced surface diffusion of the solid particle. Furthermore, *in situ* XEDS showed a composition of only Ga in the Au particle at levels *below* the eutectic melt composition, signifying that a solid alloy of Au and Ga forms and that As reacts with the Ga after precipitation.

Another landmark study by Kodambaka *et al.* probes the controversial state of the catalyst during nanowire growth below T_e.[106] They too used *in situ* TEM and showed that both liquid and solid catalysts actually coexist at the same depressed temperature, both catalyzing nanowire growth. These two growth modes occurring under the same conditions had drastically different growth rates—VSS growth was 10 to 100 times slower than VLS growth. In addition, they found that rather than the particle size being the discriminating factor, unexpectedly the catalyst state depends more on the thermal history and precursor pressure. While the existence of a liquid state below T_e is undoubtedly stabilized by the particle's nanoscale size and supersaturation, the liquid-solid phase transition exhibits hysteresis effects; once a liquid nanoparticle finally does solidify, it has to be heated up to the T_e to actually melt again. So it is not size alone that influences the melting point; high pressure appears to be as essential as temperature for stabilizing the liquid state below T_e.[106] Kodambaka *et al.* observed that a reduction in pressure causes the catalyst droplets to solidify, oddly with the *smaller* diameter particles solidifying first, seemingly in contradiction with the melting point dependence on diameter.[17] One would expect the smaller droplets would be more resistant to

solidification due to a lower melting point. Kodambaka *et al.* offer an explanation for this anomaly: the liquid phase is stabilized against solidification by Ge supersaturation, which directly relates to pressure. When the Ge source gas pressure is lowered, supersaturation in the particle decreases by excess Ge incorporation into the nanowire. The Ge loss rate from the particle is proportional to the cross-sectional area ($\sim D^2$), whereas the amount of Ge excess in the particle is proportional to the volume ($\sim D^3$). Thus the timescale for loss of the supersaturation condition increases with wire diameter.

Likewise, one of the debated issues for carbon nanostructure growth is whether the catalyst is solid or liquid during growth.[108] While VLS models assume a liquid catalyst, CVD is typically carried out at temperatures of less than 1000°C, well below T_m for Ni or its eutectic with C (see Table 3 in Section 4.6). Thus, for growth of carbon filaments, solid phase diffusion through a metal catalytic particle has been a widely accepted growth mechanism for quite some time,[43,109] where there is agreement between the enthalpy for growth and the enthalpy for bulk diffusion. However, the small size of some catalysts (< 20 nm, used mainly for CNT growth) may allow the material to melt at these temperatures.[17] Thus others are convinced of the VLS model for CNF/CNT growth, where evidence of the liquid phase is demonstrated by observations of particle shape changes during initial stages of growth (discussed further in Section 3.4.1), the droplet-like equilibrium shape of the catalyst, and the metal filling of tubular cavities.[110,111] Predicting the exact physical state of the catalyst is difficult due to several factors including shape changes of the catalyst, carbon content levels, the catalyst-support interface, and the catalyst nanoparticle-graphite interface.[111] It is highly possible that all three states (solid, liquid, and solid + liquid) may be present in a given growth due to distribution in catalyst size.

2.1.3 Physical Vapor Deposition of Thin Films

There are numerous ways to prepare catalyst particles for carbon nanofiber growth. One of the most common approaches is to deposit a thin film of catalyst material and then dewet it at elevated temperatures to form discrete nanoparticles. In this approach, a thin metal film must first be deposited either by electro-plating, electroless-plating, or most commonly by physical vapor deposition (PVD). There are three main steps in any vapor deposition process: (1) synthesis of the material to be deposited (transition from condensed phase to the vapor phase or for the deposition of compounds, reaction between the components of the compound); (2) transport of the vapors between the source and the substrate; (3) condensation of vapors followed by film nucleation and growth.[112] The third step, as depicted in Figure 2.3, is the most complex and the subject of much research. In this step atoms from the vapor become mobile adsorbed atoms on the surface that then join into small clusters that are still mobile. The clusters then grow into more stationary nuclei, which then become stable islands that grow both upwards and sideways, eventually coalescing with neighboring islands to form a continuous film. Textured or epitaxial films can occur under the right conditions and if the substrate and film have similar atomic structure and spacing.

The PVD process contrasts chemical vapor deposition in several ways; namely, it relies on solid or molten sources as opposed to gaseous precursors in CVD, it takes place in a reduced pressure environment for the efficient transport of vapor species, and there is a general absence of chemical reactions in the gas phase and at the substrate surface (with the exception of reactive sputtering).[113] In addition, in CVD all three steps above take place simultaneously at the substrate and cannot be independently controlled.[112] In PVD however, these steps can be independently influenced, giving a much greater degree control of over the structure and properties of the deposit as well as the deposition rate.

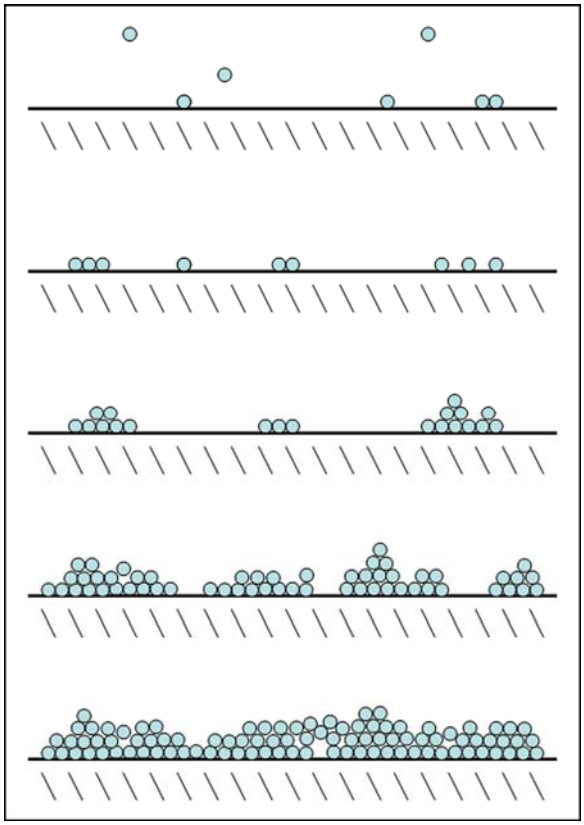

Figure 2.3 Film nucleation and growth.

PVD can be accomplished either by sputtering or evaporating techniques, both which have their advantages and disadvantages. While sputtering allows for alloy depositions from an alloy target, alloys cannot be directly evaporated due to differences in the vapor pressure of each element. Evaporation does have it advantages, though, mostly attributed to its highly directional deposition, enabling patterns to be easily transferred to the substrate by resist lift-off methods.

Since the inception of both PVD techniques in the 1850's, evaporation was the preferred technique until the 1960's due to the general applicability of evaporation to all classes of materials in addition to advances in Joule heating sources and vacuum pumping, which lead to higher deposition rates and cleaner environments for film growth.[113] However, beginning in the 1960's the need for alloy films with precise stoichiometry for the microelectronics and magnetic applications fostered the development and common use of sputtering. In parallel, the development of CVD

methods for non-metallic films also reduced the reliance on evaporation. Today, techniques such as pulsed laser deposition are finding new ways to exploit the thermal evaporation process with high deposition rates and conservation of the target source stoichiometry due to the extremely high temperatures reached.

2.1.3.1 Evaporation

In the evaporation process atoms are transferred from a heated source to a substrate located a distance away. The thermal energy given to the source atoms must be sufficient such that their temperature is raised to the point where they can efficiently evaporate or sublime into vacuum. Once this happens, the atom will continue travelling in a straight line until it hits the substrate or another surface. On the substrate, film nucleation and growth proceeds atomistically (under controlled conditions) with a typical deposition rate of 1 to 10 nm/second. In the e-beam evaporation technique, a high-energy electron beam from an electron gun is bent at a 270° angle (to avoid gun filament exposure to the evaporant flux) onto the target, boiling off a small area of source material. The evaporation flux (Φ_e), or the number of atoms evaporated from the target per unit area and unit time, is given by the Hertz-Knudsen equation:

$$\Phi_e = \frac{\alpha_e (P_e - P_h)}{(2\pi \mathrm{m} k_B T)^{1/2}}, \qquad \text{Eq. (2.1)}$$

where α_e is the coefficient of evaporation (value between 0 and 1), P_e is the equilibrium pressure, P_h is the hydrostatic pressure acting on the evaporant, m is the molecular weight of the source material, and k_B the boltzmann constant. Evaporation will only occur when $P_e > P_h$ and the maximum evaporation rate is realized when $\alpha_e = 1$ and P_h is zero.[113]

2.1.3.2 Sputtering

The mechanism of sputtering is inherently distinct from evaporation in that the impact of a gaseous ion ejects atoms from the target surface, which is usually maintained at room temperature. Typically, plasma of noble gas (i.e. Ar) is used to knock material from the target. The sputter yield (S) of a given material is a property measure of the number of ejected target species per incident ion. The optimal operating conditions are represented by the linear cascade model where one incident ion produces a cascade of atom displacements. In this regime, the sputter yield is represented by,

$$S = \frac{3\alpha 4 M_1 M_2 E}{4\pi^2 (M_1 + M_2)^2 U_S} \qquad \text{for } (E < 1\text{keV}), \qquad \text{Eq. (2.2)}$$

It is a function of the mass of both the incident ion (M_1) and the source atom (M_2), the incident angle of the ion (α, function of M_2:M_1 ratio and angle), the incident ion particle energy (E), and the binding energy of the source material (U_S).[113]

A sputtered atom typically has tens of eV arriving at the substrate surface, in comparison to thermal energies of evaporated films, which are on the order of tenths of an eV ($\sim \frac{3}{2} k_B T_S$).[113] Thus sputtering leads to better mixing at the interface and adhesion relative to evaporated films. In addition, substrate heat and bias parameters can have a profound effect on the film properties such as adhesion, residual stress, crystal structure, orientation, density, and grain size. Choi *et al.* reported controlling the grain size of sputtered Ni films by varying the power, which in turn affected the diameter, length, and purity of the CNTs grown from the film.[114]

The majority of catalyst films in this work were deposited by a radio frequency (RF) magnetron sputtering system ideal for deposition of alloy materials, multilayers, metals, semiconductors, and insulators. Features include a base pressure ~5×10^{-9} Torr, load lock, 3 positionable 2" sources, substrate heat (up to 800°C), and bias capabilities. In general, a chamber pressure of ~100 mTorr is optimal because if the pressure is too low then the plasma cannot generate ions efficiently but if the pressure is too high ion

scattering will increase, causing deposition to decrease. For the deposition of alloys and especially films of gradient composition, the co-sputtering technique shown in Figure 2.4 was used, where two or more different sources are simultaneously sputtered onto the substrate.

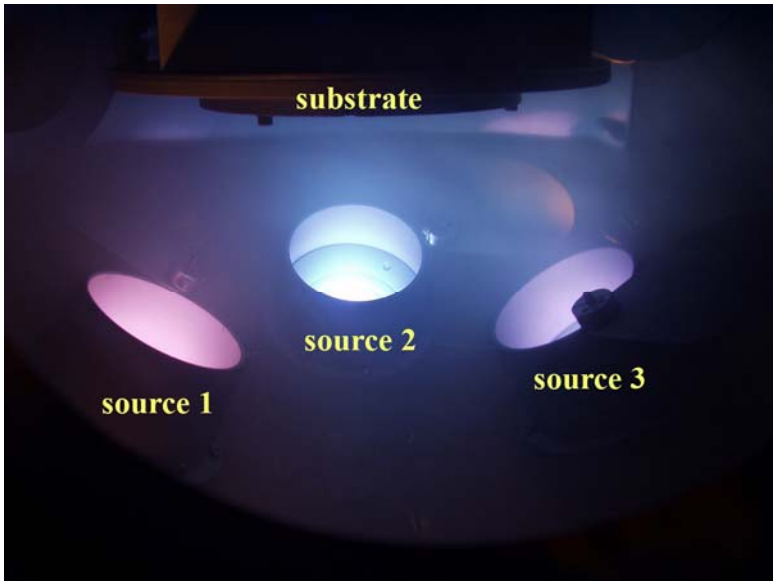

Figure 2.4 View of inside the sputtering chamber showing the co-sputtering of three different source materials onto the substrate.

2.1.4 Chemical Vapor Deposition

Chemical vapor deposition (CVD) is a technique for depositing materials commonly used for high-performance mechanical coatings and in the electronics industry for high-quality insulating and epitaxial thin films. The ability to deposit a wide variety of films including metals, semiconductors, and organics in crystalline or amorphous forms with varying stoichiometries is a unique advantage of the CVD technique. In this process, a volatile compound containing the material to be deposited is chemically reacted with other gases to produce a nonvolatile solid that deposits atomistically on the substrate.[113] It differs from PVD techniques in that it does not rely on direct material transfer from condensed-phase evaporant or sputtered sources and therefore CVD does not require vacuum and can coat non-line-of-sight surfaces. Flow conditions, pressure, and temperature are critical parameters to achieve uniform heterogeneous nucleation at the substrate rather than homogeneous nucleation in the gas phase. In addition, CVD processes often require elevated substrate temperatures (e.g. pyrolysis) to achieve the desired reaction rates and film quality. When heat is the main energy source for the necessary reactions to occur, and to differentiate from plasma activated CVD, the process will be referred to as *thermal* CVD.

In general, graphitic carbon nanostructure growth by thermal CVD requires three main things: catalyst nanoparticles (see Section 2.1.2), a carbonaceous source gas (e.g. hydrocarbon or CO), and heat. Details of the catalytic CVD growth mechanism will be discussed further in Section 3.1.2. Process temperatures for catalytic thermal CVD production of carbon nanostructures typically lie in the range from 400°C to 1000°C. The apparatus for catalytic thermal CVD usually consists of a quartz tube furnace with a controllable source gas flow. This method has been successfully used to synthesize a whole range of carbon nanostructures with the earliest observed being carbon nanofibers in the late 1950s.[115-117] More recently, catalytic thermal CVD has been optimized for growth of MWCNTs,[118] and even SWCNTs.[119]

2.1.5 Plasma-Enhanced Chemical Vapor Deposition

Plasma-enhanced chemical vapor deposition (PECVD) is similar to CVD which also uses a gaseous precursor. The central difference is that in conventional CVD only thermal energy is used to activate the gas, whereas in PECVD activation is achieved by electron impact, enabling lower temperature film growth. For example, a deposition temperature of 500 – 900°C is required for Si deposition by CVD, whereas a temperature of 250 – 350°C is sufficient in PECVD. Gas activation takes place in a non-equilibrium plasma characterized by charged species with a much higher kinetic energy than neutral species, generally referred to as a glow discharge. The discharge decomposes gas molecules into several kinds of species including electrons, ions, atoms, free radicals, and molecules in ground and excited states. A variety of plasma sources have been regularly applied for the deposition of dielectric (silicon oxide and nitride) and diamond thin films. Recently, these same methods have proven practical for carbon nanostructure growth. These plasma sources include direct current (DC-PECVD), RF capacitively coupled, RF inductively coupled, microwave, electron cyclotron resonance, hollow cathode, and corona discharge, all of which are reviewed in [44]. For the purposes of this dissertation, discussion will be limited to DC-PECVD processes. A typical DC-PECVD system, pictured in Figure 2.5, consists of a vacuum chamber (A), vacuum pumps (below chamber, not shown), and a pressure control system (B); a gas flow control system that includes mass flow controllers (C), gas manifold and inlet (D), and a showerhead (E) for uniform gas mixing and distribution over the substrate; a substrate heater (F,G) with a temperature control system (H); and a power supply for plasma excitation (not shown, bias applied to E and F).

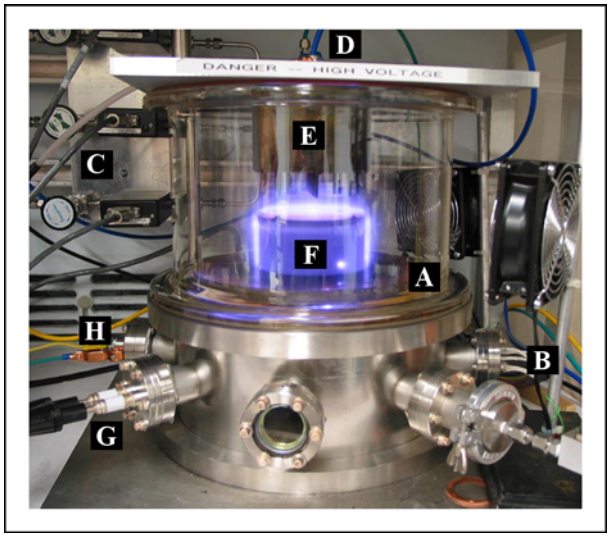

Figure 2.5 Carbon nanofiber DC-PECVD reactor with labeled components: A) glass cylinder vacuum chamber, B) pressure transducer, C) mass flow controllers for gases, D) gas inlet, E) gas showerhead/anode, F) substrate heater/cathode covered by glow discharge, G) high current heater wiring, H) thermocouple wiring.

As in the case of thermal CVD, the growth of carbon nanofibers by PECVD also occurs through a catalyst (not by direct surface deposition). The main advantage of using plasma enhancement is to reduce the activation energy for a deposition process. In order to understand the carbon nanostructure synthesis in a PECVD reactor, the basic processes involved in a plasma will be briefly reviewed. For the simplest case using DC power, the substrate must be electrically conductive. To initiate a glow discharge, a DC voltage is applied across a chamber filled with gas at low pressure (a few Torr). Upon application of the bias, any free electrons in the gas are rapidly accelerated (due to their minuscule mass) to the positively charged anode, colliding with more gas molecules on the way and producing a cascade (breakdown).

While globally neutral, the glow discharge can be divided into four visible regions due to separation of charged species. These regions labeled in Figure 2.6(a), as arranged from cathode to anode, include: cathode dark space, negative glow, Faraday dark space, and positive column.[120] The glow discharge is maintained by the processes near cathode and the positive column region is not used in PECVD processes. Figure 2.6(b) shows the physical processes occurring in the cathode dark space: (1) first an ion accelerates toward

the surface of the cathode and upon impact knocks out a secondary electron; (2) then the electron is accelerated across the dark space and collides with a neutral gas atom; (3) this collision produces an ion and an electron; (4) subsequently, the ion is accelerated toward the cathode and the electrons continue toward the anode. This series of collisions excites molecules, sometimes ionizes them, and the visible negative glow is the result of this excitation process. Figure 2.6(c) shows the effect of the substrate material on the glow discharge. This disparity is likely due to a difference in the yield of secondaries, resulting in a brighter negative glow above the silicon substrate.

In the dark space, the current is carried primarily by ions, while in the negative glow it is carried by electrons. The negative glow is therefore a low impedance region and the applied voltage drops mostly over the dark space.[113,120] Since the dark space varies from a few hundred micrometers to a few millimeters, application of several hundred volts can create electric fields on the order of 10^4 V/cm.[44] In a typical plasma, ions constitute only 1 ppm of the total gas species, whereas the fraction of neutral radicals is on the order of 1%.[120] Thus the growth of films is essentially due to the neutral radicals and species that form due to collisions of these radicals as they move across the dark space towards the substrate.[121]

A drawback of PECVD deposition is that it is an inherently "dirty" process where gas-phase reactions can cause particulate formation.[120] In addition, cross-contamination is observed between depositions of different chemistry due to interaction of the plasma with the chamber walls and other coated surfaces. Therefore, unless the chamber is dedicated to a single set of conditions, PECVD can require *in situ* cleaning processes or chamber conditioning between runs.

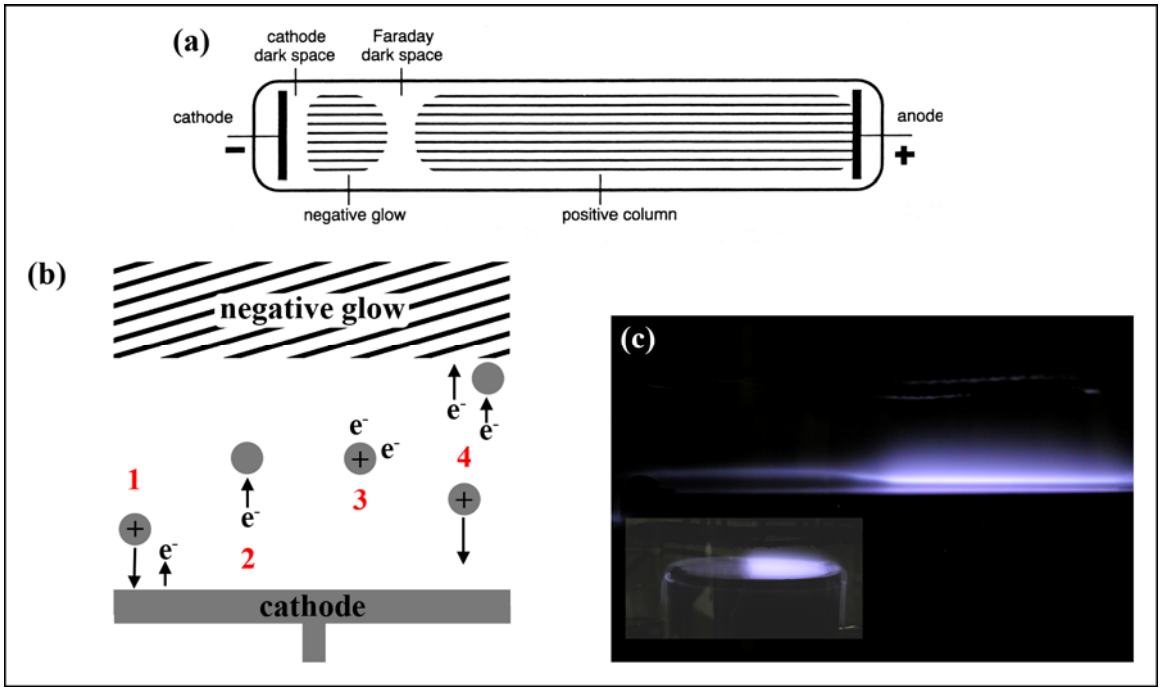

Figure 2.6 Processes in DC-PECVD. (a) Schematic of glow discharge in a long tube, adapted from [120]. (b) Physical processes occurring in the dark space above the cathode. (c) Photograph of the plasma above a 100 cm silicon wafer in which the left half is coated with 100 nm of tungsten. The plasma conditions (700°C, 80 sccm NH_3, 50 sccm C_2H_2, 3 Torr, 200 mA) are visibly more favorable for glow discharge on the right side above the bare silicon than on the left side above the tungsten.

2.1.6 Electron-beam-induced Deposition

Electron-beam-induced deposition or EBID has recently gained attention as a promising directed assembly technique for nanoscale materials synthesis. EBID is the process by which a solid material is deposited onto a substrate through the electron-mediated decomposition of a precursor molecule containing the desired species to be deposited. Figure 2.7 shows an illustration of the *ideal* process. First a precursor, typically in gaseous form (however liquid or viscous solids can be used), populates the substrate surface. Then a region is exposed to an electron beam, which dissociates the precursor. As a result, the nonvolatile component deposits as solid in the exposed area,

while the volatile byproduct component of the precursor is desorbed from the surface and pumped from the vacuum chamber.

EBID was initially observed in the context of carbon contamination or "staining" during electron microscopy as a result of residual carbonaceous gas species.[122,123] However, current applications of EBID involve the intentional introduction of precursor vapor to elevate the vacuum background to a high partial pressure of the desired species. In this manner, the primary deposit component is a derivative of the precursor species rather than the chamber's residual background species. As early as 1961, EBID was being exploited in order to selectively deposit a variety of materials. For example, Baker and Morris utilized several organometallic precursors to deposit large-area tin and lead films by EBID.[124] The *ideal* metallic EBID process is depicted in Figure 2.8 where a metal-containing vapor, M–X, is dissociated by an electron beam to produce a metal deposit, M, on a substrate, S, and a volatile byproduct, denoted by X.

EBID nanostructure controlled synthesis must be performed in a vacuum environment in order to reduce electron scatter and contamination of the deposit. Most commonly EBID has been realized in a modified SEM, but TEMs, STEMs, and dual-beam focused ion beam (FIB) instruments have also been used.[92] Typically modification of aforementioned systems with some type of vapor injection system is necessary. Standard scanning electron microscopes are capable of rastering the beam so as to deposit simplistic patterns such as points, squares, rectangles, and lines. However, more complex deposit geometries require integration of a pattern generator.

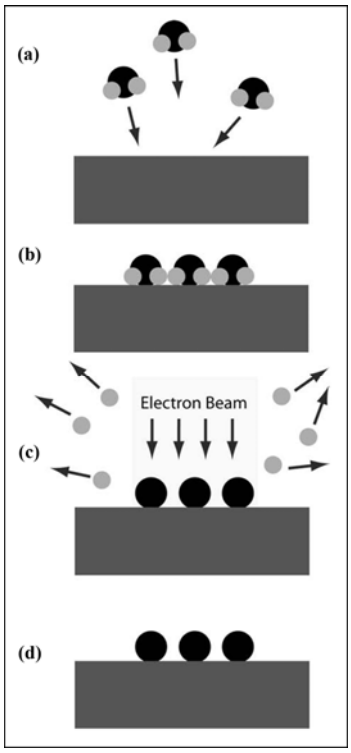

Figure 2.7 Illustration of an ideal EBID process. (a) A precursor vapor is introduced to the substrate and (b) adsorbs to the surface. (c) The substrate is exposed to an electron beam in the region of the incident vapor plume, inducing a dissociation reaction and (d) resulting in a solid deposit and a volatile byproduct. Adapted from [92].

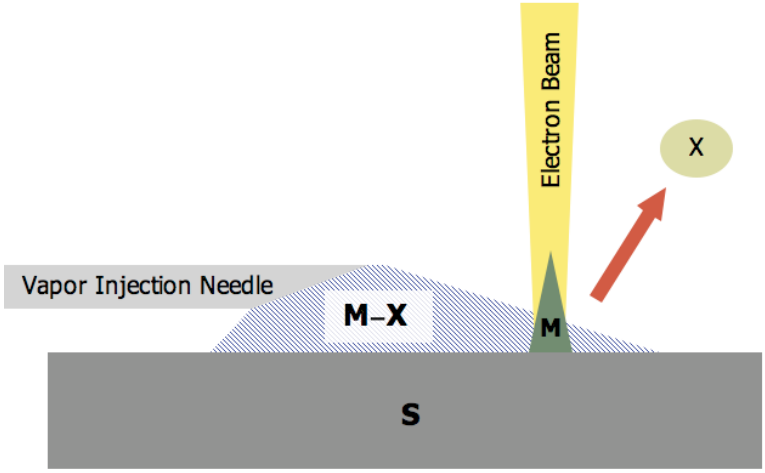

Figure 2.8 Generalized EBID mechanism. A metal-containing precursor, M-X, is introduced to a substrate, S. The substrate is exposed to an electron beam in the region of the incident vapor plume. The electron bombardment induces a dissociation reaction resulting in a metal deposit, M, and a volatile byproduct, X. Adapted from [100].

2.2 Characterization Methods[†]

Materials scientists strive to find the link between structure and properties. Structural features of a material consist of the types of atoms, the local configurations of these atoms relative to one another, and the arrangements of these configurations into nano and microstructures. The rapid surge in new synthetic nanomaterials has demanded complementary advancement in characterization techniques in order to understand and utilize these materials. The complex morphology of nanostructured materials also creates new challenges for their characterization. For example, the development of surface science over the last century has been based on the assumption that the sample presents a flat, well-defined surface, which is examined under ultrahigh vacuum. The translation of traditional surface characterization techniques to the study of complex three-dimensional functional surfaces is nontrivial and the methods employed are often specific to each particular family of nanostructured materials. The development of new techniques such as nanoindentation[125] has greatly increased our ability to characterize the mechanical properties of nanostructured materials. Other improvements such as aberration correction in high-resolution electron microscopes[126] and image modeling performed by a variety of computational methods, continually advance our knowledge of structure at the nanoscale. This section gives background on the primary materials characterization methods that were specifically employed in this dissertation research. These methods include an array of analytical microscopy, spectroscopy, and diffraction techniques as well as magnetometry.

2.2.1 Electron Microscopy

Electron microscopy is a powerful method to characterize materials especially when coupled with analytical tools. Secondary electron microscopy (SEM) is perhaps the most frequently used method of characterizing the morphological structure and

[†] This section contains lightly revised passages and figures from [39].

topography of a sample. Transmission electron microscopy (TEM) and scanning transmission electron microscopy (STEM) not only provide information about the morphology, but also reveal the atomic structure of the sample by high-resolution TEM (HRTEM). A common companion tool to the SEM, TEM, and STEM is an x-ray energy-dispersive spectrometer (XEDS), which readily gives the elemental composition of the sample and can also be useful in generating elemental maps. The electron interactions with a sample are shown in Figure 2.9. It can be seen that Auger electrons highly surface-sensitive, originating from a depth of less than ~10 Å, while secondary electrons (SE) come from ~50-500 Å deep depending on the accelerating voltage and the material density. Backscattered electron (BSE) imaging is not as useful for nanostructure characterization because the escape depths of backscattered electrons are generally on the order of 1 μm or greater. However, characteristic x-rays (discussed in Section 2.2.2.1), despite their deep escape depth, will prove extremely useful for the determination of nanomaterial composition while imaging with the SEM, TEM, or STEM. The collection of transmitted and diffracted electrons during TEM and STEM imaging require sample thicknesses of roughly 100 nm or less.

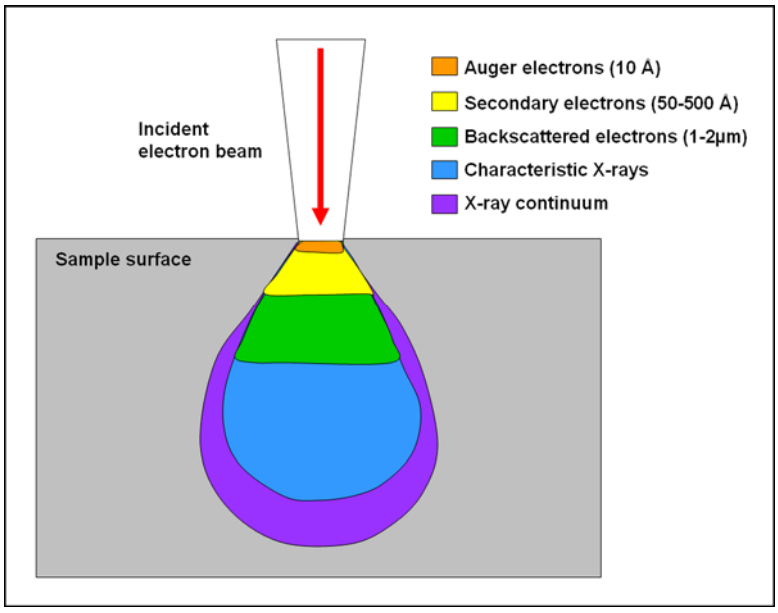

Figure 2.9 Electron interactions with the surface.

2.2.1.1 Scanning Electron Microscopy

Although scanning electron microscopy is the most widely used surface imaging technique, the depth from which the relevant secondary electrons typically escape (~5 to 50 nm) results in the image containing both surface and bulk information. As the SEM scans a sample with a focused beam of electrons that interact with the sample, some of those electrons (and other electrons generated during this process) escape from the sample and reach a detector located above the sample. The number of electrons that reach the detector at each point probed depends on the topology of the sample and the atomic weight of the atoms at the surface, thus the variations in signal strength lead to image formation. However, image contrast and brightness can also be ambiguous and not quantitatively topographical; edges are often highlighted and surface charging can result in large fluctuations in signal level as well as in distortions of the scan raster. Nevertheless, the SEM, with fairly high spatial resolution and magnification, has proven invaluable in this research for quick and easy characterization of hundreds of samples without requiring lengthy sample prep or tool alignment procedure.

In the SEM, the electron-beam interaction with specimen atoms can deflect the beam electrons elastically along a new trajectory as shown in Figure 2.10(a), which may result in the beam electrons eventually leaving the sample as BSE. The probability of elastic scattering in this process increases with atomic number (Z), proportional to $\sim Z^2$ and decreases as electron-beam energy increases, proportional to $\sim 1/E^2$. Inelastic scattering also occurs when the beam electrons transfer energy to the specimen atoms, producing SE and x-ray signals (see Figure 2.10). Those electrons located relatively close to the surface ($<5\lambda$) have a chance of escaping into vacuum. Secondary electrons from the sample are generated by two main mechanisms: SE_1 are created as the beam enters the specimen and SE_2 are created as the BSE leave. The ratio of SE_2/SE_1 increases with Z, for example the ratio for C is 0.18 while Au is 1.5.

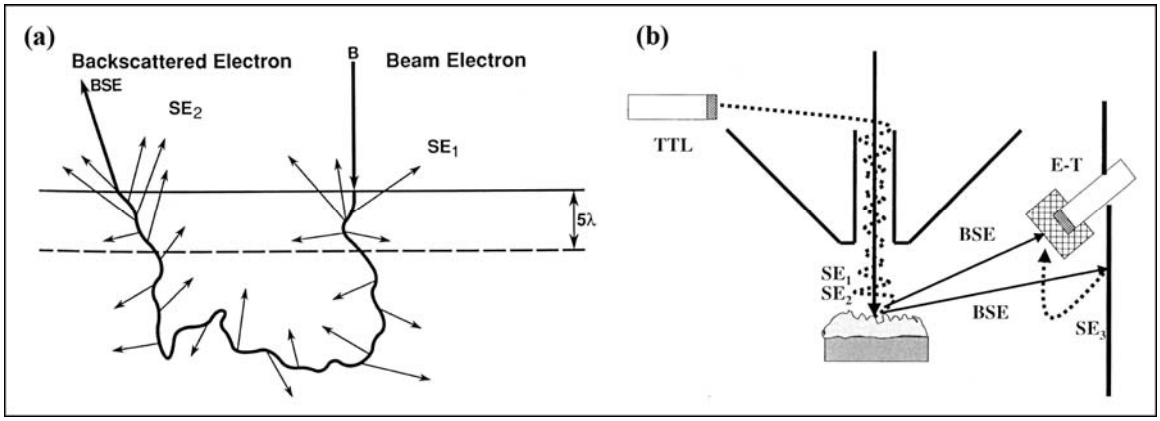

Figure 2.10 Schematic illustrations of electron interactions in the SEM. (a) Secondary electrons in the sample are generated by two mechanisms: first the incident beam electrons (B) generate secondary electrons (SE_1) upon entering the sample; second, backscattered electrons (BSE) generate secondary electrons (SE_2) while exiting the sample. (b) The "upper" TTL detector located above the objective lens collects both SE_1 and SE_2 while the in-chamber "lower" E-T detector collects SE_1, SE_2, SE_3, and BSE. Adapted from [127].

In this work, the majority of SEM imaging was done on a high-performance Hitachi S-4700 field emission microscope equipped with an Oxford Instruments XEDS analysis tool. The S-4700 has two detectors referred to as the "upper" and "lower" as shown in the schematic of Figure 2.10(b). The upper detector is a "through-the-lens" (TTL) type located above the objective lens. The strong magnetic field of the objective lens causes on-axis secondary electrons to spiraling up through the lens bore to a scintillator. The upper detector therefore only collects high-resolution SE_1 and SE_2 thus producing an image with high spatial resolution and surface sensitivity. However, the signal from the upper detector may show strong edge contrast and abnormal contrast with charged samples.

The lower detector is an Everhart-Thornley (E-T) type located in the specimen chamber. In addition to collecting the remaining SE_1 and SE_2, the lower detector also collects SE_3 (from the chamber sidewalls, contributing to noise), and BSE. Thus the lower detector often measures a strong signal due to BSE, which shows less edge contrast and a normal contrast even with specimen charging. Due to the fact that BSE are generated from wider and deeper within the sample, the lower detector produces images

with diminished spatial resolution. Nevertheless, the BSE aspect has proven useful for examining catalyst particles buried under layers of carbon.

Samples were prepared by affixing the silicon substrate to the SEM sample mount using conductive carbon tape to minimize drift and sample charging. On occasion a vertical mount with a clip was used to image the cross section profile of freshly cleaved samples.

2.2.1.2 High-Resolution Transmission Electron Microscopy

Transmission electron microscopy, whose spatial resolution extends from microstructure down to the atomic level, has unique imaging capabilities, making it a commonly used tool of growing importance in materials science and engineering. The surface as well as internal structure of nanomaterials can be analyzed using TEM. Both real space "image" and reciprocal space "diffraction" data (discussed in Section 2.2.3.2), together with chemical analytical information (derived from XEDS, discussed Section 2.2.2.1), can be obtained from the same nanoscale area. The TEM is therefore a powerful tool that provides a wide and deep range of data about the nanostructured material of interest, information which is often more detailed and more direct than can be obtained by any other experimental technique.[128]

A basic TEM consists of six major components: a source of electrons (typically with an energy between 100 and 300 keV), a thin specimen (~100nm or less), an imaging (objective) lens, intermediate lens, a projector lens, and finally a screen. The resolution of the TEM is limited by astigmatism as well as spherical and chromatic aberrations. While the astigmatism is often minimized by adjustments during alignment, and chromatic aberration is decreased with thinner specimens, full correction of the aberrations requires new post-specimen aberration correctors. To record images the screen is lifted and the electrons are recorded by photographic emulsion, an image plate or digitally by a CCD camera. However, some still argue that the resolution and dynamic range of film capture is still better than digital detectors but the convenience of digital capture is indisputable.

There are two basic operation modes of the TEM. Depending on where the intermediate lens is focused, as seen in Figure 2.11, either the back focal plane (A) or the image plane is selected (B). Since the incident beam is collimated, all transmitted electrons leaving the specimen at the same angle pass through the same point in the back focal plane of the imaging lens. Thus this plane contains an angular distribution of electrons transmitted through the specimen which is called a diffraction pattern. To look at the sample image instead, the intermediate lens is readjusted so that its object is the image plane of the objective lens.

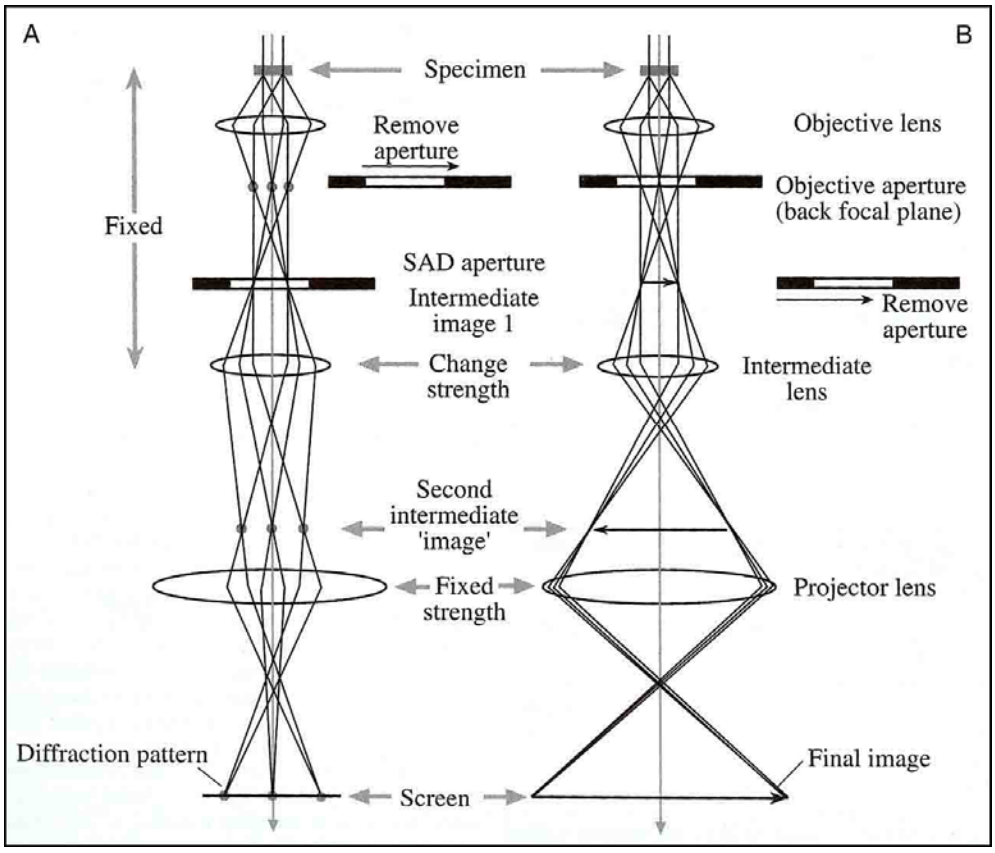

Figure 2.11 Typical ray diagrams for TEM operation modes: (A) projecting the diffraction pattern onto the viewing screen and (B) projecting the image onto the viewing screen. In the first case the intermediate lens selects the back focal plane, but in the second case the image plane is selected as its object to project. Adapted from [129].

There are two main imaging modes in a TEM, bright field (BF) and dark field (DF). Bright field is concerned with collection of only the on-axis electrons transmitted directly through the sample without interaction. This is achieved by the use of apertures to reject electrons that have been scattered, causing areas of the sample to appear dark. On the other hand, dark field mode collects the off-axis electrons that have been Bragg diffracted by crystalline regions of the sample (discussed further in Section 2.2.3), thus the contrast in the image is more or less inverse of BF. This is achieved by using the objective aperture to accept only the electrons that have been diffracted along a particular direction by moving the aperture or tilting the beam to a particular {*hkl*} position of intensity in a given diffraction pattern (see Sections 2.2.3 and 2.2.3.2) then projecting the image plane.

In order to produce meaningful images in the TEM, it is necessary to generate contrast. Contrast is the appearance of a feature in an image due to the change from dark to light or vice versa. If the specimen is infinitely thin then all the electrons will reach the screen and the image will be uniformly bright (in BF) otherwise known as zero contrast. Therefore, the microscopist must utilize mechanisms which will remove electrons from the beam according to variations in the sample. Subtleties, however, complicate the interpretation of images generated by the TEM. For amorphous materials contrast can originate from mass and thickness differences in the sample. However for crystalline samples, most of the image detail comes from Bragg diffraction. Figure 2.12, shows a schematic of how the incident electron beam interacts with a thin specimen. It should be noted that for TEM, only the transmitted and diffracted electrons contribute to the image, while the backscattered electrons from thick or dense regions of the sample are rejected. Several contrast mechanisms are described in the rest of this section.

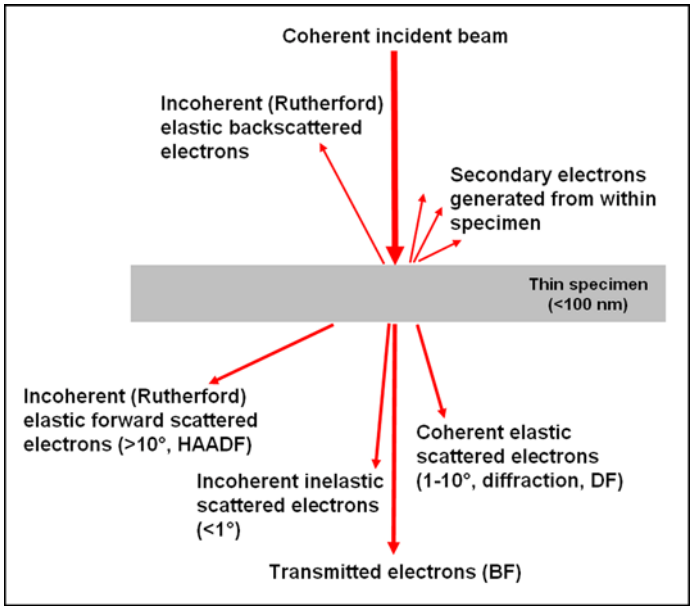

Figure 2.12 Electron beam interaction with a thin specimen.

Mass-Thickness Contrast

Mass or thickness contrast will be present if the sample has large differences in atomic number or there is a significant variation in the thickness of the material being imaged. This is a result of incoherent (Rutherford) elastic backscattering of electrons from thick or electron-dense regions of the sample. The cross section for Rutherford scatter is a strong function of atomic number as well as the thickness of the specimen. Therefore, Rutherford scattering in thin samples is strongly forward peaked. If an image is formed from electrons scattered at low angles (< than 5º), mass-thickness contrast will compete with diffraction contrast.[129] Mass-thickness contrast is crucial for examining noncrystalline materials such as polymers and it is the sole contrast mechanism for biological samples. For example, biologists exploit the mass contrast mechanism by staining regions of their samples to make them electron-dense, producing contrast in BF.

Diffraction Contrast

Contrast in BF and DF TEM images is commonly the result of coherent elastic scattering or "diffraction contrast". This Bragg diffraction, discussed further in Section 2.2.3, is controlled by the crystal structure and orientation of the sample. The electrons in

an excited <*hkl*> beam are diffracted by a specific set of {*hkl*} planes so the areas that appear light in a DF image are where the {*hkl*} planes meet the Bragg condition. Therefore a DF image with diffraction contrast contains specific orientation information not just general scattering information, as is the case with mass-thickness contrast.[129]

In addition, variations in the intensity of electron diffraction across a thinned specimen, i.e. diffraction contrast, is useful for taking images of defects, interfaces, and second phase particles. This contrast effect is generally stronger than mass or thickness contrast except in the case where there are large differences in atomic number or when diffraction is relatively weak. Diffraction contrast from crystalline interfaces often contains rows of one-dimensional bands or fringes. There are several different types of fringes that can be distinguished by how their appearance changes with the tilt of the beam or tilt of the crystal. For example, one-dimensional dislocations cause severe localized distortions of the surrounding lattice. In fact, it is the strains in the crystal that provide the diffraction contrast of the dislocation, not the core of the dislocation itself.[128] Point defects such as vacancies and impurities are generally not visible by this method, but if there are strain effects around say a small cluster of impurities or vacancies, it could be imaged and understood semi-quantitatively.

Phase Contrast Imaging

Unlike diffraction contrast, which is a measure of intensity of the diffracted waves, in high-resolution TEM the phase of the diffracted electron wave is maintained and interferes either constructively or destructively with the phase of the transmitted wave. This "phase contrast" technique is used to form images of columns of atoms in a lattice. However, it must be kept in mind that transmitted lattice images are only interference effects and there is no direct correlation between the image positions (which may vary with thickness, orientation, and focus or astigmatism of the objective lens) and the *actual* atom locations. Because of this, phase contrast lattice fringes are useful mainly for lattice spacing and crystal orientation information. Furthermore, taking a Fourier transform of a lattice fringe image yields an intensity distribution analogous to a diffraction pattern. Thus due to modern technologies of digital image capture and

analysis, evaluation of sample orientation from phase contrast images is simplified and does not necessarily require diffraction patterns.

Another evident distinction between phase contrast and other types of TEM imaging is the number of beams collected by the objective aperture. As described earlier, in standard BF and DF imaging one beam is selected using the objective aperture. However, a phase contrast image requires the selection of more than one beam—in general, the more beams collected the better the resolution of the image.[129] Phase contrast imaging can also show defects in the lattice or the overlapping of crystals through moiré effects. Moiré patterns are formed by the interference of two sets of lines which have nearly common periodicities.

In this work, the majority of TEM imaging was done on a Hitachi HF-2000 cold field emission gun TEM routinely operated at 200kV. The HF-2000 has 0.24-nm point-to-point resolution and completely digital image acquisition. The Fe-Ni catalyst samples were imaged on another microscope, a JEOL JEM-3100FEF 300kV TEM with XEDS. Digital capture was used for bright field imaging only, while diffraction images were taken on electron imaging plates, which were then digitally scanned.

Image Magnification Calibration

The high-resolution image magnification in the HF-2000 was verified by using a MAG*I*CAL® thinned silicon calibration sample. Lattice images of a crystal with a known periodicity were taken and compared to the image scale bars presets for a given magnification. Careful consideration of the objective lens focus, astigmatism, eucentric specimen height, and zone-axis tilt was taken for this calibration. Figure 2.13 illustrates this calibration. In the phase contrast lattice image, the yellow line drawn perpendicular to the Si(111) planes is plotted as a grayscale profile on the right.

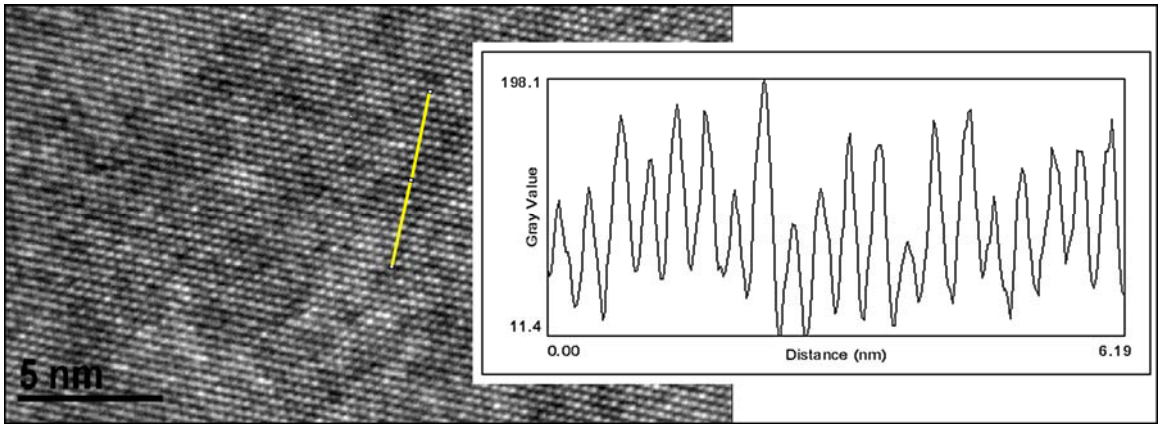

Figure 2.13 HRTEM calibration at 700 k×. Phase contrast image on the left and the profile of the yellow line drawn perpendicular to the Si(111) planes is shown on the right.

Thus by dividing the line length measured in the image by the number of peaks on grayscale profile we obtain the instrument measurement (d_i) of the lattice spacing at 700 k× magnification.

$$d_i = \frac{6.19nm}{20\,planes} = 0.3095nm \qquad \text{Eq. (2.3)}$$

Since the known value of the Si(111) *d*-spacing is 3.14 Å, the difference between this and the measured value from Equation 2.3 is 1.4%, which is well within the margin of error.

2.2.1.3 Scanning Transmission Electron Microscopy

In conventional TEM operation, a large area of the specimen is illuminated by a nearly parallel electron beam. In STEM, on the other hand, the electron beam is focused to form a small probe which is scanned over a rectangular area of the sample surface. Thus the illumination in a STEM is convergent and the scattered electrons are recorded by several angular detectors that display to a monitor. The spatial resolution of the STEM is determined by the diameter of the electron probe unlike in the TEM, where it is largely limited by the electron wavelength and spherical aberration of the lenses.

The Hitachi HD-2000, the main STEM used in this research, combines TEM technology with the simplicity of SEM operation. It has a resolution limit of 0.24 nm and a maximum magnification of 2,000 k×. However, the real advantage of this machine is the fast sample throughput and diversity of information that is readily collected. There are three main imaging modes in the HD-2000 STEM: secondary electron, transmitted electron, and *Z*-contrast. As can be seen from Figure 2.14 a powerful 200 kV electron beam, produced by a cold field emission source, is focused to small probe that is rastered on the sample by the scan coils. The detector located above the sample collects secondary electrons, providing information about the surface topography and three-dimensional nature of the sample as discussed in Section 2.2.1.1. Secondly, the electrons transmitted directly through a sufficiently thinned sample are collected by the BF detector similar to TEM (Section 2.2.1.2). Thirdly, electrons that are incoherently forward-scattered by the sample are collected by the high angle annular dark field (HAADF) detector, which is donut-shaped with a large inner radius.

While conventional BF images convey contrast due to a variety of phenomena including diffraction effects, the HAADF provides a straightforward image from elastically forward-scattered electrons with minimal diffraction effects due to the high angle of collection. The intensity of the HAADF signal yields mass-thickness contrast associated with the atomic number (Z) that approaches a Z^2 dependence at high scattering angles, hence the name "*Z*-contrast" imaging. It is a useful mode for imaging high-Z catalyst particles or metal nanowires that may be embedded within low-Z material, such as carbon or oxide. In addition, the HD-2000 is equipped with an energy-dispersive x-ray spectrometer with 0.3 steradian x-ray collection, giving superb elemental sensitivity. On a final note, sample preparation for STEM is the same as for TEM so the HD-2000 is an excellent screening tool for deciding which samples warrant further HRTEM investigation.

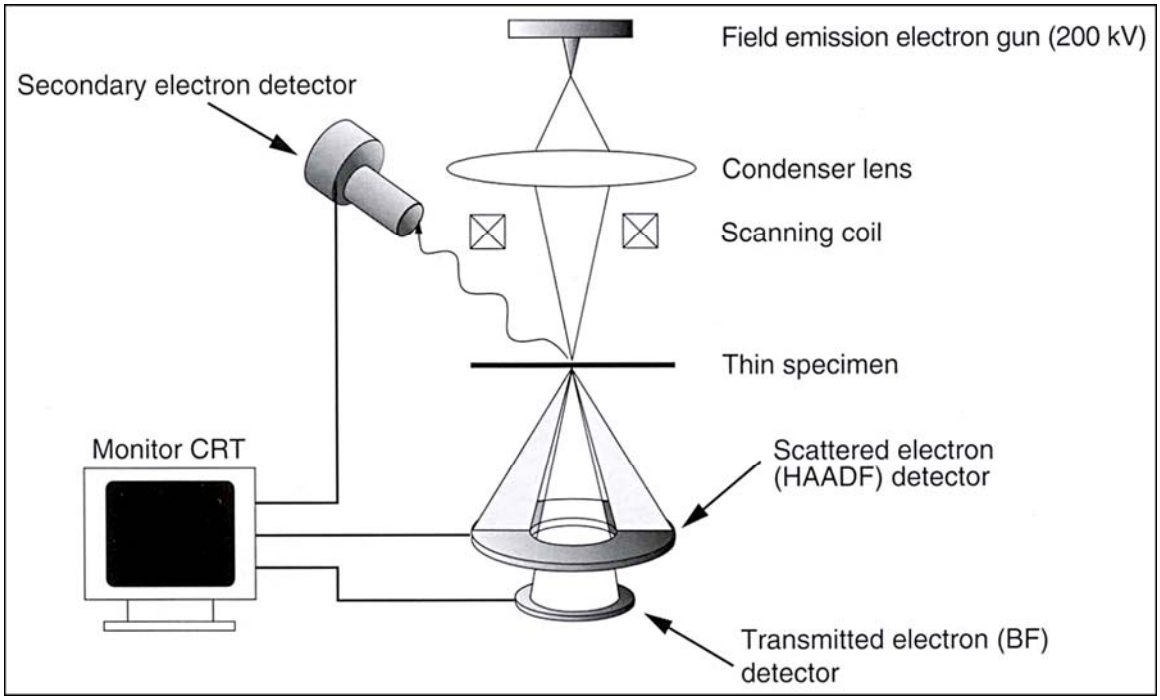

Figure 2.14 Schematic diagram of the HD-2000 STEM. Adapted from [130].

2.2.2 Spectroscopy

While electron microscopy and diffraction techniques convey information about the morphology, microstructure, and atomic arrangement of the material under examination, electron spectroscopy is a common way of obtaining chemical composition. When equipped with the elemental makeup of the sample, any subsequent image and diffraction analysis is greatly facilitated. The two primary methods of obtaining atomic composition in this research, x-ray energy-dispersive spectroscopy and Auger electron spectroscopy, are described in this section. Since electrons have a much shallower penetration depth than x-rays or other radiation sources, they are the convenient probe for obtaining chemical information from nanostructured samples.

Electron bombardment and the resulting principal relaxation mechanisms are schematically illustrated in Figure 2.15. When an electron collides inelastically with an atom, core level electrons in the atom are excited to outer, empty orbitals, or they may be

ejected from the atom completely. The ejection of these secondary electrons leaves the atom ionized. In order to minimize its energy and return to a relaxed state, the atom's inner shell "hole" vacated by the SE can then be filled by an electron from the outer orbitals and the excess energy is given off in the form of either x-ray emission or Auger electron ejection.

Thus there are two main competing relaxation mechanisms (shown in Figure 2.16): characteristic x-ray emission and Auger electron ejection, although for higher atomic number materials relaxation can also efficiently occur by means of nonradiative mechanisms. For lighter elements, the probability of Auger electron emission is significantly higher than emission of an x-ray photon. On the other hand, collection of characteristic x-ray photons is more efficient for measuring the composition of heavier elements.

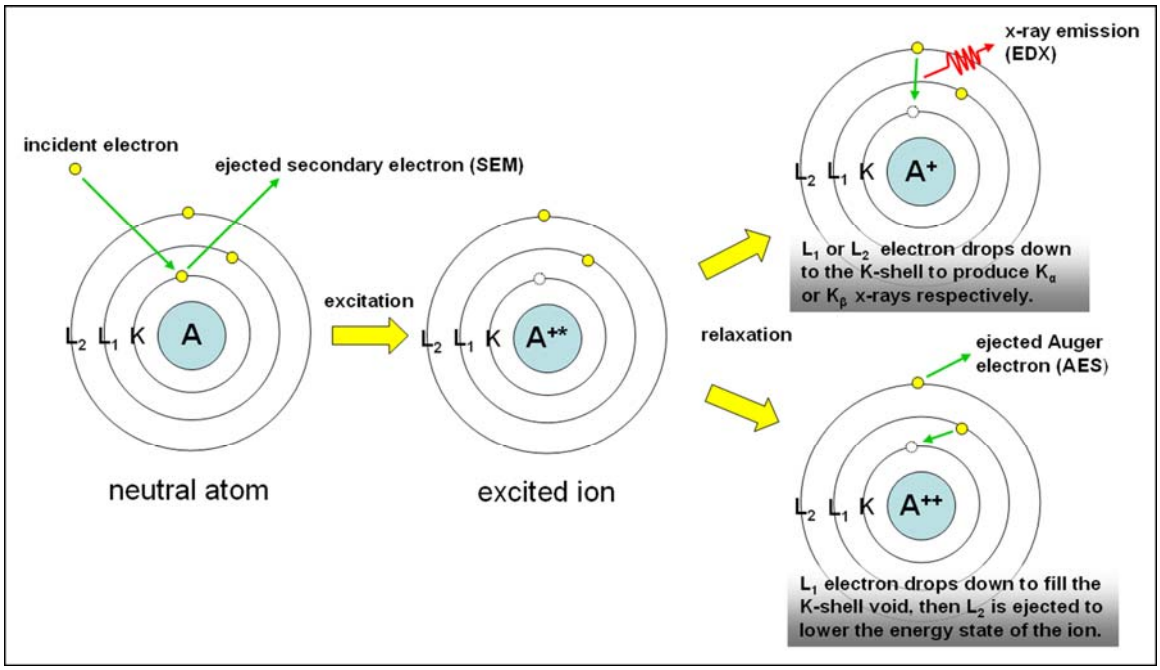

Figure 2.15 Principal atomic excitation and relaxation mechanisms from incident electron bombardment.

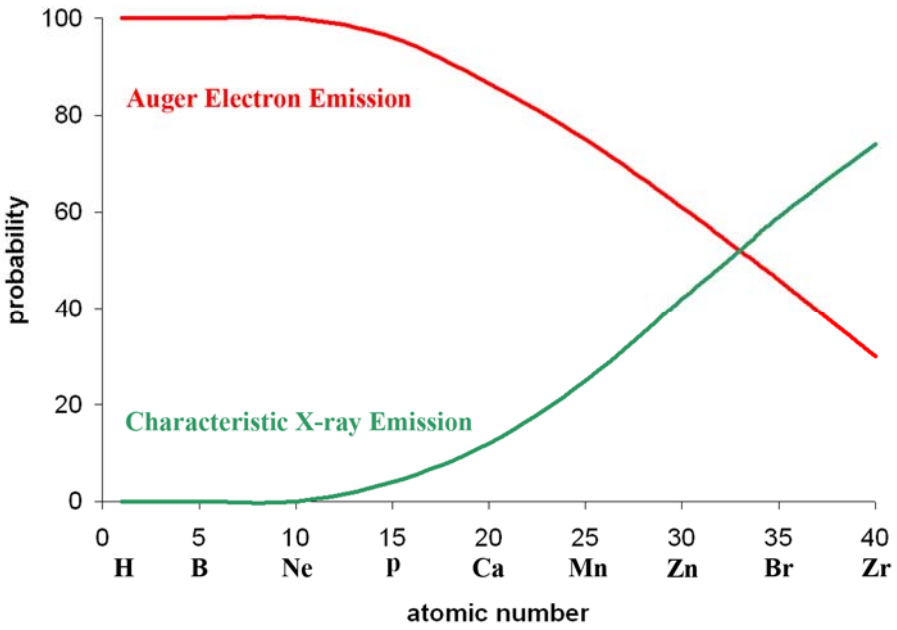

Figure 2.16 Relative probabilities of relaxation by emission of an Auger electron or emission of an x-ray photon of characteristic energy, following creation of a core hole in the *K*-shell.

2.2.2.1 X-ray Energy-Dispersive Spectroscopy

XEDS measures the energies of the characteristic x-rays generated from ionizations induced within the specimen in an electron microscope. Each element emits a unique fingerprint of x-ray energies related to the difference in binding energies of the electron shells involved in the relaxation process, as described in Figure 2.15. A Silicon drift detector is commonly employed to collect the characteristic x-rays, which must be operated at liquid nitrogen temperatures in order to achieve optimal energy resolution.[127] When an x-ray strikes the detector, it will generate a photoelectron within the silicon body and as this photoelectron travels through the semiconductor, it generates electron-hole pairs. The electrons and holes are attracted to opposite ends of the detector with the aid of a strong electric field. Thus the size of the current pulse generated depends on the number of electron-hole pairs created, which in turn depends on the energy of the

incoming x-ray. In this way, an energy histogram is acquired depicting the emitted x-ray emission spectrum from the irradiated area of the sample. This spectrum can then be analyzed to identify the elements present ("qualitative analysis") and to determine the chemical composition of the material ("quantitative analysis"). The x-ray energy-dispersive spectrometer is often interfaced to electron microscopes to give complementary chemical information. Depending on the energy of the electron beam as well as the density and chemistry of the specimen, the lateral spatial resolution can range from micrometers to tens of nanometers. While the attenuation length for x-rays in most materials is close to the size of the teardrop-shape in Figure 2.9, if the sample is thinned to ~100 nm, as in TEM, it is possible to increase the lateral resolution of XEDS by several orders of magnitude.[131]

In this work, the HD-4700 SEM was outfitted with an Oxford Instruments XEDS detector capable of elemental point, line, and mapping analysis (model 7200, 10-mm^2 SiLi drift detector, INCA Microanalysis software). Both the HD-2000 STEM and JEOL-3100 TEM were equipped with a Thermo Electron Corporation XEDS detector operated by NORAN System SIX software. XEDS analysis of samples in the JEOL-3100 TEM was carried out using the focused probe of STEM mode operation. The wealth of information collected NORAN System SIX software's spectral image data set, where a complete XEDS spectrum is recorded at every x-y position, was used to create quantitative atomic percents, produce elemental line scans, and elemental spatial maps. However, due to the highly focused, intense STEM probe, care was taken to minimize sample damage and contamination that occurs from beam dwell during data collection. In addition, automated drift correction was necessary for longer map or spectral image acquisitions.

2.2.2.2 Auger Electron Spectroscopy

As described earlier, Auger electrons are released during relaxation of the atom from an excited state and can be collected via Auger electron spectroscopy (AES). The conventional way to assign Auger transitions is to use the x-ray spectroscopy

nomenclature for the electron shells. Since three electron levels are involved in any given Auger transition, the principal quantum states n = 1, 2, 3, 4 … are designated *K*, *L*, *M*, and *N*, respectively. Thus Figure 2.15 describes an Auger KL_1L_2 process. However, if the outer levels involved in the process happen to be in the valence band, then the notation for the state is often replaced by a *V* as in a *KVV* transition. The kinetic energy of an Auger electron emitted after any *ABC* transition can approximately be expressed as $\approx E_A\text{-}E_B\text{-}E_C\text{-}U$, where *E* are the electron binding energies and *U* is the hole-hole interaction energy.[132] Therefore each emitted Auger electron's energy is characteristic of some combination of atomic energy levels of the emitter atom and can be measured by an electron energy analyzer. The resulting energy spectrum can yield quantitative elemental make-up (sensitivity of 0.1 at. %), and in some cases peak-shift and peak shape can also convey chemical bonding information.

The major advantages of the AES are its high resolution and surface sensitivity as well as the ease of depth profiling. The incident electron beam can be focused to a fine spot giving excellent lateral spatial resolution on the order of a few tens of nanometers. Additionally, since Auger electrons have low energies (typically 20–2000 eV), their escape depth is much shallower than that of x-rays, describing a region just a few monolayers deep (2–5 nm). Auger spectroscopy must therefore be performed in ultrahigh vacuum to maintain an uncontaminated surface. In addition, by sputtering the sample surface with an ion beam between successive spectra collections, depth-resolved chemical information can be obtained. It is possible to detect all elements in the periodic table (with the exception of hydrogen and helium); however, as mentioned before, the yield of Auger electrons is highest for the lighter elements such as C, Si, N, and O. The sample must also be a good electrical conductor or else charging induced by the incident beam will result in a shift in the energies of the characteristic emission edges.

In this work AES has been used to characterize both initial catalyst films and individual nanostructures. The instrument employed for these experiments was a Phi 680 scanning Auger microprobe (SAM) from Physical Electronics, USA.[‡] In this

[‡] The operation of the SAM for the collection of data for this dissertation was performed by H. M. Meyer III at the High Temperature Materials Laboratory, ORNL.

dedicated system an Auger electron detector is combined with an SE detector, thus by rastering the focused electron beam, both a high-resolution SE image and an Auger elemental map can be generated from the exact same region. Typically, the characterization work in this research employed a beam energy of 20 kV and beam current of 10 nA, resulting in a spot size of ~15 nm. The instrument is also equipped with an Argon sputter gun for specimen cleaning and depth profiling, with an ion-sputtering rate of approximately 1 nm/s.

2.2.3 Diffraction

Though the primary processes by which electrons and x-rays are scattered are different, both techniques can give similar information about the average periodicity or crystal structure of the sampled region by the use of Bragg's law. Electrons are scattered by both electrons and the nuclei in a material, where the negatively charged electrons interact directly with the local electromagnetic fields of the specimen atoms. X-rays, however, are scattered by only the electrons in a specimen via an interaction between the electromagnetic field of the x-ray beam and the electrons. The electrons in the specimen respond to a field of the x-rays by oscillating with the period of the x-ray beam, whereas the comparatively large mass of the nucleus cannot be oscillated by x-rays to any appreciable extent.[133] Then the accelerated electrons emit their own electromagnetic field, called the scattered wave, which is identical in phase and wavelength to the incident x-ray beam. Because x-rays scatter by a field-to-field exchange rather than direct scattering, x-rays are scattered much more weakly than electrons,[129] thus requiring a larger sample and brighter source to obtain a useful diffraction signal.

Many materials, especially metals, belong to the cubic crystal system. The most common cubic lattice symmetries are body centered cubic (BCC) and face centered cubic (FCC). Cubic unit cells have only one lattice parameter, a, since the sides and angles of a cube are standard. The planes in cubic systems are defined by ($h\ l\ k$) Miller indices, where each letter corresponds to the plane's inverse intercept with the x-, y-, and z-axes, respectively. By analyzing the constructive interference of electron or x-ray beams

scattered by the diffracting planes of a sample, the crystal structure (i.e. unit cell type) and lattice parameter can be deduced. The perpendicular distance, *d*, of a plane from the origin is a function of the lattice parameter and the indices of that plane (*h k l*), given by:

$$d = a/\sqrt{h^2 + k^2 + l^2}\ . \qquad \text{Eq (2.4)}$$

This interplanar distance is known as the *d*-spacing. Based on Von Laue's Nobel Prize winning work, it is known that diffracted waves are in phase *only* if the difference between the path distances travelled by waves scattered from adjacent scattering centers is a whole number of wavelengths, $n\lambda$. Bragg simplified Von Laue's work, by asserting that waves behaved as if they were "reflected" off atomic planes, as in Figure 2.17. Here the path difference between the waves reflected from the upper and lower planes is equal to AB + BC. The Bragg diffraction condition is satisfied if the *d*-spacing of the reflecting planes and the angle, θ, between the incident or reflected waves and the reflected planes are such that,

$$\text{AB} + \text{BC} = n\lambda = 2d \sin\theta\ . \qquad \text{Eq. (2.5)}$$

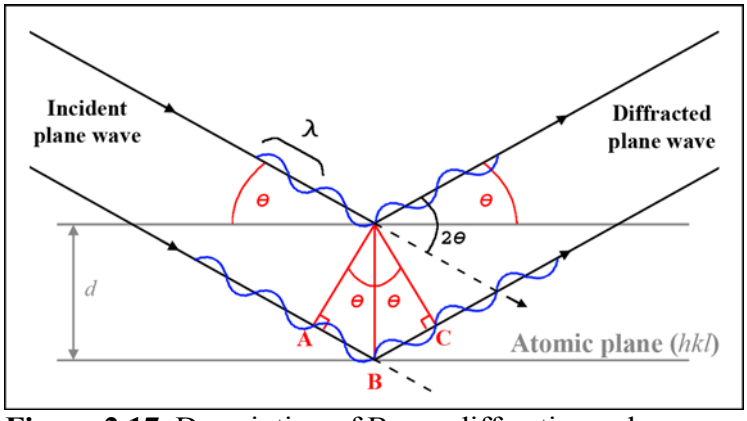

Figure 2.17 Description of Bragg diffraction, where waves reflected off parallel atomic planes must have a path difference equal to an integral number of wavelengths if they are to remain in phase.

Thus for a given incident wavelength, this condition is satisfied by each set of diffracting planes at a corresponding Bragg angle, called θ_B. It is simple to see from the Bragg equation (Eq. 2.5) that the atomic planes in a crystal which are closer together produce larger scattering angles. This reciprocal relationship, where $d \propto 1/\theta_B$, is important to the interpretation of diffraction patterns in which the experimental information is manifest in reciprocal space or "k-space". If λ is known for the incident radiation and $2\theta_B$ is measured experimentally, the interplanar spacings of the crystal can be deduced. Furthermore, Equations 2.4 and 2.5 can be combined and solved for a to yield:

$$a = \lambda\sqrt{h^2 + k^2 + l^2}\,/2\sin\theta_B\,. \qquad \text{Eq. (2.6)}$$

It should also be added that intensity of the measured diffraction signal depends on the properties of scattering material, namely the atomic scattering factor and structure factor. The atomic scattering factor (also known as the form factor), f(θ), is used to describe the efficiency of an atom to scatter in a given direction. For x-rays, $f_x(\theta)$ is defined as a ratio of the amplitude of the wave scattered by an atom to the amplitude of the wave scattered by one electron. These values are fairly well known and tabulated.[133] For incident electrons, the structure factor, $f_e(\theta)$, is slightly more complex, taking into account both elastic electron-cloud scattering and elastic nuclear scattering. It can be described as follows:

$$f_e(\theta) = \frac{\left(1 + \dfrac{E_0}{m_0 c^2}\right)}{8\pi^2 a_0}\left(\frac{\lambda}{\sin\dfrac{\theta}{2}}\right)^2 \left(Z - f_x\right), \qquad \text{Eq. (2.7)}$$

where E_0 is the electron beam energy, m_0c^2 is the electron rest energy, and a_0 is the Bohr radius of the scattering atom.[129] Both x-ray and electron scattering factors depend inversely on the scattering angle, but increase with both λ and Z.

The actual scattered intensity from a crystalline material is proportional to the square of the structure factor, F(θ). The structure factor is a measure of the amplitude scattered by a *unit cell* in the crystal rather than an individual atom. Because of the periodic arrangement of the atoms in a unit cell, the interference of waves scattered from different atoms can be either constructive or destructive depending whether they are in or out of phase, respectively. Thus F(θ) is described in Eq. 2.8 as the sum of all the atomic scattering factors from i atoms in the unit cell (with atomic coordinates x_i, y_i, z_i) multiplied by the phase factor, which takes into account the difference in phase between waves scattered from atoms on different (*hkl*) planes.

$$F(\theta) = \sum_i f_i e^{2\pi i(hx_i + ky_i + lz_i)} \qquad \text{Eq. (2.8)}$$

This structure factor equation predicts the circumstances where the amplitude of scatter is zero, resulting in kinematically prohibited reflections, which is quite useful for identifying the crystal structure. Even without knowing the precise values of the atomic scattering factors, general reflection rules for each crystal lattice can be generated just by knowing the location and type of each atom in the unit cell. For instance the structure factor for Ni, with an FCC crystal lattice having four atoms per unit cell located at the origin and three face centers [(0, 0, 0), (½ , ½ , 0), (½ , 0, ½), (0, ½ , ½)], can be calculated as:

$$F_{Ni}(\theta) = \sum_i f_{Ni}\left(1 + e^{\pi i(h+k)} + e^{\pi i(h+l)} + e^{\pi i(k+l)}\right). \qquad \text{Eq. 2.9}$$

By considering different values for the h, k, and l integers, it can be seen that if all three integers are either even or odd, then all of the exponential terms become $e^{2n\pi i}$, which equals 1 and the structure factor sums to $4f_{Ni}$. However, if h, k, and l are a mixture of odd and even integers, then two of the three exponential terms will have odd multiples of π, equaling -1 and the structure factor sums to zero. Using Equations 2.4, 2.5, and 2.8 and the lattice constant for Ni (a = 3.524),[134] tabulated values of d-spacings, diffraction

angles, and structure factors are generated for the first twenty plane indices in Table 1. The grey rows represent the kinematically prohibited plane reflections.

Table 1. D-spacings, 2θ, and structure factors for FCC Ni.

h	k	l	$h^2+k^2+l^2$	d(Å)	2θ	F(θ)
1	0	0	1	3.52	25.3	0
1	1	0	2	2.49	36.0	0
1	1	1	3	2.03	44.5	$4f_{Ni}$
2	0	0	4	1.76	51.9	$4f_{Ni}$
2	1	0	5	1.58	58.5	0
2	1	1	6	1.44	64.8	0
2	2	0	8	1.25	76.4	$4f_{Ni}$
2	2	1	9	1.17	82.0	0
3	0	0	9	1.17	82.0	0
3	1	0	10	1.11	87.5	0
3	1	1	11	1.06	92.9	$4f_{Ni}$
2	2	2	12	1.02	98.4	$4f_{Ni}$
3	2	0	13	0.98	104.0	0
3	2	1	14	0.94	109.8	0
4	0	0	16	0.88	122.0	$4f_{Ni}$
3	2	2	17	0.85	128.7	0
4	1	0	17	0.85	128.7	0
3	3	0	18	0.83	136.1	0
4	1	1	18	0.83	136.1	0
3	3	1	19	0.81	144.7	$4f_{Ni}$
4	2	0	20	0.79	155.7	$4f_{Ni}$

2.2.3.1 X-ray Diffraction

In XRD, structural analysis of polycrystalline samples is commonly achieved using the standard θ–2θ configuration. Bragg's law is applied by using monochromatic x-ray radiation of a known wavelength and a variable angle 2θ between the diffracted beam and the transmitted beam. As depicted in Figure 2.18, in the θ–2θ goniometer setup the x-ray source is stationary and the sample tilts, changing the angle θ, while the detector simultaneously rotates with the angle 2θ.

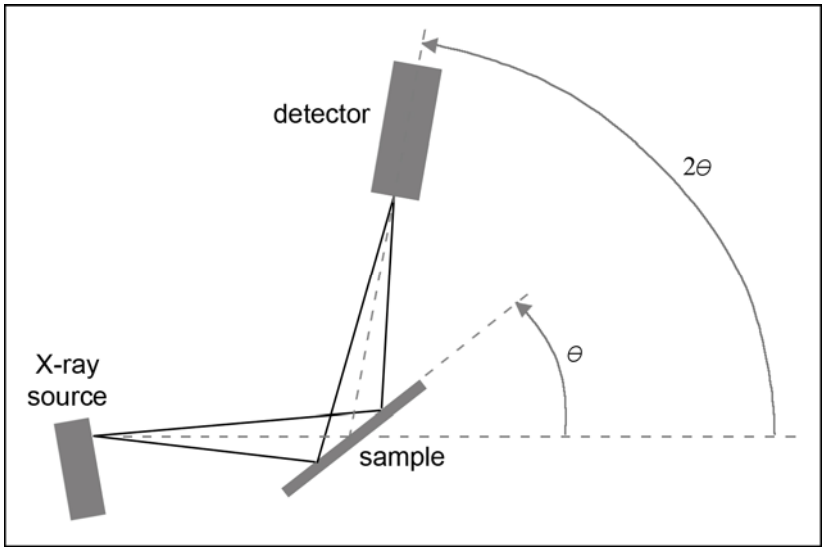

Figure 2.18 Configuration for θ–2θ x-ray diffraction.

By scanning over a range of 2θ, peaks of diffracted intensity are detected, forming a pattern. The intensity and location of the peaks in the diffraction pattern can be indexed to a particular crystal structure and the d-spacings and lattice constants calculated using Equations 2.5 and 2.6, respectively. Since this method probes only the planes that happen to be parallel to the surface (down to significant depths and across a large area of surface), it yields a straightforward measurement of the ensemble average for polycrystalline samples. For samples that may have some degree of texture, however, the peak intensities should be compared to a polycrystalline reference pattern gathered in the same way.

An alternative geometry, called grazing incidence, uses a small x-ray incidence angle (ω) relative to the specimen surface in order to maximize sampling of the surface region. For grazing incidence an ω-2θ scan is performed, where the sample stage is locked in place, also fixing the incidence angle. Only the detector rotates about 2θ to collect diffraction from planes oriented in various directions that happen to satisfy the Bragg condition. This method is used to study surfaces and interface layers because the depth of wave penetration is limited to distances on the order of nanometers, thus the Bragg reflections originate only from planes near the surface. It is especially useful in instances of limited sample volume, such as very thin films or nanoparticles distributed

on the surface, where phase identification is desired. However, unless a standard can be made, this is not a very quantitative method and may be problematic if the films are textured and the main reflections do not happen to meet the Bragg condition in this rigid geometry.

For this dissertation work a Philips/PANalytical X'Pert x-ray diffractometer was employed. The Cu K_α (1.54 Å) x-rays were generated using a source excitation voltage of 45 kV and current of 40 mA. In addition, PANalytical's HighScore software package was utilized for peak identification and fitting.

2.2.3.2 Electron Diffraction

The TEM's combination of imaging and diffraction from small volumes provides a unique approach for understanding the properties of crystals and defects. Figure 2.19 conveys the principles of electron diffraction pattern generation. When the Bragg condition is satisfied, defined spots characteristic of coherent electron scattering from planes in the crystal can be seen and identified. Consider a set of planes a distance d apart that is oriented to the Bragg condition with an incident angle θ_B. The resulting diffraction spots or reciprocal lattice points are labeled O, G, 2G, etc. The vector g, which extends from the transmitted beam or origin O [000] to the first diffraction spot G, is normal to the diffracting plane [*hkl*]. Thus if one assigns *hkl* to the spot G then the second order spot 2G is *2h 2k 2l*, the 3G spot *3h 3k 3l*, etc., defining a family of planes $\{hkl\}$.

A zone axis, signified by [*UVW*], is a special direction that is common to all the planes belonging to the zone. Thus [*UVW*] is perpendicular to the normal of each (*hkl*) plane in that zone, meaning that their dot product is zero (i.e. $hU + kV + lW = 0$). If the specimen is tilted so that the incident beam is directed along a zone axis, then a diffraction pattern with a series of spots in multiple directions will occur by different $\{hkl\}$ families of diffraction planes that belong to the zone.

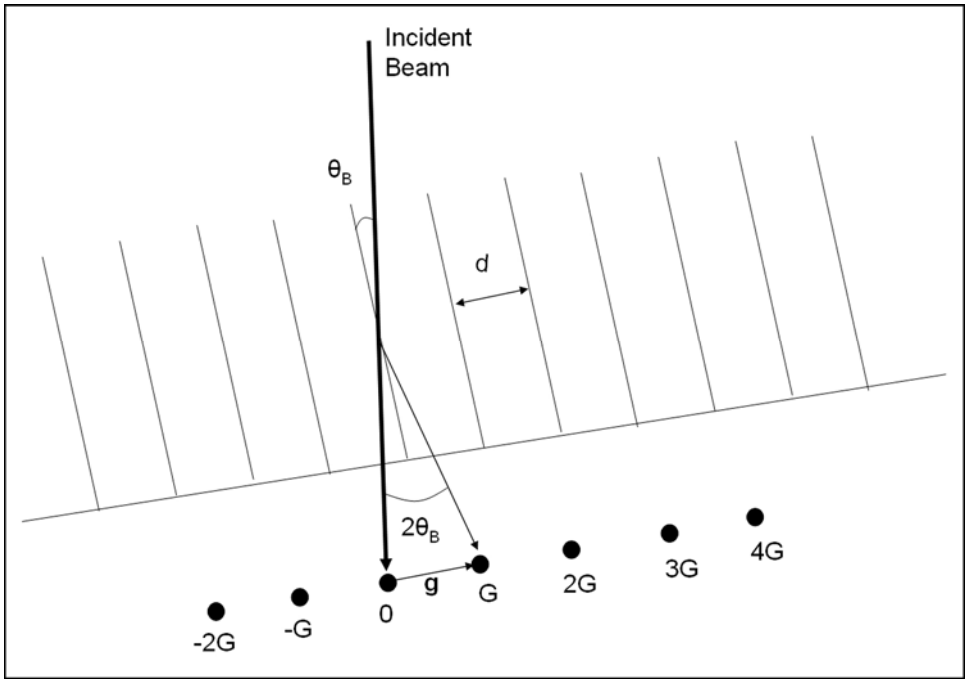

Figure 2.19 Diffraction from a set of planes a distance *d* apart. These planes are oriented to the Bragg condition, with an incident angle θ_B. The resulting diffraction spots or reciprocal lattice points are labeled O, G, 2G, etc. The vector **g**, which extends from the origin O to the first diffraction spot G, is normal to the diffracting plane. Adapted from [[129]].

In this dissertation, electron diffraction was widely used to characterize the phase and orientation of nanostructured materials. The most common approach was selected area diffraction (SAD) where a parallel beam of electrons interacts with the specimen and the diffraction contributing area is specified by the use of a SAD aperture inserted below the specimen (see Figure 2.11). By using the smallest SAD aperture, specific regions of a nanostructure and individual nanoparticles can be isolated and characterized. Lastly, to obtain a pattern that can be identified, the sample must be rotated to particular zone axis using a sample stage capable of rotation along the x- and y- directions.

Indexing Diffraction Patterns, Calibration, and Simulation

The spots in a diffraction pattern can be identified or "indexed" by several methods that utilize the unique distances and angles between the diffractions spots that are specific to a particular zone. One such method is to measure the ratio of the distance

between the two sets of diffraction spots closest to the origin as A/B, shown in Figure 2.20. This unique ratio (in this case A/B = 1.414) is used to identify the crystal system (diamond cubic) and the zone axis [110].

To measure precise *d*-spacings from the diffraction pattern, a calibration of the pattern must be made. Traditionally the magnification of the diffraction pattern has been described by a "camera length" calibration ($dr = \lambda L$) based on the effective distance, L (mm), between the specimen and the film. However, since digital capture provides images based on pixels and not actual distances, rather than determining the camera length, we perform a simple calculation to find the camera calibration constant, *c*, for a diffraction image taken at a particular magnification or cameral length setting on the microscope. The camera constant for a diffraction pattern is described as the product of the actual specimen *d*-spacing (Å) and the measured distance, *r* (px), from the transmitted beam (origin) to a given diffraction spot.

$$dr = c \qquad \text{(Eq. 2.10)}$$

Thus by capturing a diffraction pattern for a material of known *d*-spacing, the camera constant can be determined. In the HF-2000 TEM, the diffraction pattern in Figure 2.20 for a MAG*I*CAL® silicon sample was taken at a camera length setting of 400 mm. Substituting 1.92 Å[135] in for *d* and the measured length of 270 px in for *r* in Equation 2.10, we obtain a camera constant of 518.4 px Å. This camera constant and the new measured *r*-values from experimental diffraction patterns were used to back-calculate the *d*-spacings of unknown phases.

To assist in the indexing of diffraction patterns from samples of unknown crystal phases and/or orientations, electron diffraction patterns were simulated using CrystalMaker® software. In this software program, first a crystal structure file of the unit cell with the pertinent space group operators and lattice constants is created. Then the structure file is used to generate single-crystal electron or x-ray powder diffraction patterns.

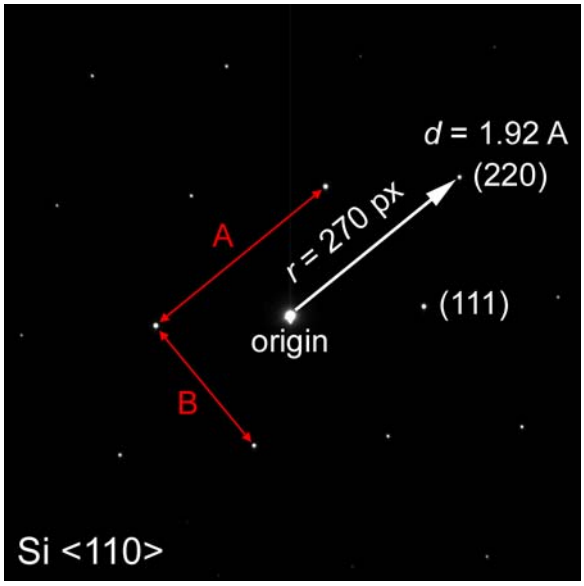

Figure 2.20 Calibration diffraction pattern from the <110> zone of silicon.

2.2.3.3 The Scherrer Formula

Electron diffraction from polycrystalline samples can be viewed in much the same way as x-ray diffraction from powders. For a completely random polycrystal, the reciprocal lattice is rotated about all axes to produce a set of nested spheres, which intersect with the Ewald sphere (in the TEM this can be approximated by a plane) to produce a pattern of concentric rings. If the polycrystal is textured, the rings will appear as arcs when the specimen is tilted. Otherwise, randomly oriented polycrystals with a large grain-size will diffract sharp speckled rings and those with a fine grain will give broad continuous rings, where the width of the rings is an inverse measure of the grain size. Thus a reasonable measure of crystal size in the range of 1 – 100 nm can be obtained using a variation of the well-known Scherrer Equation.[133,136] Since the breath of a diffraction peak in k-space is independent of the particular reflection, by measuring half the ring width at half maximum intensity (HWHM, $Å^{-1}$) in a polycrystalline electron diffraction pattern, the coherent scattering length (or average crystallite size) $\overline{D}$ can be calculated simply as,

$$\overline{D} = \frac{k}{\text{HWHM}}, \qquad \text{Eq. (2.11)}$$

where $k \cong 0.443$ for a Gaussian peak shape. When converted to a function of 2θ for x-ray diffraction peaks measured at full width half maximum (FWHM), the Scherrer Equation is expressed as,

$$\overline{D} = \frac{k\lambda}{\text{FWHM}\cos\theta_B}, \qquad \text{Eq. (2.12)}$$

where $k \cong 0.89$ (depending on the crystallite shape). Variations in k on the order of 20% are to be expected.[136]

2.2.4 Magnetometry

The magnetic measurements in this dissertation were performed using a Quantum Design MPMS-5 superconducting quantum interference device (SQUID) based magnetometer, depicted in Figure 2.21(a).[§] This machine is capable of measuring the magnetic response of materials in magnetic fields as high as 5 T, temperatures of 2 to 400 K, and times from milliseconds to days. This type of magnetometer measures the response of a material while removing the influence of the applied field, as well as the influence from the sample mounting material (in most cases). However, these benefits come at the price of being particularly sensitive to geometry and sample size. The symmetry of the pickup coil, Figure 2.21(b), is such that uniform fields and long mounting materials are invisible to the machine. By knowing the geometry of the pickup coils, features in a scan of voltage versus position can be fit to calculate sample magnetic moment, m. Such a scan is schematically illustrated in Figure 2.21(a).

[§] The operation of the SQUID magnetometer for the collection of data presented in this dissertation was performed by K. D. Sorge at Florida Atlantic University, Boca Raton, Florida.

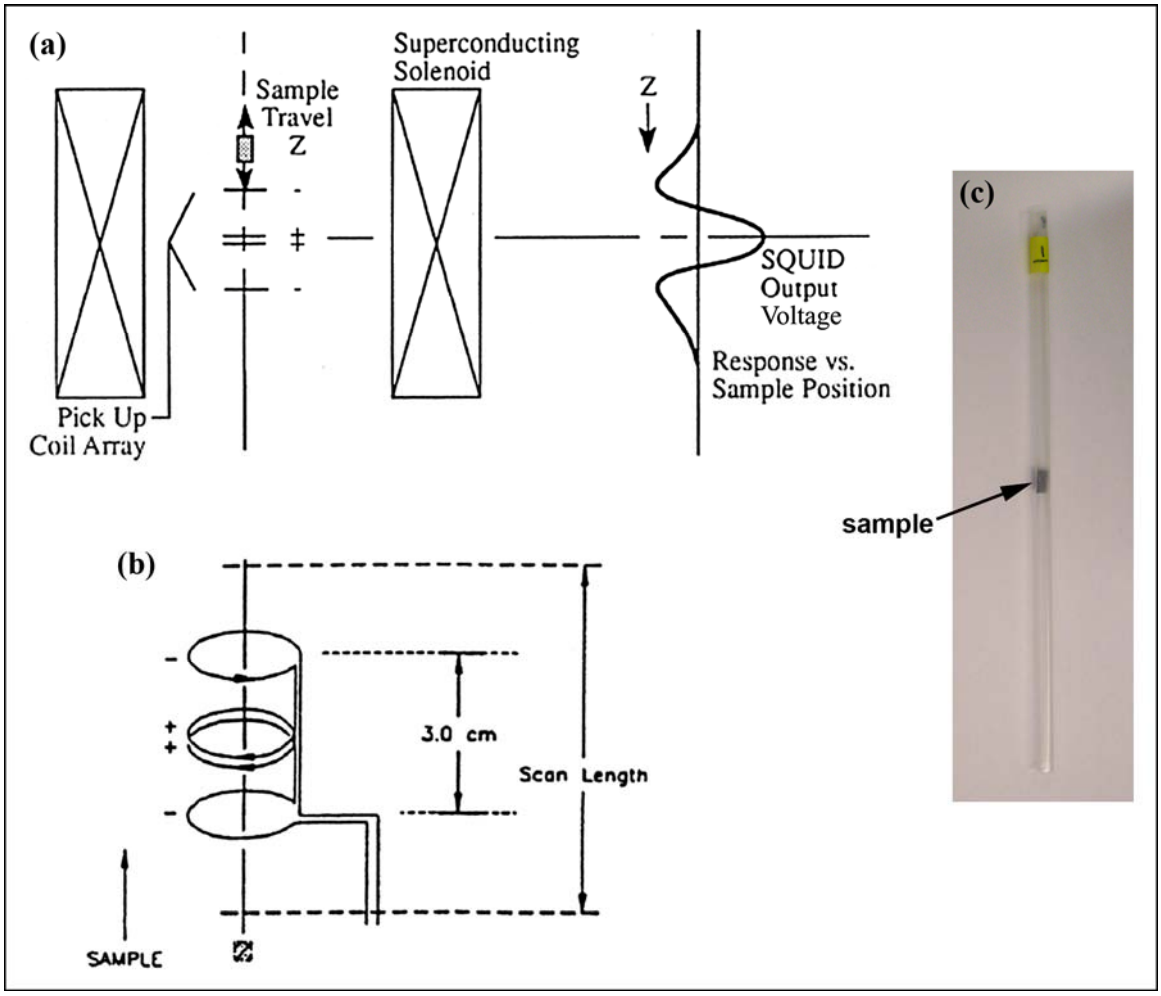

Figure 2.21 Experimental setup for the SQUID magnetometer. (a) Output voltage of the magnetometer is a function of sample position; the overall magnetizing field is not coupled to the SQUID output. (b) Close-up schematic of the pickup coil array of the magnetometer. (c) Typical magnetometer sample mounting in which the sample is inserted into a long straw.

Sample Mounting

For magnetic measurements of as-deposited metal films and VACNF catalyst particles, the sample is fixed to the surface of a Si substrate. By dicing the substrate to a 5 mm size chip, we can ensure that the sample is the proper size to be physically stabilized in the machine. Silicon is a linear diamagnet with a temperature independent susceptibility of $\chi = -1.11 \times 10^{-7}$ emu/g/Oe. By knowing the mass of the Si substrate, its contribution to the resultant moment can be removed.

Typical mounting of a sample to be measured in the SQUID magnetometer is shown in Fig 2.21(c). For convenient positioning of the sample with respect to the pickup coils, a drinking straw is used. Drinking straws are made of plastic with minimal magnetic response, and they are engineered to be long and uniform (the two attributes that make them invisible to the magnetometer). While the straw works quite well at low temperatures, it does not function as well at high temperatures. This was not an issue for our experiments as all data was taken at 300 K or below.

It should also be noted that sample cooling has to be handled carefully. Since nitrogen solidifies at 63 K and oxygen solidifies at about 55 K, either would prohibit sample motion if proper technique is not observed. During the cooling process, the sample chamber is evacuated and backfilled with helium a couple of times before arriving at the final state of vacuum. To go lower than 4.2 K, the chamber is partially filled with liquid He and pumped on. To warm above 4.2 K heaters are employed. Temperatures are monitored at the center of the pickup coils as well as the bottom of the chamber and the control of heating/cooling is automatically handled by the SQUID software.

Data Acquisition

For each data point, the magnetometer fixes temperature and field and looks at voltage as a function of sample position. This voltage is fit to an equation and a moment is determined. By changing temperature or field, moment can be examined as a function of these factors. A typical data point is shown as the curve in red in Figure 2.22. A least-square fitting technique (blue curve) is used to determine magnetic moment from this scan of SQUID voltage versus sample position. The moment is assumed to be from an ideal dipole of zero volume. However, this is not a bad assumption as long as the sample is not too large; as it turns out, a typical 5 mm sample will give a response that is virtually indistinguishable from this fit. Thus with these assumptions, the voltage as a function of position z is fit to:

$$f(z)=\alpha+\beta z+\gamma\left\{\frac{2}{\left[R^2+(z+\delta)^2\right]^{3/2}}-\frac{1}{\left[R^2+(b+(z+\delta))^2\right]^{3/2}}-\frac{1}{\left[R^2+(-b+(z+\delta))^2\right]^{3/2}}\right\} \quad \text{Eq. (2.13)}$$

Here α is related to a uniform voltage offset in the electronics, β is related to a linear drift in signal, δ is the vertical position offset of the sample from where it ideally should be, b is the vertical distance between the center of the pickup coil and the top, and R is the radius of the loops in the pickup coils (~1 cm). The remaining parameter, γ, is a special fit parameter that allows moment m to be calculated as:

$$m=\frac{\gamma\cdot(\text{longitudinal regression factor})}{(\text{SQUID calibration factor})\cdot(\text{sensitivity factor})\cdot(\text{correction factor})}. \quad \text{Eq. (2.14)}$$

Additionally, by knowing the sample volume, the moment m can be normalized to yield magnetization, M, which is often what is plotted and used for comparison.

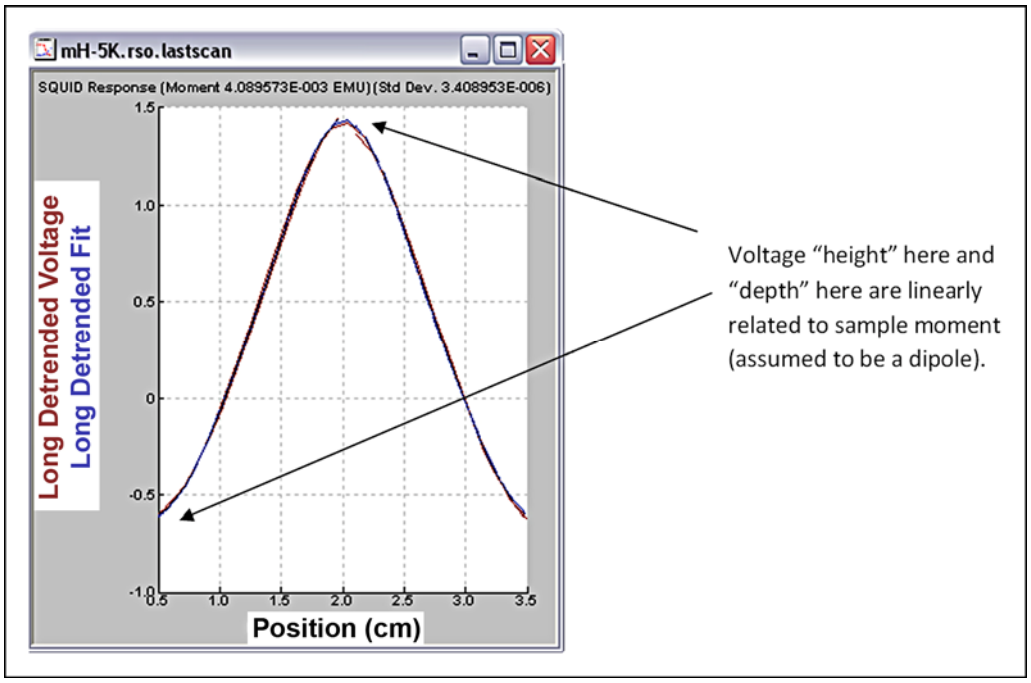

Figure 2.22 Typical SQUID experimental data point. This is a 3 cm scan of voltage as a function of position at the center of the pickup coils. Red is the experimental data and blue is the fit based on assumption that the sample is an ideal dipole.

Types of Measurements

As stated earlier, this type of magnetometer can measure magnetic response as a function of field, temperature, and time. The most common method of measurement is moment *m* as a function of field *H*. With this type of measurement, you can realize the hysteresis behavior of a sample. For this project, a typical set of data would consist of *m*(*H*) at fixed temperatures of 5, 50, 100, 150, 200, 250, and 300 K. At low temperature, the hysteresis loop often "opens up", illustrating the magnetization is not reversible and that it is history dependent. Typically at higher temperatures, *m* would be a reversible—but nonlinear—function of applied field *H*.

However, this type of hysteresis measurement makes it hard to distinguish between different types of magnetic materials: ferromagnets, paramagnets, superparamagnets, etc. The response as a function of temperature, *m*(*T*), is more discriminating in the case where mixed contributions are expected. Two types of temperature-sweep measurements are typically performed on these types of materials. The first would be a sweep from 5 K to 300 K in a high fixed field of 1 or 2 T. At high fields, the response from ferromagnetic (FM) constituents saturates and would change little with temperature. This allows for a way to attain detailed information about the paramagnetic (PM) and superparamagnetic (SPM) contributions—particularly the individual moments of the contributions. In addition, temperature sweeps in low fields of 10 or 20 mT, often referred to as ZFC-FC analysis, are used to study the thermal stability and anisotropy of the system as a whole.

In analyzing response as a function of time, AC susceptibility would be used. By adjusting an AC magnetic field, you can look at in-phase and out-of-phase response. The SQUID system is capable of AC magnetic fields with a frequency range of 0.1 Hz to 1000 Hz at field magnitudes of up to 0.3 mT. Susceptibility could then be measured as a function of temperature at various frequencies, or as a function of frequency at various temperatures. However, in this research very little work was done using this technique on the thin film or VACNF samples because low sample moment led to a very poor signal to noise ratio.

3. Vertically Aligned Carbon Nanofibers

3.1 Introduction**

As discussed previously in the introduction to nanostructured carbons (Section 1.3.1), carbon can form a number of nanostructured materials such as fullerenes,[19] carbon nanotubes,[20] and carbon nanofibers,[43,117] on account of its great versatility in covalent bonding arrangements and electronic configurations.[40] Carbon nanofibers, or CNFs, are high aspect ratio cylindrical or conical structures with diameters of a few nanometers to hundreds of nanometers and lengths ranging from less than a micron to millimeters or more. CNFs are useful for numerous applications due to their nanoscale size and unique properties such as high strength, low density, metallic conductivity, tunable morphology, chemical and environmental stabilities, as well as compatibility with organochemical modification.

Depending on the growth method, CNFs can either grow as tangled mats or as straight structures oriented perpendicular to the substrate on which they are grown. The latter are commonly called "vertically aligned", hence the term VACNF. For the many applications that require freestanding, individual elements, VACNFs are synthesized by plasma-enhanced chemical vapor deposition from a catalytic nanoparticle located at the nanofiber tip, as illustrated in Figure 3.1. Demonstrated VACNF applications include electron field emitters,[72,138,139] composite structures,[82,140] biosensors,[74,81,141,142] gene delivery arrays,[77,78,83,84] synthetic membrane structures,[80,143] electrochemical probes,[76,144,145] electrodes for neuronal interface,[85,86] and scanning probe microscopy tips.[73,79,146] This introduction will broadly discuss carbon nanofiber structure, synthesis, properties, and applications, however a more detailed review can be found elsewhere.[44,108,147,148]

** This section contains lightly revised passages and figures from [39,44,137].

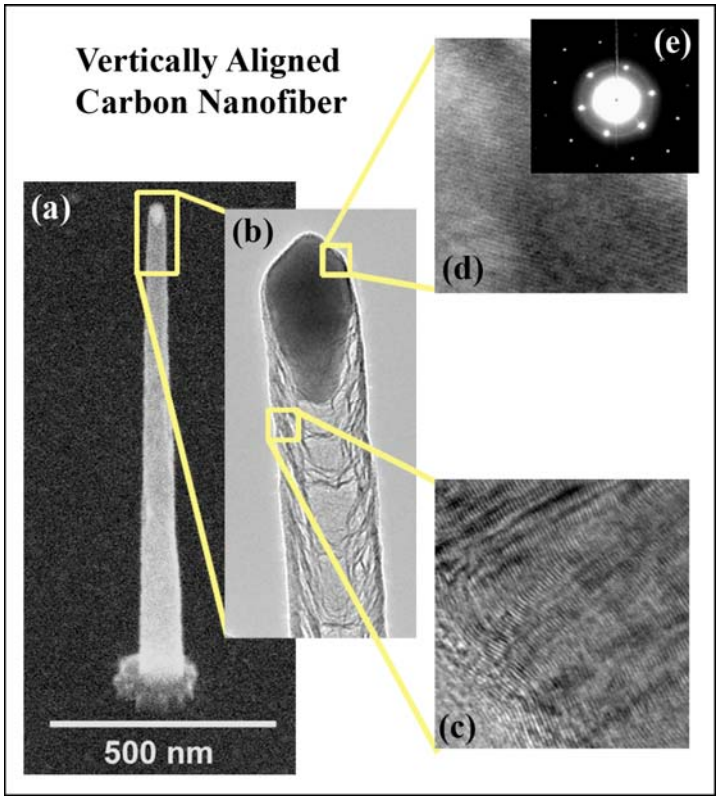

Figure 3.1 Representative vertically aligned carbon nanofiber: (a) tilted SEM image of an entire VACNF structure, (b) TEM image of the tip of the fiber, (c) HRTEM image of the defective graphitic sidewalls, (d) HRTEM lattice image of the FCC Ni catalyst nanoparticle and corresponding diffraction pattern (e).[39]

3.1.1 Carbon Nanofiber Structure

In general, the CNF's cylindrical form is comprised of assorted arrangements of stacked graphene sheets. Thanks to TEM cross-sectional imaging, many different variations in the internal structure of CNFs have been readily observed.[149] Platelet structures have been noted where the graphitic layers are stacked perpendicular to the CNF axis, as in Figure 3.2(a). By the introduction of five and seven member rings into a hexagonal graphene sheet, shown earlier in Figure 1.6(a), curved or angled layers can be formed [Figures 1.6(b) and 3.2(b)]. Additionally, this angle can become so steep as to produce graphitic layers nearly parallel to the CNF axis, as in Figure 3.2(c).

For VACNFs the two most commonly identified structural configurations, depicted in Figure 3.3, are "herringbone-type", in which dense, conical graphene layers resemble a fish skeleton when viewed in cross section, and "bamboo-type", in which cylindrical, cuplike graphene layers alternate with cavities along the length, like the cross section of a bamboo stem. It is convenient to characterize this internal graphitic structure by the cone angle α with respect to the nanofiber axis, as defined earlier in Figure 1.6. While herringbone-type CNFs have a relatively large α of ~10 – 45°, bamboo-type nanofibers have a much smaller α of generally only a few degrees and therefore are more similar to true carbon nanotubes, in which α is equivalent zero. It should be noted that the graphitic structure of a nanofiber, (i.e. number of layers, cone angle, defect density, etc.) governs the surface chemistry and many of the physical properties that are crucial to the performance characteristics of nanofiber-based devices.

A concerted effort should be made to make a distinction between CNTs and CNFs because it is their graphitic structure that determines the majority of their behavior and properties. By our definition, it is the angle α *alone* that dictates whether the structure is a CNT or CNF, regardless of the presence of a hollow cavity, which can also occur in nanofibers. It follows that CNTs with basal planes oriented completely parallel to the growth axis are therefore single crystalline materials. In contrast, CNFs, because of the stacking angle and higher presence of defects, have a grain size or structural coherence length that is small compared to their circumference.[150] This distinction is critical because it is the single crystal nature of CNTs that is responsible for their 1D quantum effects and exceptional mechanical properties.

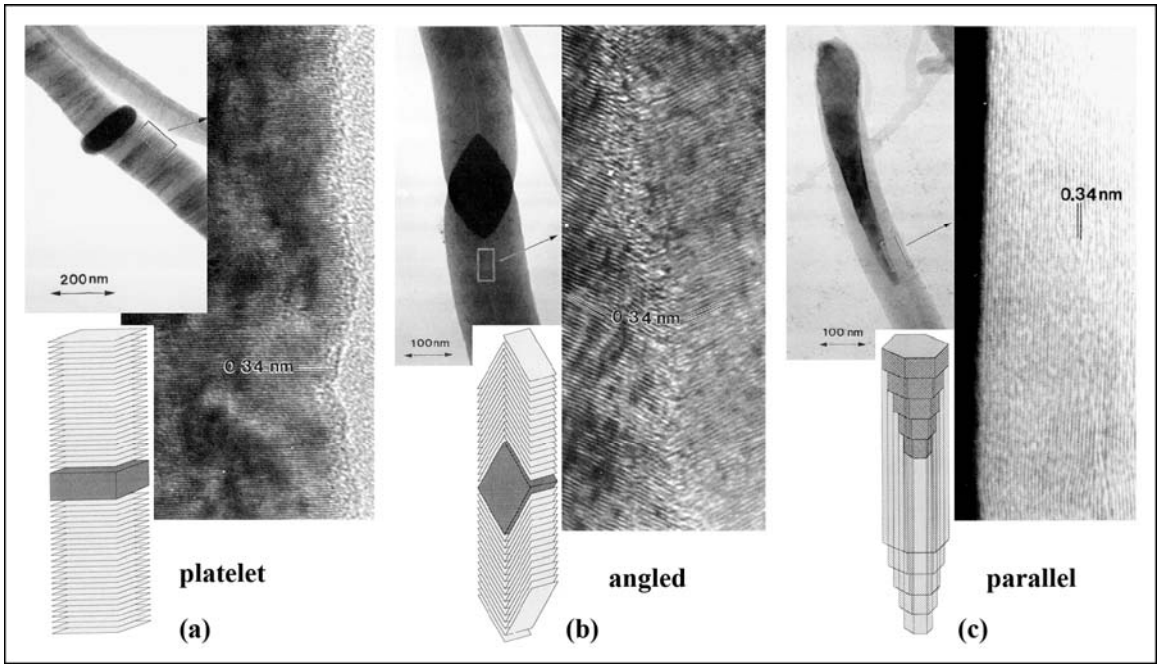

Figure 3.2 Various graphite stacking arrangements in carbon nanofibers: (a) platelets of graphite stacked perpendicular to the CNF axis, (b) angled stacking, and (c) stacking nearly parallel to the CNF axis. Adapted from [149].

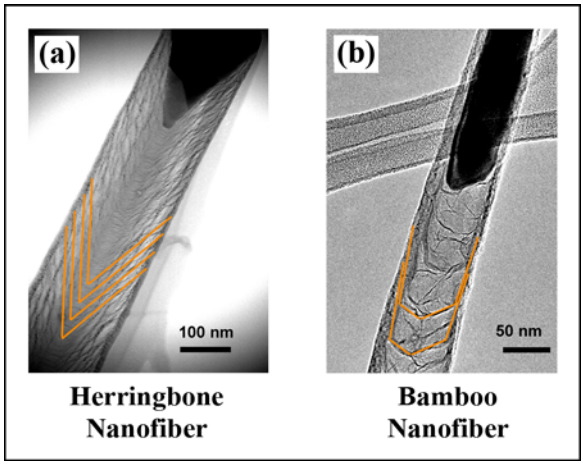

Figure 3.3 TEM images of the two common VACNF internal structures: (a) herringbone-type nanofiber grown from Ni catalyst and (b) bamboo-type nanofiber grown from Fe catalyst at the same conditions. Adapted from [44].

3.1.2 General Carbon Nanofiber Growth Mechanism

Over fifty years ago, Tesner and coworkers were the first to establish that CNF (or "carbon filaments", as they were called then) growth was associated with a catalytic metal particle.[115,116] However, even to this day the atomic-scale details of carbon nanostructure growth and the chemical processes involved are still largely unknown and may occur by different mechanisms depending on the growth conditions, leading to recent unexpected results.[151] At this time, the widely accepted growth mechanism is known as the diffusion/precipitation model, which can be attributed to the work of Baker *et al*. in the early 1970s.[43,117] In this model, growth is mediated by a solid transition metal catalyst particle that first dissolves and then precipitates carbon to form a nanofiber similar to the size of the particle. Baker *et al.* used *in situ* TEM to observe directly the manner by which nanosized metal particles generated carbon nanofibers when exposed to acetylene gas at elevated temperatures. From analysis of recorded image sequences, they measured the rates of growth of the carbon filaments and determined some of the kinetic parameters involved in the growth process. Based on these experiments they proposed the following mechanism (depicted in Figure 3.4): (i) adsorption and decomposition of the reactant hydrocarbon molecule on the catalyst surface, (ii) dissolution and diffusion of carbon species through (and around) the metal particle, and (iii) precipitation of carbon on the opposite surface of the particle and incorporation into the graphene layers of the growing CNF.

The model in Figure 3.4 illustrates the key features of what is called "tip-type" CNF growth, in which the catalyst particle remains a the tip of the nanofiber and precipitation occurs on the bottom surface of the catalyst, thereby elevating the particle with the creation of each new graphene layer. Another growth mode has also been observed, designated "base-type", wherein the catalyst particle remains on the substrate due to strong metal-support interactions,[43] i.e. wetting with a small contact angle.[44] Though the same diffusion/precipitation mechanism can be applied, base-type growth mode usually leads to irregular, unaligned CNF growth and can be avoided by the choice of catalyst and substrate materials as well as growth conditions.[152]

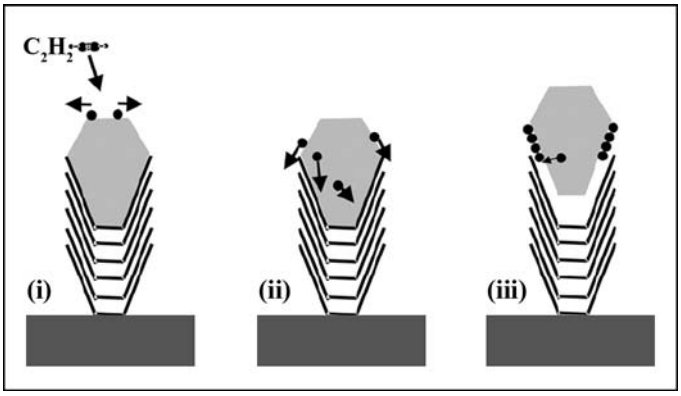

Figure 3.4 Basic CNF growth mechanism based on the diffusion/precipitation model. Adapted from [44].

The kinetics of the three steps in the diffusion/precipitation model determines the growth rate. A supply-limited process would depend on the arrival rate of carbonaceous gas species to the catalyst surface, their adsorption rates, and their decomposition rates. It is more commonly argued that the diffusion of carbon through the catalyst particle in step (ii) is the rate-determining step, as justified by the close agreement between the measured activation energy for CNF growth and the energy of carbon diffusion through the metal catalyst.[43,117] However, the driving force for bulk diffusion through the catalyst has also been a point of contention. Baker *et al.* proposed that this driving force results from a temperature gradient due to the exothermic decomposition reaction occurring on the gas/particle surface and the endothermic reaction at the precipitation interface.[43] A shortcoming of this explanation is that it cannot account for the demonstrated growth from methane, whose decomposition would be endothermic. Moreover, it is unlikely that such a temperature gradient exists across a small metal particle with high thermal conductivity, necessitating massive heat flow though the particle.[108] An alternative theory, more akin to VLS/VSS mechanisms, relies on concentration gradients to drive carbon diffusion through the catalyst, involving possible surface carbides and differing carbon solubilities at each interface.[153-156]

A second model for growth, proposed around the same time as the Baker model, proposes that the catalytic process involves the surface diffusion of carbon around the metal particle instead of bulk diffusion.[157,158] Carbon atoms diffuse over the surface of

the catalyst droplet (implying a molten state) to form a tubular structure that emanates from the circumference of the catalyst. This concept is used to explain the growth of nanotubes from small diameter droplets, where there would be an enormous percentage of dangling bonds if stacked graphite were formed.[40,159] It is, therefore, more energetically favorable for basal planes to orient themselves parallel to the catalyst surface, creating a hollow core.[159]

The validity of either of these models is difficult to assess due to the lack of direct high-resolution *in situ* determination of the nanoparticle phase, structure, and composition. Further details of the intimate relationship between the catalyst particle and the nanofiber during growth will be discussed in Section 3.4 and for more particulars on catalytic VLS, VSS and CVD, see methods Section 2.1.

3.2 Controlled Synthesis of VACNFS by Catalytic PECVD

Carbon nanostructures are synthesized by three main techniques: laser ablation/vaporization,[19] arc discharge,[20] and chemical vapor deposition.[43,119] While the laser ablation and arch discharge methods are very efficient for producing high-quality nanotube material in large quantities, they do not offer control over the spatial arrangement of the structures produced and require complex purification procedures to obtain useful material. Currently, only catalytic CVD routes provide a means for the controlled synthesis of CNTs and CNFs and it will be seen that only catalytic PECVD on supported catalysts[44,150,160,161] allows for truly deterministic synthesis. By deterministic synthesis, we imply the ability to grow individual nanostructures with *precisely* defined characteristics, such as size, location, chemical composition, internal structure, etc., all by varying the starting materials or plasma conditions during growth. Thus for the purpose of attaining this level of controlled synthesis, the focus of this chapter will only be on the catalytic PECVD growth process.

Over the past several years, it has been demonstrated that carbon nanofibers can be synthesized deterministically by PECVD using many types of catalysts and substrates.[44] This section will describe the PECVD synthesis process and the various

aspects of control. In general, the location of the VACNF is defined by patterning the catalyst material lithographically with the size of the catalyst nanoparticle controlling the resultant nanofiber diameter; the nanofiber length is controlled by the growth rate and duration of the growth process; the shape and sidewall chemical composition are tailored by the ratio of gases used during synthesis; and the alignment is directed by the electric field present in the plasma sheath. However, even with this high degree of control, command over VACNF internal crystalline structure remains elusive. Taking into account the loose use of the term CNT in the literature, thus far PECVD processes have only produced carbon nanofiber structures and not true nanotubes (defined by a single-crystalline nature and $\alpha = 0$). One of the great challenges remaining for controlled synthesis is to leverage the processes that determine the graphitic cone angle α and gain the ability to grow *either* individual vertically aligned nanofibers or freestanding nanotubes by selecting appropriate growth conditions.

3.2.1 Details of DC-PECVD Synthesis

While a variety plasma power sources have been used for CNF synthesis (e.g. radio frequency, inductively coupled, microwave, etc.), direct current systems are the simplest of the PECVD reactors. The carbon nanofibers particular to this dissertation are grown by a DC-PECVD process, where the substrate heater also acts as the cathode, requiring the substrate to be conductive. The showerhead above the heater similarly serves a dual purpose by distributing gases evenly over the sample as well as functioning as the anode. For more details on the plasma process see the methods Section 2.1.5.

The first step in the synthesis process, Figure 3.5(a), is the deposition of the catalyst onto a suitable substrate as either a patterned or uniform film (see section 3.1.3.2 for catalyst and substrate considerations). Most commonly thin films of Ni, Fe, or Co are deposited by a physical vapor technique (see Section 2.1.3). In addition, a buffer-layer such as Ti is often used as a barrier to diffusion and to promote particle formation. Once

the films are deposited, the sample is placed on the heater and the PECVD chamber is pumped down to a vacuum with a base pressure in the mTorr range or less.

Next, ammonia gas (NH_3) is flown in and allowed to pressurize the chamber at a few Torr. Meanwhile, the sample is heated to the desired temperature, usually 500 – 700°C. Then an ammonia plasma is initiated for several seconds to minutes, whereby the catalyst thin film dewets into discrete nanoparticles, as in Figure 3.5(b). This is called the "pretreatment step". Not only is this step critical for particle formation and reducing any surface oxide on the catalyst, but it is also useful to stabilize the plasma before introducing the carbon source gas. However, if the catalyst is thin enough (< 20 nm), heat alone may be enough to dewet the catalyst film and the pretreatment step can be eliminated.

The final step in the synthesis process is to introduce carbon source gas (commonly acetylene, C_2H_2) to the plasma, which immediately initiates carbon nanofiber growth, Figure 3.5(c). The VACNFs continue to grow aligned with the electric field until the desired height is reached and the plasma power and gases are turned off.

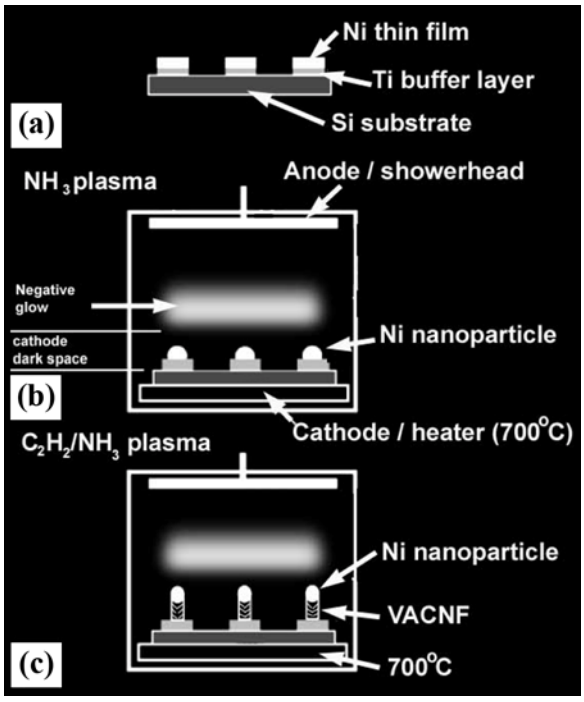

Figure 3.5 Schematic representation of PECVD synthesis of VACNFs. (a) Catalyst deposition, (b) catalyst pretreatment/nanoparticle formation, and (c) growth of carbon nanofibers. Adapted from [44].

PECVD synthesis adds a few extra components to the simplified growth model presented previously in Figure 3.4. Figure 3.6(a) presents a schematic of some of the processes occurring at the catalyst particle in a complex PECVD environment.[44] Many of these processes also occur in thermal CVD as well, including: (A) arrival of excited carbonaceous species to the surface, (B) catalytic dissociation of C_2H_2, (C) desorption of undissociated molecules, (D) formation of a carbon film on the surface, (G) solution of carbon into the catalyst particle, (H) diffusion of carbon through or around the catalyst particle, and (I) incorporation of carbon atoms into a growing graphene layer. In addition, there are processes specifically associated with PECVD processes due to application of and electric field and partial ionization of the gases: (E) chemical etching and (F) sputtering by ion bombardment.

While sputtering by ion bombardment needlessly removes valuable catalyst material in addition to surface carbon, chemical etching, on the other hand, specifically removes just the non-catalytic carbon film deposits (D) on the catalyst surface. The essential chemical etching species are supplied by an etchant gas such as NH_3 or H_2 in the plasma. As illustrated by Figure 3.6(b), a carbon shell can form on the catalyst surface, which blocks the solvation and diffusion of free carbon atoms into the catalyst nanoparticle and can lead to slowing of CNF growth by a supply-limited[162] (rather than diffusion-limited[160]) regime. The extent of this covering depends on the ratio of carbon source gas to etchant gas (i.e. C_2H_2/NH_3): (i) a small-area discrete carbon film forms at low C_2H_2 ratios, (ii) a large-area discrete carbon film forms at higher C_2H_2 ratios slowing CNF growth, and (iii) finally when the C_2H_2 ratio is too great, a continuous carbon shell completely encapsulates the catalyst and growth is halted. In fact, in order to restart growth of CNF samples, the trick entails a brief NH_3-only plasma treatment to remove the carbon from catalyst tips prior to the introduction of C_2H_2.

Thus it can be seen that as compared to thermal CVD, plasma excitation introduces an additional level of process complexity. However, this complexity simultaneously provides additional aspects of control, such as over the shape and alignment of the carbon nanofibers, to be discussed in the next several sections. Unlike CVD synthesis where temperature and total gas pressure and flow govern the growth process, PECVD synthesis also includes parameters specific to the glow discharge.

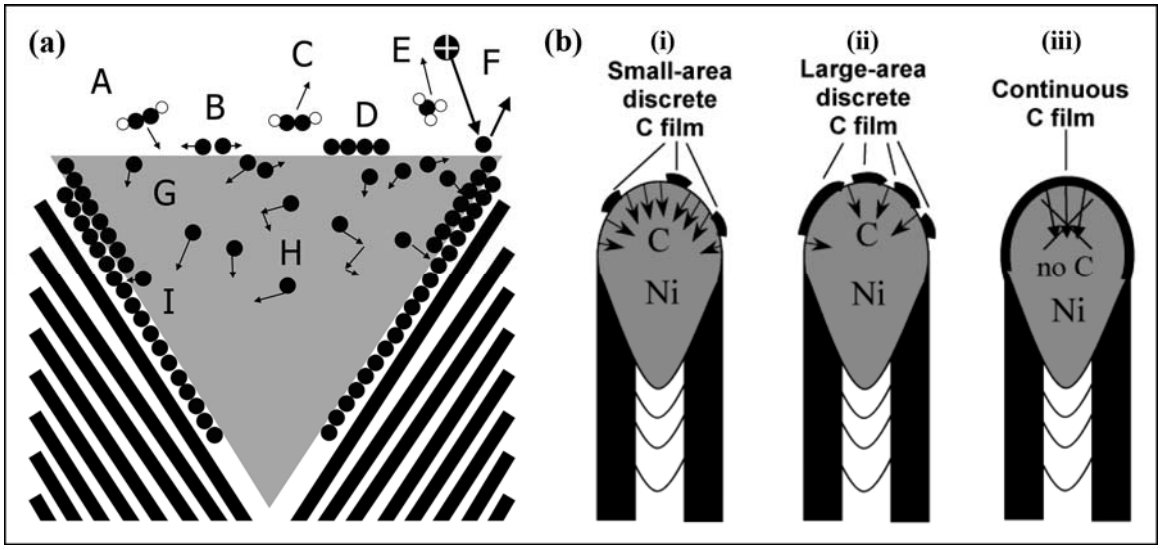

Figure 3.6 Processes at the catalyst nanoparticle during PECVD synthesis. Adapted from [44,162].

These parameters include the voltage, current, power, and electric field distributions within the discharge, which all play a critical role in shaping the outcome of the growth process. Since plasma can produce both etching and deposition of conformal films depending on the conditions, care must be taken to balance the two regimes in order to deposit only catalytic graphitic carbon and avoid thin film formation of non-catalytic amorphous carbon that can ultimately halt VACNF growth.

3.2.2 Catalysts and Substrates

The growth of carbon nanostructures is catalytically controlled, thus the choice of catalyst plays a crucial role in determining the outcome.[163,164] The catalyst particle is responsible for breaking bonds and adsorbing carbon at its surface, then diffusing carbon to an interface where the carbon reforms in graphitic planes.[43,117,165] Thus, the properties of the catalyst can determine the rate of each of these steps as well as the degree of crystalline perfection and geometric structure of the resulting carbon fiber. In the literature, a variety of metals and their alloys are reported catalysts for production of

carbon nanostructures, each with different optimal growth conditions and varying effects on the CNF structure and growth rate. By far, the most commonly employed catalyst materials are the transition metals Fe, Ni, and Co, whose physical properties and solubility of carbon are shown in Table 3 of Section 4.6. For an extensive list of catalyst and substrate materials consult reference [44].

The substrate also plays a crucial role in carbon nanostructure synthesis especially in PECVD processes. The substrate not only acts as a medium for support but it also interacts with the catalyst and plasma growth environment. Silicon and silicon dioxide are two of the most common substrates for obvious reasons of application in silicon-based technology. In reality, the choice of substrate is practically unlimited (refer to [44] for an extensive list of carbon nanofiber catalysts used with various substrates and growth methods); however there are several issues that should be considered. First, typical PECVD substrate temperatures are between 500 – 800°C. Reports of low temperature or even room temperature growth are somewhat misleading because even though there is no intentional heat applied to the substrate, the surface is inevitably heated hundreds of degrees by the plasma bombardment.[166] For applications where the growth temperature is a concern, arrays of VACNFs can be transferred post-synthesis to temperature-sensitive substrates.[167]

Additionally, in DC-PECVD systems, with the substrate as a cathode, it is necessary to have an electrically conductive surface, so insulating substrates like SiO_2 must be covered in a metal layer, which can later be removed.[144] Substrate choice also contributes to variation of secondary electron yield and the type of radical species in the plasma. Yet another issue in PECVD is the removal and redeposition of substrate material. For instance, during PECVD growth on Si substrates, silicon species can be etched or sputtered and redeposited onto the sidewalls of the fibers, creating an insulating Si_xN_y sheath,[39,168] which may or may not be desirable. To avoid Si incorporation on the fiber sidewalls, a resilient metal overlayer is again utilized to cover the substrate. Additional incompatibilities of the substrate with catalyst materials and the growth environment have prompted the use of buffer layers or adhesion layers underneath the catalyst. Buffer layers like Ti, W, and SiO_2 are often been used to prevent diffusion or intermixing of catalyst and substrate, such as the formation of silicide.[160] Underlayer

material effects on the actual carbon growth is mostly attributed to catalyst wetting and particle formation, which in turn can affect the growth mode. Aluminum, for example, is often put underneath Ni and Fe catalysts because it promotes the small particle formation required for base-type nanotube growth by CVD.[164]

High throughput methods for investigating a battery of catalyst and substrate combinations have proven fruitful. For example, Ng *et al.* came up with an efficient methodology for evaluating underlayer material compatibility with various catalysts for CVD nanotube growth[169] and Cassell *et al.* published a similar approach for exploring nanofiber PECVD growth.[170] In their experiments strips of several different metal contact layers were deposited onto a Si wafer; then the wafer was turned ninety degrees and strips of different catalysts were deposited on top. This created an underlayer-catalyst grid, which was then used to grow carbon nanostructures. For CVD growth, Ng *et al.* concluded that Ti was the best underlayer in terms of low contact resistance and high growth density, however Fe-Ni and Ni grew the most vertically aligned CNTs on an Al underlayer.[169] Cassell et al. found that for their PECVD growth process Ni catalyst on a Cr underlayer yielded the highest quality fibers on the basis of growth rate, alignment, and diameter uniformity.[170] Furthermore, the combinatorial co-sputtering methods presented in Chapter 4 of this dissertation provide an efficient means of alloy catalyst exploration.[171,172] It is these types of efforts that lead to the rapid development and implementation of the best catalyst and substrate for a given application.

3.2.3 Location, Diameter, and Array Density

VACNF location is directly defined by the deposition of the catalyst material. If catalyst patterning is required, it can be done before or after the catalyst film is deposited. Commonly, the pattern is defined beforehand using photo- or electron beam lithography and metal lift-off is subsequently employed. First, a resist is applied to the substrate and the desired catalyst pattern is exposed and developed. Then the catalyst material is deposited by PVD onto the substrate. Following the deposition, the substrate is

immersed in a solvent capable of dissolving the resist, causing the metal to be removed from the unpatterned areas. Conversely, the film can also be patterned following catalyst deposition by coating it with a resist. The pattern is then exposed and developed such that resist remains in the areas where catalyst is desired. The exposed metal is then removed by wet etching, ion beam sputtering or reactive ion etching.

If a periodic array of individual VACNFs is desired, first an array of lithographically defined catalyst "dots" is deposited. Each dot is essentially a disk of metal left after removing the surrounding catalyst film. The amount of material (diameter and thickness) deposited for each patterned dot is crucial to determining whether single or multiple fibers form. Merkulov *et al*. found that there was a critical dot diameter resulting in single nanofibers (Figure 3.7). This critical dot diameter of course would depend upon several parameters including the choice of underlayer, substrate, and type and thickness of catalyst used.[150] Subsequent work by Melechko *et al.* with larger, photo-lithographically defined dot arrays, also showed that there is a critical dot thickness for obtaining a single nanofiber from each dot.[168] These two results underline that it is really the aspect ratio of the dot (thickness/diameter) that is key, where the number of nanoparticles dewetted from a patterned dot decreases with an increase in the aspect ratio of the dot.

The VACNF tip diameter is approximately equal to the diameter of the catalyst nanoparticle.[160] For a given dot of catalyst material, the *initial* diameter of a nanoparticle, D, roughly determined from mass conservation of the catalyst, is $\pi D^3/6 = \pi d^2 t/4$ or $D = \sqrt[3]{3d^2 t/2}$, where d is the diameter of the catalyst dot and t is its thickness.[162,173] It has been observed, however, that the size of the catalyst particle decreases continually during the PECVD synthesis process,[173] eventually disappearing altogether. The loss of the catalyst material is likely due to ion sputtering from the plasma or possibly incorporation of Ni along the nanofiber body. Since particle size correlates to fiber diameter, with the particle size reduction the fiber diameter is also reduced. This trend can be used to sharpen the tips of the nanofibers for use in such applications as field emission and intracellular probes.

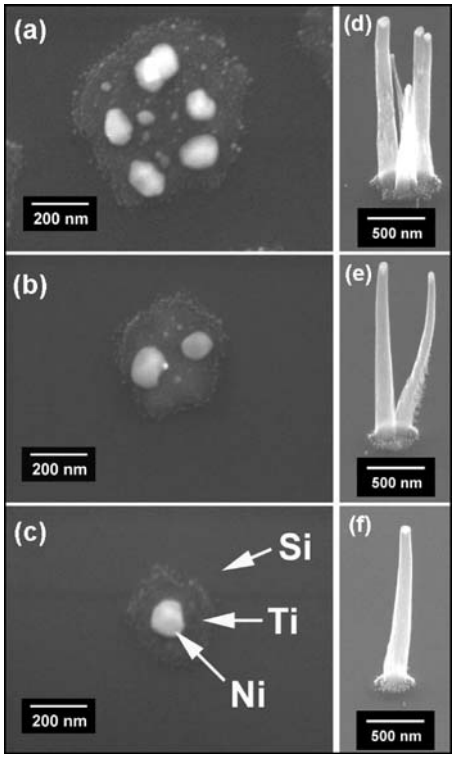

Figure 3.7 Formation of multiple or single VACNFs from one patterned 15-nm-thick Ni dot on 10 nm Ti. (a,d) When the initial catalyst dot has a large diameter, multiple nanoparticles dewet from a single dot and produce multiple CNFs. (b,e) As the size of the dot is reduced, the number of nanoparticles and nanofibers produced from a single dot decreases. (c,f) Finally, for a dot size < 350 nm, only a single catalyst nanoparticle and thereby single VACNF is formed. Adapted from [150].

However, the inevitable tip size reduction simultaneously creates a limitation on the maximum obtainable length of the freestanding isolated nanofiber. In order to achieve the desired final length, the amount of metal contained in the catalyst particle must be sufficient to last the duration of the growth process. The catalyst particle, in addition to facilitating growth, also protects the nanostructure from physical and chemical etching. Should the nanoparticle disappear before the nanofiber achieves the targeted length, the nanofiber would no longer be protected and would start to be etched back.[173] In some ways this phenomenon of "survival of the fittest" (or largest particle) has proven useful as a strategy to grow high-quality, tall arrays of VACNFs, where the smaller extraneous nanofibers are etched back and disappear.

In the case of VACNF "forests" where a stochastic array is grown from an unpatterned catalyst film, the nanofiber array density and particle size are directly related to the initial catalyst film thickness.[160,174] In our experience, a significant change in particle breakup was observed by varying the initial film thickness just a few nanometers. Figure 3.8 shows experimental results of the particle size after just a 5 second exposure to carbonaceous plasma for different initial film thicknesses. A statistical analysis of the SEM images reveals that there is a linear relationship between average particle diameter and initial film thickness with the standard deviation increasing non-proportionally with initial film thickness. In fact, remarkable uniformity is seen with the 1 nm films, which produced 10 nm particles with only a 2 nm standard deviation. On the other hand, 10 nm films formed 110 nm particles with a standard deviation of 70 nm.

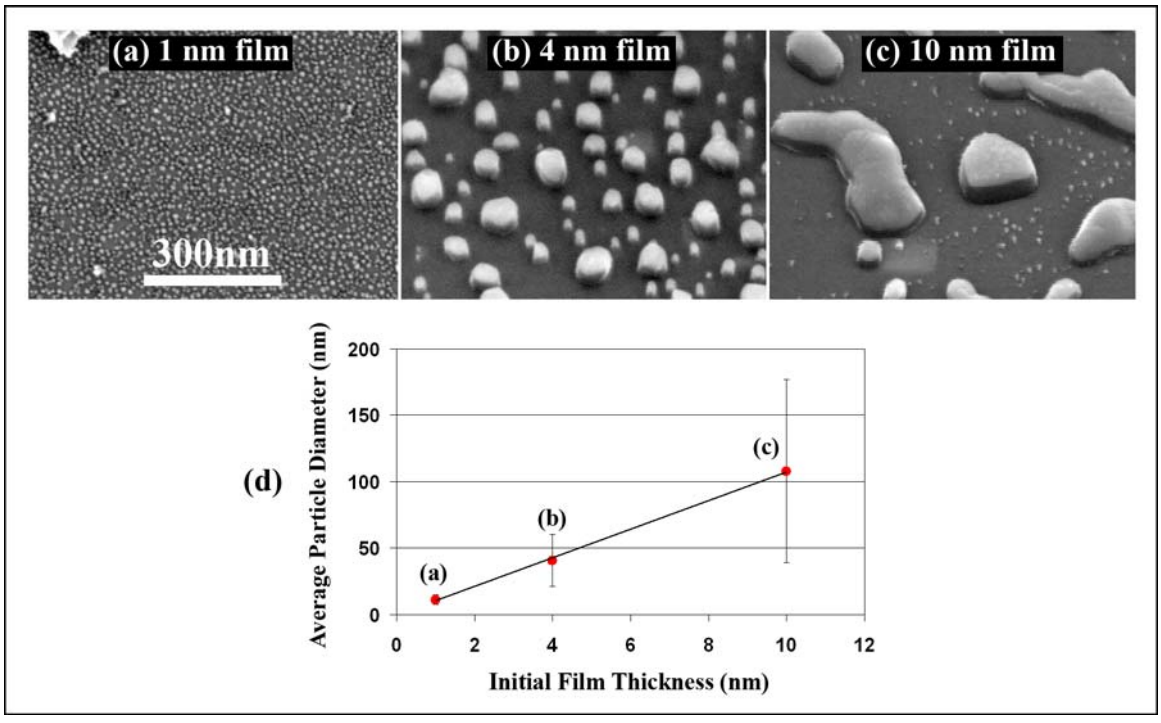

Figure 3.8 Particle size as a function of initial film thickness. At top are SEM images (taken at a 30° tilt) of particles formed after a 5 second growth at 700°C from initial sputtered Ni films in Si with thicknesses of (a) 1 nm, (b) 4 nm, and (c) 10 nm. (d) Corresponding plot showing the average particle diameter as a function of the initial film thickness, standard deviation shown by error bars.

The translation of the initial film thickness to subsequent VACNF diameters can be seen in Figure 3.9. The same films were grown for 10 minutes, yielding results analogous to the 5 second growth. The nanofiber diameter is still linearly proportional to initial film thickness, again with great uniformity in the thinner films and a large standard deviation with the 10 nm films. Plot (b) shows that the number of particles per area scales with $1/t^2$, demonstrating conservation of volume. It should also be noted that the data from the 1 nm film was omitted because of particle loss (discussed earlier in this section) during the 10-minute plasma process, which left the nanofibers obliterated as seen in the SEM image. Thus it can generally be said that for VANCF forest growth, thinner films lead to smaller particles, which in turn lead to denser arrays of smaller diameter fibers. Other factors affecting the array density and particle size include the wetting properties of the catalyst and substrate materials as well as the method of catalyst preparation, pretreatment time, and growth temperature.

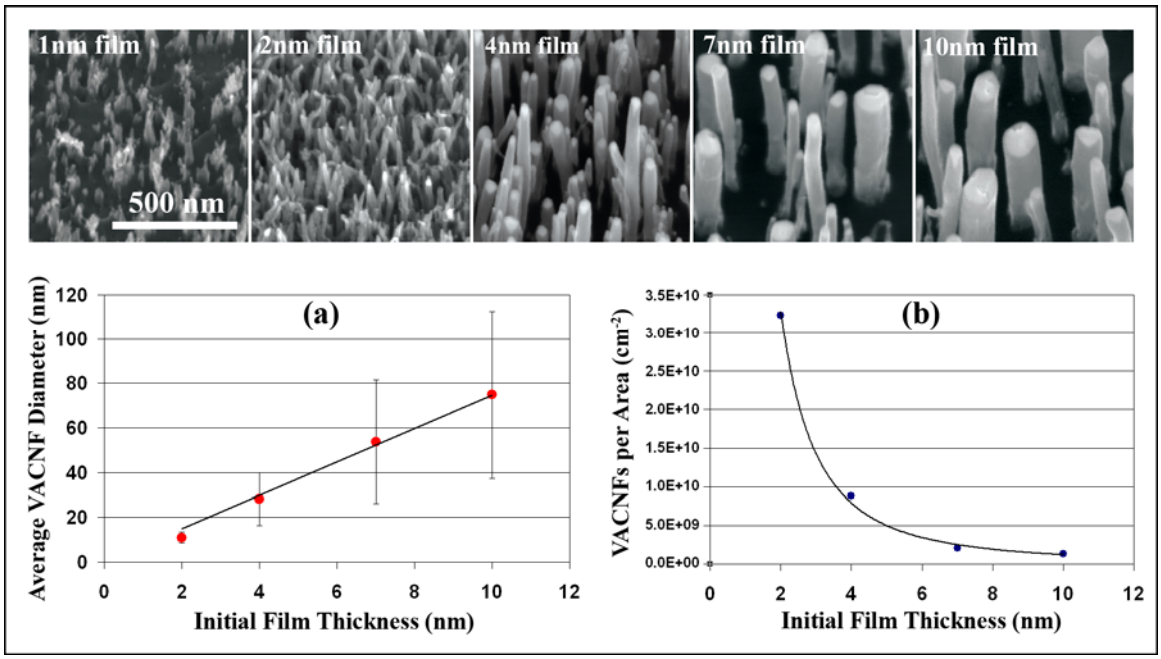

Figure 3.9 VACNF diameter and density as a function of film thickness. SEM images at top of VACNFs formed after a 10 minute growth at 700°C from sputtered Ni films on Si with initial thicknesses of 1 nm, 2 nm, 4 nm, 7nm, and 10 nm. Corresponding plots showing (a) the average VACNF diameter with standard deviation shown by error bars and (b) the number of VACNFs per area as a function of the initial film thickness.

3.2.4 Growth Rate, Morphology, and Composition

The catalytic PECVD process entails a host of parameters that are variable over a multidimensional space,[44] leading to extraordinary control over the growth rate, morphology, and composition of the resultant deposit. The main factors governing this multidimensional parameter space include: total pressure (P), total gas flow rate (F), carbon source to etchant gas flow ratio (e.g. C_2H_2/NH_3) (R), substrate temperature (T), and plasma power [current and voltage]. It should be mentioned that while plasma current and plasma voltage can have quite different effects on the growth of VACNFs, in a DC glow discharge these two parameters are coupled and cannot be changed independently.[160,162]

In this multidimensional space, there are different sets of parameters that can result in "equivalent" end products.[44,162] In other words, for a given T_1, there are a range of R_1 values for which favorable growth occurs and likewise for T_2, there is another is another range R_2 for which similar growth occurs. So the question remains, why don't we stick to one "recipe" or set of parameters for a desired outcome? The answer is that the selection of parameters used for VACNF growth is dependent upon the combination of catalysts, substrates, carbon source and etchant gases, and most importantly, the catalyst pattern, where the density of packing affects all aspects of growth.[175] Therefore, the recipe must be tailored to suit each different application. With the generation of parameter space trends navigating to the optimal conditions becomes much easier.

To begin with, the growth rate of VACNFs by PECVD has been shown experimentally to be linked to several parameters, namely total pressure, gas flow ratio, and temperature, as shown by the plots in Figure 3.10, as well as gas flow rate. It is encouraging to realize that the growth rate is fairly constant over time[160,173], given by (a); as a result, VACNFs can be grown to very precise lengths just by monitoring the growth time. As far as adjusting this rate, Chhowalla *et al*. found that the nanofiber growth rate increases almost linearly with P, at least up to 10 Torr, shown in (b).[160] By increasing P, a faster supply of carbon source material arrives at the catalyst. The relationship with R is not so straightforward, as seen in (c). A peak is observed with the maximal growth rate occurring about mid-range R.[160,162] At ratios above this optimum, increased C_2H_2 causes

a buildup of non-catalytic carbon on the catalyst surface, decreasing its activity as described previously in Figure 3.6(b). Likewise, if C_2H_2 is replaced by too much NH_3, etching processes are increased and insufficient quantities of carbon species arrive to the catalyst, leading to decreased growth rates. Temperature also shows a peaked relationship, with a maximum around 700°C.[160] This can be explained by the competing mechanisms of an increase in carbon diffusion rate with temperature and concurrent decrease in sticking coefficient of carbon species to the catalyst surface with temperature. The activation energy of 0.56 eV,[160] determined from the slope of the growth rate vs. inverse temperature plot, is much lower than that of C diffusion through Ni, about 1.5 eV. This suggests that there is either enhanced diffusion of C through the catalyst or possibly along the particle surface[109] occurring in PECVD, opening doors to the possibility of attaining true room temperature growth. Lastly, the total gas flow rate has also been found to have a considerable impact on the growth rate. Increasing *F* by using a gas inlet nozzle of variable orifice has shown that a smaller orifice, hence higher local flows, can drastically increase the VACNF growth rate.[121]

Controlling the morphology or shape of the VACNF structures as well as the elemental composition mainly involves adjusting the gas flow ratio in order to affect the same etching and deposition mechanisms that also influenced the growth rate. In PECVD, various species are present in the glow discharge, including C neutrals, C ions, and reactive etchant species (H^+, N^+, etc.) that are formed during the decomposition of acetylene and ammonia, Figure 3.11(b). By increasing the C_2H_2 flow relative to the NH_3 flow, the number of C species exceeds etchant species and condensation of amorphous carbon occurs on the surface.[175-177] While the neutrals randomly move about sticking to any surface, the electric field lines govern the direction travelled by the ions, thus creating a directional disparity in amorphous carbon accumulation. The result is the formation of conical nanostructures by two separate yet simultaneous processes shown in Figure 3.11: (a) the catalytic growth of a central cylindrical CNF and (c) the non-catalytic deposition of sloped sidewalls. This effect is most pronounced for sparse arrays compared to dense forests of nanofibers where geometric shielding by neighboring CNFs becomes a factor.[175]

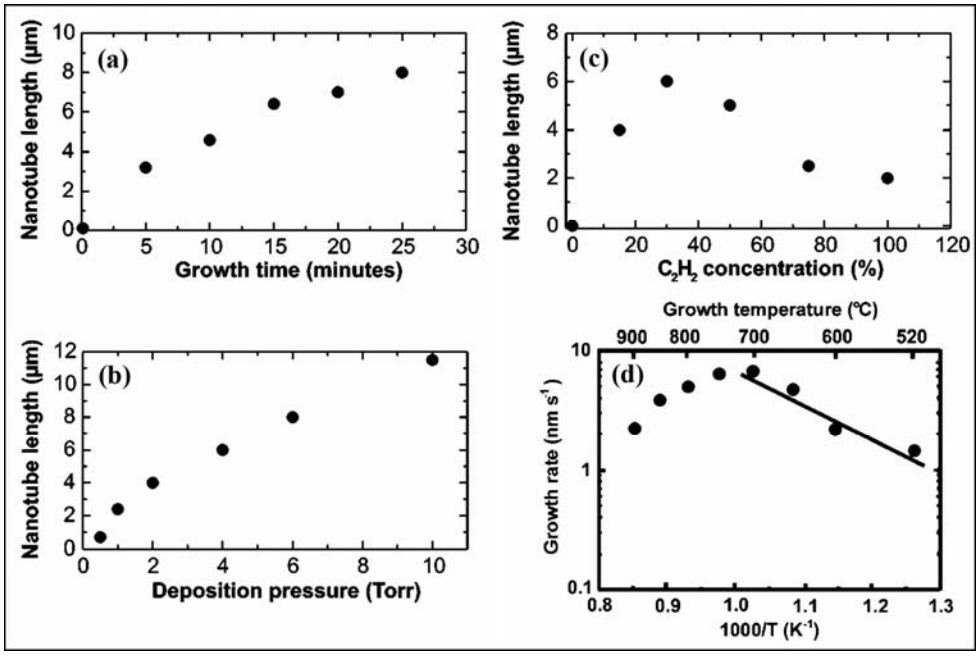

Figure 3.10 VACNF growth rate trends: (a) length as a function of growth time, (b) length as a function of total pressure, (c) length as a function of gas ratio, and (d) growth rate as a function of temperature. Adapted from [160].

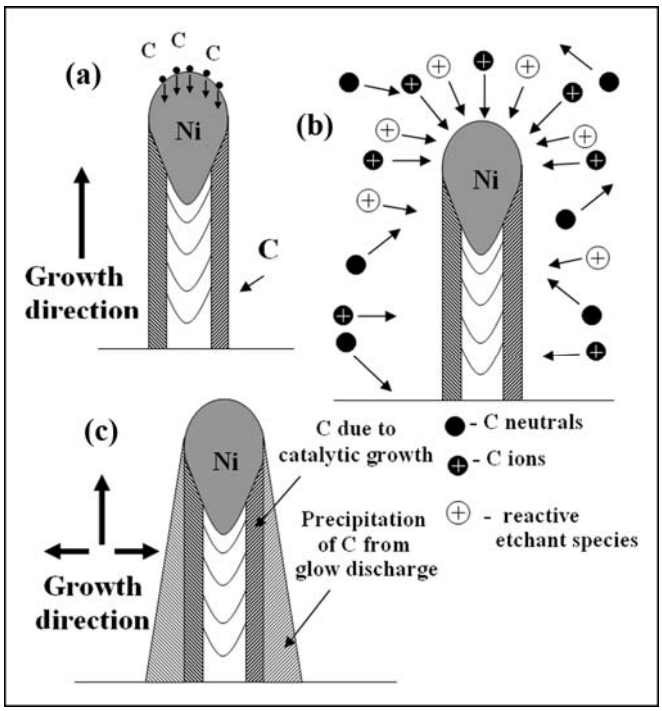

Figure 3.11 Schematic representation of growth by CVD and PECVD: (a) CNF grown using conventional thermal CVD, (b) VACNF grown using PECVD, and (c) carbon nanocone formed due to additional precipitation of C on the sidewalls during PECVD. Adapted from [176].

Thus by changing the source/etchant gas ratio, Merkulov *et al.* realized that the cone angle of individual patterned nanostructures can be controlled.[175,176] Figure 3.12(a-c) shows that VACNFs transition from cylindrical to highly conical with increasing *R*; however when *R* becomes too high, an amorphous carbon film forms, which halts growth altogether, Figure 3.12(d). Therefore the flow ratio can be used to tailor the conicity of the CNF along its length. This is useful, for instance, to create nanostructures with high aspect ratio and improved mechanical stability such as the cylinder-on-cone morphology in Figure 3.12(e), grown by a two-step process.[176]

Merkulov *et al.* noticed another trend with gas ratio, where the nitrogen content of the VACNFs increases as *R* decreases, as shown in Figure 3.13. It was initially hypothesized that due to an increase of N in the plasma, it replaced C as feedstock for growth, essentially doping the nanofibers at very high concentrations. However, this theory was soon put to rest when XEDS analysis of VACNFs detached from the silicon substrate, showed a coating with significantly high levels of Si in addition to N, which was easily removed by an SF_6-based plasma (commonly used to specifically etch Si and silicon nitride materials).[168] Therefore, it can be reasoned that a second type of sidewall deposition occurs on low-density arrays in a more etching regime (higher NH_3 flow), in which amorphous carbon is prevented from condensing. In this regime, the substrate, unprotected by carbon film, is etched by the plasma species and the etch products redeposit on the sidewalls of growing carbon nanofibers. In the case of CNF growth on silicon substrates using a C_2H_2/NH_3 mixture, the Si reacts with the N from the ammonia etchant gas to form $Si_xN_y(C,O)$ compounds on the VACNF surface.[168,171,178,179] Thus there is a delicate balance to the gas ratios used in regard the desired composition; for CNFs without an amorphous carbon coating a C_2H_2:NH_3 ratio of 20% or below must be used,[177] however for ratios lower than this, sidewall deposition of Si_xN_y material becomes more favorable.

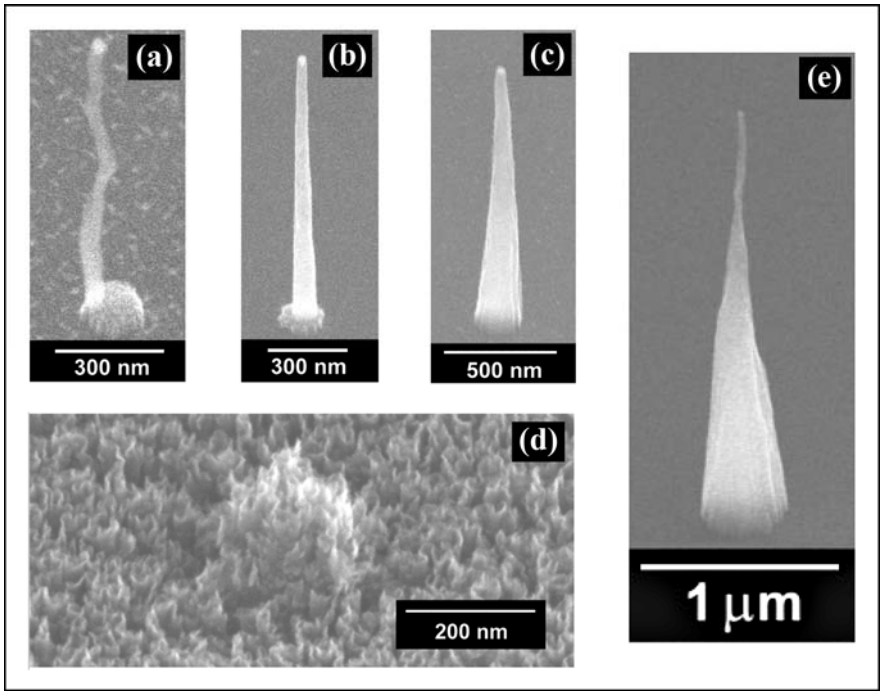

Figure 3.12 SEM images of isolated VACNFs grown with various ratios of C2H2/NH3: (a) *R*=0.38, (b) *R*=0.5, (c) *R*=0.59, and (d) *R*=0.75, while keeping the rest of the parameters constant. (e) Cylinder-on-cone morphology grown by a two-step process where *R* is decreased. Adapted from [175,176].

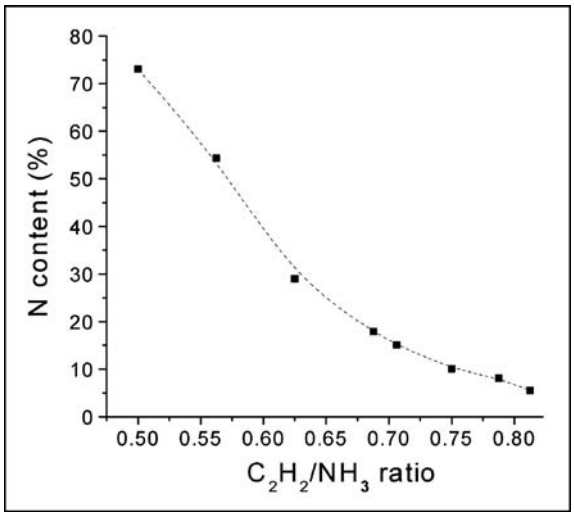

Figure 3.13 Nitrogen content of VACNFs as a function of gas ratio, determined by XEDS. Adapted from [162].

3.2.5 Alignment

Vertical alignment, where the nanostructure is oriented perpendicular to the substrate, is necessary for many applications. Commonly in the thermal CVD growth of CNTs and CNFs, vertical alignment is achieved by the "crowding effect",[151,180] which is due to the dense packing and van der Waal's interaction of the nanostructures during growth. This type of alignment does not depend on the location of the catalyst (base or tip), however it is only possible if the rate of growth of each of the nanostructures is comparable (i.e. similar diameters, catalyst size) so as to maintain the packing density. Therefore, the alignment of *spatially separated* structures is not possible through the CVD crowding method because there is not a strong interaction with the nearest neighbors.

In PECVD on the other hand, alignment can be achieved regardless of the density the CNF array. A strong correlation has been observed between the carbon nanofiber growth axis and the direction of the electric field in the plasma.[181,182] In the PECVD growth system, Figure 3.14(a), usually the electric field is perpendicular to the conductive planar substrate located on the sample holder, producing vertically aligned CNFs. However, the field direction can be changed by placing the substrate close to the edge of the sample holder to produce the angled alignment of CNF forests shown in Figure 3.14(b,c), where the tilt angle varies with distance from the edge.[182] This control mechanism was also demonstrated for the variable alignment of isolated CNFs, Figure 3.14(d), with the spatially separated structures tilting in the same way as the forests. This fact also enables the production of kinked CNFs, as in Figure 3.14(e), by a two-step growth process in which the substrate is first placed at the center of the sample holder for vertical growth and subsequently the sample is moved to the edge for tilted growth.

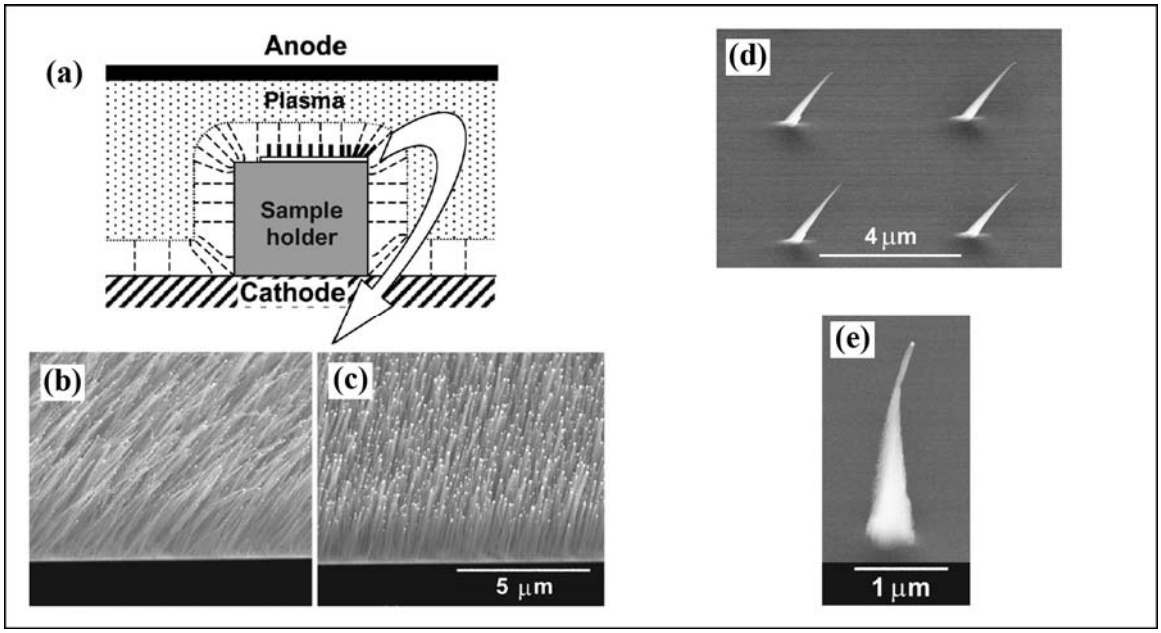

Figure 3.14 Electric field direction and the effect on CNF orientation. (a) Schematic of the experimental PECVD setup with electric field lines; the areas of the substrate located close to the sample holder edge experience a change in the electric field direction. (b) Resulting CNF forests located 100 μm away from the edge and (c) 1000 μm away from the edge, corresponding to CNFs orientated at angles of 38° and 12° off from perpendicular, respectively. (d) Tilted CNF array and (e) kinked CNFs with a vertical base and tilted tip grown by a two-step process. Adapted from [[182]].

Interestingly, there is also a direct correlation between alignment in PECVD and the growth mode.[181] Alignment with the electric field only occurs in tip-type growth and not with base-type growth, as shown in Figure 3.15(a) and (b), respectively. In tip-type growth, the catalyst particle is lifted up from the substrate and follows the path of the electric field lines in the plasma sheath. In contrast, when growth proceeds from the catalyst remaining at the nanofiber base, random growth orientation transpires. Merkulov *et al.* proposed a model to describe the alignment mechanism for both growth modes based on a stress-dependent growth rated caused by electrostatic forces, depicted in Figure 3.15(c-f).[181] In this model, when the axis of the CNF grows perpendicular to the substrate, it coincides with the direction of applied electrostatic force for both modes, resulting in uniform tensile stress across the nanofiber/catalyst particle interface (c,d). Consequently, carbon uniformly precipitates across the interface and the nanofiber

continues to grow vertically. However, if there were spatial fluctuations in the carbon precipitation along the interface (due to the catalyst shape asymmetry or supply factors), CNF growth would deviate from vertical alignment as shown in (e,f). In the case of tip-type growth (e), the electrostatic force produces a compressive stress at the section of interface where the increased growth rate is seen and a tensile stress where the decreased growth rate is seen. It is suggested that tensile stress at the interface favors carbon precipitation and therefore this combination of stresses results in a stable, negative feedback mechanism that maintains alignment with electric field. On the other hand, when the catalyst particle is located at the CNF base, the stresses are reversed creating a positive feedback situation and unaligned growth.

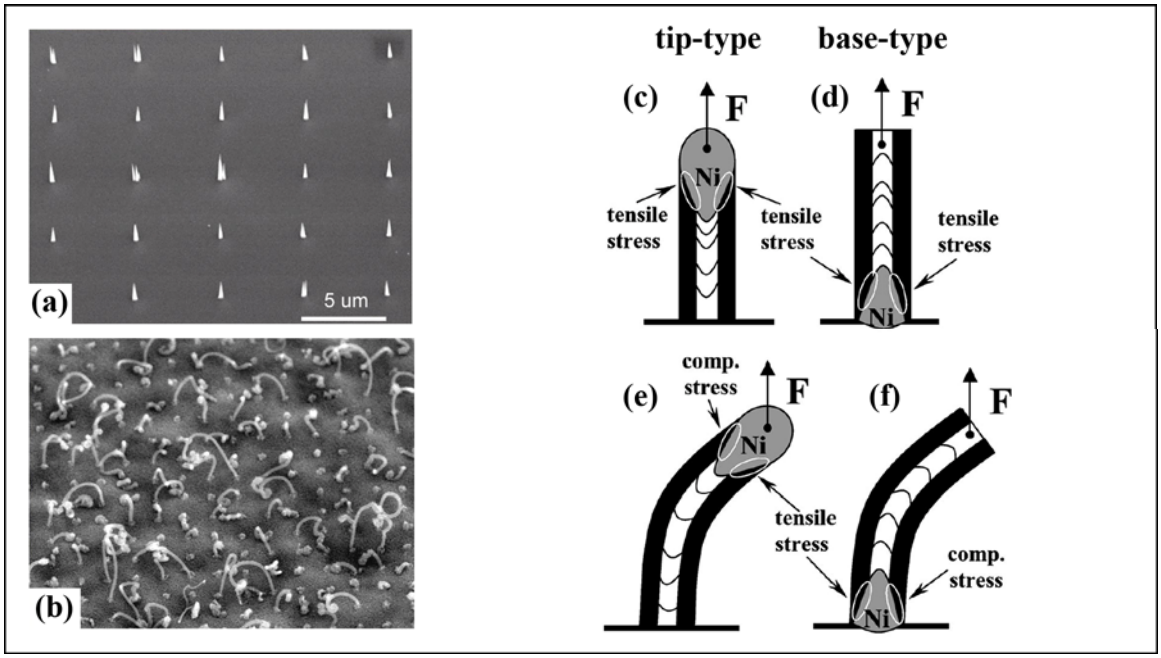

Figure 3.15 CNF alignment dependence on growth mode. SEM images of patterned arrays exhibiting (a) vertically aligned tip-type growth and (b) unaligned base-type growth. (c-f) Alignment mechanism based on a stress-dependent growth rate caused by interaction with the electric field. Adapted from [44,181].

3.3 Properties and Applications

Carbon nanomaterials have unique mechanical, electrical, and chemical properties attributable to the sp^2-hybridized bonding arrangement of carbon. The hexagonal network of atoms composing graphene sheets energetically favors the elimination of dangling bonds by creating closed structures such as nanocones, fullerenes, and nanotubes, even at the expense of increased strain. The defective graphitic structure of stacked-cup CNFs (Figure 3.3) may reduce some of this strain energy at the sacrifice of the extraordinary mechanical properties[48] and ballistic transport[47] exhibited by single-crystal CNTs. However, VACNFs afford several additional practical advantages such as compatibility with standard microfabrication processes, tunable morphology, precise patterning, and easily functionalized surfaces, while still retaining modestly high strength and conductivity, making them useful for a wide variety of applications, a selection of which are displayed in Figure 3.16.

Even though some fundamental questions about the growth mechanism remain unanswered, the technology of VACNF synthesis by PECVD has matured to the point that it can be used as a standard processing step in complex device fabrication.[72,84,138,139,144,146,167,178,183,184] The chemical and mechanical robustness of VACNFs make them resilient to standard microfabrication processes including hydrofluoric and nitric acid etches (the latter used for Ni catalyst removal), photoresist development, fluorine-based dry etches, and a variety of PVD, CVD, and PECVD processes for metal, oxide, and nitride coatings.[39] Thick SiO_x coatings have been used to improve mechanical strength and electrically insulate VACNFs from the surrounding environment for electrochemical probe[144] or biosensing[81] applications.

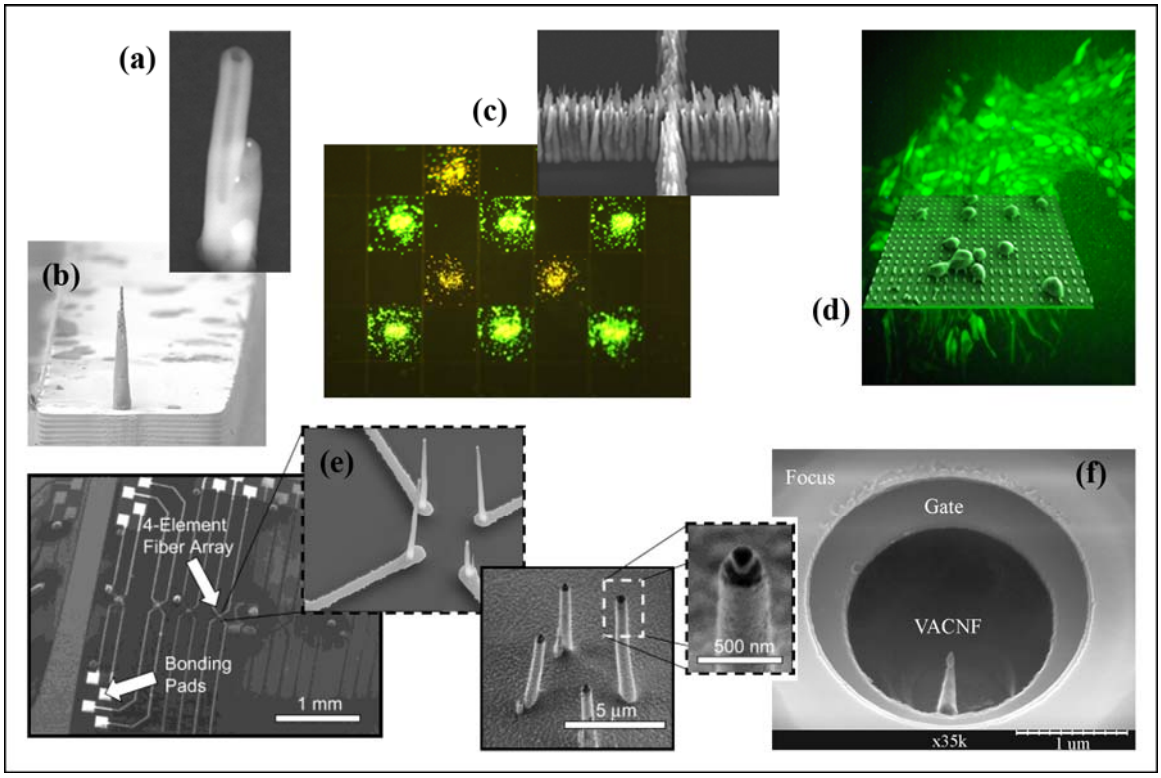

Figure 3.16 Selected applications of VACNFs: (a) templated nanofluidic pipe structures,[185] (b) scanning probe microscopy tips,[73] (c) membrane and cellular mimetic structures,[80] (d) massively parallel gene delivery arrays[77] (e) individually addressable intracellular electrochemical probes,[76] and (f) microfabricated field emitters.[72]

In addition, if the removal of graphitic CNF material is desired, etching is accomplished by oxygen-containing plasmas and electrochemical or thermal oxidation. In this way, freestanding, vertically aligned SiO_x nanopipes, Figure 3.16(a), have been produced by either partially or entirely removing the interior CNF scaffold inside the oxide coating through reactive ion etching of the VACNF in an oxygen plasma.[84,185] VACNF compatibility with these standard fabrication processes enables both the physical measurement of VACNF functional properties as well as their integration into numerous devices.

3.3.1 Mechanical Properties and Applications

The literature shows great variance in the mechanical properties of carbon nanostructures.[44] The high volumetric density of short, strong sp^3 bonds gives diamond the highest stiffness of any known materials (Young's modulus ≥ 1 TPa). Similarly, the high areal density of short, strong sp^2 bonds in the basal plane of graphite results in a Young's modulus that is comparable to that of diamond. However, single crystal graphite has a Young's modulus over 28 times higher in the direction parallel to basal planes than in the perpendicular direction.[186] Consequently, even though the sp^2 graphite bond is actually the strongest of all chemical bonds, the weakness of the *interplanar* bonding means that ordinary graphite is of little value as a structural material.[187] One way the great in-plane strength of graphite can be exploited is by the creation of nanofibers and nanotubes with their basal planes preferentially oriented along the axis. This has lead to measurements of extraordinary tensile strengths in MWCNTs of 63 GPa [48] and Young's modulus rivaling that of diamond.[48,187] Carbon nanofibers have been less studied, but still show promising results. Gao *et al.* observed the mechanical properties of a individual bamboo-type carbon nanofibers by electromechanical resonance via *in situ* TEM.[188] An oscillating voltage with tunable frequency was applied to the CNFs to induce resonance. The bending modulus, which depends on the length and diameter of the CNFs, was calculated to be 23–32 GPa for nanofibers with diameters of 33–64 nm and lengths of 4.6–5.7 μm. Demonstrated mechanical robustness is of high importance for CNF use in such applications as advanced polymer-matrix composite reinforcement,[189,190] scanning probe microscopy tips [Figure 3.16(b)],[73,79,146] membrane components [Figure 3.16(c)],[80,140,143] and cellular probing [Figure 3.16(d,e)],[77,78] where VACNFs have to penetrate cellular membranes.

3.3.2 Electrical Properties and Applications

The electrical properties of VACNFs have been investigated by several methods.[75,191-194] CNFs show typical linear current-voltage characteristics at low positive

and negative applied voltages with stable current-carrying ability over time. However, at higher bias, on the order of several volts, the current response becomes nonlinear, indicating that the CNFs experience physical changes caused by current-induced electrical breakdown. [191,193,194] Lee *et al.* calculated the resistivity of suspended CNF bridges to be in the range of $10^{-6} – 10^{-5}$ Ω·m, using the assumption that conduction occurred through the entire cylindrical cross-sectional area of the nanofiber.[193] Improvements on these two-probe measurements were carried out by Zhang *et al.* using a more precise four-point probe technique that excludes contact resistance contribution.[192] Their results showed that the resistivity of VACNFs is approximately 4.2×10^{-5} Ω·m. Zhang *et al.* proposed that this value is consistent with a dominant transport mechanism of electrons traveling through intergraphitic planes in the VACNFs. Detailed knowledge of nanofiber electrical properties is essential for many types of devices, including vertical electronic interconnects,[75] Schottky-barrier junction diodes,[178] electrochemical probes [Figure 3.16(e)],[76,144,145] and field emitters [Figure 3.16(f)].[72,138,139]

3.3.3 Chemical Properties and Applications

Carbon-based materials generally have superior long-term chemical stability even at elevated temperatures due to the extremely high melting point of carbon. However, the structural nature of CNFs, without a doubt, exposes graphitic edge planes all along the exterior surface, as shown in Figure 3.17. Since it is not energetically stable to leave dangling chemical bonds on the surface, these edge planes are most likely terminated by hydrogen or other moieties. Due to abundance of exposed edge planes, herringbone carbon nanofibers have higher chemical reactivity and electron transport across their sidewalls than nanotubes, which is important for functionalization[141,142,195,196] and electrochemical applications,[76,142,197] respectively. In fact, early studies of HOPG and glassy carbon have shown that the edge planes of graphite have electron transfer rates on the order of 10^5 times higher than basal planes.[198]

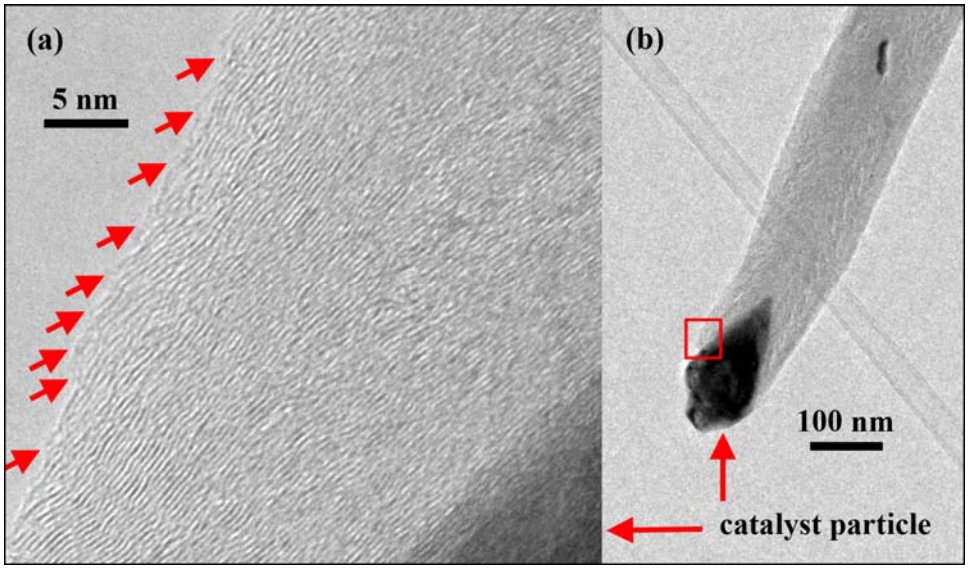

Figure 3.17 HRTEM of a herringbone VACNF sidewall showing graphitic edge plane termination: (a) HRTEM of the boxed area in (b), with graphitic edge planes marked by arrows.

The stacked-cup structure of CNFs can also be useful for charge[199] and hydrogen storage[200] media. Chambers *et al.* reported promising experiments indicating CNF material is capable of sorbing and retaining in excess of 20 L (standard temperature and pressure) of hydrogen per gram of carbon when the nanofibers are exposed to the gas at pressures of 120 atm at 25°C.[200] They argued that this result is due to the unique crystalline arrangement existing within the graphite nanofiber structure, in which the graphene planes make a system of sub-nanometer pores with only the edge sites exposed. Since the interplanar spacing within graphite is 3.36 Å,[201] sorption of molecular hydrogen, which possesses a kinetic diameter of 2.89 Å, is a facile process due to the short diffusion path.

3.3.4 Surface Functionality and Biocompatibility

The surfaces of carbon nanofibers can vary substantially depending on synthesis and post-synthesis processing conditions such as those encountered during microfabrication, and subsequent operations such as heat treatment or oxidation. For

many applications it is necessary to modify the CNF surface in order to change its properties and induce additional functionality. Particularly for biological or composite applications, manipulations of the surface chemistry are often needed in order to amplify the number of potential attachment sites, maximize the specificity and selectivity of adsorption processes, or to maintain the stability of the surface. Controlling the surface chemistry of carbon nanofibers is critical to defining their functionality. Whether being used for microfluidic or intracellular devices, the surface charge, hydrophobicity, and chemical reactivity of carbon nanofibers can be altered through both physical and chemical modifications. Throughout the literature[39] it can be seen that surface coatings not only improve the mechanical strength and chemical stability of CNFs but also add functionality such as variable conductivity/electrical isolation or the ability to selectively activate certain regions on the surface through microfabrication routes. A second method, covalent attachment of functional groups, is commonly used to increase wettability, dispersibility, and surface reactivity of carbon nanofibers, enabling further functionalization such as the attachment of polymers or large biomolecules.

Carbon nanofibers have exhibited excellent specificity and reversibility in binding biomolecules such as DNA.[141] DNA modification of VACNFs has been implemented for both sensing[164,195] and gene delivery applications.[77,78,83] Fletcher *et al*. illustrated relatively homogenous functionalization of the tips and sidewalls of oxygen plasma etched VACNFs with covalently attached amine-terminated oligos, as shown in Figure 3.18.[195] Confocal microscopy following incubation with complementary dye-labeled oligos presented fluorescent response along the entire length of the 4-μm-tall nanofibers, putatively due to the presence of –COOH and oligo capture along the entire length of the herringbone-structured fibers. McKnight *et al*. demonstrated the capture and transcriptional activity of large (5081 base pairs) double-stranded DNA sequences on VACNF arrays.[77,78] Periodic arrays of VACNFs were oxygen plasma etched and functionalized using an overnight incubation of buffered plasmid DNA. Following extensive rinsing, the nanofibers remained functionalized with covalently bound, active full-length promoter/gene sequences, as evidenced by expression of fluorescent proteins encoded by these genes following penetration of the nanostructured arrays into mammalian cells, show in Figure 3.16(d). Subsequent quantitative analysis of the

amount and transcriptional activity of tethered DNA was subsequently documented by Mann *et al.* using quantitative polymerase chain reaction and *in vitro* transcription bioassay.[83]

Biological applications have been one of the most significant examples of the successful implementation of VACNFs, generating a swiftly growing appreciation of the utility of these materials. VACNFs offer a particularly suitable means of interfacing with biological systems because they intervene at the same scale where life processes transpire. Carbon nanofibers are especially appropriate for biological interfacing because of their high surface area coupled with an abundance of dangling bonds terminated in hydrogen or other functional groups. Recent milestones have seen the effective biocompatibility of VACNFs demonstrated by successful interfacing with live cells, for example as vectors for genetic manipulation[77,78,83] or electrodes for recording of neuronal electrophysiological signals.[85,86]

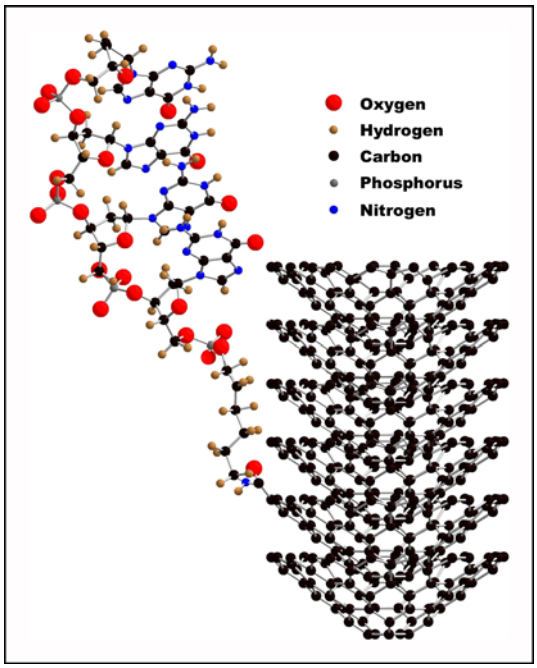

Figure 3.18 Illustration of biomolecular functionalization of a carbon nanofiber with an amine-terminated oligonucleotide, first four bases shown of 5'-amino-c6-G-GGG…. Attachment upon the nanofiber is provided by an amide bond, such as that resulting from an EDC condensation reaction, presumably at a nanofiber–COOH site. Adapted from [39].

Thus the structure, surface chemistry, and attributed properties of the nanofibers play a crucial role in the performance characteristics of nanofiber-based devices. These diverse applications are made possible by the *nearly* deterministic synthesis process of catalytic PECVD, which offers substantial control over geometrical characteristics such as location, length, diameter, and alignment. It is likely that many more applications would also be enabled if we could leverage control over the nanofiber's internal graphitic structure as a final step in the controlled synthesis of carbon nanostructures.

3.4 The Co-Synthesis Concept

Several gaps in our understanding of the fundamental nature of the synthesis processes preclude the control of these processes toward designed endpoints. In particular, the central role of the metal catalyst has been the object of study for some time in the synthesis of carbon nanofibers and nanotubes. Nevertheless, the fundamental mechanisms are not well understood and the predictive ability of existing models is quite limited.

To approach the structure control problem we must first understand the growth process. Though the growth of carbon nanofibers and nanotubes can be likened to the VLS and VSS mechanisms for nanowire growth (as discussed in Section 2.1.2), the uniqueness of carbon with its ability to form stable planar arrangements causes a need for differentiation. In nanowire growth, the catalyst dutifully rides atop, precipitating material to form single-crystalline structures at a defined interface; however, in the case of carbon, the catalyst is *clearly* affected—morphologically and crystallographically evolving during the synthesis process.[109] The chemical nature of carbon allows it to form graphene sheets that can be stabilized independent of 3D bulk layering, which in turn enables the formation of voids, cavities, high curvature layers, and defective structures. These extra degrees of freedom give the graphite some influence over the interface. Therefore, while the simple VLS/VSS models can give us some insight into the mechanisms involved, we believe that carbon has a more complex, intertwined relationship with its catalyst.

The Baker model is a simplified catalytic CVD growth model, which relies on bulk diffusion and conservation of the catalyst properties. From this model we know that the catalyst is of central importance, responsible for three basic functions: adsorption, diffusion, and precipitation. The simplified Baker model does not account for the dynamic ability of the catalyst to transform shape, how growth *actually* transpires at the interface. The reality of nanofiber growth should more accurately be described as a sort of "co-synthesis", in which the carbon nanostructure and catalyst nanoparticle simultaneously evolve together; the metal nanoparticle catalyzes the formation of graphitic carbon layers while the carbon layers shape and ultimately encapsulate the metal nanoparticle. Thus we would like to understand more fully this co-synthesis exchange in order to gain means of control over the internal graphitic structure and the shape of the catalyst-nanoparticle interface.

Most of the characterization of catalyst particles by SEM and TEM is performed *ex situ* once the substrate has cooled down. The particle in this final state can show an elongated conical end or remain spherical. Some particles have a faceted shape on top, connoting a crystalline solid;[109,202] yet the faceting might have occurred during the cooling process so this is not definitive of the growth state. Only *in situ* observation can really get to the root of the problem. However, experimentally it has proven difficult to track the dynamics of the high temperature catalytic reaction with sufficient spatial and temporal resolution to observe growth at the atomic scale. Thus, so far there have been just a few accounts that capture the catalyst evolution and the graphitization phenomenon *in situ*.[109,203]

A few years ago, Helveg *et al.* presented what was hailed as "a long-awaited solution to the mystery of nanofibre growth."[204] The group from Denmark performed time-resolved, atomic-resolution *in situ* TEM observations of the formation of carbon nanofibers from methane decomposition over supported nickel nanocrystals at ~500°C.[109] Carbon nanofibers were observed to develop through a reaction-induced *reshaping* of the nickel nanoparticles, as shown by the series of frames in Figure 3.19 (extracted from captured movies). The nucleation and growth of graphene layers were found to be assisted by a dynamic, repetitive formation and restructuring of mono-atomic step edges at the nickel surface. The authors proposed a mechanism, supported by density-

functional theory calculations, that involves *surface* diffusion of carbon and nickel atoms. In their picture, the dissociative methane adsorption is facilitated at the step edges and C atoms adsorb preferentially at the step sites. The graphene layer forms at the terrace between the steps, on the dynamically changing catalyst nanoparticle surface. Surface diffusion of C and Ni to the step edge on the free surface includes the breaking of the C-bond at the Ni step, incorporation under the graphene sheet, and diffusion at the graphene-Ni growth interface. Moreover their observations and calculations suggest it is not necessary to include the bulk diffusion of C through the Ni particle, however they do not eliminate such possibility.

One phenomenon worth pointing out is the repeated liquid-like stretching-retracting behavior of the particle inside the body of the growing nanostructure exhibited in Figure 3.19. This invoked stretching-retracting mechanism of the catalyst nanoparticle could explain the periodic formation of horizontal graphene planes characteristic of bamboo structure. As will be seen in the next section, the drastic shape change is even more evident in the initial stages of growth. It should be questioned, however, whether because a process is dynamic does it necessarily mean the catalyst is liquid. Rapid restructuring may be possible by enhanced surface diffusion and/or melting at the surface. Helveg *et al.* report that the particles in their study remain crystalline based on diffraction and the faceted equilibrium shapes of particles, although there is no diffraction data for particle in Figure 3.9. This leaves the door open to the interpretation that there could still be a variety of phases present given the differences in particle sizes and morphologies. While there are valid concerns over the state of the particle during co-synthesis and whether the shape of the particle changes upon cooling, one thing is certain: the history of the catalyst nanoparticle-graphite interface is recorded by the internal structure of the nanofiber when viewed in transmission. This aspect can be used to investigate and model changes in nanoparticle shape and internal graphitic structure over time.

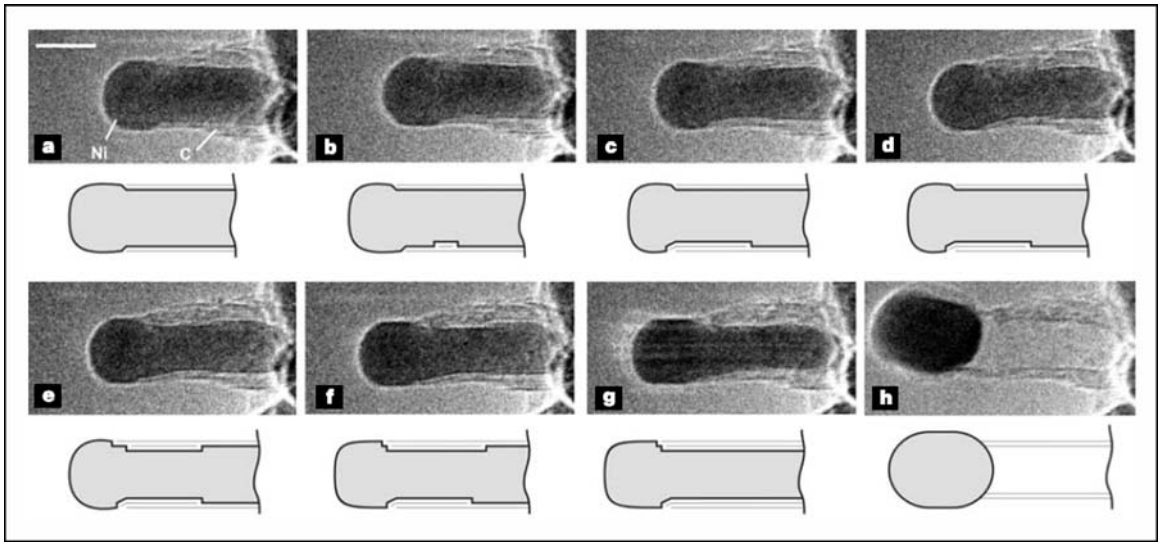

Figure 3.19 Image sequence of a growing carbon nanofiber taken by *in situ* TEM at 536°C. Images (a-h) illustrate the elongation/contraction process with visual schematic below each image to aid the eye. Scale bar in upper left is 5 nm. Adopted from [109].

3.4.1 Nanoparticle Evolution from Thin Film to Catalyst

The co-synthesis concept is most evident at the initial stages of VACNF growth, when it undergoes radical transformation. The catalyst material morphologically evolves from a thin, planar film, to nanodroplet mounds, serving as the seeds for carbon growth, to its final place of residence at the tip of the growing carbon nanofiber, often taking on a conical geometry. Here we trace this evolution of the catalyst particle and its interface with the carbon nanofiber in the PECVD growth process.

In order to grow carbon nanotubes or nanofibers from a thin film catalyst, the film must first be broken into discrete nanoparticles or nanodroplets. This process, referred to as dewetting, is achieved through heating of the catalyst film as shown in Figure 3.20(a,b), often in a reducing environment (NH_3, H_2), prior to initiating PECVD growth.[160] Typically, the dewetting of catalyst material occurs at temperatures *well* below the bulk melting point, achieved here for a 4-nm Ni film at 700°C. This phenomenon of thin film dewetting or surface melting at temperatures below T_m, though commonly observed, is still not fully understood. The general thought is that thin films

experience viscous flow driven by capillary forces originating from the imbalance of surface and interface energy.[205] This transformation is likely aided by surface diffusion[71] and if the film is thin enough or the grain size small enough, it is also possible that nano size effects[17] could further accelerate this process. The formation of catalyst nanodroplets can also be explained by a substantial compressive stress buildup in the film due to a difference in expansion coefficient from the substrate.[113,150]

The actual temperature required to dewet the catalyst film depends on the substrate and film materials as well as the film thickness. In some cases, though, heat alone is not enough to elicit nanoparticle formation catalyst film and additional strategies are required. For thicker (> 20 nm) or higher melting point catalysts, the supplement of energy in the form of a plasma pretreatment[44,162] or ion bombardment[205] is useful in breaking up the film, as discussed earlier in Section 3.2.1. However achieved, the outcome is the same—the catalyst thin film dewets into separate nanoparticles with large surface areas available for carbon adsorption.

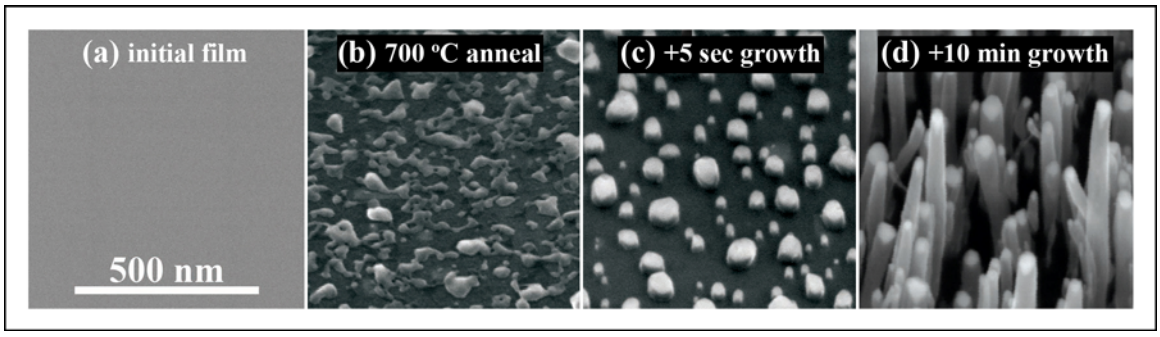

Figure 3.20 Evolution of the catalyst from thin film to nanoparticles at the tips of VACNFs: (a) initial 4 nm sputtered Ni film deposited on a Si wafer, (b) dewetting of the film after heating to 700°C in NH_3, (c) "balling-up" of the nanoparticles after just a 5 seconds exposure to a carbonaceous plasma, and (d) emergence of a mature VACNF forest after 10 minutes of growth. All SEM images were taken at a 30° tilt at the same magnification.

The next step involves both the initiation of plasma and introduction of carbon source gas to the NH_3 atmosphere. As shown in Figure 3.20(c), after just 5 seconds in carbonaceous plasma, the nanoparticles "ball-up" at stochastically separated sites, leaving little trace of Ni behind on the substrate. After 10 minutes of growth, Figure 3.20(d), the particles are now atop a dense forest of VACNFs greater than 1 μm tall.

Complementary work by Cui *et al.* gives more details on how this nanoparticle evolution relates to the internal structure of the growing VACNF (Figure 3.21).[206] Nanoparticles formed by dewetting a thin film metal generally have a disclike hemispherical shape, as in (a), due to a large contact area with the substrate before growth is initiated. This succession of "stop-motion" cross-sectional SEM images show that during the initial few seconds of growth, the particle is rapidly pushed upward by the flux of carbon and becomes elongated, (b). As growth continues the bottom surface of the particle begins to slope upward (c), until it has a conical or teardrop shape (d) with the tip of the cone directed toward the growing carbon nanostructure and pointing in the direction of carbon diffusion. Additional HRTEM observations made by Cui *et al.* show that the graphene sheets in carbon nanofibers form an angle with the fiber axis, alternating with voids and spaces, for most of the length (e).[206] However, this sloped structure disappears at the interface between the nanofiber and the substrate. The base of the carbon nanofiber consists of dense, somewhat disordered graphic material, where the planes are essentially parallel with the substrate, as shown by the inset (f). There is a clear boundary between the VACNF and the silicon substrate with an interface layer of only two graphitic planes.

As a result of this initial interface structure, nanofibers are relatively weak and subject to shearing at their base as compared to the more mechanically stable, stacked cone geometry found throughout the rest of their length. This fact has serious implications for the electrical and mechanical properties of the VACNFs. It explains why, for example, it is easiest to harvest VACNFs (i.e. for TEM samples) by mechanically shearing them from their bases near the substrate where the graphitic planes are most parallel.[44]

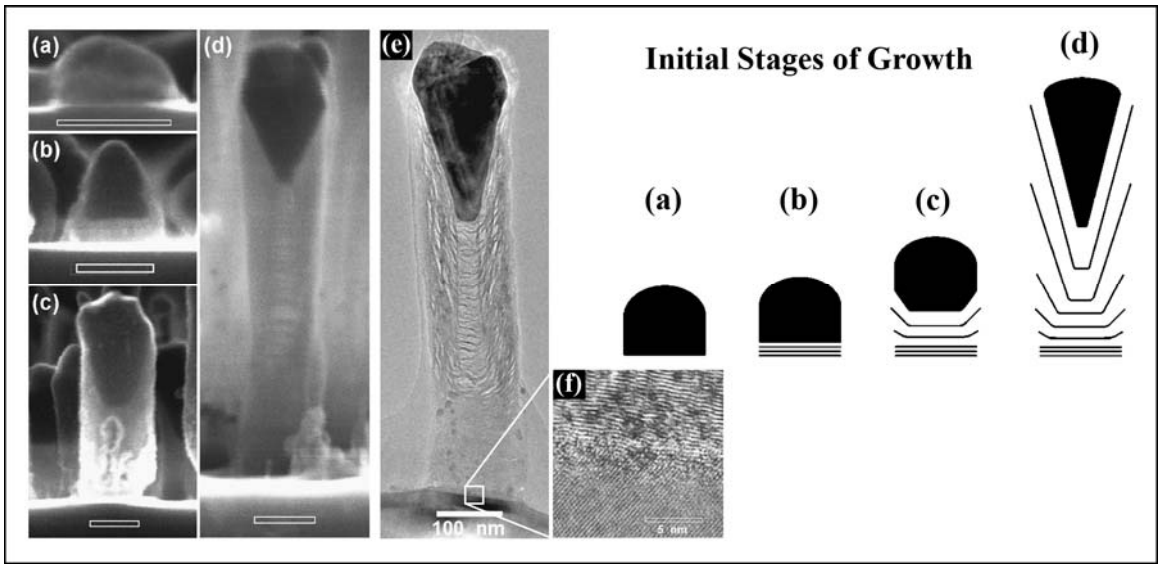

Figure 3.21 Initial stages of VACNF growth. (a-d, right) Schematic model of the initial stages of growth and (a-d, left) corresponding cross-sectional SEM images of each stage: (a) 700˚C anneal, (b) 5 seconds of growth, (c) 1 minute of growth, and (d) 5 minutes of growth (scale bar is 100 nm). TEM image (e) of a nanofiber after 5 minutes of growth, revealing the evolution in curvature of the interface. Adapted from [44,206].

3.4.2 Growth Interface Model ††

Detailed modeling of the internal structure of the CNFs is crucial to comprehending the growth process and the interplay of the catalyst with the resultant graphitic layers. Understanding this interface and how it relates to the structural outcome and growth rate is imperative to developing better methods of nanofiber property control. Given the manifestation of a wide variance in the carbon nanofiber structure, we desire to know what causes this variation and whether we can interchangeably switch between herringbone, bamboo, and nanotube growth modes. At the root of this challenge is defining the catalyst nanoparticle-graphite (CNP-G) interface and modeling the evolution of this interface with respect to time. The internal structure of the nanofiber is utilized as a recorded history of the CNP-G interface, allowing for the comparison of

†† This section is based on work from [207] and contains lightly revised passages and figures.

phenomenological modeling to experimental data. Previously in Figure 3.21, an experimental account of this interface evolution is told, and modeled schematically.

Merkulov *et al.* have devised a kinematic model of the catalytic carbon nanofiber growth, which considers the dependence of the normal growth velocity, v_n, on the curvature of the growth interface.[207,208] This curvature is a function of the radius, r, and θ (the angle between the growth axis, z, and the tangent to growth interface curve), as shown below in Figure 3.22(a). Here a cylindrical symmetry of the interface is assumed such that each position can be represented by just z and r using a system of partial differential equations shown in (b). With this algorithm the time dependence of the growth interface shape may be modeled and can give us insight into the structures manifest in experimental results.

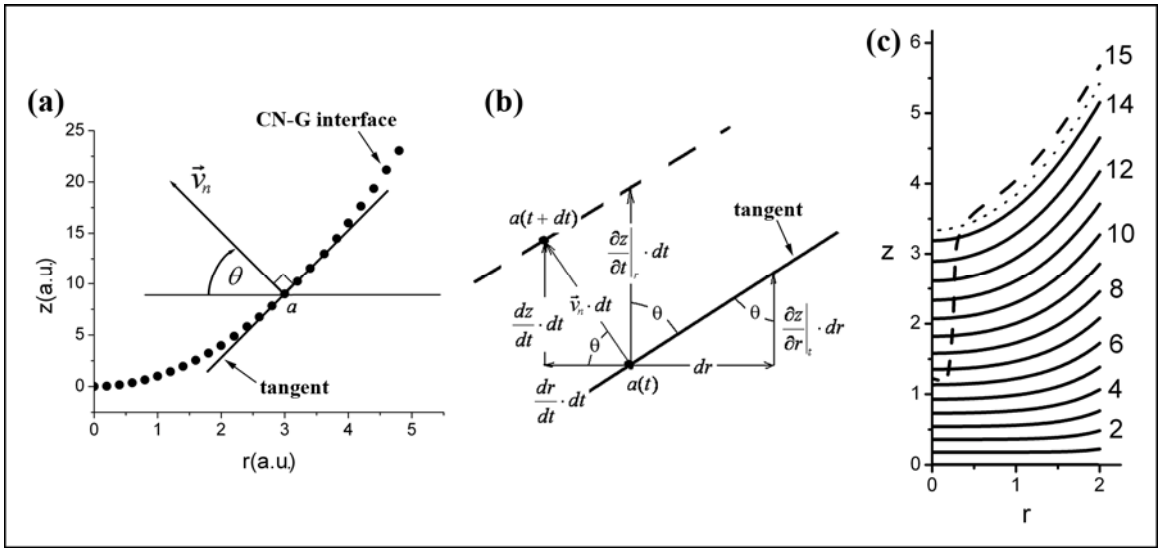

Figure 3.22 Model of CNF internal structure formation. (a) Schematic depicting one curve of the CN-G interface. Here the normal growth velocity, $\vec{v}_n$, is shown for point a on the curve. The angle θ is defined as the angle between the r-axis and $\vec{v}_n$. (b) Detailed diagram of the translation during time dt of a section of the interface, showing the connection between the ordinary derivatives, partial derivatives, and the angle θ. (c) Change of the interface shape at the initial stages of growth for a nanofiber with central cavity formation (i.e. discontinuous solution).

For calculation of the change of shape of the interface between the catalyst and nanofiber an approach is based on phenomenological dependence of the interface velocity of on its curvature (κ) with precision up to the second order (κ^2). Dimensionless variables are used to express the growth rate:

$$v_n = v_{n,\max} - \sum_{m=1,2} (1 + \kappa_m)^2 \,, \qquad \text{Eq. (4.1)}$$

where κ_m are two components of the curvature tensor. The maximum growth rate of v_n is given by:

$$v_{n,\max} = v_{n,0} + 2 \,, \qquad \text{Eq. (4.2)}$$

which is reached at curvatures $\kappa_1 = \kappa_2 = -1$. The curvature of the growth front completely determines the growth rate, and successfully models the initial stages of growth where the graphene sheets curve upward. Furthermore, it is shown that if the magnitude of the interface curvature exceeds a critical value, the interface looses stability and a cavity forms at the center of the nanofiber, as shown in Figure 3.22(c). This phenomenological description of the behavior of the CNP-G interface with model parameters, such as maximum normal velocity and maximum tilt angle at the outer edge of the CNP-G interface, can ultimately be mapped onto macroscopic experimental parameters.[209]

3.5 Methods of Internal Graphitic Structure Control: *Control of carbon nanofiber structure—from nanofiber toward nanotube and back*[‡‡]

Catalytic PECVD is a growth method that offers unparalleled control over the nanofiber external geometry and location of VACNFs, enabling extensive device integration. Yet true deterministic synthesis has not been demonstrated, as command of the internal graphitic structure of the nanofibers, which controls mechanical strength, electron transport, and surface chemistry, has remained elusive. In catalytic thermal CVD processes the structure and properties of the fibers (as shown earlier in Figure 3.2) can be influenced by a number of factors, including the nature of the catalyst surface, the composition of the gas-phase reactant, the temperature, and the incorporation of either gas-phase or solid additives;[149] however other important properties like alignment and conicity are not controllable in thermal CVD. Here we demonstrate that the internal structure of vertically aligned carbon nanofibers can be controlled by the preparation of catalyst nanoparticles with defined crystallographic structure and orientation, and by the selection of growth conditions. We have found that the selection of growth conditions corresponding to the highest growth rate results in nanofibers with an internal structure approaching that of multiwalled nanotubes. Even though crystallographic and morphological properties of the catalyst nanoparticle definitively *influence* the internal structure of the carbon nanofiber, ultimately it is the growth conditions that are the *overriding* factor. We further show that the deliberate modulation of growth parameters results in modulation of CNF internal structure, translating to variation in the density of edge plane termination. This property has been used to control the VACNF surface along its length for site-specific chemistry and electrochemistry.

Experimental Details

Vertically aligned carbon nanofibers were synthesized from Ni or Fe films evaporated directly onto n-type Si (100) substrates. No pre-treatment of the silicon substrate was performed prior to Ni deposition, leaving the native silicon oxide layer

---

[‡‡] This section is based on work from [137] and contains lightly revised passages and figures.

intact. In the PECVD chamber, the samples were heated to 700˚C and pretreated in an ammonia (80 sccm flow rate) plasma at 3 Torr, 200 mA for 1 minute to facilitate the formation of catalyst particles from the continuous metal film. Next, acetylene was introduced to the plasma at 40 sccm initiating the growth of nanofibers. Following a 10-minute growth, the sample was imaged using SEM (Hitatchi S4700), STEM (Hitachi HD-2000) and HRTEM (Hitachi HF-2000). For cross-sectional SEM, the silicon substrate was cleaved in the middle and imaged in the direction perpendicular to the nanofibers. For STEM and TEM analysis, the nanofibers were removed from the substrate and transferred to holey carbon-coated TEM grids.

3.5.1 Influence of Catalyst Composition

The metals that catalyze carbon nanofiber growth include several elemental transition metals, including Ni, Fe, Co, Pt, Pd, Ru, their alloys, and alloys with metals which alone are not catalytic, such as Cr and Cu (see Section 3.2.2 and 4.1). The most widely used catalysts Fe, Ni, and Co each have a different crystal lattice (see Table 3 of Section 4.6). A survey of the literature shows that a number of different nanofiber structures and morphologies are produced by different catalysts,[149] although growth conditions are usually not comparable.

As established earlier in the chapter, the nucleation of graphitic planes in carbon nanofibers occurs on the step edges of the catalyst,[109] following the contours of the interface. Assuming the catalyst is solid during the synthesis reaction, distinct crystallographic faces are generated—some that are efficient at chemically dissociating gas molecules and others that are efficient at the precipitation of carbon, the latter of which controls the degree of crystalline perfection and alignment of the graphitic layers.[149] We have found that elemental composition, which determines the crystallographic equilibrium shape of the catalyst nanoparticle, can influence the structure of the nanofiber in PECVD processes. In Figure 3.23, the formation of different equilibrium catalyst shapes is shown to depend on alloy ratio. The catalyst nanoparticle shape changes from spherical at Co-rich compositions to rectangular at Fe-rich

compositions, with a transitional conical shape at the intermediate composition. The magnetic and crystallographic implications of these assorted equilibrium shapes still remain to be investigated.

As a second example, we provide a qualitative comparison between pure Ni and Fe catalysts. Figure 3.24 shows nanofibers that were grown from a 5 nm Fe film deposited on Si (100) substrate with the same fiber growth conditions as for the Ni catalysts in Figures 3.3 and 3.25. The Fe catalyst invariably produces bamboo-like nanofibers, while both bamboo and herringbone nanofibers may be grown from Ni catalyst. The internal structure of Fe-catalyzed nanofibers consist of sections of graphene cups with a very small cone angle, and are thus more cylindrical (or nanotube-like) than conical [Figure 3.24(a)]. The bottoms of these graphitic cups consist of curved sections across the center of the nanofiber, which we refer to as cross-struts. The SEM image in Figure 3.24(b) is taken at 30° viewing angle to show the corrugated bamboo-like appearance of the nanofiber sidewalls. A top view of the Fe nanoparticles is shown in Figure 3.24(c) and inset (d), which reveals that they have preferred faceting geometry of a rhombus with rounded vertices. The absence of observed herringbone-type fibers is consistent with the observation that Fe more readily catalyzes the formation of nanotubes than Ni, which is reflected in Fe being the most common catalyst for the production of carbon nanotubes. Even in thermal CVD processes it has been shown that in some cases Ni forms herringbone structures instead of nanotubes, while Fe and Co produce nanotubes at the same conditions.[210]

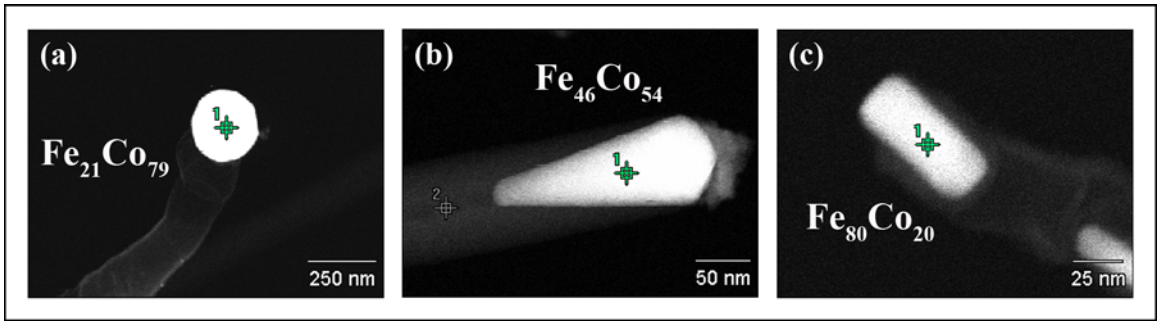

Figure 3.23 *Z*-contrast STEM images of Fe-Co nanoparticles of varying compositions and resulting equilibrium shapes. The elemental compositions were obtained by XEDS at the marked spots on each particle.

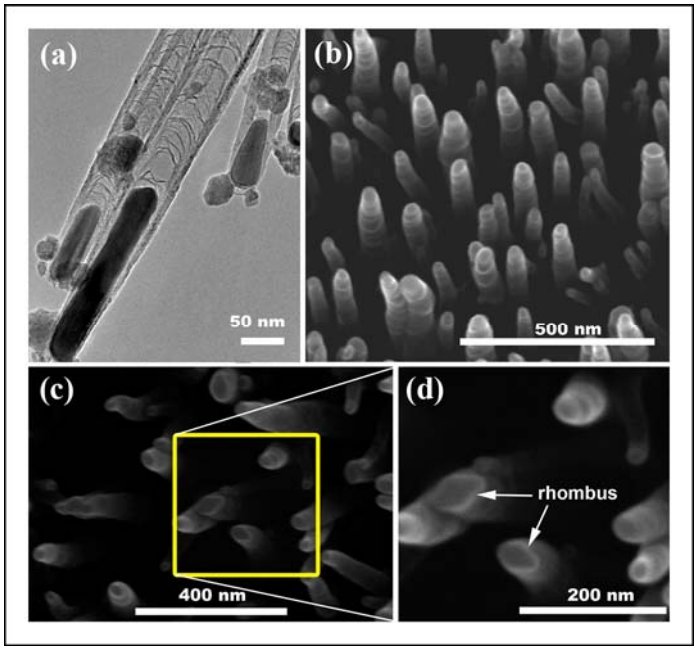

Figure 3.24 Structure and morphology of Fe catalyst nanoparticles: (a) TEM image of Fe nanoparticles at the tips of bamboo carbon nanofibers; (b) SEM image at a 30° view of Fe-catalyzed carbon nanofibers showing the corrugated bamboo-like appearance of the nanofiber sidewalls; (c) top view of Fe nanoparticles and (d) higher magnification of the boxed area indicated in (c), exhibiting rhombus-shaped particles.

3.5.2 Influence of Catalyst Crystallographic Orientation

Catalyst particle crystallographic orientation is also speculated to be factor governing the structure of carbon nanofibers. Recently, Kiselev *et al*. have reported on their studies of the relation of the structure of VACNFs to the orientation and faceting of Ni catalyst particles.[202] VACNFs were grown in acetylene/ammonia atmosphere by inductively coupled PECVD from a 10-μm-thick Ni film electroplated onto bronze plates. TEM and diffraction observations showed that catalyst Ni particles are faceted single crystals. They found that {100} facets preferentially decompose carbon while {031} facets deposit carbon. Kuang *et al.*, on the other hand, showed that the axial direction of VACNFs grown by DC PECVD on Ni wafers is mainly parallel to the <110> and <210> directions of Ni.[211] However, the graphene cone angle varied around 30° and they concluded did not match the {110} Ni planes, corresponding instead to higher-index planes. From these experiments it is not clear that the graphene cone angle α is governed by nanoparticle shape and orientation. At the same time, the *in situ* video recordings by Helveg *at al*. clearly show the formation of graphene layers on the step edge of a [111] surface of Ni.[109] It is interesting to note that in their experiment both herringbone- and bamboo-type nanofibers are produced, which could be the result of different orientations of Ni nanoparticles.

In our experience crystallographic orientation does have an observable influence on catalyst shape and VACNF structure. This is exemplified by the Ni system where VACNFs grown from a 10 nm evaporated film display a noticeable variation in height, shown in Figure 3.25(a). Careful inspection of (a) shows that the majority of nanofibers on average have one height with a portion of the population having grown taller, suggesting a bimodal distribution. This visual observation is supported by a histogram of the height distribution as presented in Figure 3.25(b). Curve fitting with two Gaussian functions (green and blue curves) gives 0.8 and 1 μm height centers for each distribution component. Heights were measured only on the nanofibers that are in the line of view and in focus, thus some of the shorter fibers may not be accounted for in the statistical distribution. Top-view SEM inspection (Figure 3.25(c)) of the nanoparticle at the tips of

the fibers reveals that some of the nanoparticles form complete or a partial hexagon geometry, while other nanoparticles have a square shape. This faceting suggests that the nanoparticles are oriented with respect to the substrate with the hexagonally shaped particles indicating that the <111> direction is perpendicular to the surface and the square shaped particles indicating a <100> orientation for FCC Ni. However, some particles have an unidentifiable shape that is not suggestive of crystallographic orientation.

Examination of the nanoparticles by STEM reveals a difference in the transverse geometry of the nanoparticles. Two varieties of nanoparticle shapes were identified Figure 3.25(d): (1) conical with sloping sides interfacing to the fiber; and (2) rectangular shaped with sides almost parallel to the axis of the fiber. This difference in nanoparticle geometry is reflected in the structure of the graphene layers, with the conical particles producing herringbone-like fiber structure and rectangular particles producing bamboo-like fiber structure. This result illustrates that the crystallographic orientation of the nanoparticle plays a critical role in the resultant carbon nanofiber structure. Our previous work demonstrated that the orientation texture of the nanoparticles can be preserved throughout the nanofiber growth process.[212] Preparation of catalyst films with preferred crystallographic orientation could enable the synthesis of VACNFs with uniform internal structure. Physical vapor depositions methods allow for a degree of orientation texture control. The prevalent orientation of the catalyst film depends on the thin film deposition conditions, such as pressure, temperature, and bias. X-ray diffraction studies confirmed the prevalence of either <111> or <200> orientation textures in Ni films deposited by magnetron sputtering depending on deposition conditions.[212,213] In contrast, nanofibers grown from electroplated films reportedly exhibit a large variation of nanoparticle orientations.[202]

As a final note on catalyst orientation, a proof-of-principle test was done to explore the possibility of new methods of characterizing the crystal structure. Orientation imaging microscopy (OIM) also called electron backscatter diffraction (EBSD) is a technique that utilizes the backscattered electron signal to generate a diffraction pattern that can be used for orientation mapping and phase identification from planar surfaces. If successful, OIM would provide a means of characterizing the phases and orientations present at the tips of *individual* carbon nanofibers without having to remove them from

the substrate while at the same time providing a reference SEM image. The initial results of OIM from a VACNF sample grown on a Si chip from 50 nm Ni is shown in Figure 3.26. Despite the non-planar topography of the sample, these results are encouraging. The fact that high confidence indices for the FCC phase are seen confirms that the level of signal was substantial enough to assign an orientation. One issue that will have to be addressed though, in order to get quality results in the future, is thermal drift of the sample. Since the detector in OIM requires the sample to be mounted at a 70° angle, subsequent attempts should not use tape to affix the sample. It may also help to leave the sample mounted in vacuum overnight to equilibrate thermally.

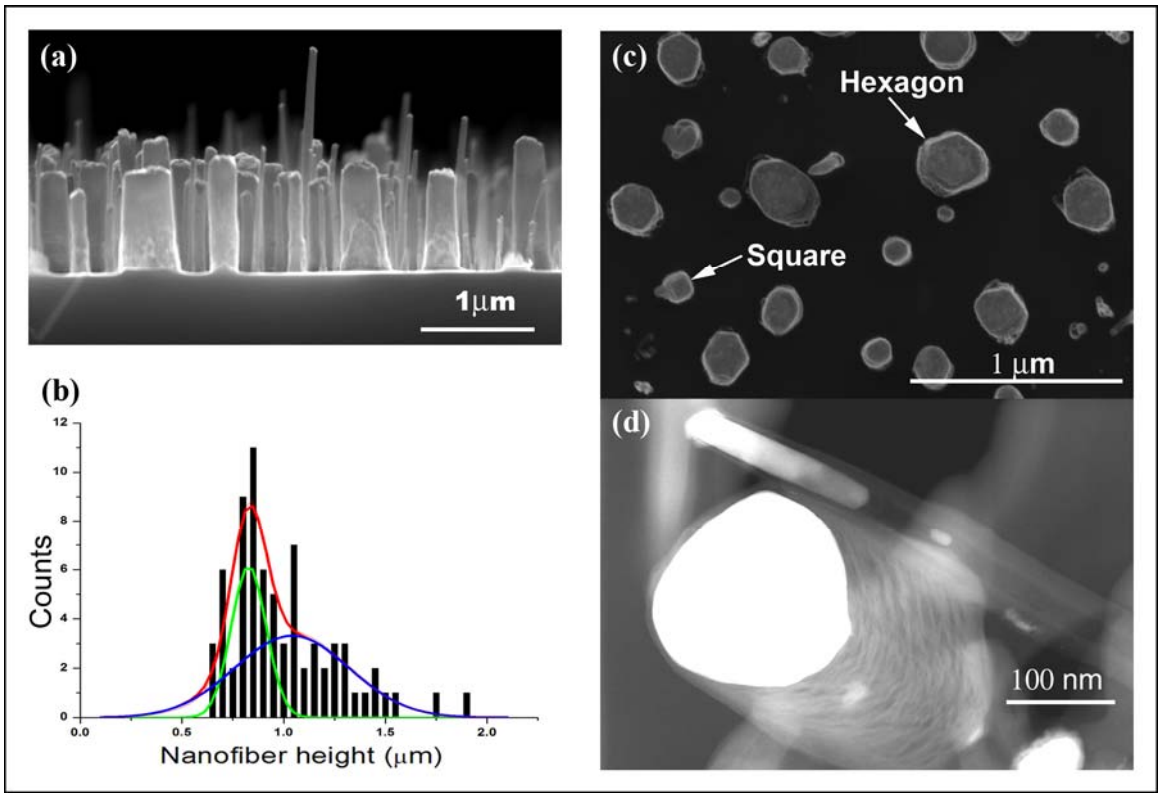

Figure 3.25 Two possible types of VACNFs synthesized from a 10 nm Ni thin film on Si(100): (a) SEM cross-sectional image showing difference in fiber heights; (b) histogram of nanofiber height distribution: total curve (red) can be split into bimodal components (green and blue curves) with centers at 0.8 and 1 μm tall; (c) SEM top view image of nanofiber tips with equilibrium-shaped particles; (d) STEM image of nanofibers with two types of particle geometries and their corresponding nanofiber internal structures (herringbone and bamboo).

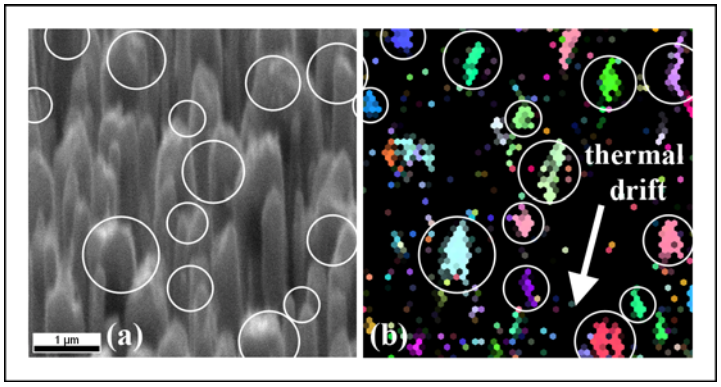

Figure 3.26 Orientation imaging microscopy of Ni catalyst particles atop carbon nanofibers: (a) SEM image and (b) corresponding color-scaled crystal orientation map with intensity indicating confidence index. Crystals with confidently identified orientations are circled in (b) and these circles were then overlaid on (a) to show how thermal drift is problematic.

3.5.3 Influence of Growth Conditions

The formation of graphite layer-by-layer occurs in an asymmetrical fashion as there is a significant difference between in-plane (tangential, v_t) and out-of-plane (normal, v_n) growth velocities (Figure 3.27(a)). Helveg *et al.* [109] observed that carbon incorporation into a growing nanofiber is faster along the graphene plane (parallel to the catalyst surface) than in the perpendicular direction. Indeed, inspection of Figure 3.25(d) shows that the taller nanofiber has graphene layers with a smaller cone angle with respect to the nanofiber axis than does the shorter nanofiber. Based on this observation, it appears likely that the growth rate of carbon nanofibers depends on the angle between the graphene layers and axis of a nanofiber [Figure 3.27(b)], and we hypothesized that the inverse also holds true (i.e. that the graphitic structure of the fiber depends on the growth rate). Calculations based on a phenomenological model of the evolution of growth interface with curvature dependent velocity v_n discussed in section 3.4.2,[207,208] predict that drastic changes in the shape of the interface can occur under certain conditions. Although this model shows a complex relationship between nanofiber growth rate and internal structure, the specific relationship may not be imperative, as one might expect in

general that growth conditions corresponding to higher growth rate will produce nanofibers having an internal structure with a smaller cone angle α.

We and others have shown experimentally that the growth rate can be varied with PECVD synthesis parameters such as temperature, total pressure, total gas flow rate, gas flow ratio, and plasma power.[121,160,162] The dependence on temperature has a maximum around 700°C,[160,214] as the carbon diffusion rate increases with temperature, while the sticking coefficient of carbon species to the catalyst surface decreases with increasing temperature. An increase in the total gas flow rate also raises the growth rate,[121] as this results in a faster supply rate of carbon source material to the catalyst surface. Most importantly though, it has been shown that higher pressure shifts the phase diagram to increased solubility of C in Ni,[215] which would enhance a diffusion-limited process. Chhowalla *et al.* showed that the nanofiber growth rate increases almost linearly with pressure up to at least 10 Torr.[160] The growth rate continues to increase at higher pressures. However, optimization of growth is complicated as these parameters are interlinked and maximization has to be performed in a multi-dimensional space.[121,160,162]

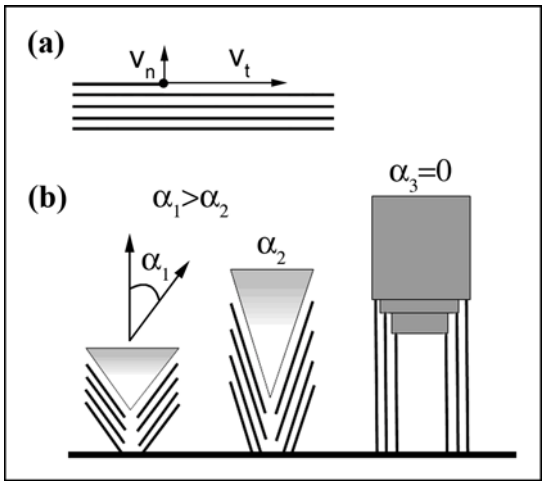

Figure 3.27 Growth rate dependence on internal structure. (a) Diagram indicating the difference of the growth rates ($v_t>>v_n$) in the layer-by-layer growth of graphite, where v_t is the tangential velocity and v_n is the normal velocity; (b) schematic of the nanofiber growth rate dependence on the cone angle α.

In this work, a growth rate maximization procedure was performed based on the known empirical trends in growth conditions described above. The starting point for the growth parameters was: 3 Torr total pressure, 40 sccm C_2H_2, 80 sccm NH_3, 400 mA current, and 700°C. This recipe results in standard herringbone-type nanofibers from Ni catalyst, as shown in Figure 3.28(a) and (b). After each growth attempt lasting 10 minutes, the nanofibers were inspected in the SEM and the growth rate was determined based on the measurement of the average nanofiber height. The growth rate maximization strategy involved stepwise changes in total gas flow rate, substrate temperature, total pressure, and plasma current. At every new set of parameters the growth rate was maximized by varying the NH_3/C_2H_2 gas flow ratio. Since it has been shown that the growth rate increases with gas flow rate, the total gas flow rate was increased to the limit of the mass flow controllers ~300 sccm (a true maximum flow rate was not achievable in this study due to limits of the available mass flow controllers and showerhead configuration). The growth rate increased monotonically with pressure, however all of the other parameters had to be optimized at each new pressure setting; the increase in pressure had to be accompanied with an increase in plasma power to maintain the glow discharge and since plasma power inevitably influenced the actual substrate temperature, the search in heater temperature was repeated. Part of this maximization procedure was performed in one reactor that was equipped to work with pressures below 10 Torr and power below 1.5 kW. In this part of the search we observed a tenfold increase in growth rate, however, practically no change in structure of nanofibers was observed. That is, an increase of growth rate did not result in a gradual change of the angle between graphene layers and the axis of a nanofiber. This result implies that the relationship between growth rate and internal structure is ambiguous. Nevertheless, a drastic change in the internal structure was observed by extending the maximization search in a new reactor designed to work at pressures up to 100 Torr and powers up to 30 kW.

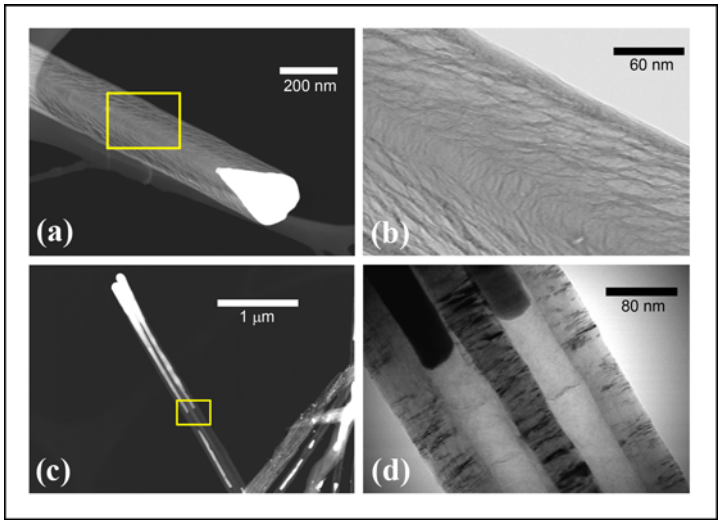

Figure 3.28 STEM analysis of Ni-catalyzed CNF internal structure: (a) *Z*-contrast image of a nanofiber and a catalytic particle grown by the "slow" regime displaying herringbone structure with a large cone angle; (b) transmission image at higher magnification of (a); (c) *Z*-contrast image of two nanofibers grown in "fast" regime, displaying bamboo type, almost nanotube-like, structure with a small cone angle; (d) transmission image at higher magnification of (c).

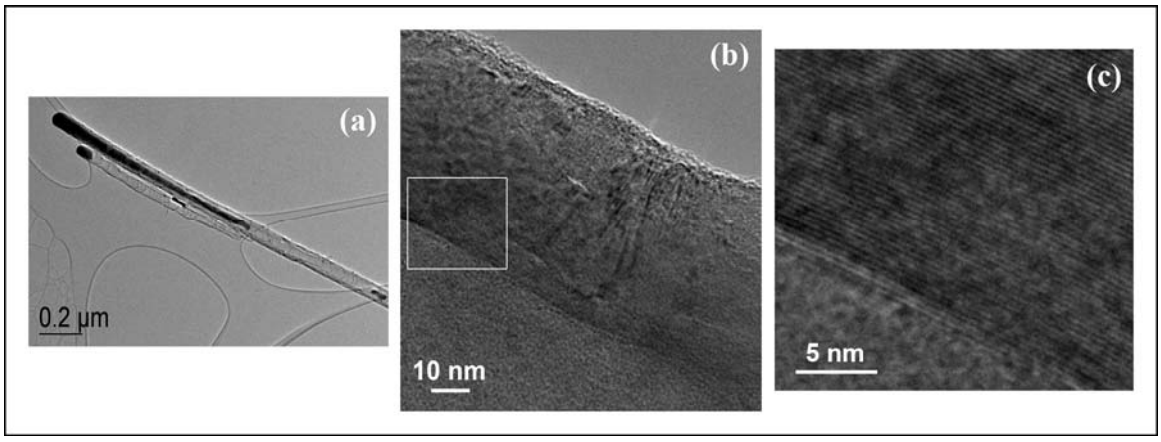

Figure 3.29 TEM images of the internal structure of a CNF grown in the fast growth regime with an elongate Ni nanoparticle: (a) low magnification image, (b) HRTEM image of the CNF sidewall below the catalyst nanoparticle in (a), and (c) magnified view of the area indicated by the rectangle in (b) displaying graphite lattice fringes with average (002) *d*-spacing of 3.4 Å.

The maximum growth rate in the new reactor was achieved in experiments performed in the range 20 to 30 Torr (the maximum pressure at which a stable glow discharge could be achieved in this reactor) with a 3 A current. Growth at these pressures resulted in a drastic structure change as shown in Figure 3.28(c) and (d) and a 100-fold increase in growth rate. At these conditions, the relatively high plasma current increased the temperature of the substrate holder, thus the actual growth temperature of the sample was estimated to be about 850°C with an infrared pyrometer. In essence, this high growth rate and structural change was achieved at much higher pressure, temperature, and plasma current than has previously been reported in the literature. Figure 3.28 (c) and (d) shows an image of a "fast" growing nanofiber (from maximized conditions) with angle α of about 1° (approaching a multiwall nanotubes structure) compared to about 25° degrees for the "slow" growing nanofiber in 3.28(a) and (b). The "fast" growth rate (8000 nm/min) exceeded the "slow" growth rate (80 nm/min) by two orders of magnitude. The particle morphology also changed from a teardrop shape to an elongated rectangle as shown in Figure 3.28(a) and (c). High-resolution TEM images in Figure 3.29 show the well-ordered graphitic structure of the nearly parallel sidewalls. This result confirms the existence of the link between growth conditions, growth rate, and nanofiber internal structure, and suggests that growth condition can override the structure influence imposed by the preparation of catalyst material.

One of the important implications of this result is that the internal structure can be modulated along the nanofiber by switching growth conditions during the synthesis process. This modulation of structure is demonstrated in Figure 3.30, which shows the transition region between fast and slow growth modes. In this example, the fibers were initially grown at a high growth rate to produce nanotube-like fibers with a small cone angle and then conditions were switched to the slow growth regime, producing herringbone structure. In order to switch growth conditions, the plasma was turned off for several seconds while the pressure equilibrated to a new setting. Then the plasma was turned on again and growth resumed, following a brief 10-second pretreatment in ammonia plasma, which removed a thin carbon layer covering catalyst particle.

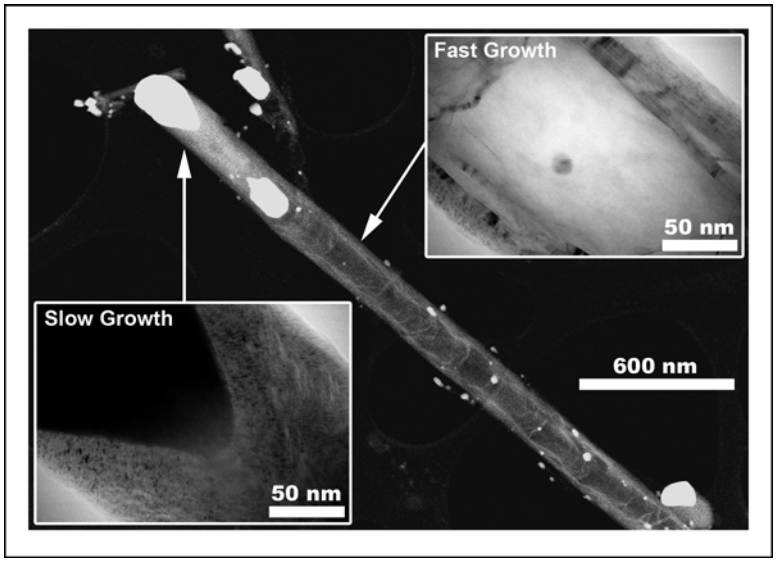

Figure 3.30 *Z*-contrast STEM image of the modulated structure of a nanofiber grown in a sequence of slow-fast-slow conditions (just fast-slow portion shown). Inserts show higher magnification transmission images of the slow and fast growth sections.

The variation of nanoparticle shape in the two growth regimes and the dependence of this shape on crystallographic orientation (as discussed above) have led us to hypothesize that the nanoparticle changes its orientation when transitioning between the two regimes. This seems possible since the shape of the catalyst particle can dynamically change during synthesis, as has been observed by *in situ* TEM.[109] It is also interesting to note that the transition between fast and slow regimes often causes the catalyst nanoparticle to split into two pieces, with one section of catalyst material remaining at the transition point between fast and slow growth. In addition, some nanoparticles exhibited multiple crystalline domains (as seen by diffraction contrast in the TEM, results not shown), which could be artifacts from the orientational re-ordering of the particle during growth or possibly from the cooling process.

However, grazing incidence XRD shown in Figure 3.31 shows no marked differences in the nickel reflections between the slow and fast growth regimes. In order to avoid a strong Si [311] peak at the grazing angle, the Ni films were deposited onto off-axis wafers (3° off of [100] toward [110]). There is a possibility of highly preferred orientation which may not manifest observable changes in grazing incidence x-ray

diffraction, and warrants further investigation. Pole figure analysis and extensive electron diffraction statistical analysis is necessary to determine if the link between the nanofiber structure change and crystallographic orientation of the particles exists. To establish the unequivocal orientation, diffraction patterns from two different zone axes from each particle would have to be obtained. Thus far, efforts to study the orientation change in the two-step growth process have been thwarted by tilting capability limits and polycrystalline particles resulting in complex overlapping patterns.

Modulation of the fiber internal structure has some useful applications. As was discussed earlier, the variation of the internal graphitic structure of the nanofiber inevitably results in a variation of the surface structure. The modulation of the nanofiber structure causes the modulation of graphene edge density along the nanofiber length. Much higher electron transport in the regions featuring high densities of graphene edge-planes can be demonstrated by the electrodeposition of metals onto a nanofiber electrode. Figure 3.32(a) shows gold nanoparticles electrodeposited at the graphene edges of a nanofiber sidewall using commercially available plating solution (Orotherm Gold HT). This phenomenon should allow favored attachment gold at the regions that have a higher density of exposed edges, providing a strategy for preferential decoration and subsequent biochemical modification along the nanofiber length. Figure 3.32(b) shows a variation of electroplated Au nanoparticle density along a nanofiber that was synthesized in a fast growth/slow growth regime, indicating a higher density of gold nucleation within the edge-plane rich, slow growth region.

3.5.4 Conclusions

We have demonstrated that the internal structure of vertically aligned carbon nanofibers grown by catalytic PECVD can be influenced by the crystallographic structure, orientation, and shape of the catalytic nanoparticle. However, growth conditions are overriding factor in determination of the internal nanofiber structure. The synthesis conditions that correspond to much higher growth rate produce nanofibers with only slightly angled graphene layers, approaching the structure of multiwalled carbon nanotubes. The variation of synthesis conditions during nanofiber growth allows for the modulation of internal structure and surface properties along the length of the nanofiber.

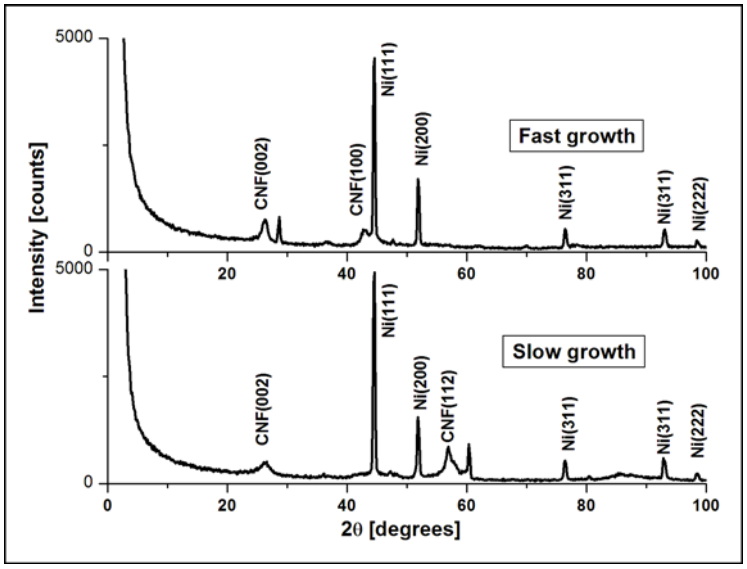

Figure 3.31 XRD grazing incidence scans of substrates after fast and slow fiber growth regimes.

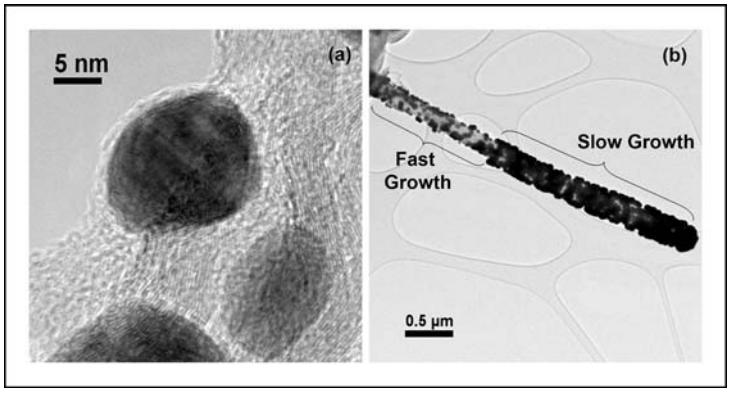

Figure 3.32 TEM images of gold electroplated VACNFs: (a) HRTEM of gold nanoparticles nucleated after electroplating on the graphene edges of a nanofiber sidewall, (b) TEM image of a VACNF grown in a modulated regime (fast-slow) with Au nanoparticles electroplated along the nanofiber sidewalls.

3.6 Additional Commentary about VACNF Structure

It is likely that both solid and liquid catalytic growth mechanisms do occur, and in some cases, can occur simultaneously as observed in nanowire growth. The size of the catalyst plays a key role—in determining both the diameter of the fiber or tube as well as the growth mode. Double- and single-wall nanotube growth by CVD requires catalysts of less than a few nanometers in diameter, whereas nanofibers commonly grow from much larger catalysts. As shown in VLS, the smallest particles have a wider liquid-solid transition temperature and can exhibit hysteresis, meaning that they are easier to melt and harder to freeze.[106] Solid catalyst particles must rely on slow step edge layer-by-layer growth,[109] where the size of the particle has quite an impact on the growth rate. On the other hand, liquid particles with much higher solubility of carbon are capable of rapid "extrusion" of graphitized carbon, without reliance on the step edge contours of the particle, which allows the formation of a hollow cavity.

In this chapter it has been established that the external geometry (i.e. location, height, diameter, conicity) of VACNFs can be controlled with a high degree of precision, and we now have demonstrated that the internal graphitic structure can also be controlled in several ways. For solid-state growth where the graphene layers trace the outlines of the catalyst, inescapably the catalyst shape and orientation play a role in the interface geometry and the carbon diffusion pathways through or around the crystal. However, one of our most astounding discoveries was the role that pressure plays in influencing not only the growth rate but the growth mode and internal graphitic structure. The factor of growth conditions, which can induce a change from herringbone to bamboo to MWCNT structure, may also be "turning a switch" on the growth mode. These transitions do not involve just a gradual change in the angle α to zero slope (i.e. practically no change in structure was seen with a tenfold increase in growth rate at pressures below 10 Torr). It seems, rather, that some energy barrier had to be overcome that was achieved with higher pressure, temperature, and current. Perhaps there is a change in the crystallographic orientation for the fast and slow growth modes, which could explain why part of the catalyst particle is left behind during a transition in multi-step growth. This energy

barrier could also be an alteration in the state of the particle, where the fast growth conditions enable the Ni catalyst to melt and achieve much higher solubilities of carbon, taking on an very elongated, streamlined shape as shown in Figure 3.28(c,d) and 3.29(a).

This poses the question: can freestanding aligned true single- or double-wall CNTs ever be obtained by this growth rate maximization PECVD process? Aside from experimental limitations to maintaining plasma at even higher pressures, other factors are working against this outcome. First, small particles are necessary for smaller diameter growth. The plasma would rapidly degrade these particles and etch the nanostructures back as it did for the 1 nm Ni films in Figure 3.9. In the "fast" growth experiments a rather thick catalyst of 50 nm had to be used. Secondly, higher pressure inevitably invokes a higher power plasma, which not only jeopardizes the catalyst but bombards the nanofiber sidewalls, knocking out atoms and causing defects. Single- or double-wall nanotubes could not withstand these conditions, while large MWCNTS and VACNFS can because they have a "thick skin".

4. Catalytic Alloy Nanoparticle Systems

4.1 Introduction to Alloy Catalysts

In the catalytic growth of carbon nanostructures, the catalyst particle is responsible for breaking bonds and adsorbing carbon at its surface, then diffusing carbon to an interface where it reforms into graphitic planes.[43,109,117,165] As discussed in Chapter 3, the properties of the catalyst can determine the rate of each of these steps as well as influence the internal graphitic structure of the resulting carbon fiber; therefore the choice of catalyst is crucial.[163,164] The catalytic activity of a variety of transition metals and alloys have been studied for production of carbon nanostructures, for a complete list see reference[[44]]. Included in this list are several binary or multi-metal alloys, which have been shown in some cases to provide certain advantages over single element catalysts.[216] Whereas the trusted transition metals Fe, Ni, and Co (properties given in Table 3 at the end of this chapter) are known to be very active in their ability to break and reform carbon-carbon bonds, their alloying with other non-catalytic metals such as Al or Cu, are thought to enhance carbon diffusion and reaction rates.[165] In some cases, alloy catalysts have resulted in higher activity,[165] low temperature growth,[217] and branched nanostructures.[218-220]

Furthermore, since most of the catalyst metals used in carbon nanostructure synthesis are well known ferromagnets, thus the co-synthesis of carbon nanostructures and magnetic nanoparticles presents a unique opportunity to study the fundamental aspects of magnetism under nanoscale confinement. The carbon shell that shapes the nanoparticle during synthesis can also be utilized as a capsule, protecting the nanoparticles from coalescence, aggregation, and chemical degradation. The ability to encapsulate various metals within these carbon nanostructures thereby enables the study of metallurgical processes at the nanoscale and the behavior of these metals under nanoscale confinement (i.e. increased surface to volume ratio, decreased long-range symmetry, abnormal stress-strain fields).[90,91,221] For instance, the understanding of

crystallographic order-disorder phenomena of magnetic alloys within nanoparticles is limited,[222,223] as is the understanding of the relationship between the degree of crystallographic order and the magnetic structure and anisotropy.[224]

The use of carbon nanostructures as an interface to biology could play a role in fundamental biological discovery and perhaps even diagnosis or therapeutic intervention in human disease. The unique properties possessed by the magnetic nanoparticles, when coupled with nanofibers, offer great potential for biomedical applications such as drug delivery, gene delivery arrays, and tissue repair. For example, the self-regulating magnetic hyperthermia of cancer cells is achievable by synthesizing magnetic nanoparticles with a specific Curie temperature, above which there is a sharp decrease in magnetic coupling. Materials with a Curie temperature in the range of 314-319 K are desired to provide a safeguard against overheating of normal cells through conduction. The binary alloy Cu-Ni has shown a promising magnetic phase transition in the desired range for inducing hyperthermia in cancer cells.[58] Particles with the preferred Curie temperature can be obtained by varying the weight percent of Ni and Cu in the alloy. In fact researchers have shown that alloy particles (D ~ 436 nm) composed of 71% Ni and 29% Cu (wt.%) had a Curie temperature of 319 K, which is in the range of cancer cell treatment. Encapsulation within VACNFs would provide a means of delivery as well as a biocompatible coating for the nanoparticles that minimizes the metabolic interaction with the nanoparticle *in vivo*. Demonstrated intracellular integration of VACNFs within viable cells proves that they have promising biocompatible properties at the nanoscale.[77]

In this chapter the bimetallic alloy systems Cu-Ni,[171,225] Fe-Co,[172,226] and Fe-Ni[227] are studied throughout their transition from thin film to encapsulated catalyst particles. The catalytic activity of these metal particles and their influence on the nanofiber morphology are discussed. Moreover, the effects of the growth process and nanoscale confinement on the alloy behavior are investigated using techniques including HRTEM, electron diffraction, XEDS, AES, XRD, and magnetometry.

4.2 Cu-Ni Alloy System: *Cu-Ni composition gradient for the catalytic synthesis of vertically aligned carbon nanofibers*[§§]

4.2.1 Introduction

Copper and nickel present one of the simplest binary alloy systems. The Cu-Ni system is termed isomorphous because the two components are completely soluble in both liquid and solid states.[228] At temperatures below 1085°C (melting point of pure Cu, see phase diagram in the Appendix) Cu-Ni forms a continuous solid solution for all compositions, due to the fact that Cu and Ni have similar valences and the same FCC lattice with nearly the same lattice constant (a_{Cu} = 3.615 Å, a_{Ni} = 3.524 Å).[134]

There have been several studies showing that binary or multi-element alloys provide certain advantages over single element catalysts for the growth of filamentous carbon.[216] In fact, some studies have shown that certain Cu-Ni mixtures have a higher catalytic activity than for pure Ni.[165,229] In addition, a 1:1 Cu-Ni sputtered alloy film was found most suitable for low temperature fiber growth.[217] There have also been several reports of Cu-Ni alloys producing multi-directional or branching nanostructures,[220,229-231] which may be useful for nanoelectronic wiring or synthetic membrane applications. However, each of the previous studies reflect growth from discrete alloy compositions under specific conditions. Even slight variations in catalyst composition can substantially affect fiber composition, growth rate, structure, and morphology. Furthermore, the behavior of the catalyst depends on growth conditions such as temperature, source and etchant gas, as well as substrate material.[170] In other words, catalyst composition in combination with the set of growth parameters ultimately determines catalytic performance and the resulting fiber properties.

The control of properties through catalyst selection may be advantageous for tailoring carbon nanofibers to specific applications or for optimizing growth in a particular process. For example, a catalyst for highly branched nanofibers might be desired if high surface area is preferred, while another catalyst could provide small tip

---

[§§] This section is based on work from [[171]] and contains lightly revised passages and figures.

diameters useful for field emission or probe devices. Likewise, the process itself may be of utmost importance and certain catalysts are better suited for the desired synthesis parameters such as growth at low temperatures or growth on insulating substrates. An understanding of the relationship between the catalyst material and the resulting fiber growth is vital to selection of the optimal catalyst for each application. Thus, there is need for an efficient method of evaluating a wide range of metallic alloys in order to attain the best catalyst for the given synthesis conditions and desired fiber properties.

The co-sputtered catalyst approach used here, allows for the examination of a large composition space for binary or ternary phase diagrams from a single wafer deposition. The alloy range can also be skewed to span a certain composition range by adjusting the source power and tilt angle of each target. Due to elevated energies, the sputtering technique has the advantage of better mixing and adhesion as compared to evaporated films. In addition, substrate heat and bias capabilities can control film properties such as grain size.[114] Thin sputtered films are also compatible with standard resist patterning.

In this study we present electron microscopy and spectroscopy analysis of vertically aligned carbon nanofibers synthesized from Cu-Ni alloy catalysts by DC-PECVD. A Cu-Ni alloy gradient, with composition varying linearly from 81% Ni to 80% Cu, was prepared by co-sputtering in an RF magnetron sputtering system. The changes in morphology and structure of the resulting carbon nanofibers as well as the level of segregation of catalyst components are investigated at several locations along the composition gradient.

4.2.2 Experimental Methods

Catalyst preparation and composition analysis

First, a binary gradient was created by co-sputtering Cu and Ni targets onto a 100mm diameter Si (100) wafer using a radio frequency magnetron sputtering system equipped with three 2-inch diameter sputtering sources. For the Cu-Ni catalyst deposition, two sources were used 180^{o} apart, with the substrate centered and equidistant

(13.6 cm) relative to the two sources. By varying individual source powers and source tilt angles the gradient slope was adjusted so that the 50%-50% atomic ratio was targeted for the middle of the wafer. Based on the sputter yields and predetermined rate data for Cu and Ni, the source powers for Cu and Ni were 100 W and 141 W, respectively. The Cu and Ni sources were sputtered for 1.6 minutes and the film was about 20 nm thick as predicted by the sputtering rate of 12.5 nm/minute. Next, eight collinear points 1 cm apart along the central axis of the wafer were marked and spectrally analyzed by SAM in a PHI 680. The composition at each of these points was also verified by XEDS in a Hitachi S-4700.

Carbon nanofiber synthesis

Then VACNFs were grown on the catalyst gradient film by DC glow discharge PECVD. Upon a 2 minute pretreatment at 700°C in an ammonia plasma, the Cu-Ni thin film broke into nanoparticles which catalyzed the nanofiber growth. Acetylene (C_2H_2) at 25 sccm and ammonia (NH_3) at 80 sccm were used as the carbon source and etchant gases. The sample was grown for 30 minutes at a pressure of 2.5 Torr, with a current of 150 mA and a bias of 550 V. More details on the apparatus, experimental conditions and carbon nanofiber synthesis can be found elsewhere.[162]

Electron microscopy and spectroscopy analysis

The as-grown sample was characterized at each of the eight points of different catalyst composition by scanning electron microscopy (SEM) in a Hitachi S-4700. Then fibers were transferred to lacey carbon coated beryllium grids by scraping them from the substrate using a precision razor blade. The fibers on the grids were then analyzed by transmission electron microscopy (TEM; Hitachi HF-2000) and by scanning transmission electron microscopy (STEM Hitachi HD-2000). The STEM's XEDS mapping capabilities were utilized to compare the changes in fiber body and catalyst particle compositions across the wafer.

4.2.3 Results and Discussion

Catalyst film characterization

Figure 4.1 shows the Auger SAM analysis results of the Cu-Ni gradient prior to nanofiber growth. There is a linear composition gradient ranging from about 80% Ni at the first point to 80% Cu at the last point, where the 50%-50% atomic ratio fell only a few mm left of center on the wafer. Furthermore, the Auger results closely matched XEDS analysis and an empirical sputtering model. The film thickness was verified by atomic force microscopy (AFM) to be approximately 20 nm.

Carbon nanofiber characterization

The results of VACNF growth on the Cu-Ni gradient are depicted graphically in Figure 4.2. The feature size is the fiber diameter at its widest point as measured from a top view SEM image, implying the average space occupied by a fiber in each area. In some cases this was the breadth of the tips of a branching fiber, or in other cases the span of a broad fiber base was measured. The density of fibers was also calculated from the top view SEM images at each composition point, as the number of fibers in an area of $7\mu m^2$. As can be seen from Figure 4.2 (a) and (b), increasing the level of Cu reduced the feature size from roughly 400 nm to 100 nm, while the fiber density increased six-fold. A qualitative analysis of the SEM top view images showed a change in the general shape of the fibers across the gradient from a branchy, random structure to a round uniform structure as the concentration of Cu increases.

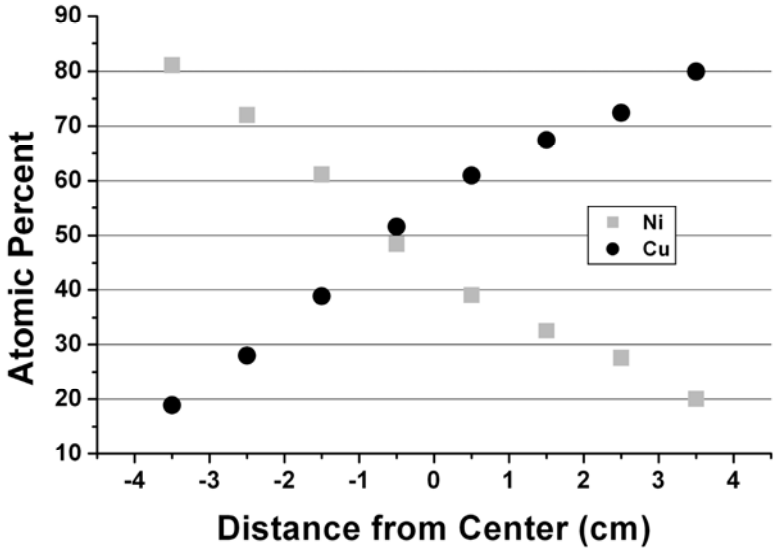

Figure 4.1 Auger analysis of the Cu-Ni gradient showing the atomic percent composition of the catalyst film as a function of position on the substrate.

In addition, tilted SEM imaging revealed a dramatic decrease in fiber tip diameter, from an average of 57 nm down to 12 nm, with increasing Cu content in the catalyst film [Figure 4.2(c)]. In Figure 4.2(c) it must be noted that for the branched structures on the Ni rich end of the gradient, several tip diameters from each fiber were measured. In contrast, on the Cu-rich side of the gradient where conical fibers with a single tip were produced, only one tip diameter per fiber was measured. This implies that the initial Ni-rich catalyst particles were at least several times larger than 57nm prior to splitting. Tilted SEM images also revealed a sharp decrease in fiber height with increasing Cu concentration [Figure 4.2(d)]. The drastic reduction in fiber height, or growth rate, with elevated levels of Cu may be due to the low catalytic activity of Cu relative to Ni, which is considered to be the most active metal for carbon catalysis.[170]

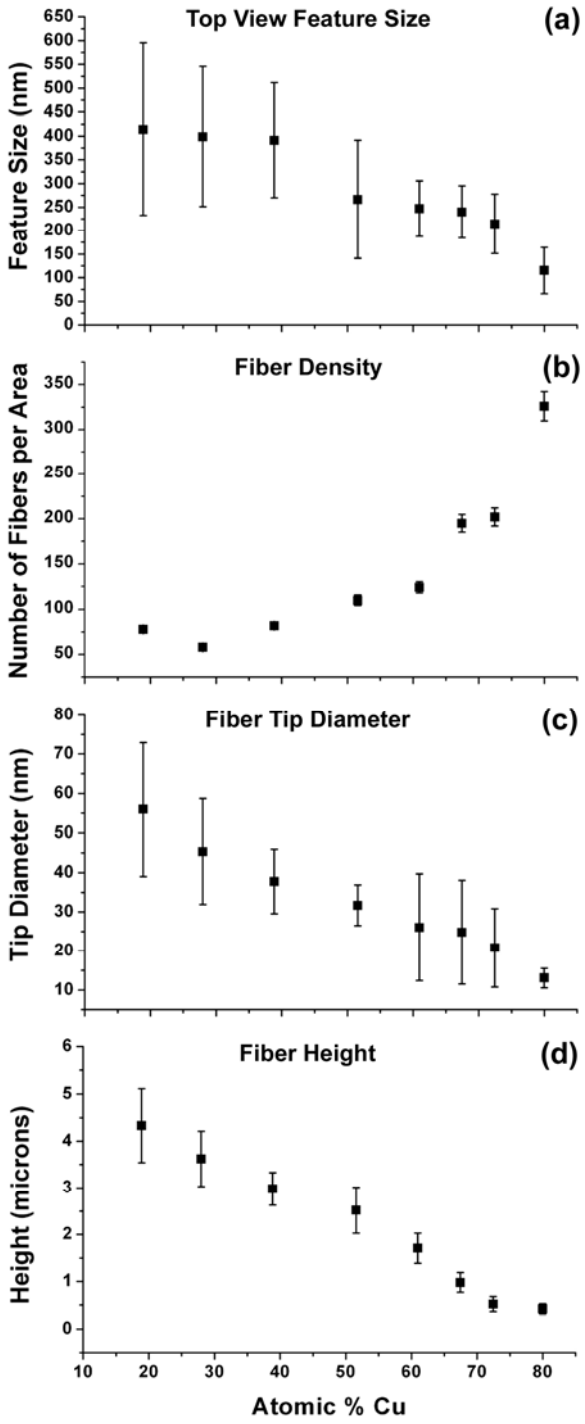

Figure 4.2 Graphical trends as Cu content in the catalyst is increased, depicting (a) a decrease in the top view feature size, (b) an increase in fiber density, (c) a reduction in fiber tip diameter and (d) a reduction in fiber height. The standard deviation of each data point is shown by the error bars.

Images of the resulting VACNFs grown from three different alloy film compositions are shown in Figures 4.3 (81% Ni), 4 (39% Ni) and 5 (20% Ni). The 81% Ni-rich catalyst grew tall, branched structures with multiple tips as shown in the SEM images in Figure 4.3 (a) and (b). Branched structures have often been attributed to Cu incorporation in the catalyst.[218,220,229-232] However the multidirectional or "nano-octopus" structures first observed by Nishiyama *et al.*, and later by many others, exhibit many limbs emanating from a single catalyst particle, presumably in a base-type growth mode.[218,220,229-231] Conversely, in our case Cu alloying with Ni caused the particle to split during tip-type growth. This is similar to y-junction branching where catalyst splitting can occur from the use of Cu catalysts,[232,233] catalyst impurities,[219] templates[234] or a rapid drop in temperature during growth.[108]

Figure 4.3(d) shows XEDS line scan analysis at a fiber tip particle where the alloy film composition was 81% Ni. The result demonstrates that the ratio of Ni to Cu stayed at about 81% and therefore there was no segregation of the alloy. However, as the level of Cu increases we observe the alloy segregate, as can be seen in Figure 4.4(d). Here the original film was 39% Ni but the fiber tip particles consisted of slightly more Ni than Cu, about 52% Ni. The Cu on the other hand, appears to collect at the base of the growing fiber, where a Cu-rich particle resides. While mostly carbon, residual amounts of metal (throughout) and silicon (increasing abundance near the substrate) were seen in the fiber body.

The SEM images in Figure 4.4 (a) and (b) illustrate a transition to shorter, more conical, less branched structure. In fact, when Cu levels reach 80% we see dense arrays of uniform, aligned, high aspect ratio cones as shown in Figure 4.5. High-resolution TEM reveals 10 nm tips [Figure 4.5(c)] and an average cone angle of 10 degrees. Large characteristic base particles can be seen in Figure 4.5(d). XEDS revealed that these base particles were *entirely* Cu as shown in the line scan along the fiber body in Figure 4.5(e).

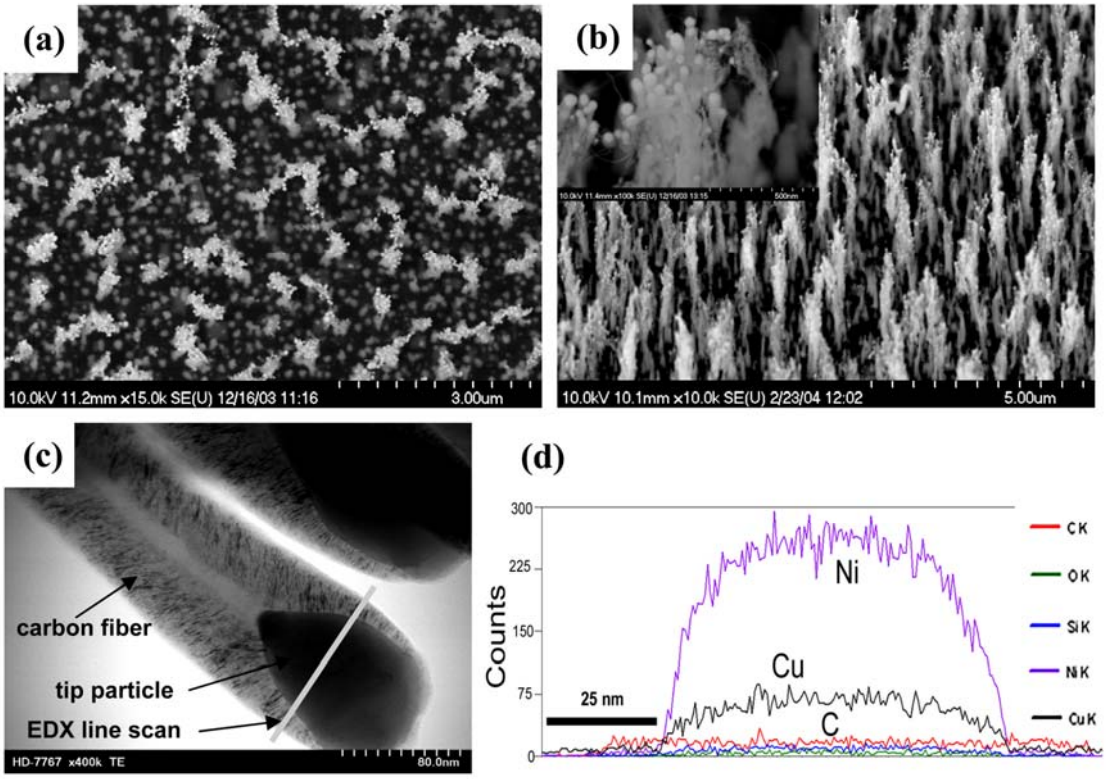

Figure 4.3 Analysis of 81%Ni-19%Cu nanofibers. SEM images taken at (a) top view and (b) 30° tilt angle with close-up inset of branched fiber tips. TEM image (c) of the carbon nanofiber tips with XEDS line scan across the catalyst particle shown in (d).

The Cu-Ni system is generally thought to form a continuous solid solution at all compositions. However, as a result of the lower melting point of Cu (1085°C, as compared to 1455°C for Ni), the melted portions of the alloy will tend to be Cu-rich. This effect is exacerbated with the introduction of C to the binary system. While carbon and nickel form a simple eutectic with a limited solubility of C in FCC Ni (maximum 2.7 at. %), there is no reported solubility of C in Cu.[235] Thus not only do the Cu-rich alloys melt at a lower temperature but they are also less able to dissolve carbon, both of which may favor segregation of the alloy components.

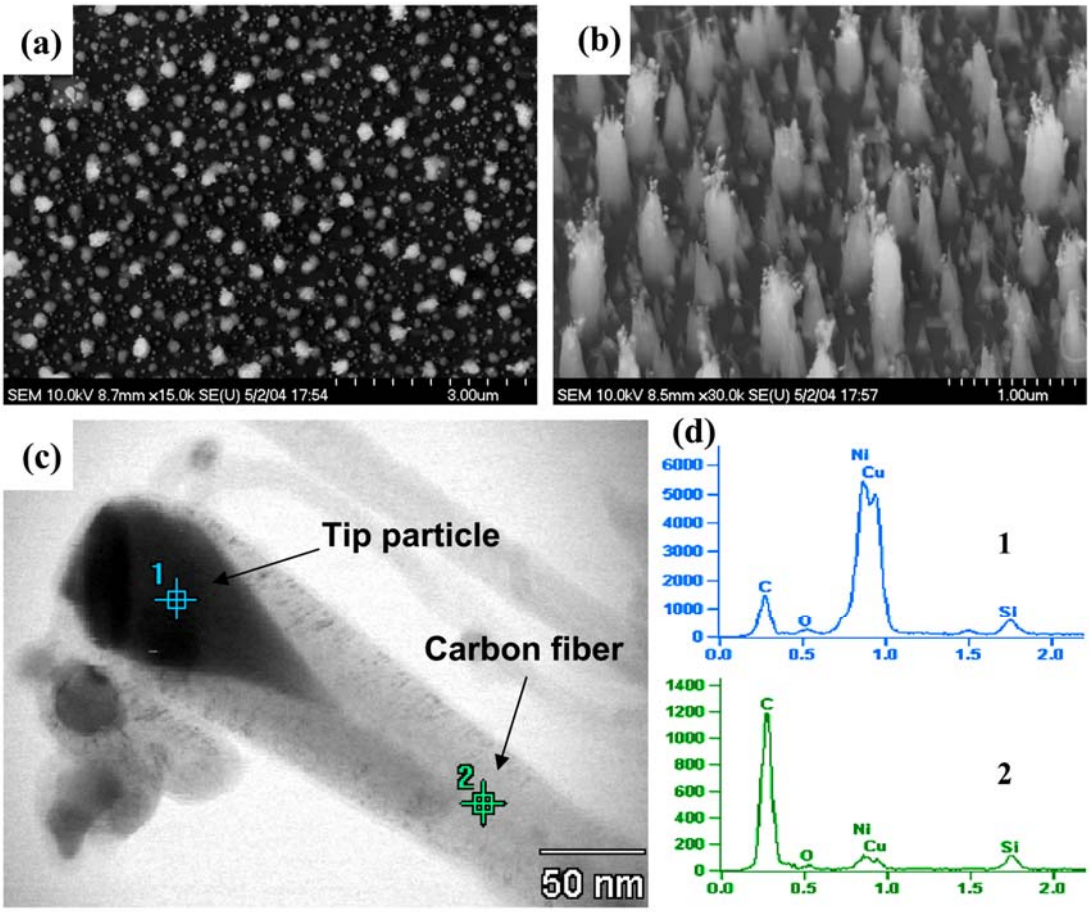

Figure 4.4 Analysis of 39%Ni-61%Cu nanofibers. SEM images taken at (a) top view and (b) 30° tilt angle. TEM image (c) of a carbon nanofiber tip with XEDS analysis at points labeled 1 and 2 shown in (d).

For the 20%Ni-80%Cu initial catalyst ratio, the nanocone body was composed of an amorphous mixture of Si, C, O, and N. It is unlikely that growth occurred from the Cu base particle because of the definitive alignment of the structures, which is a result of tip-type growth.[236] The catalytic activity of pure Cu for carbon nanofiber synthesis was further tested to be sure of this point (results presented in Section 4.3). In addition, a small amount of Ni, presumably left over from the segregated alloy, appears to be located at the tips of many of the fibers. Although, some fibers lack these tip particles, it's possible that they were once there and either diminished due to ion sputtering, were incorporated into the fiber body, or broke off due to an undercutting etch beneath the particle.[173] This unusual structure may be explained by the following sequence: (1) initial

Cu and Ni segregation and formation of a small Ni particle; (2) tip-type growth of a thin nanofiber from this small Ni particle; (3) continual etching of the nanofiber by the ammonia plasma, but before complete etching (4) encapsulation of the nanofiber within a sheath composed of a silicon-nitride-oxide mixture formed from substrate sputtering and the plasma gases.[84] The fact that the cones without tip particles still remain sharp in the plasma environment is a testament to the resilience of this material to etching, seeing as how pure carbon fibers under these plasma conditions would be eroded without possessing a tip particle etch-mask. This type of conical fiber may be of interest due to its high aspect ratio, small tip size, and robust outer coating.

4.2.4 Conclusions

The catalyst particle plays a critical role in the deterministic growth of carbon nanofibers. Previous studies have indicated that alloy catalysts can have certain advantages over traditional single element catalysts. In order to find the optimal catalyst for each application an efficient method to assess a wide range of alloy compositions for carbon nanofiber synthesis was needed. A co-sputtered Cu-Ni gradient was used to evaluate carbon nanofiber growth over a wide composition range. The results show substantial changes in fiber composition, growth rate, structure, and morphology across the gradient. As the concentration of Cu increased, general growth trends include a reduction of feature size, slower growth rate, morphological change from branching fibers to uniform cones, increased incorporation of Si in the fiber sidewalls, and segregation of the alloy catalyst with the formation of a Cu base particle. Explanations of the growth modes for branched structures and conical structures were proposed.

Furthermore, co-sputtered gradient films can be used to evaluate and optimize carbon nanofiber growth from other multi-metal alloys. These gradient films are applicable to the diverse parameters of both CVD and PECVD systems. Since PECVD conditions used for VACNF growth differ significantly from conditions for thermal CVD nanofiber growth, catalyst performance should be evaluated for each. From this type of study, a catalyst composition can be rapidly optimized for any growth system and the desired fiber qualities.

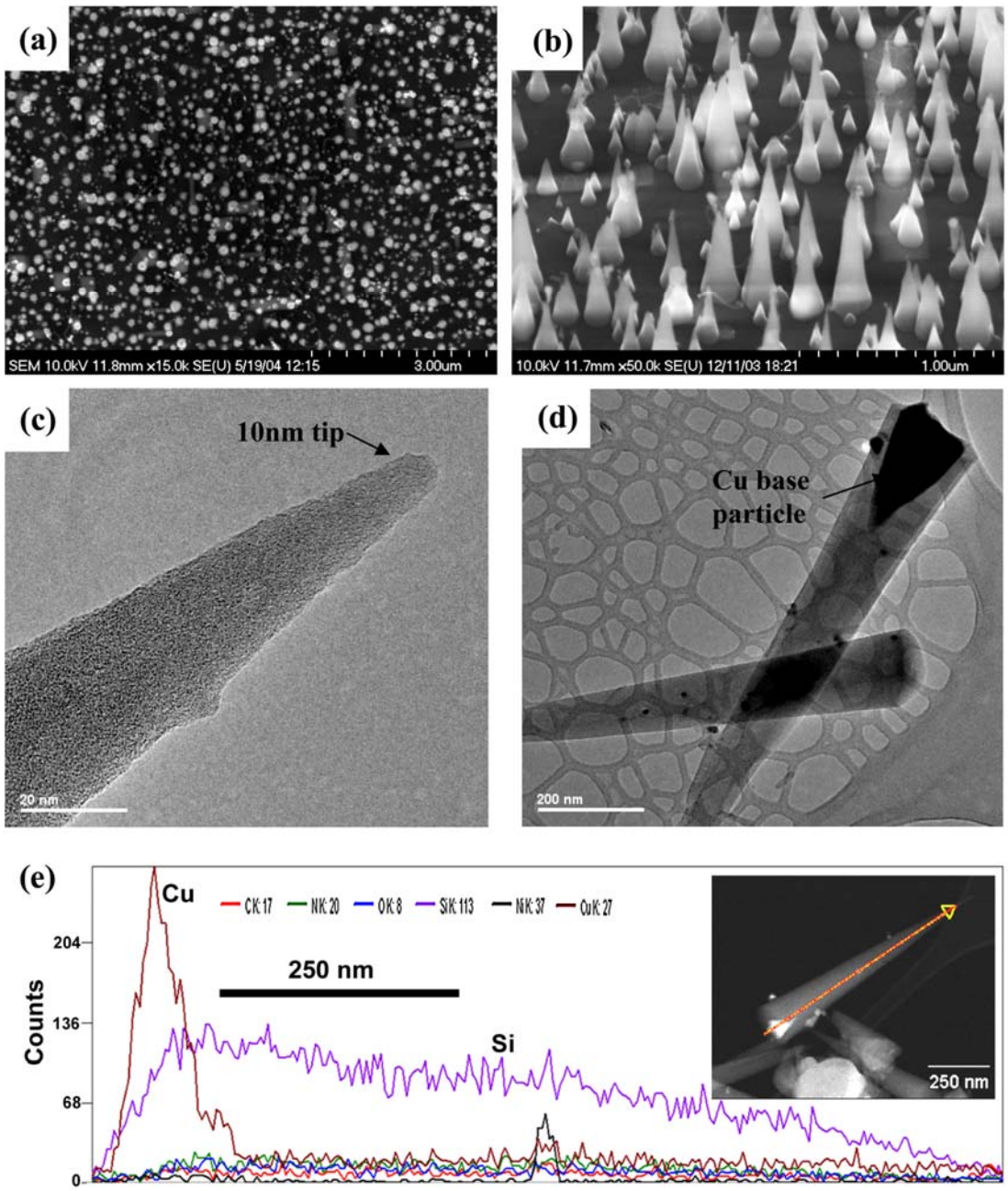

Figure 4.5 Analysis of 20%Ni-80%Cu high aspect ratio nanocones. SEM images taken at (a) top view and (b) 30° tilt angle. TEM images (c) of a 10nm cone tip and (d) cone with a Cu base particle. The elemental composition of the conical fiber in the lower right can be seen from the line scan (e).

4.3 Incidental Formation of Cu-Si Nanocones: *Formation of Ultra-sharp Vertically Aligned Cu-Si Nanocones by a DC Plasma Process*[***]

4.3.1 Introduction

In the preceding study of Cu-Ni catalysts, it was seen that the addition of Cu in small amounts to Ni catalysts caused the nanoparticles to split during growth, producing branched structures. With addition of even more copper, reaching levels as high as 80%, the alloy segregated to form what is believed to be a non-catalytic Cu particle at the base of the growing nanostructures and a small Ni nanoparticle, which catalyzed growth from the nanostructure tip. In order to verify the non-catalytic activity of *pure* Cu under similar growth conditions, single element Cu films were investigated. This section recounts the interesting and unexpected outcome of this experiment.

In this work we present the fabrication of ultra-sharp nanocones by a DC plasma process. Copper films deposited on a silicon substrate were subjected to plasma conditions similar to the PECVD growth of carbon nanofibers,[150] with slightly elevated plasma energy. However, this process yielded nanocone structures with an entirely different morphology, internal structure, and chemical composition. The self-assembled copper particles proved to be poor catalysts for carbon nanofiber growth, and were instead excellent seed material for the formation of silicon nanocones. This section investigates the structure and mechanism of formation of these nanostructures as well as ways to control their synthesis deterministically. Furthermore, this study provides insight on the behavior of copper films and silicon substrates at elevated temperatures in a reactive ion etching environment, which is a subject of high interest for the semiconductor industry.[237-239]

[***] This section is based on work from [225] and contains passages and figures.

Significance and Background

High aspect ratio conical nanostructures are of significant interest because of their diverse applications including scanning probe microscopy tips,[79] gene delivery arrays,[77,240] and microfabricated field-emission sources.[72] However, the functionality of these devices depends on the control of the nanocone characteristics such as tip size, height, location, and chemical composition. Smaller tip sizes enhance the performance of many nanoscale devices such as improved resolution in scanning probe microscopy, damage-free delivery of materials through cell membranes for biological applications, and greater field enhancement at the tip for field-emission applications. Carbon nanofibers or nanotubes, grown catalytically by thermal chemical vapor deposition (CVD)[118,119] or by plasma-enhanced chemical vapor deposition (PECVD) methods,[150,241,242] are used commonly for such applications. However, other materials deserve exploration and may offer unique advantages such as robustness, greater uniformity, simpler fabrication, novel chemical functionality, and compatibility with semiconductor processing.

Conical nanostructures provide considerably more mechanical and thermal stability than their cylindrical counterparts because of their large bases, while still affording the precision associated with small tip sizes and high aspect ratio. Nanoscale cones can be shaped out of numerous materials. Pure carbon conical nanostructures have been formed by the pyrolysis of hydrocarbons resulting in folded concentric graphene sheets[42] and conical crystals have been discovered in the pores of glassy carbons.[243,244] Recently, efforts to generate graphitic nanocones on substrates by a catalytic growth approach have proven successful using microwave plasma CVD.[245-247] Furthermore, composite conical structures have been produced by DC-PECVD, whereby cylindrical carbon nanofibers are encapsulated by precipitates of varying thickness.[171,173,179] Similar results have been reported for SiC nanowires covered in SiO_2.[248]

Conical nanomaterials can also be shaped by a substrate etching approach in a plasma environment. This type of process is capable of providing greater height uniformity since the tips remain at the original surface of the substrate, and orientation control by the directionality of physical and chemical etching. Sharp nanotips have been fabricated conventionally by focused ion beam (FIB) milling of the substrate with a high

degree of control.[249] The drawback to the FIB method is that it is a serial process for producing conical structures on an individual basis. Other etching or sputter-induced methods, such as those reported by Hsu *et al.* and Fujimoto *et al.*, provide an efficient parallel process but lack control over the nanotip location.[250,251] Being able to control the location, orientation, size, and shape of the nanocones in a deterministic way is necessary for many applications, but scalability of the process also important.

4.2.2 Experimental Methods

For stochastic nanocone arrays, substrates were prepared by electron beam evaporation of 20 nm uniform Cu films at room temperature onto Si(100) and Si(111) n-type wafers. In the case of periodic nanocone arrays, 700-nm-diameter 150-nm-thick Cu dots were photolithographically defined at 5-μm intervals on the silicon substrate. Titanium was also applied as an etch-stop on some samples, in which case a 100-nm Ti layer was evaporated directly onto the Si substrate prior to Cu film deposition.

The Cu-Si nanocones were produced from a Cu-facilitated plasma process. In this process, the substrate described above was subjected to a DC glow discharge (setup described in detail elsewhere).[150,181] Upon a 2 minute pretreatment at 700°C in a 2.5 Torr ammonia plasma, the continuous Cu thin film dewets into nanoparticles on the surface, which served as seeds for the nanocone formation. In the case of periodically patterned Cu dot arrays, the pretreatment step was omitted because seed particles had been defined lithographically. Following seed particle formation, acetylene (C_2H_2) was introduced at 25 sccm into the plasma as a moderating agent for the remaining duration of the process. It was found that without the moderating gas, the seed material as well as any developing nanocones would have been etched away within minutes. The samples were exposed to the plasma for intervals of time ranging from 30 to 240 minutes. Optimal conditions required a plasma bias of 550-650 V at 150 mA.

The samples were first characterized by scanning electron microscopy (SEM) in a Hitachi S-4700 and by SAM in a PHI 680. Then the nanocones were transferred to lacey carbon coated beryllium grids (to avoid any x-ray signal from traditionally used Cu grids)

and analyzed by high-resolution transmission electron microscopy (HRTEM; Hitachi HF-2000) and by scanning transmission electron microscopy (STEM; Hitachi HD-2000). The STEM's high sensitivity XEDS mapping capabilities were utilized to determine the elemental composite structure of the nanocones. In addition, XRD was performed on the as-evaporated Cu film, annealed, plasma pretreated, and plasma processed samples for comparison. Si(111) substrates were used for this experiment to avoid the overlap of the Si(220) peak with the high intensity copper silicide peaks. For these data, a Philips X'Pert diffractometer was used to produce grazing incidence ω-2θ scans of the samples in order to probe the Cu-Si interface structure and composition. The Cu K_α (1.54 Å) x-rays were generated using a source excitation voltage of 45 kV and current of 40 mA. The divergence of the incident and diffracted beam was minimized using a 0.04 radian Soller slit. The rectangular x-ray beam was shaped using a 10-mm incident beam mask and a fixed slit of 1/8°. A beam attenuation optic was activated in the incident beam path to prevent detector saturation.

4.2.3 Results and Discussion

Nanocone structure and composition

Effectively, the DC plasma process described above transformed the surface topography of the substrate. What was originally a silicon substrate covered with thin film copper transformed into a dense array of aligned ultra-sharp nanocones like the one shown in Figure 4.6(A). Figure 4.6(B-H) shows a collage of HRTEM images and diffraction patterns from a typical nanocone after a 105-minute process at optimal conditions described in the experimental methods. The central image, Figure 4.6(B), shows a base segment of lighter contrast and a tip segment of darker contrast due to the difference in mass; both the base and tip are oriented to show some diffraction contrast as well. Figure 4.6(C) shows the tip diameter measures only 10 nm. The entire structure is encapsulated by a few nanometers of amorphous material, which becomes thicker at the top of the structure. The HRTEM close-up of the interface region of the base and tip segments, Figure 4.6(D), reveals phase contrast from the Si lattice overlapping with the

Cu_xSi lattice. The boundary of these two phases is characterized by a moiré pattern, inferring that the two crystals are aligned but have differing periodicities. An FFT [Figure 4.6(F)] of the silicon lattice region [Figure 4.6(E)] yields the same results as the diffraction pattern [Figure 4.6(G)]. The diffraction pattern reveals that the nanocone base is single-crystal Si with the same <100> orientation as the substrate. For the (022) planes, a *d*-spacing of 1.93 Å was measured, corresponding to a lattice parameter of 5.45 Å, which agrees with literature values.[135] The nanocone tip is likely a crystalline copper silicide as given by the diffraction pattern in Figure 4.6(H); however, we have been unable to index the pattern.

The XEDS map shown in Figure 4.7(A) illustrates the elemental distribution for several nanocones after a 240-minute process. The nanocones are predominately silicon with sharp Cu-rich tips and occasional Cu-rich aggregates within the silicon crystal lattice. Point XEDS of a nanocone base segment [foreground, Figure 4.7(B)] shows that the ratio of copper to silicon is less than 1%. The minor C and O peaks originate from elements in the amorphous outerlayer. The XEDS analysis of the nanocone tip [background, Figure 4.7(B)] shows an atomic ratio of 38.7% Si to 61.3% Cu. Because a compound of Cu_2Si is not thermodynamically stable it, seems most probable that the tip is composed of the η-phase Cu_3Si stoichiometry with additional Si contribution originating from the outerlayer. This outer amorphous coating encapsulating the nanocone is composed of a mixture of C, N, O, and Si, as shown by the Auger results plotted in Figure 4.7(C). After briefly sputtering the sample with argon in the SAM, the outerlayer was removed completely, resulting in a purely Cu and Si nanocone underneath. This silicon-rich amorphous outerlayer is a result of sidewall deposition of condensed species from the plasma.[171,179] The carbon and silicon contained in the outer coating may play a crucial role in protecting the sidewalls of the conical structure during the plasma process and is believed to be facilitated by the supply of carbon-rich acetylene gas.

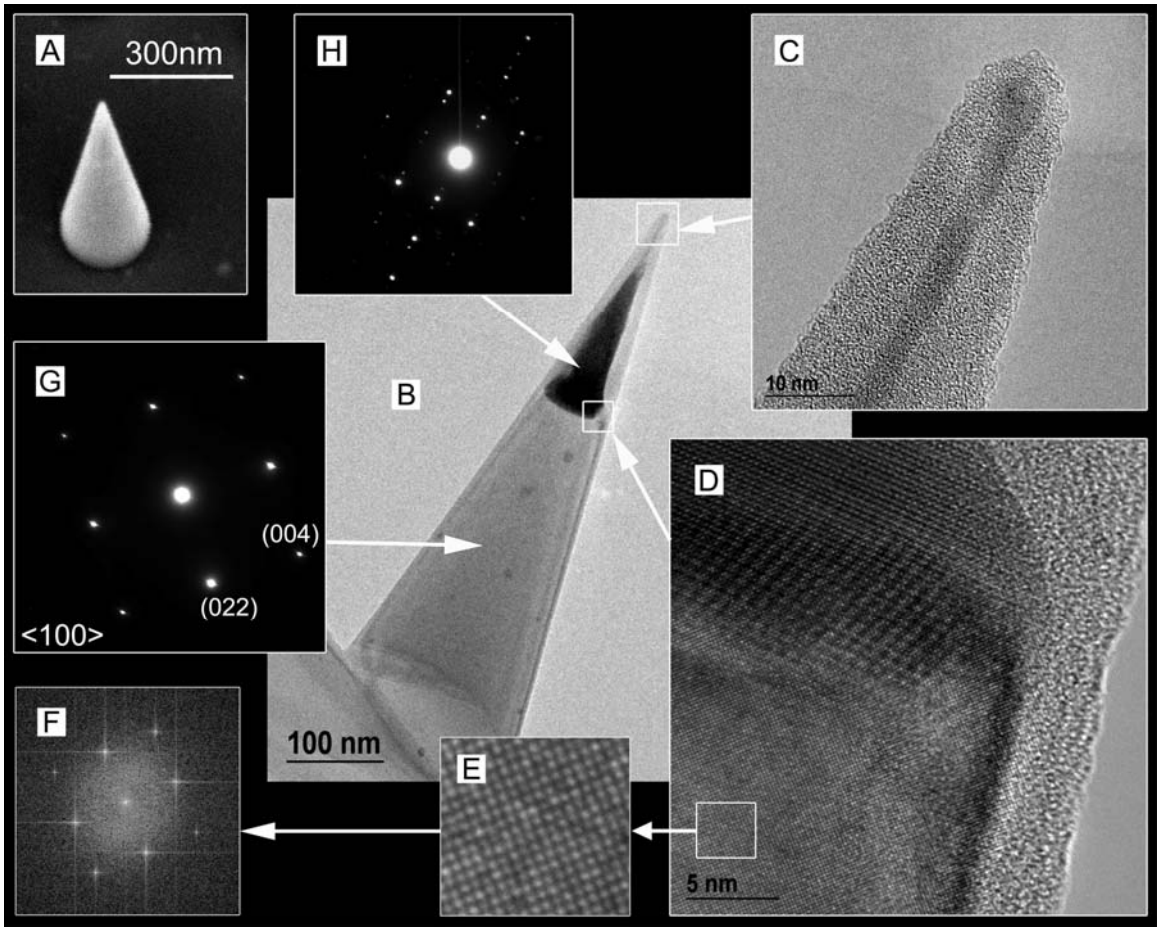

Figure 4.6 Image collage of a typical nanocone after 105-minute plasma process. (A) SEM image at a 30° tilt. (B) TEM profile image of a cleaved nanocone. (C) Zoomed-in image of the 10-nm tip. (D) HRTEM of the tip-base interface with (E) inset of the Si lattice and (F) FFT of the same area boxed in white in (D). SAD patterns from (G) the single-crystal silicon base and (H) crystalline Cu-Si tip.

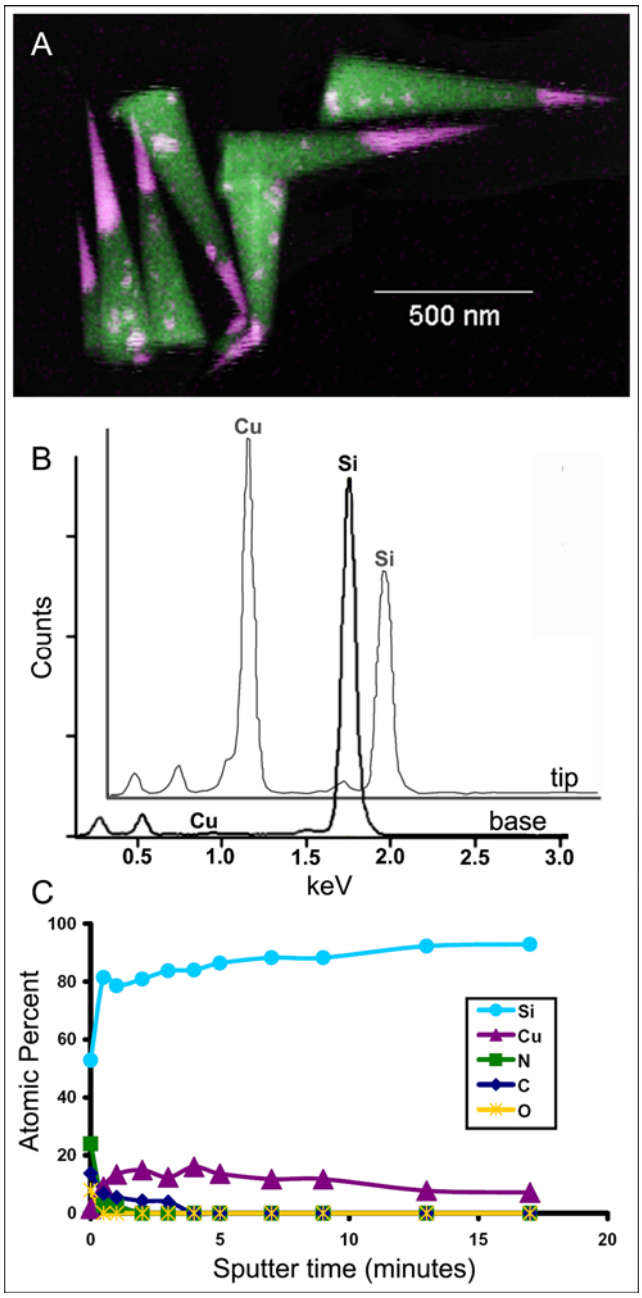

Figure 4.7 Chemical analysis of typical nanocones: (A) XEDS elemental map of several cones showing copper in pink (light) and silicon in green (dark), (B) point XEDS from a cone base overlaid on an XEDS spectra from a cone tip, and (C) Auger depth profile of a nanocone.

Time Evolution of Nanocone Formation

A time evolution of the nanocone structure demonstrated by three stages in the formation process is displayed in Figure 4.8. After 30 minutes in the DC plasma environment, examination of the sample revealed emerging stump-like structures shown in Figure 4.8(A). These "pre-cone" structures were spaced relatively evenly at ~1 μm apart and stood between 400 and 600 nm tall. Most of the pre-cone structures contained a Cu tip particle of variable size between 20 and 200 nm in diameter. All of the structures had a silicon base segment of roughly the same size of 200 nm tall, shown in Figure 4.8(B) and 4.8(C). The cone angle varied from 22 to 26 degrees.

Subjecting the Cu-covered silicon substrate to a longer plasma process of 105 minutes resulted in the formation of uniform cone structures as shown in Figure 4.8(D). The nanocones were not much larger than the pre-cones from the 30-minute plasma process, standing only 600-700 nm tall; however, each structure had a sharp cone angle ranging from 18 to 21° and a very small tip diameter. Further analysis by TEM revealed that the copper silicide particles located at the tip had been formed into a conical shape, sharing a distinct (often angled) grain boundary with the underlying silicon [Figure 4.8(E)].

Investigating further, the substrate was exposed to an even longer DC plasma process of 240 min, which resulted in ultra-sharp nanocones with an angle range of 9 to 14° shown in Figure 4.8(F-I). Additionally, there was a doubling in height of the structures to 1.5 μm. The nanocone tips, covered by a few nanometers of amorphous substance, were only 10 nm in diameter. Thus, as the nanocones became taller, they were continually sharpened. An interface is observed in Figure 4.8(I), which is believed to be the phase boundary between Cu and the copper silicide. The presence of a subarray of smaller secondary cones should also be noted in the longer process, as observed in Figure 4.8(F). These secondary cones are considerably shorter than the original cones and therefore thought to be the result of Cu seed material sputtering and redeposition.

The presence of rectangular crystallites or "islands" on the plasma treated surface should also be noted in Figure 4.8(A,D). To elucidate the nature of these islands we exposed a nanocone sample surface to a brief inductively coupled plasma (ICP) etch (30 sec, 100 mTorr, ICP 500 W, RIE 50 W, SF_6 45 sccm, O_2 5 sccm). Figure 4.9 shows the

results of this treatment, which is designed to efficiently and selectively etch silicon. It can be seen in Figure 4.9(A) that only the nanocones located on the bare silicon regions were undercut by the isotropic etch. On the other hand, the cones which formed on the islands remained unscathed. In addition, a closer look at one of the felled nanocones in (B) reveals that the Si ICP etch continued to eat away at the interior of the nanocone base while the outer coating was left intact. It is thus believed that while the Cu particles are located at the tips of the forming cones, much of the copper is left behind in the form of silicide crystallites on the surface. Interestingly, cone formation does not appear to preclude the silicide island sites and appears to show no preference.

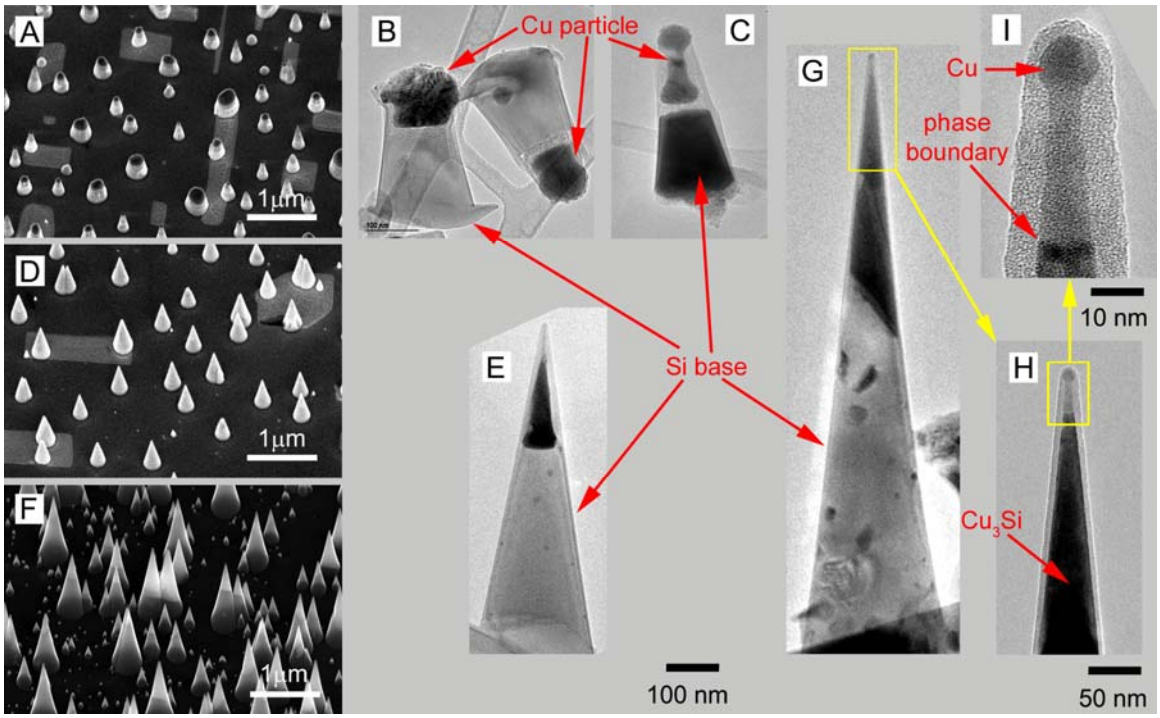

Figure 4.8 Time evolution of nanocone formation shown at three stages. Stage one, following a 30-minute plasma process: (A) SEM image at 30° tilt, (B and C) TEM images of early pre-cone formation. Stage two, following a 105-minute plasma process: (D) SEM image at 30° tilt and (E) TEM image. Stage three, following a 240-minute plasma process: (F) SEM image at 30° tilt and (G) TEM image of a typical nanocone with insets (H) and (I) of the sharpened tip. Scale bars are 1 μm for (A), (D) and (F); 100 nm for (B), (C), (E), and (G); 50 nm for (H); 10 nm for (I).

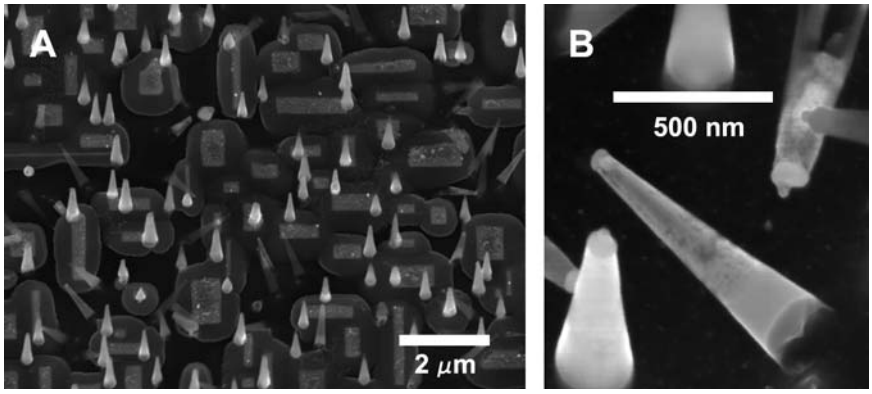

Figure 4.9 Nanocone sample after exposure to a silicon ICP etch for 30 seconds. (A) SEM image at 30° tilt showing the selective etching of just the pure silicon regions. (B) SEM image at 30° tilt showing the undercut bases of the nanostructures.

Grazing incidence x-ray diffraction of the substrate surface gives further evidence of the morphology and phase changes occurring during the cone formation process. As can be seen from the SEM image and corresponding spectra in Figure 4.10(A), the initial Cu film evaporated onto the Si(111) substrate gives broad Cu(111) and Cu(200) peaks at 2θ angles 43.37° and 50.53°, respectively, indicative of a fine-grained polycrystalline film. After annealing at 700°C, the Cu peaks become sharper, indicative of a larger grain size in the dewetted film shown in Figure 4.10(B). Comparing the integrated peak intensities to a polycrystalline copper standard also reveals some degree of texture in the annealed nanoparticle film, with a preference for Cu(200). Customarily, the annealing and plasma pretreatment steps occur simultaneously; once 700°C is reached the plasma is initiated and stabilizes during the pretreatment. However, by analyzing the sample after only annealing we can see the effect of heat alone versus heat *and* plasma. We found that during the 2 minute pretreatment in the ammonia plasma at 700°C, much of the copper reacted with the silicon substrate to form what is believed to be the hexagonal Cu_3Si phase (a = 4.04 Å, c = 2.44 Å). This is shown by the appearance of 2θ peaks at 44.61° and 45.17° in Figure 4.10(C), corresponding to the $(11\bar{2}0)$ and $(10\bar{1}1)$ reflections, respectively.[238] At this stage the copper reflection intensity is significantly reduced as a result of its partial conversion to silicide. After cones are formed from prolonged interaction with the plasma, the Cu (111) and (200) peaks re-emerge, this time with no

preferred texture. Thus we believe that it is the Cu particles which sit atop the nanocones and serve as the seed for their formation. This elevating of the Cu would geometrically suppress the silicide reflections from the surface as seen in Figure 4.10(D). To verify the location of the Cu particles, we removed the cones from the substrate by scraping with a razor blade, and the XRD result [Figure 4.10(E)] is analogous to the pretreated sample, with the recurrence of the silicide peaks [Figure 4.10(C)].

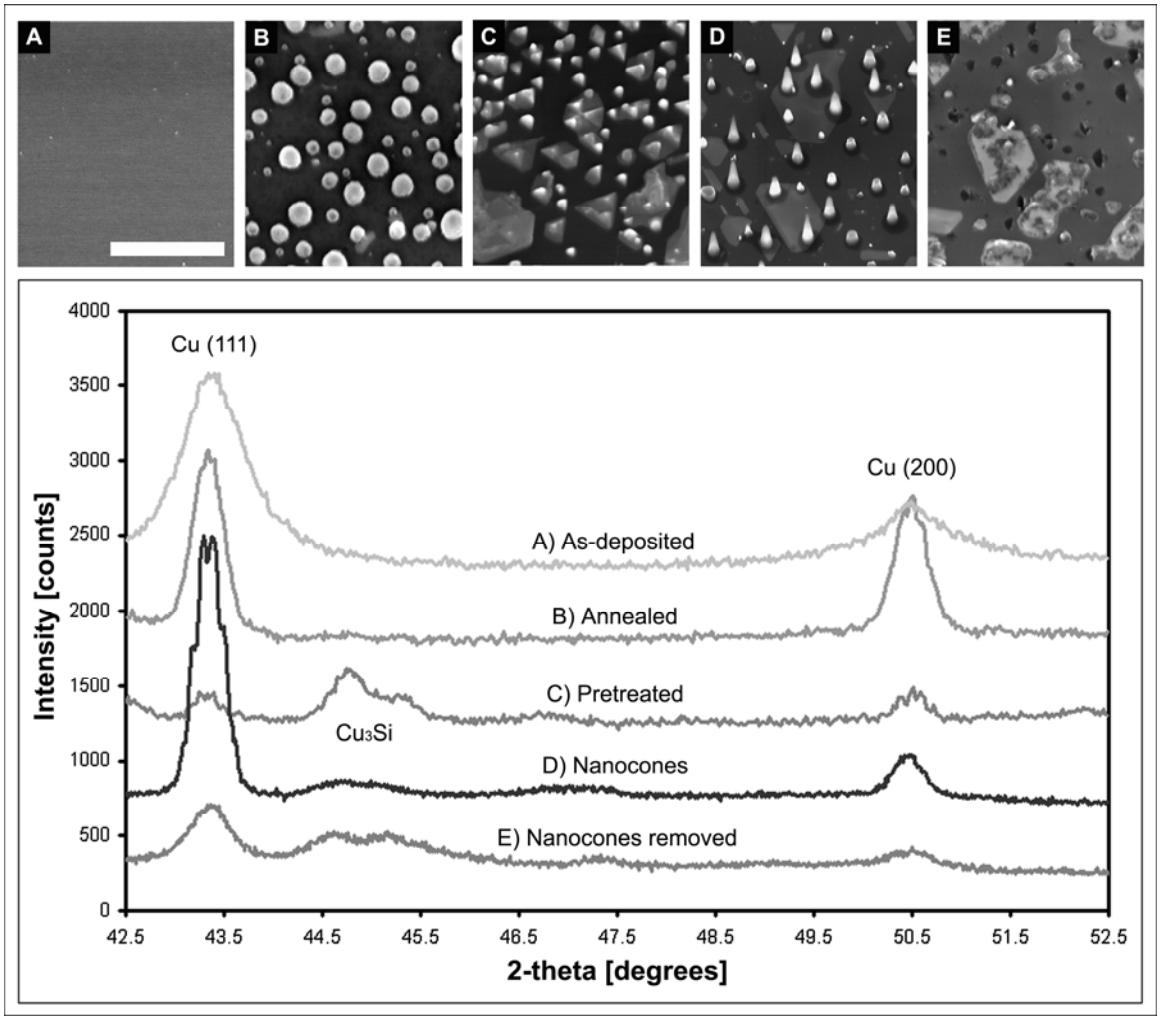

Figure 4.10 SEM images at 30° tilt and corresponding XRD grazing incidence scans of sequential stages in the cone formation process: (A) as-deposited 20 nm Cu film on a Si(111) substrate, (B) sample annealed at 700°C for 2 min, (C) plasma pretreated sample, (D) 120-minute plasma processed sample with nanocones, and (E) substrate after nanocones were removed. All SEM images were taken at the same magnification and the scale bar in A is 2 μm.

Nanocone Formation Model

A model of the cone formation process is presented in Figure 4.11. Here a patterned layer Ti is employed as an etch barrier material to mark the original substrate level and control the location of the nanocones. Formation of the cones is prohibited where the Ti layer is defined on the Si substrate. After Ti is deposited, copper is evaporated over the entire surface [Figure 4.11(A)]. At elevated temperatures the Cu film breaks into nanoparticles [Figure 4.11(B)], which react with the substrate with the initiation of plasma to form Cu_3Si on the silicon surface [Figure 4.11(C)]. This silicide formed at the Cu-Si interface acts as a barrier for further copper diffusion[239] and the copper particles remain, shielding the underlying substrate from the plasma. As time passes the unprotected Si and silicide regions are etched away indiscriminately at a rate of ~4 nm/minute and the pre-cones are formed [Figure 4.11(D)]. With even more time, the copper particles themselves slowly erode, as the nanotips become sharper and the structures become taller [Figure 4.11(E)]. The experimental result in Figure 4.11(F) shows such an array of high aspect ratio Cu-Si nanocones. In the regions where the Ti film served as a buffer layer, the surface remained unetched by plasma. Beneath the titanium, the original substrate level can be seen, which expectedly is the same height as the nanocone formations.

It is believed that the nanocones presented in this paper are the result of a reactive ion etch (RIE) process occurring at the substrate. RIE is the likely explanation because there appears to be characteristic evidence of both physical and chemical etching. To begin with, there is a high degree of directionality in the process, resulting in an anisotropic, physical etching of the cones out of the substrate. Hence, portions of the substrate that are covered by the copper seed material (serving as an etch mask) are preserved.[250,251] Furthermore, there is sufficient energy in the plasma to induce sputtering of the substrate, indicated by the Si sidewall deposition and the formation of secondary cones from redeposited material.[251] In fact, the evolution of surface features and cone growth has often been observed on sputtered targets and is attributed to sputter-resistant impurities.[113] However, there are additional aspects characteristic of a dry chemical etch such as the high-pressure plasma environment, the relatively fast etch rate, and the selectivity favoring the etching of Si and Cu_3Si over pure Cu, which actually has a *higher*

sputter yield.[113] In addition, the nanocones do not exhibit any faceting on their external surfaces, which is often a characteristic of physical etch profiles. It should also be noted that substrate doping did not affect the etch rate significantly. Perhaps the hydrogen plays a large role in the chemical etching of the silicon, while the removal of the copper in the silicide phase is facilitated by physical sputtering, where the balance of the two rates and simultaneous condensation of plasma species enables the Cu-tip particles to survive.

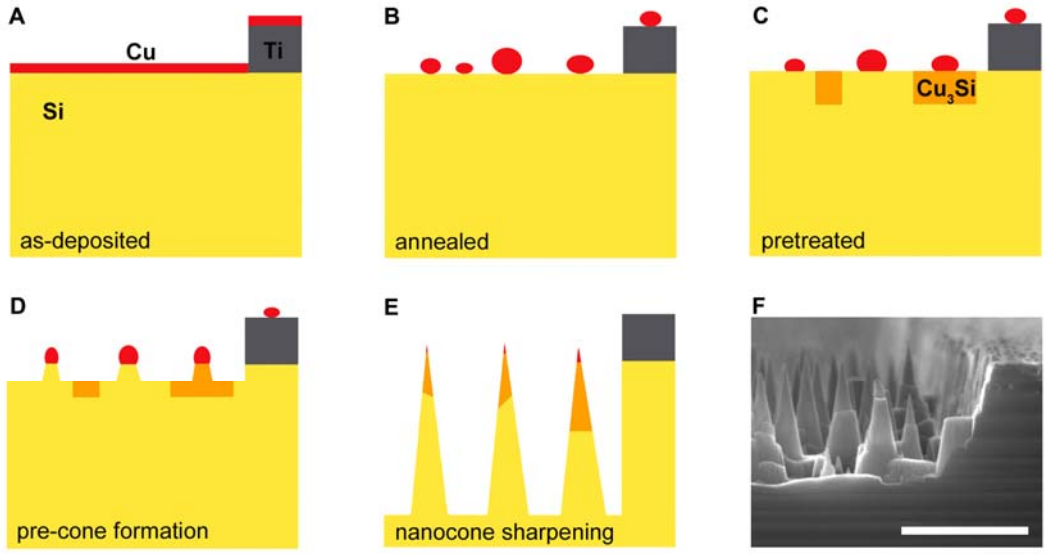

Figure 4.11 Model of the cone formation process: (A) deposition of patterned 100-nm Ti film followed by a continuous 20-nm Cu film, (B) heating of the substrate to 700°C to form Cu nanoparticles, (C) plasma pretreatment and formation copper silicide, (D) plasma etching of the substrate surface forming pre-cone structures beneath the Cu particles, (E) continued interdiffusion of Cu and Si and plasma etching to form ultra-sharp nanocones, and (F) cross-sectional SEM image of the experimental result of (E) (scale bar 1μm).

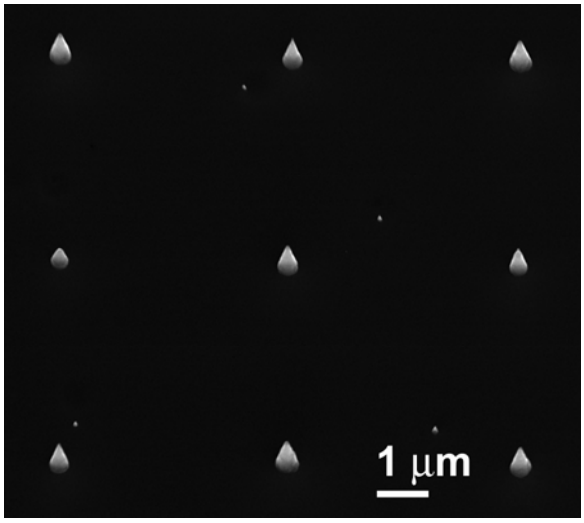

Figure 4.12 SEM image at 30° tilt of a periodic nanocone array produced from photolithographically defined Cu dots at a 5-μm-pitch.

Recent success in forming periodic arrays of the nanocones is presented in Figure 4.12. By lithographically defining the location of the Cu seed particles, the nanocone location is controlled effectively. This concept, coupled with the etch selectivity for Si versus Ti, can be utilized to pattern the substrate such that nanocones will only form in the absence of a Ti film and the presence of Cu seed particles. This results in a deterministic process to form nanocone arrays of variable heights and spatial organization.

4.2.4 Conclusions

In this chapter, a method of producing ultra-sharp nanocones via a Cu-facilitated acetylene and ammonia DC plasma process was described. Copper was confirmed to be a poor catalyst for carbon nanofiber growth and instead produced dense arrays of high aspect ratio nanocones with tips less than 10 nm in diameter. Thorough characterization of these structures has revealed that the nanocones consist of single-crystal silicon bases (preserving the orientation of the substrate) and crystalline copper silicide tips capped

with a small amount of etch-resistant copper. We conclude that the mechanism for the formation of these interesting structures is not a VLS process, but rather reactive ion etching of the silicon substrate facilitated by copper seed particles. In this process, the nanocones become sharper as they increase in height. Furthermore, it has been shown that by patterning seed and etch barrier materials the location of the nanocones can be predetermined.

4.4 Fe-Co Alloy System: *Magnetic Properties of Fe-Co Catalysts Used for Carbon Nanofiber Synthesis*†††

4.4.1 Introduction

Nanostructured ferromagnetic materials are of great scientific interest due to their size dependent properties.[252] At the nanoscale, properties like saturation magnetization,[253], coercivity,[254] anisotropy,[255] and thermal sensitivity[256] can all be very different than those measured in larger systems. One drawback of studying magnetic nanoparticles is that the high surface to volume ratio makes these materials more prone to rapid environmental degradation. With minimal oxidation the bulk magnetization in ferromagnetic (FM) nanoparticles should essentially be preserved, however if significant oxidation occurs then the magnetization can be reduced[257] by the antiferromagnetic behavior of the surface oxide and, in some cases, depending on the thickness of core-shell structures, exchange biasing has been observed.[55,258] Finding unique ways of passivating these highly reactive ferromagnetic nanoparticles is therefore crucial to maintaining their magnetic properties for such applications as hysteretic heating.

Using carbon coatings to isolate and protect magnetic nanoparticles is an established technique that is implemented in a variety of ways.[87,253,257,259,260] While these particles retain much of their FM properties, many other properties such as saturation magnetization and coercivity can change drastically due to the formation of carbides,[223,260,261] conversion to superparamagnetic particles,[223,259-261] or possibly particle shape changes associated with the carbon nanofiber growth process.[109,206] Carbon nanofibers are a particularly interesting carbon-based system because they are highly compatible with microfabrication processes[44] and their surfaces can easily be biochemically modified[39,141] to enable applications from gene delivery arrays[78] to microelectrodes for electrophysiological recording.[86] In addition, magnetic nanoparticles can be encapsulated within nanofibers, adding multifuctionality with the ability to

†††This section is based on work from [[172]] and contains lightly revised passages and figures.

physically manipulate the particles by magnetic field driving.[222] Carbon nanofibers are catalytically grown from a variety of magnetic metals, mainly Fe, Ni, Co, and their alloys. The alloys of Fe and Co, chosen for this study, are a particularly interesting class of soft magnetic materials with a unique combination of high saturation magnetization, high Curie temperatures, and good permeability.[87,252,262] Alloy catalyst material can be produced from aerosol thermolysis,[87] coprecipitation methods,[263] or by vacuum PVD techniques.[170] Simultaneous sputtering from multiple targets onto a substrate is a convenient and controllable way to prepare the alloy thin films of tailored compositions.[171] Encapsulation of these alloys within graphitic carbon can be accomplished through catalytic plasma-enhanced chemical vapor deposition, the result of which is a freestanding vertically aligned carbon nanofiber with a magnetic nanoparticle the tip.[44]

In this work, we characterize the composition, structure, morphology, and magnetic properties of Fe-Co alloy catalysts used for the synthesis of VACNFs. The nanofibers are grown by DC-PECVD and characterized with electron microscopy, XEDS, and XRD. Magnetic properties are measured with a SQUID based magnetometer.

4.4.2 Experimental Methods

Fe-Co alloys were sputtered onto Si substrates by two different techniques. The first was a co-sputtering technique that produced a binary gradient film on a 100 mm Si wafer. In this technique, sputter sources were configured at opposing sides of the chamber, at an angle of 32^{o} with respect to the substrate normal, and 16.5 cm from the substrate center. By sputtering Fe and Co (3 mTorr, 200 W) at the same time onto a stationary substrate, the independently optimized sources provided a gradient in alloy composition across the substrate surface. This allowed for different catalyst compositions to be deposited under the same chamber conditions. Further details of this technique can be found elsewhere.[171,264] The Fe_xCo_{100-x} gradient films were deposited to a nominal thickness of 115 nm, as measured by AFM (Dimension 3100). Alloy

compositions as measured by XEDS (Hitachi S-4700 SEM) in Figure 4.13, reveal a linear gradient down the center of the wafer from Fe concentration x = 11 to 70. Samples taken from various positions along this linear composition scale will be referred to as the *gradient system*.

A second type of Fe-Co film was prepared in order to minimize stoichiometry and phase variations inherent to the gradient samples and to produce a larger quantity of sample with a uniform composition and thickness. Wafers of single-composition alloys were deposited for several atomic ratios. These films, deposited by a more traditional co-sputtering approach where the substrate is rotated for compositional uniformity, measured to be nominally 15 nm thick by AFM and had compositions ranging from x = 0 to 100, as measured by AES (PHI 680). These samples will be referred to as the *uniform system*.

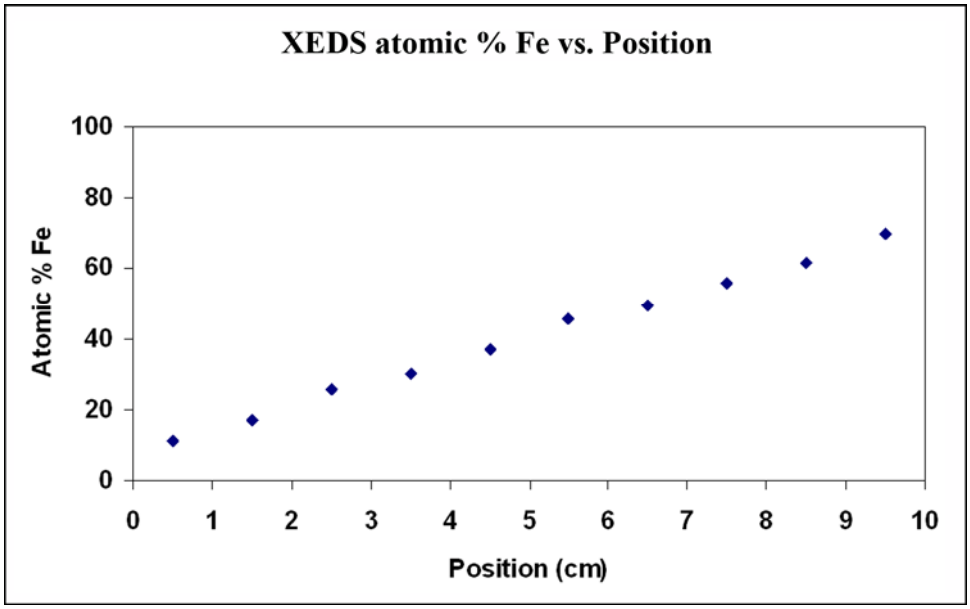

Figure 4.13 XEDS analysis of the Fe-Co gradient showing the atomic percent composition of the catalyst film as a function of position across a 100 cm substrate.

Following metal film deposition on the Si wafers, the substrates were diced into ~5 mm chips. A sample chip from each system and composition was loaded into a DC-PECVD chamber for VACNF growth. To prepare the catalyst films for nanofiber synthesis, the substrate was slowly heated to 570°C with ammonia (NH_3) flowing into the chamber at 150 sccm with a pressure of 10 Torr for the gradient samples and 6 Torr for the uniform samples. The films were then pretreated in a DC ammonia plasma with a current of 2 A for 5 minutes for the gradient system and a current of 1.5 A for only 45 seconds for the uniform system. This is referred to as the *pretreatment* step, which is used to break the continuous metal films into nanoparticles. After pretreatment, VACNF growth was initiated by adding a flow of acetylene (C_2H_2) to the existing plasma at a rate of 35 sccm for the gradient samples and 45 sccm for the uniform samples. The VACNF growth process continued for 30 minutes for the gradient system and 10 minutes for the uniform system, typically yielding fibers several microns tall. The evolution of these alloy systems from thin films to pretreated particles to encapsulation within carbon nanofiber tips was characterized by SEM (Hitachi S-4700), STEM (HD-2000), and XEDS chemical analysis. In addition, powder XRD analysis of the VACNF particles from the 115-nm-thick films near equiatomic composition (removed from wafer by scraping) was performed using a Siemens D5000 powder diffractometer operating at 45 kV and 40 mA with Cu K_α radiation and diffracted beam monochromator. Data were collected in the 2θ range of 8 – 90 degrees with a step size of 0.02 degrees and a counting time of 20 seconds at each step.

Magnetic measurements on the two Fe-Co systems were performed in a SQUID magnetometer (Quantum Design MPMS-5) in a temperature range of 2 to 330 K and applied magnetic fields $|H| \leq 20$ kOe. The magnetic properties were also studied at the three stages of synthesis: as-deposited films, pretreated films, and after VACNF growth. In each case, the magnetic field was applied parallel to the substrate plane (perpendicular to fiber growth). The magnetic contribution to the signal from the diamagnetic Si substrate was removed by subtracting the mass susceptibility of Si. For each sample, the measured magnetic moments were normalized with respect to the estimated volume of

the as-deposited film based on the chip dimensions and the film thickness as measured by AFM.

4.4.3 Results and Discussion

Comments on Catalyst Particle Formation

The 115-nm-thick gradient films were difficult to dewet into nanoparticles, especially at high Fe compositions. Figure 4.14 shows a representative image of the films following the pretreatment step where the film breaks into "islands" on the silicon substrate. The SEM image in Figure 4.14(a) reveals a "Swiss cheese" appearance of the Fe-rich gradient composition following a 2-minute pretreatment where the film did not fully dewet and was therefore not suitable for VACNF growth. However, at another composition near $Fe_{50}Co_{50}$ following same pretreatment, XEDS conveys that dewetting did occur and it can be seen that the metal remains alloyed (Figure 4.14(b), Si is blue, Fe green, and cobalt red). The pretreatment time for the gradient system was therefore increased to 5 minutes in order to ensure dewetting at all compositions. The thinner uniform films, as pictured in Figure 4.14(c), did not have any difficulty dewetting with a pretreatment time of just 45 seconds.

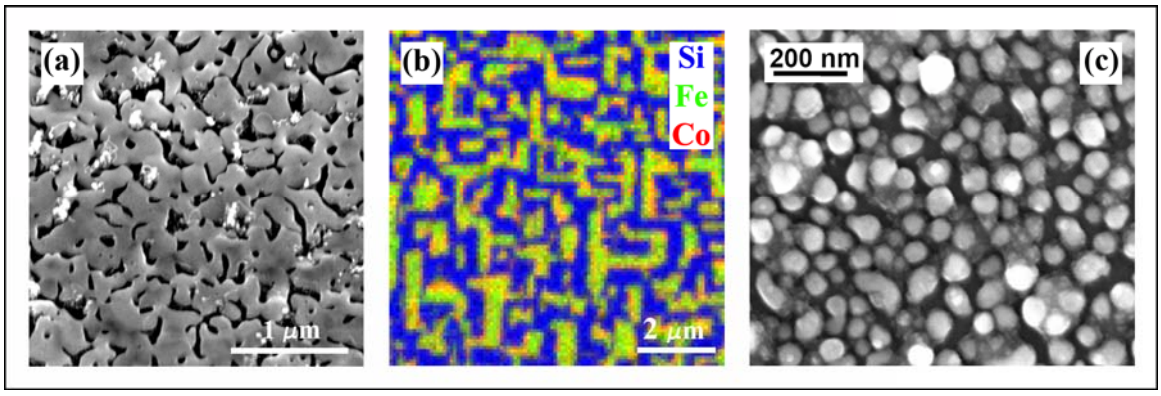

Figure 4.14 Representative top views of catalyst thin films following the pretreatment step, specifically, (a) SEM image of the Fe-rich gradient film, (b) XEDS map of the $Fe_{50}Co_{50}$ gradient film, and (c) SEM image of the $Fe_{41}Co_{59}$ uniform composition film.

Analysis of VACNF Catalyst Particles

SEM images of the VACNFs as a function of composition in the 115-nm-thick gradient film are illustrated in Figure 4.15. At low Fe concentrations, Figure 4.15(a-c), the samples have the appearance of a rather uniform "forest" of nanofibers with a narrow diameter distribution (100 – 200 nm). However, as the Fe concentration is increased to ~50% [Figure 4.15(d,e)], a bimodal distribution in diameters is seen where smaller particles that are able to break away from the film grow into tall wispy fibers while the larger particles (300 – 500 nm) remain behind. Indeed as high Fe concentrations are reached [Figure 4.15(f)], it appears difficult to dewet the film even after a 5 minute pretreatment, and large angular particles were formed, which are not highly active catalysts under these conditions. In our experience we have observed that the growth conditions such as temperature, gas flow ratio, pressure, and plasma current need to be optimized for each catalyst composition. As was mentioned earlier, the pretreatment time also needs optimized for the type of catalyst and film thickness. In this work we have used the same synthesis conditions for all compositions of each system for the sake of proper comparison of the magnetic properties. Thus the growth conditions for VACNF synthesis were compromised for some compositions but optimal for others. While the nanofiber growth conditions in this work proved optimal for Co-rich alloys, the Fe-rich alloys would catalyze better in a higher energy process.

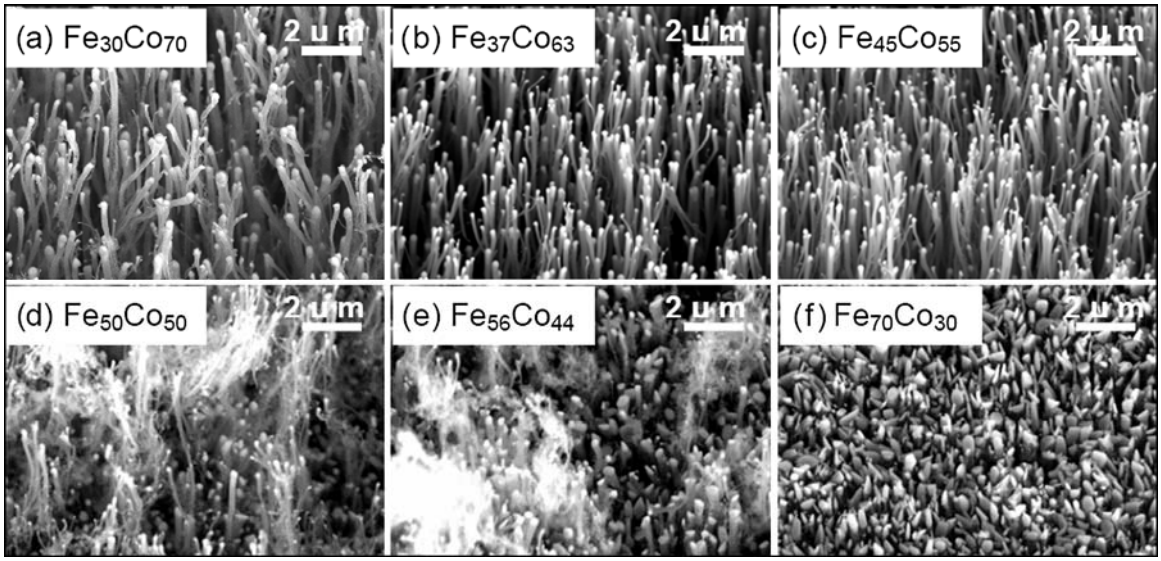

Figure 4.15 SEM images at 30° tilt of VACNFs grown from the gradient Fe_xCo_{100-x} film including: (a) $Fe_{30}Co_{70}$, (b) $Fe_{37}Co_{63}$, (c) $Fe_{45}Co_{55}$, (d) $Fe_{50}Co_{50}$, (e) $Fe_{56}Co_{44}$, and (f) $Fe_{70}Co_{30}$.

Similar morphologies are seen with VACNF growth from the 15-nm-thick uniform composition alloy films. However, since the initial catalyst films were thinner, the nanoparticle size is significantly smaller (20 – 100 nm). For comparison, Figure 4.16 provides SEM images of the CNFs grown from the uniform films with composition (a) pure Co, (b) $Fe_{76}Co_{24}$, and (c) pure Fe. In addition, STEM images of the catalyst particles following nanofiber growth are shown in Figure 4.17 for (a) pure Co, (b) $Fe_{41}Co_{59}$, and (c) pure Fe initial films. Again, we find that the Co-rich catalysts [elongated and teardrop-shaped, Figure 4.16(a) and 4.17(a,b)] worked well for VACNF synthesis under the present growth conditions. However, as the concentration of Fe increases, the catalyst particles became more angular and less able to dissolve and graphitize carbon, leading to a buildup of amorphous carbon on its surface and resulting in minimal fiber growth at the Fe-rich compositions [Figure 4.16(b,c), 4.17(c)]. Nevertheless, for the purpose of magnetic characterization, the encapsulation within carbonaceous layers was consistent for *all* alloy ratios. The XEDS spectra from the catalyst particles in Figure 4.17, confirm that the particles were not significantly oxidized given the absence of an oxygen signal, which would appear at 0.523 keV. Furthermore, XEDS data collected

from the VACNF catalyst particles are in agreement with AES compositions as measured from the as-deposited films to within a few atomic percent, confirming that the carbon-encapsulated particles do remain alloyed. It should also be noted that some of the catalyst material can break off during the synthesis process and reside as inclusions in the central cavity of the nanofiber or as small isolated clusters decorating the sidewalls [shown by arrows, Figure 4.17(a)].

X-ray diffraction analysis of the VACNF gradient system broadly sampled near the equiatomic composition revealed the presence of two cubic phases.[226] Figure 4.18 shows the XRD pattern from the VACNF catalyst particles, with low signal intensity due to the small volume of sample. Peaks indicate the presence of the FCC $Fm\bar{3}m$ phase (austenite structure, γ-Fe, a = 3.60 Å)[87,265] that is stable at room temperature for higher Co concentrations and to a lesser extent, the disordered FeCo BCC $Im\bar{3}m$ phase (ferrite structure, α-FeCo, a = 2.8552),[87,265-267] which can't be distinguished from the ordered phase (α'-FeCo, $Pm\bar{3}m$)[262,268] at our signal intensities. Ordered FeCo reflections for the (100) and (111) peaks would only appear very weakly at 31.28° and 55.68°, respectively.[268]

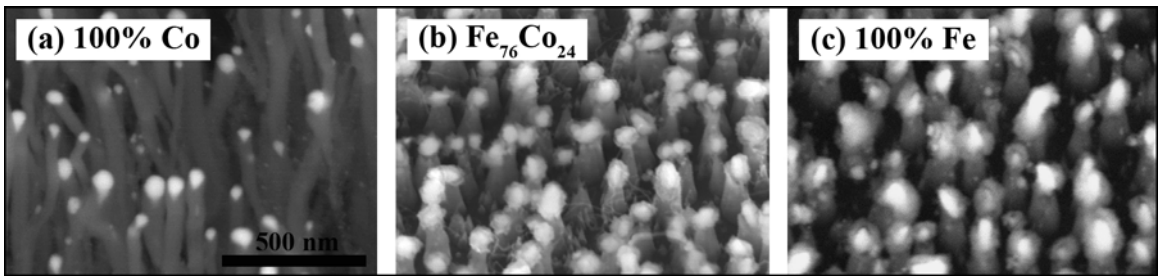

Figure 4.16 SEM images at 30° tilt of VACNFs grown from the uniform catalyst films including: (a) Pure Co, (b) Fe76Co24, and (c) pure Fe.

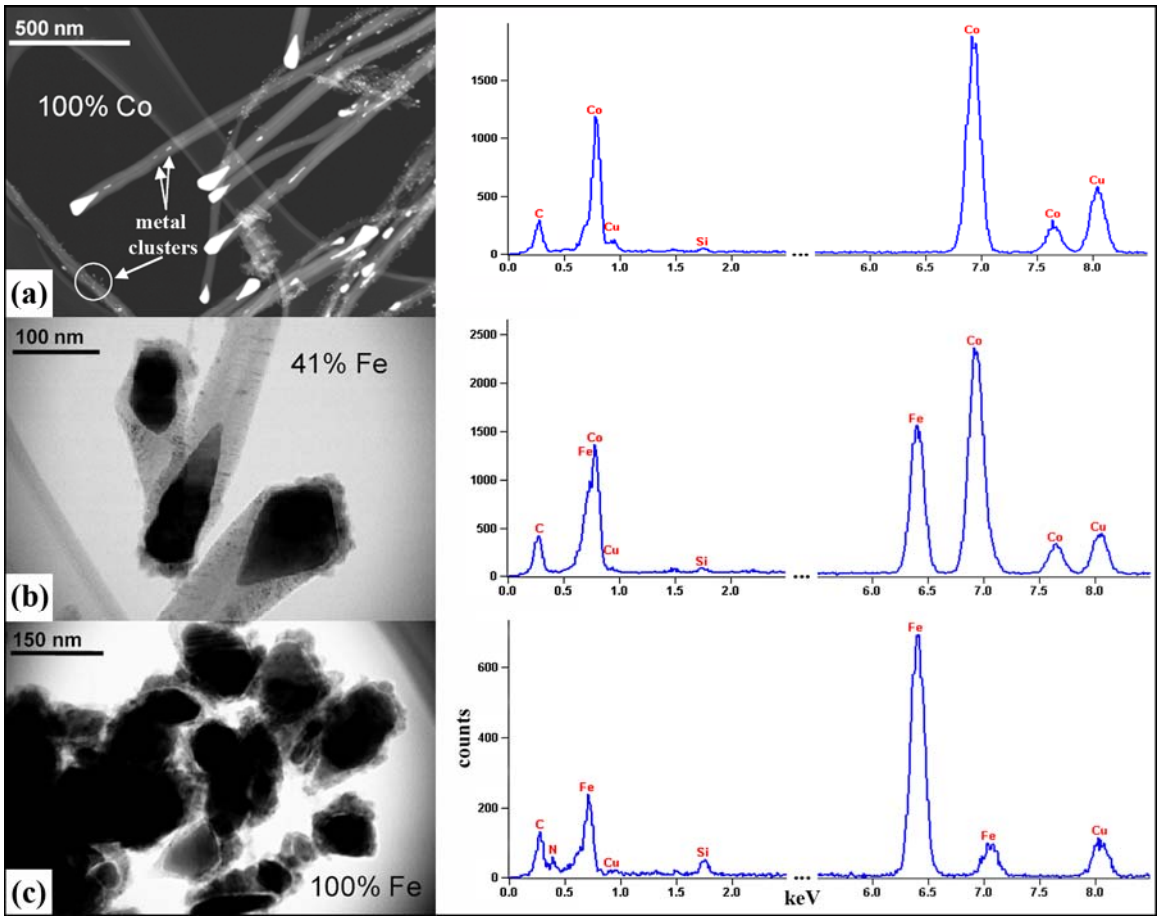

Figure 4.17 STEM and XEDS of uniform alloy catalyst particles. (a) *Z*-contrast image and XEDS spectrum from pure Co catalyst, (b) transmission image and XEDS spectrum from $Fe_{41}Co_{59}$ catalyst, and (c) transmission image and XEDS spectrum from pure Fe catalyst. As the concentration of Fe increases, the particles become less efficient as catalysts at these conditions. Small metal clusters are marked by arrows in (a).

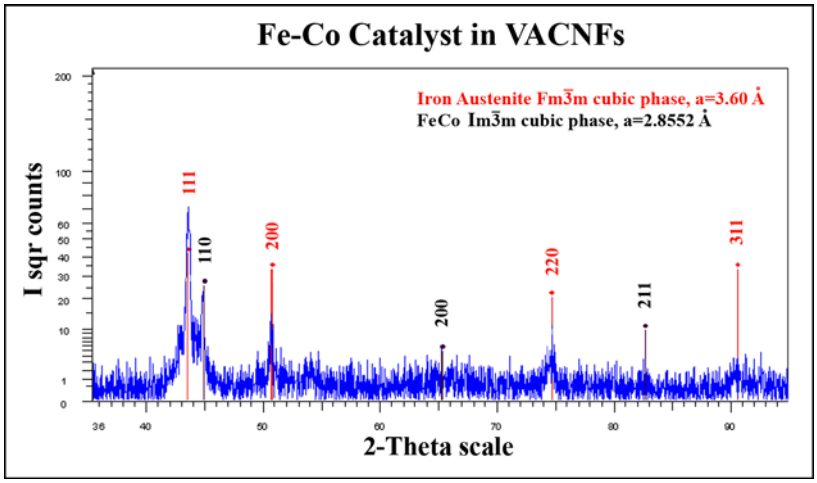

Figure 4.18 XRD from the middle of the Fe-Co gradient system following VACNF growth.[226]

Magnetic Measurements

Magnetization curves for (a) the co-sputtered gradient-alloy and (b) the uniform-alloy (at roughly equiatomic compositions) are shown at the three stages of synthesis in Figure 4.19. It is obvious from this data that there are significant changes that occur to the initial deposited films. During pretreatment, the thin film is exposed to intense plasma bombardment in a reducing atmosphere, such that any oxide that is present on the catalyst surface will be reduced or removed by etching or sputtering. Since a long pretreatment is required to dewet the thick gradient films [Figure 4.19(a)], we see a drastic drop in magnetization comparing the as-deposited to the pretreated films. On the other hand, very little pretreatment is necessary to break the uniform-alloy film into particles, as reflected by the little loss of magnetization between the as-deposited and pretreated stages in Figure 4.19(b).

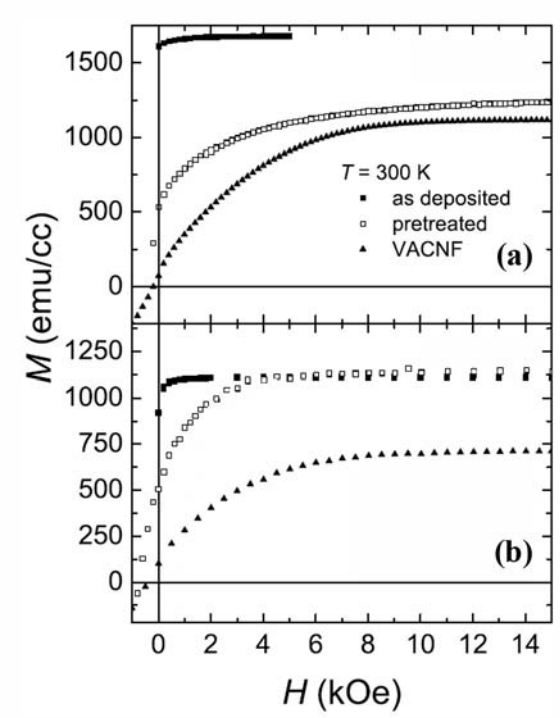

Figure 4.19 Room temperature hysteresis curves at the three primary stages of synthesis: as-deposited film, pretreated film, and VACNF particles in both the (a) thick gradient-alloy $Fe_{50}Co_{50}$ and (b) thin uniform-alloy $Fe_{41}Co_{59}$ samples.

The shapes of the curves in Figure 4.19 are exactly what would be anticipated from the anisotropy of the magnetic metal at each stage. The as-deposited films are expected to have a very small demagnetizing factor because the magnetic field is in the plane of the film. This is manifest by the steep slope and the small field required for saturation. However, during pretreatment, the film dewets into separate particles on the substrate. While the shape anisotropy is still primarily in-plane, the demagnetizing factor does increase due the altered size of these spatially separated metal "islands" as compared to the continuous film. After VACNF synthesis, the demagnetizing factor of the catalyst metal gets even larger as the particle shape evolves from a mound on the substrate to a free elongated particle inside the VACNF, with the field now perpendicular to the axis-of-rotation of the catalyst particle. This increase in the demagnetizing field through the VACNF-particle formation process is illustrated by not only the slope of the curves, but also by the increase in the field it takes to saturate fully the magnetization.

In addition, we see a logical trend in coercivity, H_c (where the curve crosses the y-axis), through the evolution of the alloy systems. The as-deposited films in both systems have very little hysteresis and a low coercivity due to easy domain wall motion. However, once the film dewets into nanoparticles, the hysteresis and coercivity increase due to pinning of the domain wall at the particle boundaries.[266] As a result, reducing the particle size (up until a critical diameter) creates more pinning sites and increases the coercivity ($H_c \propto 1/D$),[266,267] which could explain why we see greater coercivity in the pretreated uniform films with an inherently smaller particles size than the pretreated gradient films (for the relation of initial film thickness to particle size see Section 3.2.3). However, when a nanoparticle is less than the critical diameter it becomes energetically favorable for it to be single domain, and depending on the material, typical domain sizes can be <100 nm. Below this diameter threshold, the coercivity decreases rapidly ($H_c \propto D^6$) with size because in monodomain particles spins rotate their direction coherently and the energy required to rotate the spins relates to the number of spins, i.e. number of atoms in the particle.[266,267] If the carbon growth process creates a portion of monodomain particles, this phenomenon could account for the decreased coercivity of the VACNF particles as opposed to the pretreated films.

In Figure 4.20, the room temperature saturation magnetization as a function of alloy composition is shown for both (a) the as-deposited films and (b) the VACNF nanoparticles. In bulk, Fe is expected to have a magnetization of 1707 emu/cm^3 and Co a magnetization of 1440 emu/cm^3. However, intermediate alloys of Fe-Co should have *higher* magnetizations than either of these metals alone (as shown by the Slater-Pauling curve, shown as a guide in Figure 4.20), with a peak magnetization of 1930 emu/cm^3 at $Fe_{65}Co_{35}$.[269] This behavior is exhibited in the as-deposited film data of Figure 4.20(a). We do note, however, a suppressed magnetization of both of the as-deposited sputtered systems, which is most likely due to overestimation of contributing magnetic film volume due to film density variation/porosity,[270,271] oxidation,[271] and possibly even silicide formation.[213] In fact, the experimental saturation magnetization of Fe thin films sputtered under conditions similar to those in this work was shown to be lower than the theoretical value by as much as 25% due to voids and oxidation.[271] Increasing the energy or

mobility of the depositing atoms by use of substrate heating, substrate bias, or lower pressures would lead to densification of sputtered films to approach bulk values. However, in this work, moderate pressures were used without substrate bias or heating; thus the films may exhibit grain size, surface roughness, and oxidation levels that lessen the density of the film. The effect of surface roughness and oxidation are even more evident in the thinner 15 nm films of the uniform system. Auger analysis in Figure 4.21, performed on a 10 nm pure Fe film sputtered under similar conditions as the Fe-Co films, shows oxygen incorporation at the surface to be as high as 50 at. % at a depth of several nanometers into the film. In addition, Auger peak-shape analysis shows that all of the iron near surface oxidizes, as shown in the sputter depth profile. As such, the ratio of metal oxide compared to magnetically contributing metal therefore would be more pronounced in the thinner films, hence the even lower magnetization values of the as-deposited uniform films.

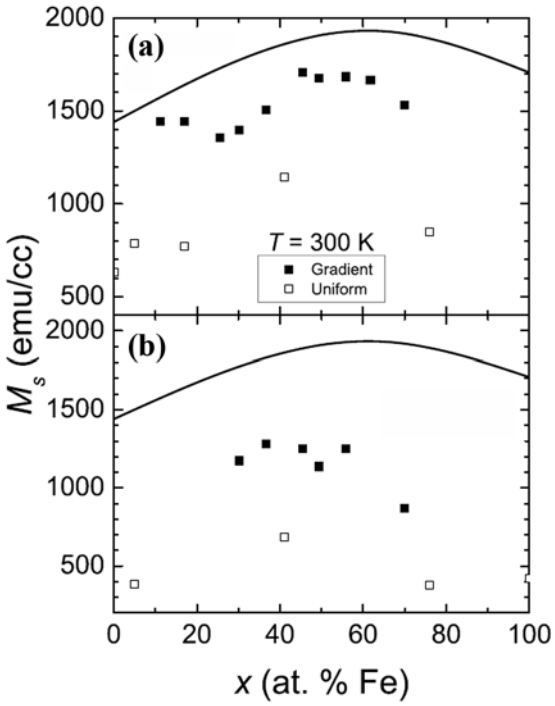

Figure 4.20 Room temperature saturation magnetization as a function of alloy composition in the (a) as-deposited films and (b) VACNFs of both systems. The solid line gives the standard bulk magnetization of Fe-Co alloys (Slater-Pauling curve).

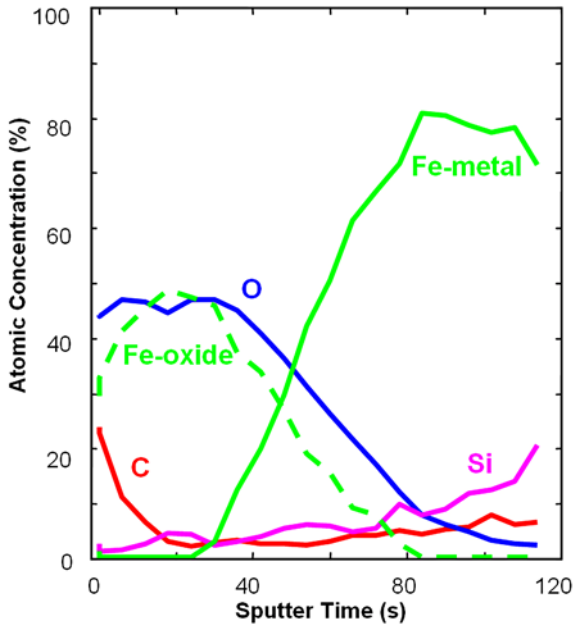

Figure 4.21 Auger depth profile of a 10 nm Fe sputtered film after exposure to ambient conditions.

The "peaked" behavior in saturation magnetization is also reflected in the ferromagnetic catalyst particles encapsulated in the VACNFs, illustrated in Figure 4.20(b), which has also been reported in a comparable Fe-Co system.[265] While the VACNF particles are protected from oxidation (unlike the as-deposited and pretreated samples), the greatly reduced magnetization in the particles is expected from removal of catalyst material by sputtering or etching associated with the plasma synthesis process.[173] In addition, any FM metal that converted to superparamagnetic (SPM) clusters would contribute little to the saturation signal at room temperature, further suppressing the data. It should be noted that significantly depressed saturation magnetizations at room temperature have been commonly reported in the literature for similar systems due to oxidation[55,257,258] or SPM behavior for particles $\leq$ 10 nm in size.[55,223,258-261]

The temperature dependence of the saturation magnetization was also analyzed. In Figure 4.22, the magnetization as a function of temperature *T* in a saturating field is illustrated for a selection of alloys in both the gradient (a,b) and uniform alloy (c,d) systems. Not only, is the high temperature magnetization magnitude much smaller than

anticipated (also seen in Figure 4.20), but there is a large Curie "tail" signified by a sharp upturn in moment at low temperature. The combination of these two features gives strong evidence for a significant fraction of the signal at low temperatures coming from either SPM clusters or paramagnetic ions. In SPM particles the spin directions are randomized by thermal energy, time averaging to zero net moment, therefore decreasing the magnetization measured at higher temperature. As will be seen, the magnetic moment of these species at low temperature is too high to originate from paramagnetic ions.

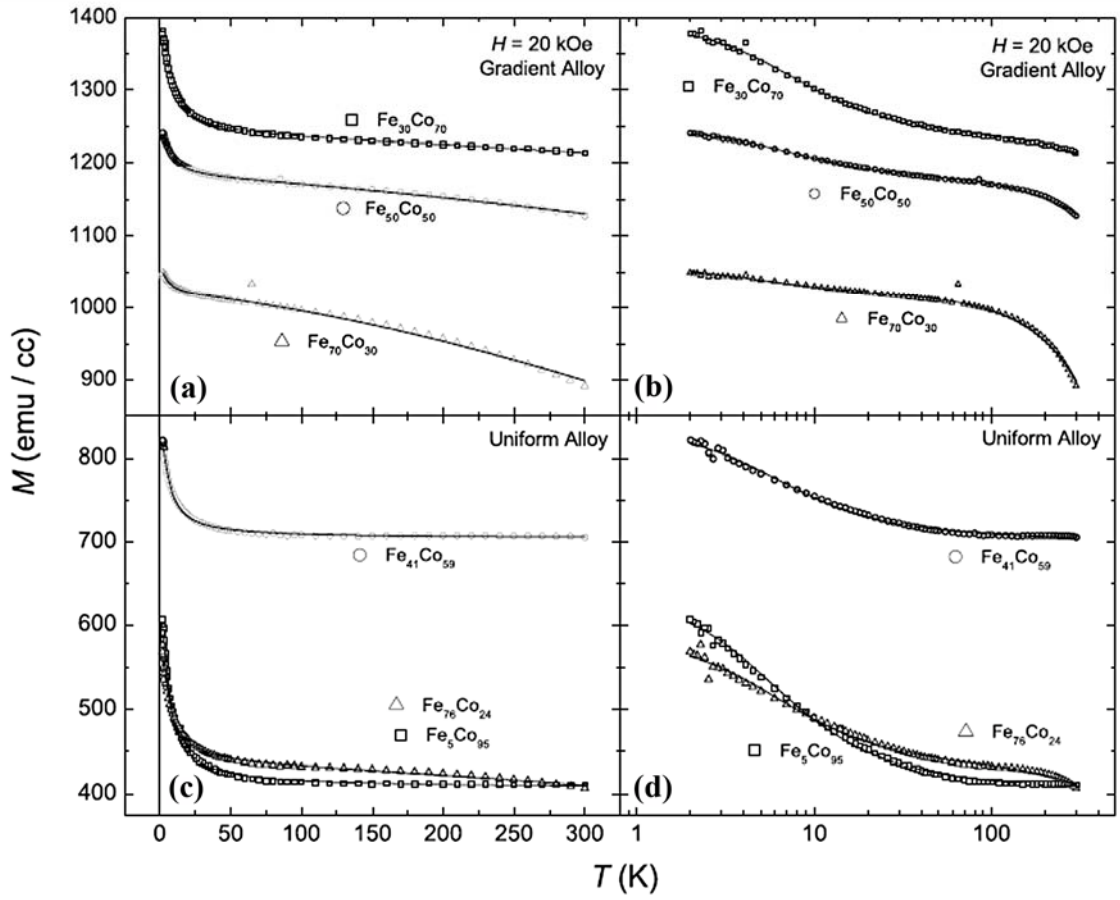

Figure 4.22 High-field magnetization as a function of temperature in the VACNF samples for (a, b) the gradient-alloy and (c, d) uniform-alloy systems at selected compositions. On the left, data are presented on a linear temperature scale. On the right, the same data are presented on a logarithmic temperature scale. The trend lines were fit assuming the combination of a δ-function SPM distribution and spin-wave activated FM metal, while the Si substrate contribution has been removed.

The cluster moment of SPM systems is typically found using measurements of magnetization as a function of field. In this system that contains both FM metal and SPM clusters, the features of such a measurement (such as coercivity or remanence) would mask the response from the SPM clusters. Measurements of magnetization as a function of temperature in saturating fields will enhance our sensitivity to SPM clusters because there will be little temperature dependent behavior from the FM particles. The data in Figure 4.22 were modeled as the combination of large, ferromagnetic nanoparticles and SPM clusters of moment μ_0 to give the trend lines. In this model, contribution from ferromagnetic metal is approximately a vertical offset of the curve but does allow for the activation of spin waves with the form:

$$M_{\mathrm{FM}}(T) = M_{\mathrm{FM}}(0)\left[1 - AT^{3/2}\right], \qquad \text{Eq. (4.1)}$$

where A is the spin wave parameter and $M_{FM}(0)$ is the magnetization of the ferromagnetic metal at zero temperature. The SPM clusters were modeled by the classic Langevin theory of paramagnetism, given by:

$$\begin{aligned} M_{SPM}(\mu_0, H, T) &= M_{SPM}(0) L(\mu_0, H, T) \\ &= M_{\mathrm{SPM}}(0)\left[\coth\left(\frac{\mu_0 H}{k_B T}\right) - \frac{k_B T}{\mu_0 H}\right], \end{aligned} \qquad \text{Eq. (4.2)}$$

where $M_{SPM}(0)$ is the saturation magnetization of the ensemble at zero temperature. By fitting the data of Figure 4.22 with the models in Equations 4.1 and 4.2, we find the parameters listed in Table 2.

Table 2. Fit parameters for each of the high-field $M(T)$ curves.

System	Alloy Ratio (at. % Fe)	μ_0 (μ_B)	$M_{SPM}(0)$ (emu cm^{-3})	$M_{FM}(0)$ (emu cm^{-3})	A (10^{-5} K$^{-3/2}$)
Gradient	30	10.3±0.1	167±0.8	1230±0.3	0.34
	49	9.99±0.2	74±0.6	1180±0.3	0.79
	70	7.31±0.9	40.6±2.2	1020±0.6	2.3
Uniform	5	8.16±0.2	237±2.4	407±0.5	—
	41	8.69±0.2	136±1.5	704±0.3	—
	76	8.67±0.2	158±2.1	432±0.7	1.03

This model assumes that all SPM clusters would have the same moment, which is a rather unrealistic expectation. If $f(\mu)d\mu$ is the number of particles of a given moment μ, distributions of SPM particles can be modeled as a weight function $f(\mu)$ scaling the Langevin function of Equation 4.2:

$$M_{\mathrm{SPM}}(H,T) = \int_0^\infty \mu f(\mu) L(\mu) d\mu \,. \qquad \text{Eq. (4.3)}$$

As a note, a weight function $f(\mu) = \delta(\mu - \mu_0)$ will reproduce Equation 4.2 when properly normalized. Systems of nanoscale magnetic particles are often modeled with a logarithmic-normal distribution,

$$f(\mu) = \frac{1}{\sigma\mu\sqrt{2\pi}} \exp\left[-\frac{\ln^2(\mu/\mu_0)}{2\sigma^2} \right]. \qquad \text{Eq. (4.4)}$$

Simulations of magnetization curves[272,273] with different parameters for the log-normal distribution show that it is difficult to distinguish a weight function with $\sigma \leq 0.1$

from that of the δ-function behavior of Equation 4.2. As the σ parameter increases, $M_{SPM}(T)$ no longer fits the model of Equation 4.2. The simulated data drift above and below the δ-function data, giving only a lower limit on $M_{SPM}(0)$ and an upper limit on effective moment. This is particularly evident on a logarithmic-temperature scale and can be observed in the fits of Figures 4.22(b) and 4.22(d). Furthermore, a logarithmic-normal distribution is not the only weight function that fits these data. A uniform function (*f* constant within a range of moments) also gives features similar to those in Figure 4.22. It is then clear that we have a range of moments contributing to the SPM signal, but details of the distribution cannot be given.

Origins of the SPM signal

In small clusters, Fe and Co would contribute a moment of 3 and 2 μ_B/atom, respectively.[253] If the SPM clusters are assumed to be Fe-Co alloy particles, clusters consisting of as little as four atoms could provide the moments calculated in Table 2. Larger clusters in the nanometer range consisting of metal-rich carbides, oxides or silicides that exhibit SPM are a possible source of this signal. However, metal-rich clusters formed by incorporation of carbon, oxygen, or silicon at the surface of the large catalyst particle will not exhibit this SPM behavior because the magnetization will be pinned by the magnetic anisotropy of the catalyst particle. In other words the SPM behaving particles must be spatially isolated from the larger ferromagnetic catalyst nanoparticles. It is clear from Table 2 that there is a considerable amount of deposited metal that is acting as small SPM particles.

It has been observed that small parts of the catalyst split off during the growth process to remain imbedded in the nanofiber[44,137,207] and that physically etched catalyst material can be redeposited on the substrate or the nanofiber sidewalls. The small bright clusters labeled in Figure 4.17(a) are an indication that we should expect some amount of SPM contribution to the magnetic signal. Particles larger than a few nanometers would likely be indistinguishable from the ferromagnetic behavior of the main catalyst nanoparticles. However, smaller isolated clusters would have sufficient superparamagnetism to contribute a curvature of the magnitude in Figure 4.22. While

this kind of cluster is a plausible explanation, it is surprising that such a significant portion of metal (in some cases up to 37% of the signal) could be involved in clusters a nanometer or less in size. It should also be noted that only roughly 7% of the magnetization signal from the gradient VACNFs compared to roughly 27% of the signal from the uniform VACNFs (at low temperature) is due to SPM. This marked difference could be attributed to the thickness of the initial film and the increased likelihood of creating nanometer-sized clusters with a thinner initial film and smaller catalyst particles. In addition, any SPM material that was removed from the main catalyst particles during the PECVD process would be more statistically significant in the thinner uniform system.

4.4.4 Conclusions

In this work, the magnetic properties of Fe-Co alloys used as catalysts for carbon nanofiber synthesis were studied via SQUID magnetometry. A co-sputtering approach was taken to generate *gradient* and *uniform* composition alloy films of 115 nm and 15 nm thicknesses, respectively. The morphology and magnetic properties of these systems were traced throughout the three main stages of synthesis: as-deposited film, pretreated film, and following VACNF growth (i.e. carbon encapsulation). Chemical analysis revealed that the nanoparticles remained alloyed and the VACNF carbon coating effectively protected the ferromagnetic nanoparticles from oxidation.

The shape of the hysteresis curves at each stage of synthesis demonstrates a change in the anisotropy of the systems with an increasing demagnetizing factor as the films dewet and the particles become encapsulated in freestanding carbon nanostructures. This morphological change in the metal is also reflected in the coercivity or the difficulty of domain wall motion in the samples. Coercivity increases in the dewetted particles due to pinning at the particle boundaries, however as the volume of the particles reduces during fiber growth, some particles become monodomain with lower coercivity.

Analysis of saturation magnetization as a function of alloy concentration exhibits a peak near equiatomic alloy ratios, mimicking what would be expected from the Slater-Pauling curve for this binary alloy system. Magnetizations lower than bulk were

measured in all compositions at each stage and are explained by different reasons. First, the initial volume of the as-deposited films was likely overestimated due to density variation and the magnetization signal was additionally diminished by oxidation of the film surface. Second, pretreated films exhibited a loss of magnetization from the removal of catalyst material over long plasma pretreatment times necessary to dewet the films and also suffered from oxidation after exposure to air. Third, the saturation magnetization of the VACNF particles, in addition to initial volume overestimation and PECVD losses, is depressed further not by oxidation, but rather from the formation of isolated nanometer-sized superparamagnetic clusters. These clusters could be in the form of catalyst material trapped in the CNF cavities or segregation of metal-rich carbides, oxides, or silicides during the PECVD growth process. This conversion of ferromagnetic material is evidenced by temperature-dependent magnetic behavior in the VACNF systems, where the signal from SPM clusters is quite significant. Overall, we see the magnetization losses at all stages exacerbated in the thinner uniform system, where the various factors (volume loss, oxidation, or SPM) become more statistically significant.

4.5 Fe-Ni Alloy System: *$FeNi_3$ Alloy Nanoparticles Encapsulated within Carbon Nanofibers*[‡‡‡]

4.5.1 Introduction

The carbon shell that shapes the catalyst nanoparticle during the co-synthesis process can also be utilized as a capsule, protecting the nanoparticles from coalescence, aggregation, and chemical degradation. The ability to encapsulate various metals within these carbon nanostructures[221] is increasingly recognized as an opportunity to study the physical properties of metals and metallurgical processes at the nanoscale.[87-91] For instance, the understanding of crystallographic order-disorder phenomena of magnetic alloys within nanoparticles is limited,[274-277] as is the understanding of the relationship between the degree of crystallographic order and the magnetic structure and anisotropy. Important questions include: (1) how do order-disorder temperatures depend on nanoparticle composition and size; (2) what are the limits on the degree of long range order that can be attained in nanoparticles of a given size and composition; and (3) how do the magnetic properties depend on the degree of order and the nanoparticle size.

In this collaborative project with researchers at the National Institute of Materials Science in Japan, the objective was to use the carbon nanofiber-catalyst nanoparticle system to examine an aspect of a metallurgical phase diagram on the nanoscale. In particular we elected to investigate the material properties and behavior of bimetallic Fe-Ni nanoparticles encapsulated within carbon nanofibers. This study utilized electron diffraction, dark field imaging, HRTEM and XEDS to characterize the system and attempt to observe the crystallographic order-disorder phase transition of $FeNi_3$. More specifically we examined the morphology, atomic composition, and crystal structure of the system as well as its *in situ* response to elevated temperature.

The $FeNi_3$ phase transition was chosen in particular for two reasons. First, both Fe and Ni are highly active and commonly used catalysts for VACNF synthesis. Second, the order-disorder transition temperature (~517°C for compositions of 25–29% Fe,[278] see

---

[‡‡‡] This section contains unpublished work for future publication as [227].

Appendix for phase diagram) is attainable with *in situ* TEM heating techniques that are limited to < 800°C. At room temperature the ordered phase with *Pm-3m* structure is stable, where Fe occupies the corners of the unit cell and Ni occupies the face centers, as shown in Figure 4.23(b). Above the transition temperature, the atom locations are randomized and the lattice becomes the standard FCC *Fm-3m* structure, as shown in Figure 4.23(c). The location of Fe at the ordered sites in the FCC lattice at temperatures below the transition, allows reflections that were previously kinematically prohibited to now be theoretically permitted (e.g. {110} and {110}, see grey rows in Table 1 of Section 2.2.3). These reflections would have an intensity dependent on the atomic scattering factors of Fe and Ni, as given by Equations 2.7 and 2.8. It was hoped that these superlattice diffraction spots would be detectable for the room temperature ordered phase as shown in the simulated diffraction pattern in Figure 4.23(a).

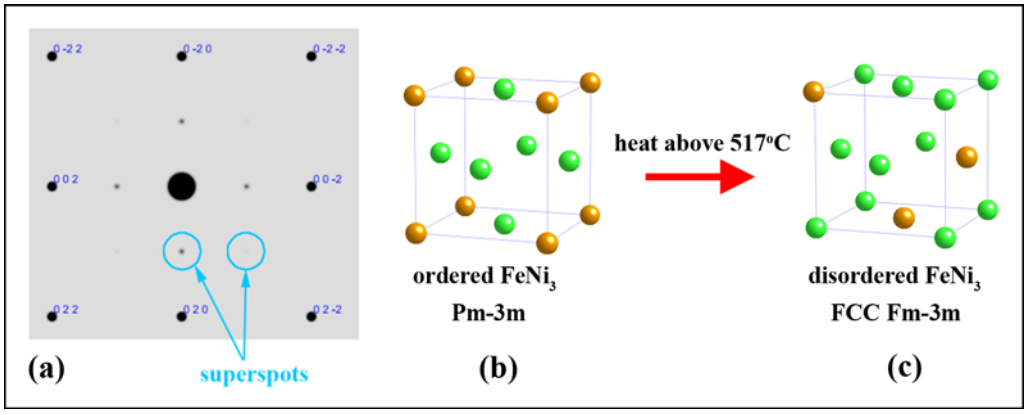

Figure 4.23 Theoretical aspects of the $FeNi_3$ order-disorder transition. (a) Simulated electron diffraction pattern from the <100> zone for ordered $FeNi_3$ showing the appearance of weak superspots. (b) Unit cell of the ordered room temperature phase with *Pm-3m* structure. (c) Unit cell of the disordered high temperature phase with FCC *Fm-3m* structure.

4.5.2 Experimental Methods

A co-sputtering approach from Fe and Ni targets was used to deposit a uniform stoichiometric composition alloy film by rotating the substrate during deposition. In this way, 5 nm of $FeNi_3$ were co-sputtered onto a silicon substrate (with native oxide intact). AES (PHI 680) was performed to verify the stoichiometry of the as-deposited films. Nanoparticles were then formed by dewetting the Fe-Ni thin film in an ammonia atmosphere at 700°C, followed by the initiation of a DC plasma with the immediate addition of acetylene gas flow for 10 minutes. This catalytic PECVD process produced VACNFs with the alloyed nanoparticle catalysts located at their tips. After a 10-minute growth, the samples were slow-cooled in NH_3 at the following rate: from 700–540°C decreased 20° every 10 minutes, from 540–400°C decreased 10° every 10 minutes, from 400–300°C decreased 20° every 10 minutes, and finally the sample was left at 300°C overnight and then allowed equilibrate to room temperature. This slow-cool treatment was intended to allow the FCC lattice time to order upon cooling. Following growth, the nanofiber/nanoparticle system was harvested from the substrate, statically transferred to lacey-carbon coated TEM grids, and characterized by dark field imaging, SAD (using charge image plates), HRTEM (with digital capture), and XEDS (JEOL JEM-3100FEF at 300 kV). *In situ* annealing of the sample was performed on a Mo TEM grid mounted on a single-tilt heated stage with temperature measurement by a Pt-Pt/Rh thermocouple.

4.5.3 Results and Discussion

The films prepared by co-sputtering Fe and Ni films onto the silicon substrate contained ~23 at. % Fe as measured by AES. Figure 4.24(a) indicates that the $FeNi_3$ film functioned well as a catalyst for carbon nanofiber synthesis. The 5-nm-thick initial metal film yielded on average 37 nm diameter particles at the nanofiber tips. Further inspection by TEM revealed the particles had an oblong shape with a tapered interface with the nanofiber. The main catalyst particle stoichiometry measured by XEDS was on average $Fe_{29}Ni_{71}$ [Figure 4.24(e)], with SAD from 20 particles indicative of the FCC phase (*Fm-*

3m, a = 3.552 Å).[279] Additionally, a small particle was observed at the "throat" of the fiber (base of the main catalyst particle) in about half of the nanofibers, as shown in BF images (b,c) and dark field (d). SAD of the two particles reveals an epitaxial relationship with both crystals oriented to the [112] zone. Indexing of the large *d*-spacing superlattice (a = 8.396 Å) corresponded to the Fe_3O_4 *Fd-3m* phase, which is in agreement with the XEDS composition of the throat particle. We believe that the throat particle is a result of Fe segregation occurring at both the surface of the initial film and the substrate interface to form an iron oxide. In fact, the oxide Fe_3O_4 is the primary phase found on surface of Fe thin films.[271] While the ammonia environment likely reduced the surface oxide layer, the native oxide layer under the film was not reduced and reacted with the Fe in some cases to form an epitaxial oxide particle at the base of the catalyst. Often an iron oxide "cap" was also observed on the exterior surface of the main particle which may be the result of post-synthesis oxidation. Cooling in an ammonia atmosphere could have removed some of the protective surface carbon making the surface of the catalyst susceptible to oxidation once taken out of the growth chamber.

Evidence of superstructure, representative of the ordered $FeNi_3$ room temperature phase, was either non-existent (meaning the atoms in the nanoparticles were unable to stoichiometrically order in the crystal) or perhaps was unobservable by our methods. To our dismay, the almost identical scattering factors of Ni and Fe coupled with the small volume of material, makes the ordered phase very difficult to identify by electron diffraction and the few reported observations have been by XRD.[278] Furthermore, the position of the broad graphite (200) arcs at ~3.36 Å[201] would likely overlap with the brightest possible superlattice spot at (100) 3.55 Å.

Even though we did not observe superstructure in the room temperature phase we still decided to continue with the planned *in situ* heating experiment. The heated stage only allowed for tilting in one direction, so a nanoparticle had to be located that was well-supported, close to a major zone axis, and oriented along the stage tilt direction in case thermal drift or beam interactions required some minor adjustments of the tilt. In addition, the stage would heat the entire sample so we had one chance to perform the experiment before altering the entire sample. After much searching, a suitable candidate was found, pictured in Figure 4.25. This particle was ~40 nm in diameter and an oxide

throat particle can be clearly seen in the DF images. XEDS of main catalyst particle measured an alloy of $Fe_{27}Ni_{73}$. The progression of increased temperature is shown from left to right, with selected BF, DF, and SAD images taken at 20°C, 460°C, 600°C, 800°C and after the heater was turned off and the sample allowed equilibrated to room temperature, which resulted in virtually quenching the sample in a matter of minutes.

Inspection of the SAD results in Figure 4.25 shows that temperatures of to 800˚C did not induce bulk melting or significantly change the crystal structure of the encapsulated Fe-Ni nanoparticle. However it was noticed in the BF images that upon heating above ~180°C, a skin forms around surface of particle (beneath the carbon layer), which appears in the DF image at 460°C to contain particulate clusters. However, this skin curiously seems to disappear again with further heating above 600°C. Other observations include the formation of a void at the interface were the intersection of the main particle, oxide particle, and CNF. Heating also smoothes catalyst particle step edges and reduces size of oxide particle by shifting grain boundary, which could be the cause of the void formation at this interface. The shift in the grain boundary remained after quenching. The intensity of the graphite arcs in the SAD also increased after quenching, likely due to the annealing of defects and improved graphitic order.

Unfortunately, the diffraction patterns were captured on charge plates that had to be scanned and analyzed after completing the *in situ* experiment. Therefore, proper indexing of the pattern could not be done during the experiment. Upon inspection of the room temperature diffraction pattern, what was assumed to be a [110] zone pattern is actually quite distorted. To be sure that our calibration is correct, the graphitic (200) arcs at ~3.4 Å can be used as a sort of internal calibration check.[280] While the spot at 1.77 Å corresponds nicely to the (200) reflection, the other two spots are supposed to be (111) reflections with a *d*-pacing of 2.05 Å, but instead have dimensions with one significantly larger (tensile) and one smaller (compression) than this value.[279] Furthermore, the tensile (111) direction precisely coincides with the growth direction of the fiber. Similar diffraction patterns were taken for two other particles with exactly the same orientation of tension along the axis of the fiber. This preliminary evidence leads us to believe that some of the particles exhibit unusually high strains of 5-10% in the direction of growth.

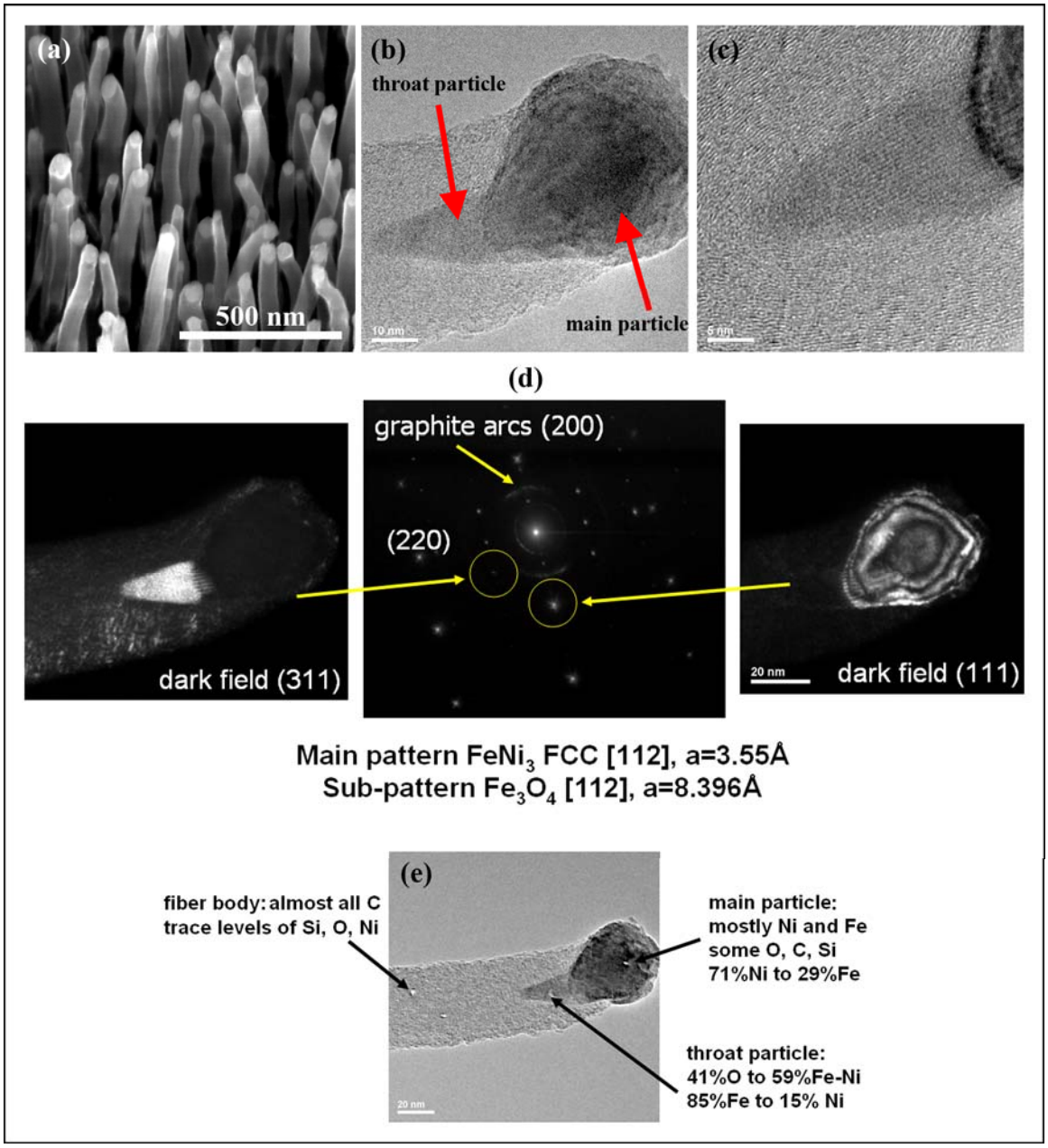

Figure 4.24 Characterization of $FeNi_3$ nanoparticles at the tips of VACNFs. (a) SEM image at 30° tilt (b) Representative TEM image illustrating the main particle and particle at the throat of the VACNF. (c) HRTEM image of the throat area in (b). (d) SAD pattern and corresponding dark field images from the (311) sub-pattern reflection on left and the (111) main pattern reflection on right. (e) TEM image after focused probe XEDS from the three labeled regions.

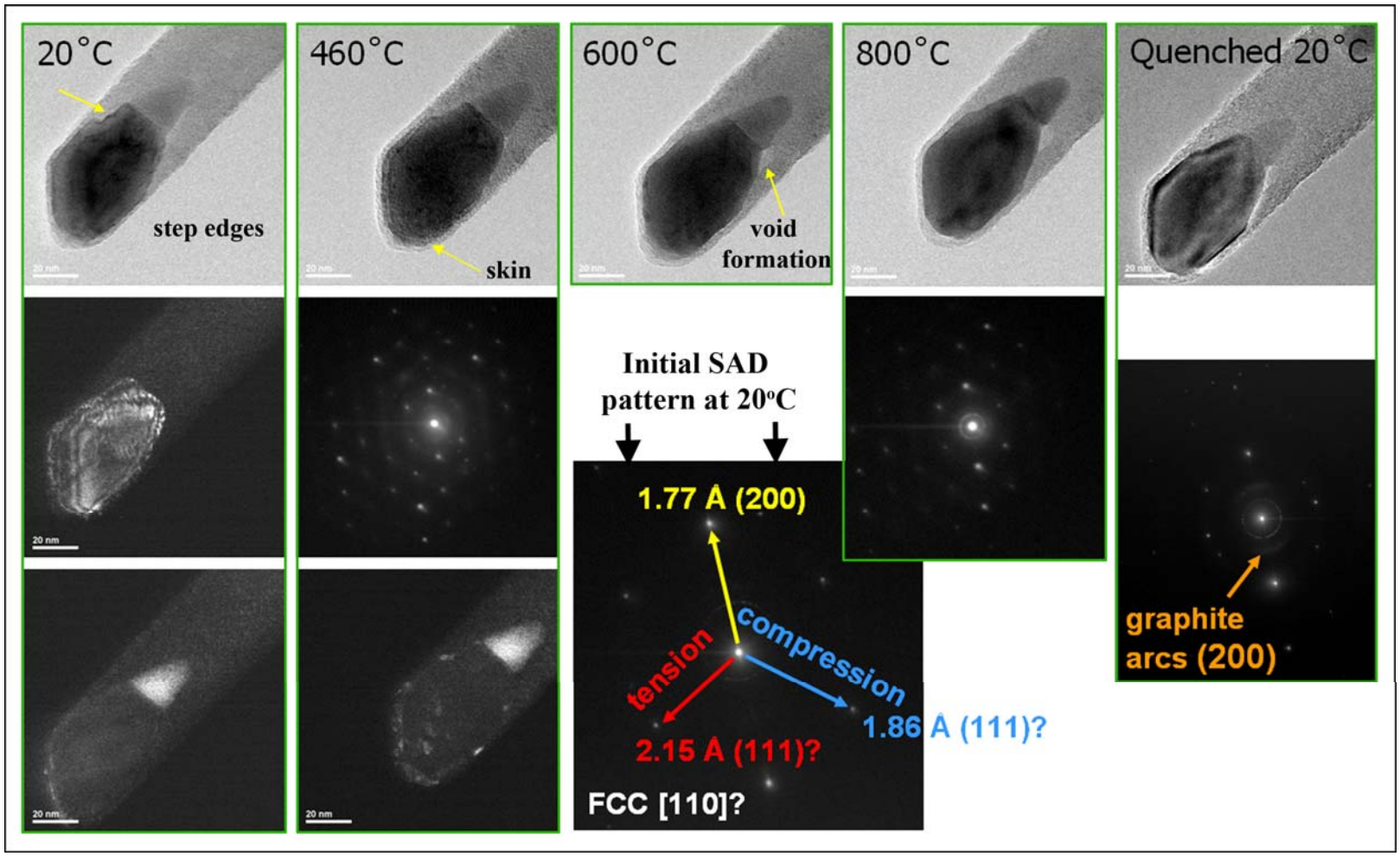

Figure 4.25 *In situ* TEM heating experiment. Images and diffraction patterns show the progression of temperature from left to right, with the initial room temperature SAD pattern enlarged at center.

4.5.4 Conclusions

This work characterized and probed the behavior of the encapsulated metal alloy nanoparticle system in a confined nanoscale state. More specifically, using TEM techniques we looked at the morphology, atomic composition, and crystal structure of the system as well as the *in situ* response of the system to thermal heating. In conclusion, we found that $FeNi_3$ catalysts work well for carbon nanofiber synthesis with 5 nm thick initial films yielding ~37 nm diameter particles. The metal remains alloyed $Fe_{29}Ni_{71}$, a composition which should be exhibit the ordered *Pm-3m* phase at room temperature. However, we only observed the standard FCC (*Fm-3m*) structure after CNF synthesis. Evidence of superlattice from the ordered $FeNi_3$ phase was either non-existent (meaning the atoms in the nanoparticles were unable to stoichiometrically order in the crystal at room temperature) or was more likely unobservable by our methods. In addition, commonly an Fe_3O_4 particle formed at the throat of the fiber (base of the main catalyst particle), which is likely due oxygen transfer at the initial substrate-film interface. In addition, heating up to 800˚C did not induce bulk melting or significantly change the crystal structure of the $FeNi_3$ nanoparticles. Lastly, it is believed that several asymmetric diffraction patterns can be attributed to a large tensile strain along the growth direction and should be confirmed by further investigation.

4.6 Additional Commentary about Catalysts

The state of the catalyst and its ability to catalyze graphitic layers, similar to the VLS mechanism (Section 2.1.2), is dependent upon eutectics and solubilities, which are given in Table 3 at the end of this section. We have seen in both this chapter and Chapter 3 that each catalyst requires different optimal growth conditions and results in diverse nanofiber morphologies, internal structures, and growth rates. Take iron for instance: α-Fe has very little carbon solubility—0.1 at. %—until it transitions to γ-iron at temperatures close to 912°C (possibly lower for nanoparticle sizes > 20 nm).[17] However, once Fe transitions to the γ-phase with FCC structure, then it can dissolve up to 9 at. % carbon—three times more than Ni and twice that of Co. Conceivably, this could be why Fe is the catalyst of choice for nanotube growth. Co has a situation similar to Fe, with practically no solubility of carbon in the HCP ε-phase configuration, but when it transforms (at significantly lower temperatures than Fe, 422°C) to the FCC α-phase, suddenly it acquires a solubility of 4.2 at. %. Ni on the other hand, has FCC structure at all temperatures below T_m but maxes out at a solubility of 2.7% carbon, much lower than the high-temperature solubilities of Fe and Co. However, the fact that Ni *can* dissolve carbon at low temperatures explains why Ni is such a favored versatile catalyst for CNF growth. Lastly, let us consider the situation of Cu, which is kind of odd since it has such a low T_m. The addition of C to Cu actually increases the eutectic above T_m to form a peritectic—where the L + (C) → (Cu). While Cu shares the FCC structure that appears to be so conducive to dissolving C and in many other ways is similar to Ni, for some reason it does not dissolve carbon to any practical extent.

Retrospectively, we have seen these melting temperature/solubility issues manifest in several ways in our experiments. One of which is the catalytic activity of Cu and Cu alloys. In small doses, it appears the Cu can increase the activity of Ni catalyst by causing fractionation to occur (Figures 4.3). This could be due to the fact that it lowers the melting point of Ni, yet even in the liquid form does not dissolve carbon well so it causes frequent dissolution of carbon, possibly splitting the particle in doing so. The non-catalytic activity of C is demonstrated in Figure 4.5 where Cu segregates and is left

behind at the base of the nanostructure while what Ni is left continues on to catalyze growth. This point is further proven in Section 4.3 where pure Cu films fail to catalyze *any* carbon.

A second example is the troublesome growth conditions for Fe-rich catalysts. Not only is it difficult to dewet iron films thicker than ~20 nm because of its relatively higher T_m (Figure 4.14), but favorable conditions for CNF growth also occur at higher temperatures, where Fe likely transitions into the γ-phase or possibly even Fe_3C. Figure 4.15 illustrates this dichotomy in favorable growth conditions that occurs for Co and Fe. While cobalt is content to catalyze in a lower temperature, lower energy process, Fe-rich catalysts from films of the same thickness require a higher energy process for substantial carbon conversion. In addition, without the proper temperature for substantial carbon dissolution in the catalyst material, not only will CNF growth be incredibly slow and disordered but the top surface of the catalyst will likely build up with undissolved amorphous carbon, further deactivating the catalyst (see TEM image in Figure 4.17(c)). However, when the conditions are changed to a higher temperature and higher energy process (results not shown here), the tables turn to favor Fe catalysts and bamboo-type CNFs are readily formed. Lastly, if there is not enough carbon dissolved in the catalyst during growth to form a protective cap upon cooling or conditions are etching enough to remove any amorphous carbon from the top of the catalyst, then inevitably the surface of the catalyst will oxidize, especially in the case of Fe-containing alloys.

Table 3. Physical properties of selected transition metals.

Element	Atomic Number	Crystal Structure	Lattice constant (Å)	Melting Point (°C)	Eutectic with C (°C)	Maximum Solubility of C (at. %)
Fe	26	<912°C BCC(α)	2.866(α)[281]	1538	1153(γ)	~0.1(α)[215]
		>912°C FCC(γ)	3.647(γ)[282]			9.06(γ)[215]
Co	27	<422°C HCP(ε)	2.507, 2.507, 4.068(ε)[283]	1495	1320(α)	~0(ε)[235]
		>422°C FCC(α)	3.566(α)[284]			4.2(α)[235]
Ni	28	FCC	3.524[134]	1455	1326.5	2.7[235]
Cu	29	FCC	3.615[134]	1085	~1100 (peritectic)	<0.04[235]

5. Electron-beam-induced Tungsten Nanowires: *Single-crystal nanowires grown via electron-beam-induced deposition*[§§§]

5.1 Introduction

The realization that "smaller is different" and the promise of the nanoscience and nanotechnology revolution have encouraged the development and investigation of techniques capable of manipulating materials on the near-atomic scale. Several nanofabrication methods utilize charged particle beams to direct the assembly or removal of materials. Advancements in magnetic and electrostatic lens systems have enabled sub-nanometer probing, making charged particle beams ideal for direct-write nanoscale materials synthesis. One such process, electron-beam-induced deposition (EBID),[92] is capable of synthesizing complex three-dimensional structures and has recently realized 1 nm resolution.[286]

In the EBID process (described further in Section 2.1.6), a gas precursor adsorbs to the surface and is decomposed into volatile and nonvolatile components by electron bombardment. Ideally, the nonvolatile component remains "deposited" on the substrate, while the volatile byproducts are desorbed from the surface and pumped from the vacuum chamber. EBID was first observed in the context of carbon contamination or "staining" during electron microscopy as a result of residual hydrocarbon species.[122,123] Years later, the intentional introduction of organometallic precursor vapors at high partial pressures by Baker and Morris resulted in tin and lead deposits whose high electrical resistivity led them to believe that carbon incorporation from background gases and/or the organic component of the precursor was considerable.[124] EBID work following the Baker and Morris effort continues to demonstrate the deposits to be severely contaminated with nonvolatile byproducts.

[§§§] This section is based on work from [285] and contains lightly revised passages and figures.

Nevertheless, the EBID process has been successful in synthesizing nanoscale elements for field emission devices[93-96] and advanced scanning probes,[97,98] has been used for nanoscale welds and electrical contacts,[94,287] and has been commercialized for nanoscale repair of advanced lithography masks[99] and integrated circuits. However, its full impact as a more universal nanoscale synthesis approach has not yet been realized because of the inability to produce high purity and high crystallinity deposits. Controlling the quality of the deposit is a complex process that is a function of the precursor, beam current, beam energy, scanning parameters, partial pressures of gas species, etc., as well secondary effects such as beam-induced heating[288] and electron stimulated desorption. These considerations are crucial as EBID features approach nanometer resolution, where the properties and uniformity of the deposited material become increasingly important. Consequently, an emphasis on characterization and control/manipulation of EBID materials is of great importance and several recent publications have investigated these issues for variety of deposition precursors (for a review see Randolph *et al.*[92]).

Perentes *et al.* compared the purity of deposits from three different organosilane precursors and found that the use of an oxidizing gas in addition to the precursor practically eliminated carbon contamination of EBID SiO_2.[289] Mølhave *et al*. have investigated numerous beam and chamber conditions and their effects on the properties of as-deposited EBID gold deposits.[290] Their results indicated that the use of a carrier or background gas could influence the structure and morphology of the gold nanorod deposits. A cored structure consisting of three distinct layers was observed: a central core, an intermediate "crust" layer, and an outer contamination layer. When a nitrogen carrier gas was used, the structures were composed of gold nanocrystals dispersed in an amorphous carbon matrix and no central core was deposited, but when water vapor was used, a central core consisting of dense, pure, polycrystalline gold was observed. Additionally, Weber *et al*. showed that gold structures deposited at 20 keV were completely amorphous when a current of less than 20 pA was used but the gold content increased with increasing substrate temperature.[291] The properties of EBID cobalt[292,293] and copper[294] have been investigated by Utke *et al*. In these studies, it was shown that the metal content of the deposit increased with increasing beam current in the range of 20

pA to 3 μA with a beam energy of 25 keV. Transmission electron microscopy (TEM) analysis of the deposited material revealed that metallic crystallites were dispersed in an amorphous matrix. At higher beam currents, a structural transition to a polycrystalline and corrugated structure was observed; the improvement in crystallinity was attributed to beam-induced heating and subsequent thermal decomposition of the precursor.

Tungsten is one of the most studied EBID materials with numerous publications regarding both modeling[288] and experimental[295] aspects, yet few have focused on characterization of the deposited material with regard to processing conditions. It is well known that tungsten hexacarbonyl ($W(CO)_6$)[295-298] and tungsten hexafluoride (WF_6)[96,299] precursors can produce tungsten-containing deposits during EBID processing. For $W(CO)_6$ however, the deposits often incorporate high levels of impurities, namely carbon and oxygen.[295] Tungsten nanorods, deposited in a scanning transmission electron microscope (STEM) using the $W(CO)_6$ precursor and a 200 keV beam, have been shown to be composed of a mixture of multiphase amorphous and nanocrystalline grains.[101] The nanocrystals ranged from 1.5 to 2.0 nm in size and were comprised of the equilibrium phases: bcc W, WC, WO_2, and WO_3 as determined by electron diffraction. In later work, these tungsten nanostructures were post-treated with 1 MeV electrons for 100 minutes.[300] Following this treatment, the amorphous regions were observed to transform into nanocrystalline, bcc tungsten. The effect of beam energy on the structure of tungsten dendrites was further investigated by varying the accelerating voltage from 400kV to 1MV during deposition.[301] The crystallinity of the as-deposited structures (consisting of bcc tungsten nanocrystals embedded in an amorphous matrix containing carbon and oxygen) was found to improve for higher beam energies. This effect has been attributed to enhanced tungsten atom mobility due to high-energy irradiation, thus allowing for rearrangement and crystallization. Others researchers have shown that crystallization of 100 keV EBID tungsten can also be facilitated by 800°C post-deposition anneal.[302]

The less commonly used tungsten hexafluoride precursor gas has the potential for producing high purity deposits presumably because it does not contain carbon and oxygen. Early chemical analysis by Matsui *et al.* indicated that deposition from WF_6 yielded tungsten deposits with a purity of 85%, with the balance being oxygen and fluorine.[299] In their process, a WF_6 adlayer irradiated at high energy, high current, and

low chamber pressures (10^{-8} Torr) formed 5 nm β-W clusters, as determined *in situ* by HRTEM.

In this work we have investigated the structure and composition of EBID tungsten nanostructures, namely nanowires, whose growth is depicted in Figure 5.1. These nanostructures are deposited from a WF_6 precursor under the various conditions listed in Table 4. We found that while beam energy, current, and precursor pressure had subtle effects on the nanowire structure, the most influential effect was the scan condition. High-resolution transmission electron microscopy, energy-dispersive x-ray spectroscopy, and Auger electron spectroscopy were employed to determine the effects of scan conditions on the deposit quality. Detailed electron diffraction data are also reported and the conflicting literature on the A15 crystal structure of β-W and W_3X (X=O, C, Si) ordered phases is discussed in light of the results in this work. Evidence is presented that indicates rapid, two-dimensional scanning results in high-purity (~90 at. %), polycrystalline tungsten deposits. In contrast, slow one-dimensional lateral scanning produces high purity (~98 at. %), (100)-textured β-W nanowire cores surrounded by a WO_3 layer. And lastly, stationary vertical growth can lead to [100]-oriented, single-crystal W_3O nanowires. We also correlate how the growth kinetics, mainly dependant on the scan mode, affect the resultant nanowire structure and composition.

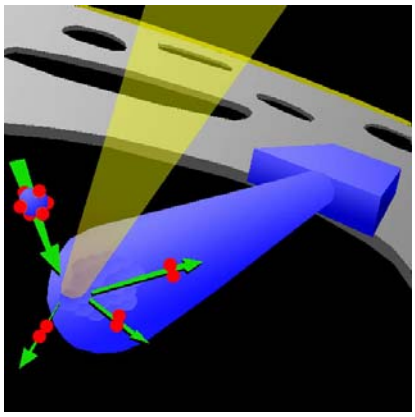

Figure 5.1 Illustration of nanowire directed assembly by electron-beam-induced deposition from a WF_6 precursor.[****]

[****] Unpublished image courtesy of Jason Fowlkes.

5.2 Experimental Methods

The tungsten nanowires were deposited in a modified Hitachi S-4300 SE/N variable pressure scanning electron microscope (SEM). The SEM was fitted with a vapor injection system[295] for localized precursor delivery via hypodermic needle. Approximations of our vapor injection system based on analysis of similar systems[303] and capillary flow data[304] suggest that the localized growth pressure is on the order of 10 to 100 times higher than the chamber pressure. Tungsten hexafluoride was introduced to the system during deposition and flow/pressure was controlled by means of an external ultra-high vacuum leak valve.

Tungsten nanostructures were deposited with several different scanning and stationary SEM beam positioning modes as shown in Table 4. Two-dimensional "box" structures [Figure 5.2(a)] intended for AES depth-profiling were deposited on a silicon substrate coated with an amorphous silicon thin film using the two-dimensional area analysis mode of the SEM. A frame rate of ~32 frames per second was used and the deposit thickness was proportional to the deposition time. The first area deposited consisted of a 2.5 μm square (deposit #11, Table 4) that was scanned for 22 min, while the second square region (deposit #12, Table 4) was only 1.25 μm on a side and scanned for 12 minutes. Common deposition conditions to both box scans were as follows: no objective aperture, 20 keV beam energy, 2.6 nA beam current, 8 mPa WF_6 chamber pressure, magnification of 1.2×10^4, working distance of 12 mm, and a substrate to needle spacing of 1.7 mm. The frame rate was constant for both scans, so decreasing the scanned area effectively increased the dwell time per unit area. Based on the SEM conditions, the estimated pixel size was ~15.6 nm with the large box being 160 × 160 px and the small box being 80 × 80 px. Thus, the average total irradiated time per pixel for the large box was 0.05 s and for the small box 0.11 s.

Table 4. Parameters for tungsten EBID deposition.

Deposit #	Beam Energy (keV)	Beam Current (pA)	Chamber Pressure (mPa)	SEM Scan Mode	Scan Rate (μm/min)
1	30	200	7.3	line	0.55
2	30	72	7.3	line	0.55
3	30	5500	7.3	line	0.55
4	30	5500	3.7	line	0.55
5	30	5500	1.7	line	0.28
6	15	72	7.3	line	0.55
7	3	72	7.3	line	0.55
8	20	41	7.0	line	1.20
9	20	41	7.0	line	0.55
10	20	41	7.0	point	0.23 (vertical)
11	20	2600	8.0	area	18.72
12	20	2600	8.0	area	8.51

The two-dimensional box scans were characterized by scanning electron microscopy (Hitachi S-4700) and by SAM (PHI 680). A brief sputter-clean (30 seconds at ~2 nm/minute sputter rate) was performed prior to analysis to reduce the amount of surface contamination. Following AES mapping and point analysis, a sputter depth profile was performed to a depth about 225 nm.

One-dimensional tungsten nanowire growth from the WF_6 precursor is illustrated in Figure 5.1. Laterally-grown wires were deposited using the linear scan mode of the SEM, 5.2(b), to produce in-plane structures for transmission electron microscopy (TEM) analysis. This lateral growth method involves a slow raster of the beam over an edge, which has previously been reported.[294,305] In this work, nine wires (nanowires #1 – 9, Table 4) under varying conditions were grown laterally over hole edges in a lacey-

carbon-film-coated copper TEM grid. In addition, a vertically grown tungsten wire (nanowire #10, Table 4) was deposited in point analysis mode onto a TEM grid with deposition conditions similar to those previously reported for the synthesis of field emitter cathodes.[96] To produce such a wire compatible with the TEM imaging, first a large tungsten box-like platform was deposited on the surface of the carbon film at the edge of a hole [Figure 5.2(a)]. Then the SEM stage was tilted to a high angle (~60°) such that the side of the tungsten platform provided enough surface area for point mode nanowire deposition [Figure 5.2(c)]. Constant deposition conditions for all nanowire deposits were as follows: 30 μm diameter objective aperture, working distance of 11 mm, and a substrate to needle spacing of 3.4 mm.

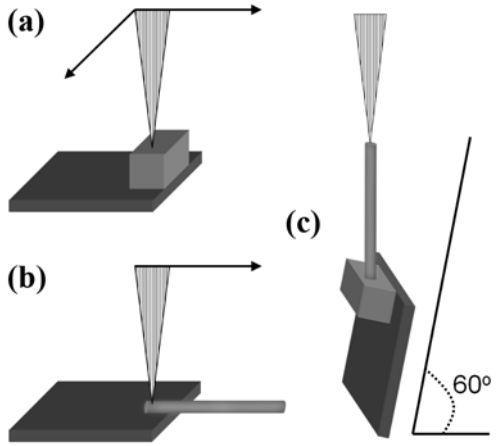

Figure 5.2 Depiction of scan modes used to deposit EBID tungsten boxes and nanowires. (a) Boxes are deposited by operating the SEM in area analysis mode, in which the beam is rastered in two dimensions. (b) Lateral nanowires are deposited by scanning slowly over an edge film and the wire grows at a rate governed by the scan rate. (c) Vertical nanowires are prepared by first depositing a box platform as in (a), followed by tilting the specimen to ~60° and depositing in point mode on the side of the box platform.

The EBID nanowire samples deposited directly onto TEM grids were analyzed by 200 kV STEM and XEDS (Hitachi HD-2000), 200 kV electron diffraction and HRTEM (Hitachi HF-2000), as well as AES (PHI 680). STEM imaging and XEDS analysis were problematic due to carbon staining with the intense probe. In addition, the XEDS data was not considered quantitative due to a large carbon signal originating from the surrounding lacey carbon film. Nevertheless, oxygen, fluorine and tungsten levels were qualitatively compared. Following STEM and TEM analysis, the samples were briefly sputter-cleaned and their composition characterized by SAM; however, the highly directional sputter-cleaning did not sufficiently remove the carbon contamination along length of the EBID wires, and instead damaged the carbon support film and the wires, causing them to bend and distort. For this reason, linear Auger scans were taken across the clean bases of some of the nanowires.

5.3 Chemical Analysis of Box Deposits

In order to observe the effect of the total area scanned per unit time on deposit purity, compositional analysis of EBID tungsten was performed on two box deposits that were grown by two-dimensional, area analysis scans as illustrated by Figure 2(a). As detailed in the *Experimental*, the parameters for both deposits were the same except the dwell time per unit area was essentially two times higher for the smaller box. The electron micrograph in Figure 3(a) shows a top-down view of the larger box feature as-deposited (Table 4, deposit #11). AES point composition and mapping reveal that there is a significant amount of tungsten deposited in the areas surrounding the exposed box area, with the tungsten fraction decreasing with distance from the deposit. This is likely due to deposition induced by backscattered and SE_2 electrons. The high level of carbon evident in point 2 of Figure 3(a) is likely due to competitive carbon staining in the electron interaction region. Furthermore, it appears that the sputter clean did not remove all the surface oxygen and carbon, which varies radially from the box center. The primary deposit is mostly W, with a ~ 1 μm peripheral area surrounding the box that has

high levels of O and W, surrounded by outer radii of C and W, O and C, mainly C, and finally O and Si.

The post-sputter-depth-profile image and elemental map of the smaller deposit (#12), as shown in Figure 5.3(b), reveal that preferential sputtering occurs along what appear to be tungsten grain boundaries while the surrounding amorphous silicon film sputtered uniformly. This nonuniformity of the deposit is perhaps due to polycrystalline structure. The sputter depth profiles of the large and small box deposits in Figure 5.3(c) and 5.3(d) respectively, indicate high purity deposits of up to 88 at. % W with slight differences in composition. The larger box, with a shorter dwell time per area, has about 5% C and O throughout the thickness of the deposit with lower Si levels. On the other hand, the smaller box has C and O levels only detected at the surface with higher Si levels throughout. Both samples reach 50% Si levels by about 175 nm deep, suggesting the vertical growth rates are comparable. There are two possibilities conjectured for the origin of the silicon signal observed throughout the deposit: (1) during characterization, preferential sputtering occurs along grain boundaries or amorphous regions which expose the underlying Si substrate, (2) the fluorine byproduct from the WF_6 reacts and forms volatile SiF_x species during growth, which subsequently are incorporated in the deposited films.

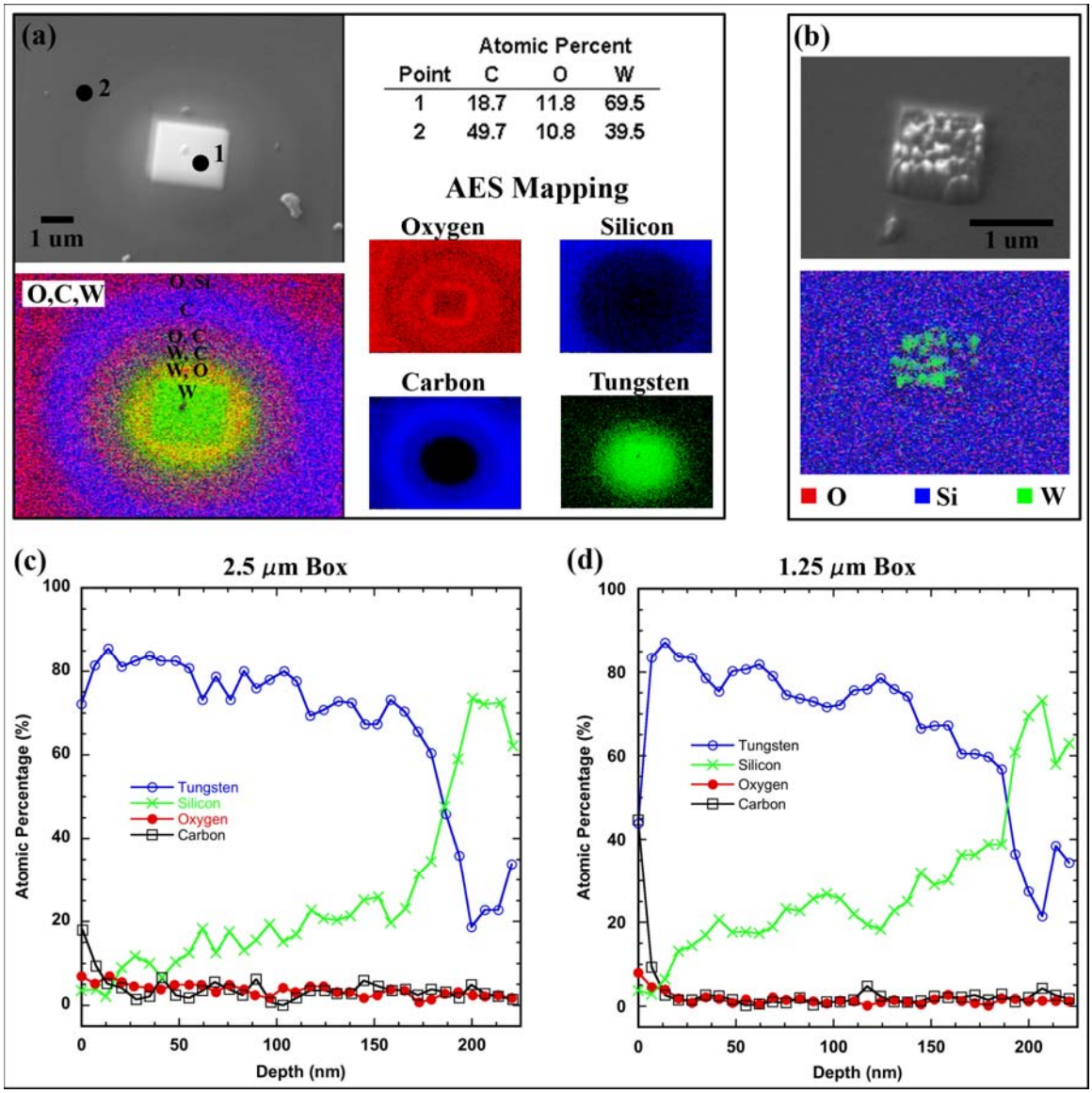

Figure 5.3 AES results from area analysis mode EBID tungsten deposition. (a) AES point composition and elemental mapping of the 2.5 μm box deposit #11 prior to sputter profiling (combined map is of O, C, and W only). (b) SEM image and corresponding AES elemental map of the 1.25 μm box deposit #12 following sputter depth profiling. (c,d) depth profiles taken for the 2.5 μm box and the 1.25 μm box, respectively.

5.4 Nanowire Structure and Composition Determination

All of the EBID nanowires exhibited the same cored structure, an example of which is illustrated in Figure 5.4. The tungsten-rich core of the EBID wire is highly diffracting and dense, thus appearing dark in bright field TEM [Figure 5.4(b)] and light in *Z*-contrast STEM [Figure 5.4(c)]. We note several trends throughout the deposition parameter study. Overall, the core width was observed to correlate with the primary beam diameter. Higher current results in a larger diameter wire core, which is consistent with increased spot size of the primary beam. An analogous trend is noticed with respect to beam energy, where increased beam energy yields a smaller spot size and thereby a smaller core diameter. In addition, a secondary layer of varying thickness can often be seen [labeled in Figure 5.4(b)], similar to the "crust" observed by Mølhave *et al.* on gold deposits.[290] This secondary layer has much lower *Z*-contrast than the tungsten core and is virtually unseen in the *Z*-contrast image [Figure 5.4(c)], however it seems to have more contrast than the amorphous carbon layer [Figure 5.4(b)]. The secondary layer, as described further below, is a tungsten-oxide layer that likely forms either *in situ* from residual oxygen species in the chamber or subsequently from exposure to air. The outermost layer observed is a contamination layer, also noted by Mølhave *et al.*,[290] that is due to carbon staining during characterization and is not a result of the original EBID process. Contamination was difficult to avoid in the high-energy, focused probe STEM with an abundance of adsorbed species on the sample's surface, which presented challenges for subsequent chemical analysis of the nanowires.

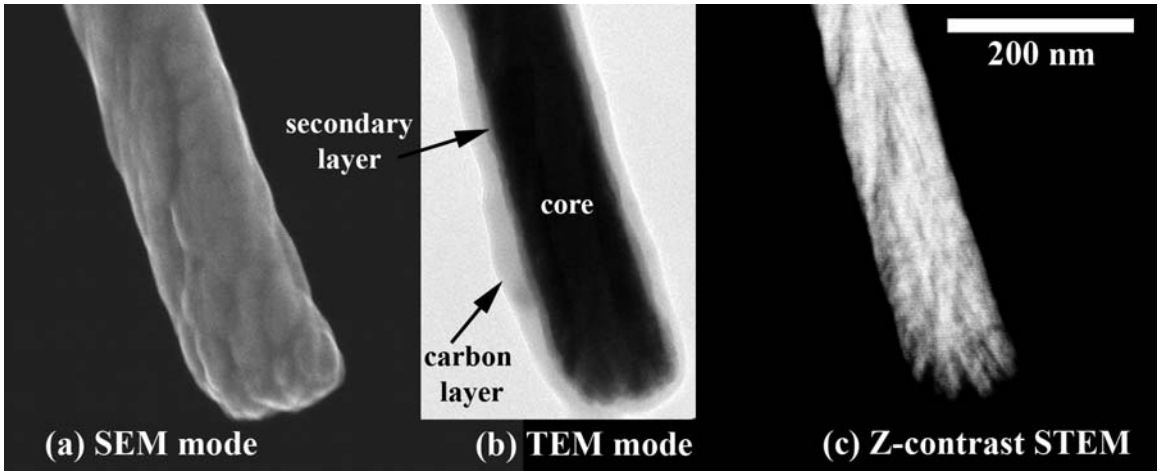

Figure 5.4 STEM micrographs of EBID nanowire #4 (all at the same scale): (a) secondary electron image showing surface roughness; (b) transmitted electron image showing three distinct layers of different contrast due to mass, thickness, and diffraction differences; (c) *Z*-contrast image showing an internal core of high *Z* material with density variation.

On closer examination of nanowire #4 displayed in Figure 5.4, we observe surface roughness in the SEM image, as well as a columnar, polycrystalline nanostructure morphology evidenced by density variation in the *Z*-contrast image. Similar morphologies were observed for the other wires grown at high current (5500 pA); however, at lower pressures (such as nanowire #5) the scan rate had to be decreased because the lateral growth could not keep up with the scanning electron beam. This suggests that deposition at high current (deposits #3-5) is mass transport limited and the resulting wires, with relatively large diameters, resemble bulk-like polycrystalline film growth covered by a native oxide.

In addition to morphology variation, the phase and composition of the core and secondary layer also vary with deposition conditions. While beam energy, current, and precursor pressure had the aforementioned effects on the nanowire structure, the most remarkable parameter investigated was the scan condition. The remainder of the results will focus on the comparison of three distinct nanowire structures (#8, #2 and #10) each grown under a different scan mode.

5.4.1 Chemical Analysis of Nanowires

The EBID nanowire samples deposited directly onto TEM grids were analyzed by 200 kV STEM and XEDS, as well as by AES. STEM imaging with XEDS analysis was problematic due to carbon staining with the intense probe. In addition, the XEDS results from the wires were not considered quantitative due to a large carbon signal originating from electron scatter from the dense wire core causing excitation of the surrounding lacey carbon film. Nevertheless, the oxygen, fluorine, and tungsten levels given in Figure 5.5 can be qualitatively compared.

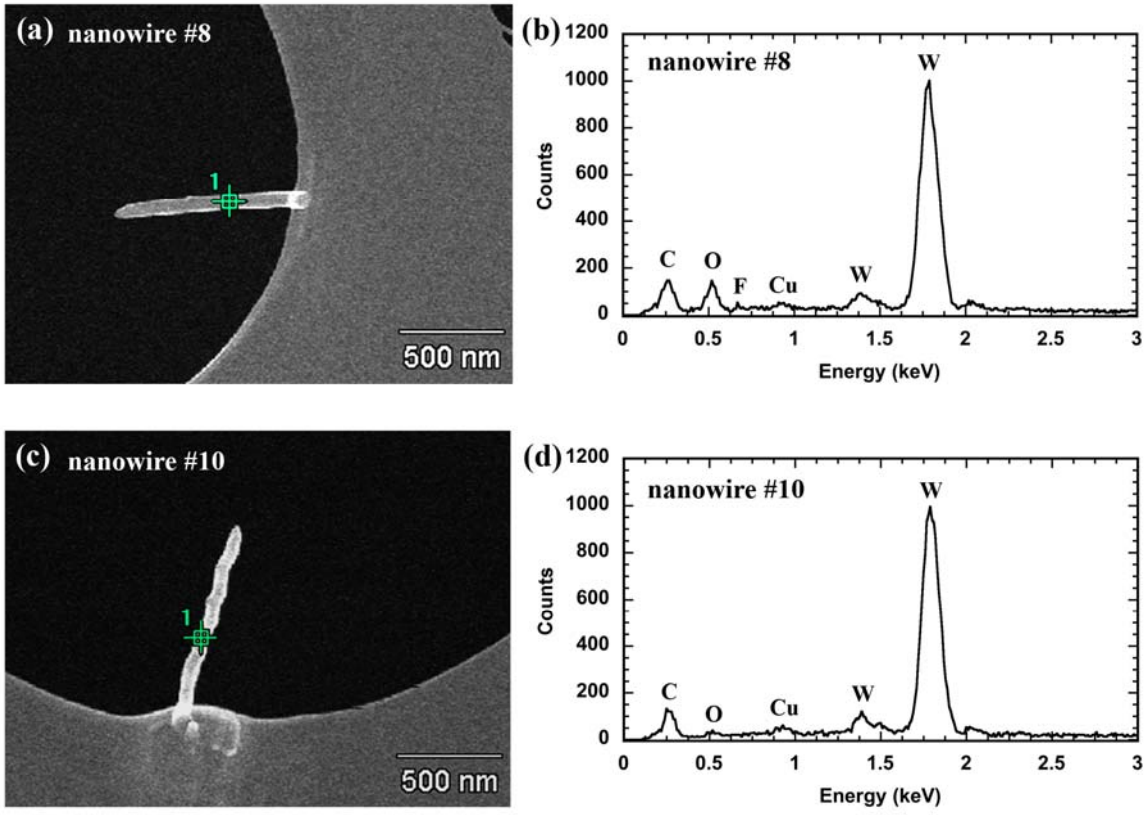

Figure 5.5 SE images and corresponding XEDS spectra for nanowires #8 (a,b) and #10 (c,d).

Subsequent to STEM analysis, which left a thick contamination layer on the wires, the samples were briefly sputter-cleaned for compositional characterization by SAM; however, the highly directional sputter-cleaning did not sufficiently remove the carbon contamination along length of the EBID wires, which often shifted out-of-plane, and instead damaged the carbon support film, causing them to bend and distort. However, the bases of the fibers were sufficiently cleaned as shown by the AES map below. For this reason, a linear Auger scan in Figure 5.6 is shown across the clean base of nanowire #4. The atomic percentage of tungsten measured as high as 98%; *to the best of our knowledge, this is the highest level of purity reported for EBID tungsten*.

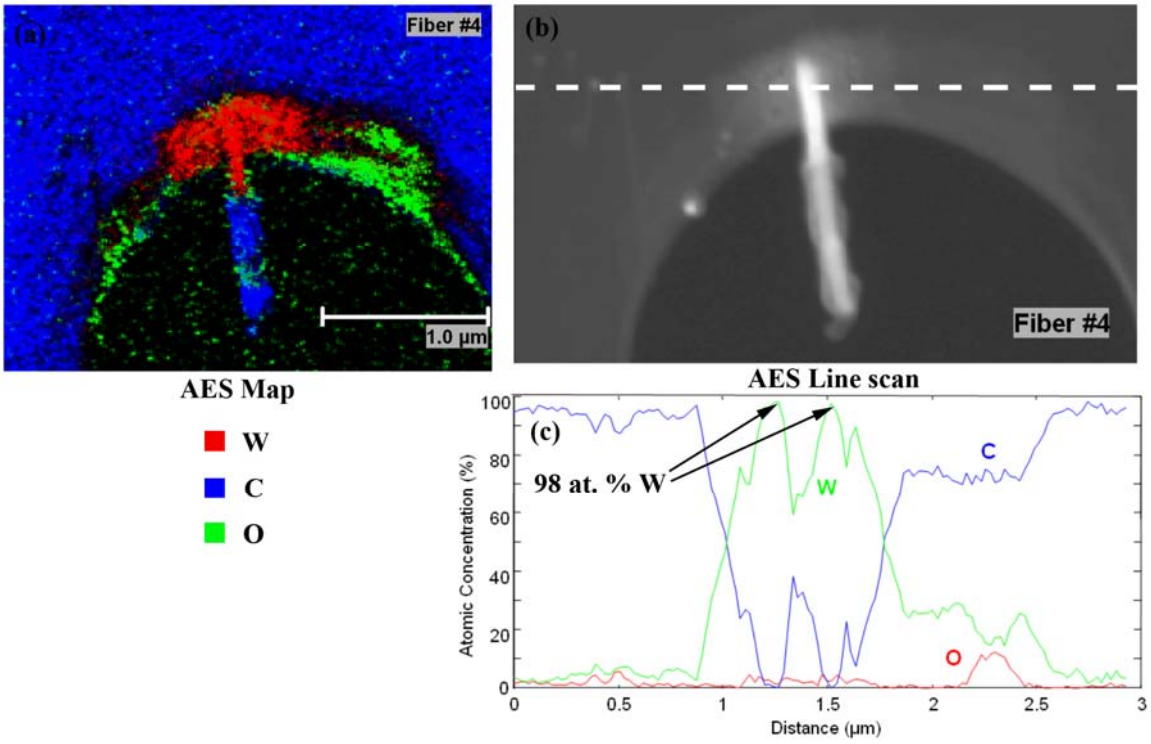

Figure 5.6 Auger analysis of nanowire #4. (a) AES map for W, C, and O. (b) SEM image and (c) corresponding AES line scan along dashed white line.

5.4.2 Analysis of W Nanowire Deposited by Rapid, Lateral Raster

Figure 5.7 shows EBID nanowire #8 grown using a fast linear scan rate of 1.2 μm/minute. The wire core, ~28 nm in diameter, is encased in a ~21-nm-thick secondary layer. Inspection by HRTEM in Figure 5.7(b) reveals 2.48 Å lattice fringes from the solid nanowire core, corresponding to the (200) *d*-spacing of β-W (*Pm-3n*).[306] In addition, HRTEM in Figure 5.7(c) shows that the secondary layer is composed of 5-10 nm crystallites with a *d*-spacing of 3.78Å, corresponding to the {100} planes of the cubic WO_3 phase (*Pm-3m*).[307] SAD in Figure 5.7(d) confirms the presence of both β-W and WO_3 phases. Discontinuous, moderately sharp rings associated with the β-W phase indicate that the core is polycrystalline with some degree of texture, whereas the continuous, diffuse rings of the WO_3 phase indicate the presence of a randomly-oriented, fine-grained, nanocrystalline coating. The Scherrer relation (see Section 2.2.3.3), in which the sharpness of the diffraction rings is inversely proportional to the grain size, is in agreement with the estimation from the TEM micrographs of oxide crystals ~5 nm in size.

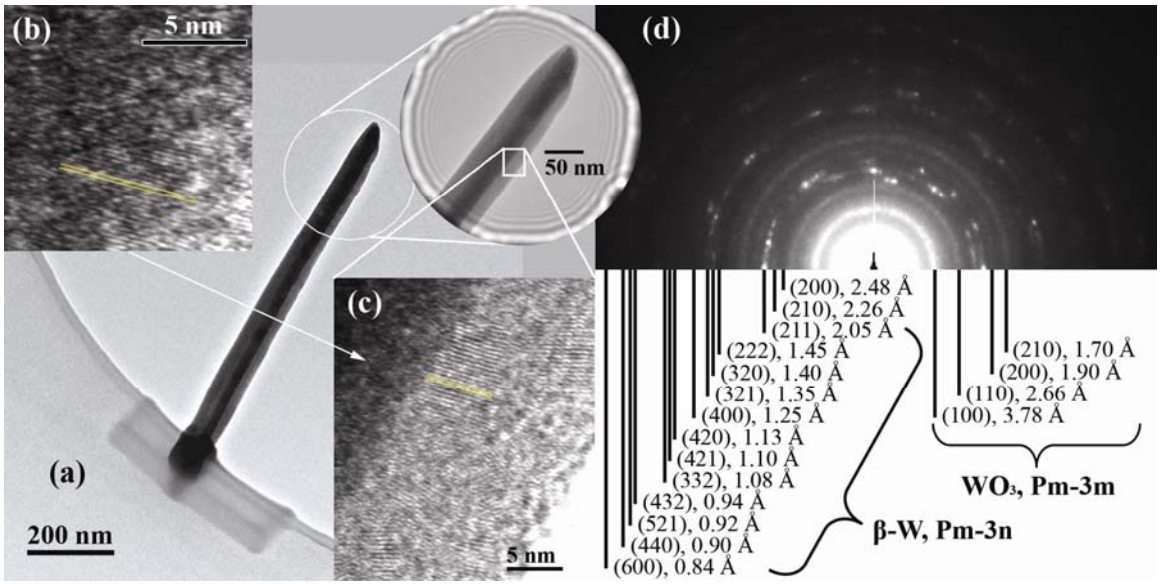

Figure 5.7 TEM analysis of laterally grown EBID nanowire #8. (a) BF image the nanowire with HRTEM images of: (b) the polycrystalline β-W core with a (200) *d*-spacing of 2.48 Å and (c) the nanocrystalline oxide secondary layer with a (100) *d*-spacing of 3.78 Å. (d) SAD pattern sampled from the portion of the wire in the circled and enlarged region shown in (a).

5.4.3 Phases of Tungsten

Elemental tungsten has been known to exist in two structural forms, most commonly as the body-centered cubic phase with a = 3.16 Å, and a second more complex cubic arrangement having eight atoms per unit cell with a = 5.04 Å, designated the α and β phases respectively. β-tungsten is considered a metastable phase found to irreversibly transform into α-W at temperatures above 700°C[308] and can also spontaneously transition to the α-phase when the crystallites become larger than a critical size[306] or in thin films this transition can occur at temperatures as low as 100-200°C.[309] In addition, many studies have indicated that the formation of the metallic β-W phase is most likely stabilized by oxygen during deposition[309-313] and may even require the presence of oxygen as a necessary condition for its nucleation.[310,314,315]

β-tungsten is an A_3B (Cr_3Si) compound, depicted in Figure 5.8, with A15 structure (space group *Pm-3n*, 223) and is often referred to as W_3W since tungsten

occupies both the A and B lattice sites. The table in Figure 5.8 shows the structure factor calculation for each unique *hkl*. The reflections where the structure factor is non-zero for $f_A=f_B$, are legitimate W_3W reflections designated with a "b". Whereas the reflections where the structure factor is non-zero only if $f_A \neq f_B$ (i.e. A and B are occupied by different atoms), are of the ordered phase type "o". If the structure factor is zero regardless of whether A and B are the same atom, the reflection is deemed the kinematically prohibited "p" type. Lastly, the ordered phase and prohibited reflections that have been reported in the literature[309,312,316] as extra reflections in faulted β-W crystals are designated with an "f". It can be seen that the tungsten nanowire in Figure 5.7 exhibits all the legitimate β-W "b" reflections without any additional reflections, indicating that the grains in the nanowire core are composed of high-purity β-tungsten.

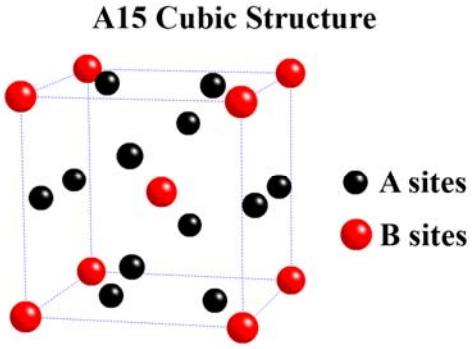

hkl	theoretical F	type
100	0	pf
110	$2f_B-2f_A$	of
111	0	p
200	$2f_A+2f_B$	bo
210	$4f_A$	bo
211	$2f_A+2f_B$	bo
220	$2f_B-2f_A$	of
221,300	0	pf
310	$2f_B-2f_A$	o
311	0	p
222	$2f_B-6f_A$	bo
320	$4f_A$	bo
321	$2f_A+2f_B$	bo
400	$6f_A+2f_B$	bo

hkl	theoretical F	type
322,410	0	pf
330,411	$2f_B-2f_A$	of
331	0	p
420	$2f_A+2f_B$	bo
421	$4f_A$	bo
332	$2f_A+2f_B$	bo
422	$2f_B-2f_A$	of

type	
b	β-W reflections
o	ordered phase reflections
p	prohibited reflections
f	faulted structure reflections

Figure 5.8 A_3B compound with A15 cubic structure (space group *Pm-3n*, 223) with 6 A atoms at ¼, 0, ½; ½, ¼, 0; 0, ½, ¼; ¾, 0, ½; ½, ¾, 0; 0, ½, ¾ and 2 B atoms at 0,0,0; ½, ½, ½. The table of reflection rules for A15 structure contains the theoretical structure factor F as a function of the atomic scattering amplitudes for atoms A and B (f_A and f_B) and the type of reflection that would be observed for each (*hkl*). The faulted structure reflections are the additional reflections observed in faulted β-W crystals as reported in the literature.[36, 39, 43]

5.4.4 Analysis of W Nanowire Deposited by Slow, Lateral Raster

Nanowire #2 in Figure 5.9, grown under conditions similar to wire #8 discussed above, but with a notably slower scan rate and slightly higher energy and current, yielded quite a different result. This wire has a dense core with a diameter of ~20 nm, where faint lattice fringes, as shown in Figure 5.9(a), can be seen throughout the length of the nanowire. These lattice fringes have a *d*-spacing of 5.14 Å, compatible with slightly expanded β-W (001) planes. Thus the [001] direction corresponds to the growth direction of the wire. In addition, a secondary amorphous layer, shown in the HRTEM image, covers the wire core. This coating is ~12 nm thick as can be seen in Figure 5.9(b). The broadness of the faint WO_3 (100) ring at 3.7 Å in the SAD pattern [blue dashed circle, Figure 5.9(c)] confirms that the oxide layer coating this tungsten nanowire is amorphous rather than nanocrystalline. Electron diffraction from the core [Figure 5.9(c)] substantiates the presence of β-W with the wire orientation along the [001] direction. Most of the reflections in this complex SAD pattern originate from two zone axes, the [210] (shown by yellow dots) and [320] (shown by green asterisks), which have the (002) and (004) spots in common. It is believed that this complex pattern is produced from a nanowire core that grew as a uniaxially-oriented β-W crystal, meaning that the (001) planes stacked-up in the growth direction with an occasional slight rotation of these planes about the [001] wire axis direction. This misalignment caused diffraction spots from [210] and [320] zones to simultaneously occur in the pattern because these two zones are only about 7° apart on the primitive great circle for [001]. Faint (012), (-112), and (-222) reflections can also be observed (shown in purple), which suggest the distant [110] and [100] zones. Furthermore, the elongation of the individual diffraction spots is consistent with a <10° rotation of the crystal.

Additional weak, structure factor prohibited reflections are also observed in the Figure 5.9(c) diffraction pattern, including the (001) and (-111) reflections (shown by orange open circles). Petroff *et al*. addressed the issue of additional reflections (both structure factor prohibited and ordered phase reflections) that were present in their polycrystalline TEM diffraction patterns from β-tungsten films by attributing the extra reflections to a mixture of ordered W_3W structure and faulted W_3W structures generated

by partial dislocations.[309] This concept of an ordered and faulted mixture was also adopted by Shen *et al*., who used it to justify the appearance of (100) and (110) reflections in A15 tungsten films containing ~5-15 at. % oxygen.[312] Extensive HRTEM and electron diffraction of A15 tungsten films by Kizuka *et al*. also revealed many of the same reflections kinematically forbidden for β-W, which they attributed to two main factors.[316] First, coalescence of β-W nanocrystals resulted in a series of connected stacking faults rotated about the <100> axis. Secondly, the A15 structure of the nanocrystals could be stabilized by ordered lattice defects such as substitutional or interstitial impurity atoms, which also contribute to the weak appearance of forbidden reflections. Thus our theory described earlier for the growth of a <100> uniaxially-oriented β-W crystal fits well with literature reports on faulted β-W structure, where impurities and stacking faults could have contributed to the slightly expanded lattice of nanowire #2.

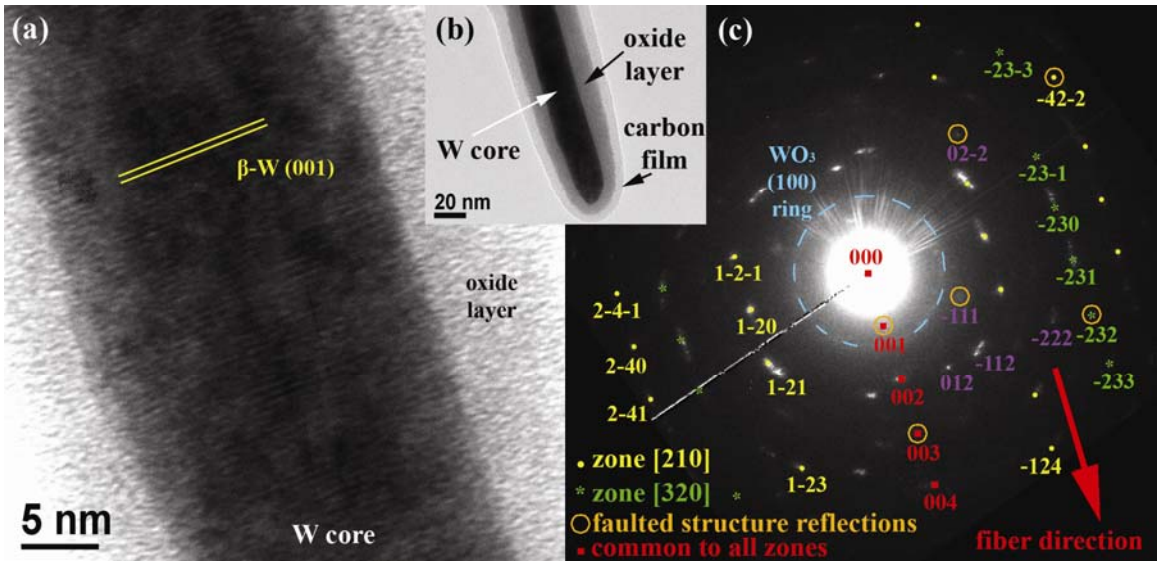

Figure 5.9 TEM analysis of laterally grown EBID nanowire # 2. (a) HRTEM image of the nanowire core showing (001) β-W lattice planes. (b) TEM BF image of the wire tip showing a tungsten core surrounded by a tungsten oxide layer and an amorphous carbon film (contamination layer from imaging). (c) SAD pattern from a ~300 nm area about the wire tip, showing β-W reflections for the [210] and [320] zone axes.

5.4.5 Analysis of W Nanowire Deposited Vertically by Stationary Point Mode

Lastly, in order to investigate the structural properties of nanowires grown in vertical point mode, the deposition method shown in Figure 5.2(c) was employed, which resulted in a ~30°-off-horizontal, free-hanging nanowire over the edge of a hole in the carbon film. This EBID nanowire was grown under the same conditions as wire #8 except that a stationary beam was employed in this case. Inspection of the TEM image in Figure 5.10(a) reveals significant differences from the previous examples: the nanowire has a dense solid core ~70 nm wide with a virtually non-existent secondary layer (only observed at the tip). This vertically deposited wire is essentially straight, although there are slight deviations likely due to charging deflection and beam drift during the 5-minute growth. Because of the density and size of the deposit, it was difficult to penetrate with an electron beam for high-resolution imaging. However, selected area diffraction of the region shown in Figure 5.10(b) produced a single-crystal [111] diffraction pattern (Figure 5.10(c), which was preserved along the length of the wire (compensating for the tilt and morphology of the specimen). This pattern matches the [111] zone for an *ordered* A15 cubic structure with the same lattice constant as β-W. *To our knowledge this is the first demonstration of single-crystal growth by the EBID process.* It should also be noted that the direction of the vertically grown wire in Figure 5.10 is in alignment with the [2-1-1] crystallographic direction in the diffraction pattern. Taking into account the fact that the wire axis is ~30° out-of-plane from the TEM grid and the specimen was tilted an extra 4° to reach the [111] zone for a total tilt of ~34°, it is likely that this single-crystal wire also grew in the <100> direction which is approximately 35° from the [2-1-1].

There are several possible W_3X phases that share the A15 crystal structure and have a virtually indistinguishable lattice constant of ~5.04 Å. For example, since oxygen has an ionic radius of 126 pm, which is identical to tungsten's atomic radius in an A15 unit cell, there is very little distortion with the substitution of oxygen into the W_3W lattice. From this issue many inconsistencies arise in the debate over whether β-W is a suboxide, carbide or silicide of tungsten, or a true metastable allotrope of the metal, as discussed in further in Section 5.6. However, since there are two very different atomic positions in the A15 structure (labeled A and B in Figure 5.8), the absence of the (110)

and other ordered phase reflections, *should* only be possible if similarly scattering atoms are in the two different atomic positions (i.e. W_3W structure). Likewise, ordered phases, where O, C, or Si occupy the B sites in place of W, *should* produce strong additional reflections such as the (110), (220), etc. It is our belief that both phase types are capable of forming during EBID: a β-W phase stabilized by impurities and/or oxide coating, as well as a stoichiometric W_3X ordered phase where X is most likely O.

In Figure 5.10 (nanowire #10) there are ordered phase lattice reflections present in the SAD pattern [Figure 5.10(c)], including the (110), (220), (330), and (422). Judging by the high intensity of these ordered phase reflections they are not likely to be result of lattice defects or faults. *To our knowledge this is the first experimental demonstration of a W_3X single-crystal with clear ordered phase structure.* Attempts to quantify the atomic composition of this and other EBID nanowires by XEDS has proven problematic due to contamination buildup, excitation of the surrounding carbon film, and the direct overlap of the Si K-lines with the W M-lines at ~1.75 keV. Nevertheless, XEDS analysis from nanowire deposits #8 (laterally grown) and #10 (vertically grown) yielded qualitative composition information (spectra displayed in Figure 5.5). Interestingly, the vertically grown wire contains no detectable fluorine levels and significantly less oxygen than the laterally grown wire. Looking closer at the relative ratio of oxygen to tungsten in the XEDS spectra as well as the Auger spectra (not shown), we observed that the vertical wire (#10) contained 3 times less oxygen than the lateral wire grown under the same conditions (#8). This is likely attributed to the ~3-fold difference in oxygen content when comparing W_3O (core of wire #10, which appears to lack secondary layer) to WO_3 (coating of wire #8). This suggests that the single-crystal vertical wire is composed entirely of the W_3O low-level oxide phase.

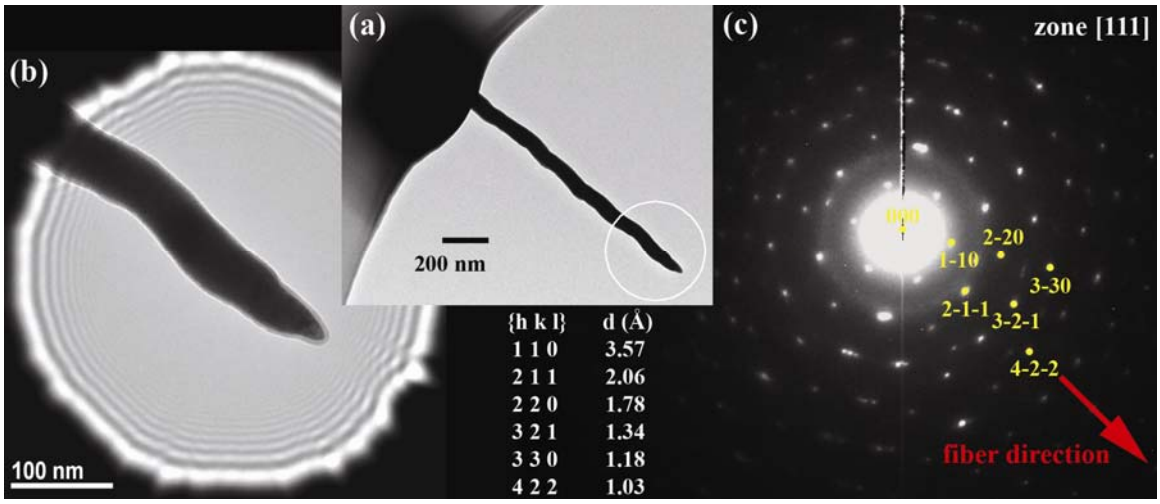

Figure 5.10 TEM analysis of vertically grown EBID nanowire #10. (a) BF TEM image. (b) Close-up of the circled region shown in (a). (c) Diffraction from the area shown in (b) resulted in a single-crystal [111] A15-type SAD pattern with *d*-spacings given at the figure center.

5.6 Clarification over the Existence and Nature of the β-W Phase

To characterize unequivocally the crystal structure of the nanowires grown via EBID, a thorough review of the literature was performed. The A15-type β-tungsten phase, originally reported by Hartmann *et al*., was generated from the electrolysis of fused melts[308] and was later discovered again by Charlton in his work on the reduction of WO_3 in hydrogen.[317] Hägg and Schönberg repeated the experiments of Hartmann *et al*. and claimed that the sample density was about 20% too low to be pure tungsten with A15 structure, and instead suggested that β-W is a low oxide of the metal with a maximum oxygen content corresponding to a ratio of three tungsten to one oxygen.[318] A year later Charlton supported the W_3O theory.[319] The efforts of Mannella *et al*. to gravimetrically study the kinetics of the problem by reducing WO_3 pellets in hydrogen, lead to the contrary finding that β-tungsten is a low temperature, highly pyrophoric form of tungsten metal with oxygen present only as a low level impurity.[320] Subsequent studies have also found that tungsten with A15 structure can be prepared with considerably less than the 3:1 stoichiometric amount of oxygen needed for the metallic oxide.[309,310,312,313,321]

Furthermore, some have gone so far as to assert that the formation of the metallic β-W phase is most likely stabilized by the presence of oxygen during deposition[309-313] and may even require the presence of oxygen as a necessary condition for its nucleation.[310,314,315] Neugebauer *et al*. have also noted that the addition of impurity atoms such as Al and Ce to β-W can delay the transformation to α-W up to 800°C.[322] Morcom *et al*. attribute this phenomena to the formation of a two-dimensional oxide (of varying stability depending on the impurity atom) covering the surface of the metastable β-W particles, which helps to stabilize the high surface energy of the β-W particles.[313] The incorporation of low-level impurities into the A15 lattice or the formation of a two-dimensional surface oxide would logically account for the apparent dependence on oxygen or other impurities for the stabilization of β-W without significantly altering the crystal structure so as to observe the extra ordered phase or faulted structure reflections.

Diffraction studies published in the literature are conflicting; what has been presumed to be W_3O—not β-W—shows no evidence of the extra reflections that should be present for ordered phase structures, including the (110), (220), (310), (411), and (422) reflections. In fact, the reports of W_3O,[318] W_3C,[323,324] and W_3Si[325] furnish diffraction results that are indistinguishable from that of β-W,[306,308] i.e. missing the ordered phase reflections. Hägg and Schönberg tried to reconcile W_3O stoichiometry with the absence of (110) and other ordered phase reflections by postulating that oxygen atoms randomly inhabit the A and B sites.[318] However, due to significant differences between these two positions and the electronic nature of the W and O, it is highly unlikely that such a random distribution would occur.[306,313] Furthermore, all other A15 structured A_3B-type compounds are consistently ordered and show very little deviation from the stoichiometric ratio.[313] Other ambiguous data are also found in the literature, with reports of β-W indexed diffraction results that do not allow for the discernment between ordered or disordered W_3W or W_3O compounds.[311,321] Furthermore, since many of the samples reported in the literature were prepared in the presence of O, C and/or Si, without precise sub-surface chemical analysis it is questionable whether the samples were W_3W, W_3O, W_3C, W_3Si or some mixture thereof, leading to these contrary reports.

5.7 Energy Considerations

The well-oriented, crystalline growth of the W_3O ordered phase by vertical deposition methods (nanowire #10, Figure 5.10) can be explained in that the beam provided sufficient energy to order the lattice during the growth process, with the slow growth rate allowing for the migration and incorporation of impurities into the A15 structure. In vertical point mode the beam interaction volume is larger and the effective growth rate is slower, both of which favor impurity incorporation and more ordered crystal growth in general. More specifically, the energy deposited per volume, calculated using a single scattering Monte Carlo simulation with the beam conditions for wire #10, was estimated to be 6,400 keV per nm^3. Furthermore, because of the slower growth rate, the integration of substitutional O atoms from the vapor phase is greater. These impurity atoms ultimately stabilize the lattice and inhibit the wire from further oxidation, as evidenced by the lack of a thick secondary layer.

We speculate that in the case of the lateral wire grown under the same conditions (nanowire #8, Figure 5.7), deposition occurred so rapidly (due to the fast scan rate) and with minimal beam interaction that individual β-W grains in the core region grew only somewhat textured. In fact, the energy deposited per volume for wire #8 beam conditions was calculated to be only 670 keV per nm^3. The fast growth rate also minimizes the ability of vapor phase impurities to be incorporated, thus creating a high-purity β-W core, which would be extremely susceptible to post-synthesis surface oxidation.

Lastly, the lateral nanowire #2 (Figure 5.9), grown at roughly half the scan rate of wire #8, received enough energy to uniaxially orient the β-W lattice but lacked sufficient energy to anneal out the stacking faults or diffusively integrate impurities into the lattice in an ordered fashion. The estimated energy deposited for this wire was a moderate 1,770 keV per nm^3. Additionally, the growth rate may be sufficiently high (twice as fast as vertical nanowire #10) as to reduce the incorporation of oxygen below the stoichiometric W_3O value, making this wire also susceptible to oxidation.

5.8 Conclusions

In this chapter we have investigated the structure of tungsten EBID deposits grown from the WF_6 precursor using chemical analysis, high-resolution electron microscopy, and electron diffraction. We have measured tungsten purity levels as high as 98 at. %. Evidence is presented indicating that rapid, two-dimensional scanning results in high-purity (~90 at. %), polycrystalline tungsten deposits whose composition varies slightly with dwell time per area. EBID nanowires deposited under a range of conditions exhibited interesting morphology and structure, generally consisting of a dense, crystalline, tungsten-rich core surrounded by an oxide secondary layer. In the three cases analyzed in-depth by HRTEM and diffraction, A15 cubic structure was observed in each of the nanowire cores. Despite much debate in the literature over the existence and nature of β-W and related phases, we reason that lateral EBID growth methods yield textured, high-purity, β-W cores surrounded by an oxide secondary layer. On the other hand, stationary vertical EBID growth, yields W_3O, single-crystal, [100]-oriented nanowires.

6. Conclusions and Future Work

As the size of a material is reduced and the surface-to-volume ratio increases, the properties of nanomaterials can differ substantially from the bulk material. It is for this reason that basic research and exploration of material properties at the nanoscale are so important. Central to the study and successful application of these materials is the ability to control the synthesis process to produce a desired outcome. In this dissertation a variety of growth parameters were explored in order to understand the mechanisms that affect the morphology, composition, and crystal structure of nanostructured materials. Characterization of the nanostructured materials was achieved by several methods including high-resolution transmission electron microscopy, electron diffraction, and chemical spectroscopy.

Here, the carbon nanofiber growth process has been described as a sort of "co-synthesis", where the carbon nanofiber and catalyst particle evolve together. While control over the nanofiber external geometry and location has been previously established, management of the internal quality remained elusive. However, in this work it has been shown that the internal graphitic structure of vertically aligned carbon nanofibers can be directly modulated from herringbone structure to nearly multi-wall carbon nanotube structure by changing the PECVD synthesis conditions. This internal modulation in turn affects the density of surface sites available for the attachment of functional elements, important for numerous applications. Future work will continue investigation of the mechanisms of structure control by exploring matters such as the effect of the fast growth conditions on the catalyst and whether increased pressure simply increases the solubility limit of C in Ni. We may find instead that there is a change in the crystallographic orientation for the fast and slow growth conditions or even an alteration in the physical state of the particle. Additional *in situ* TEM investigation will be invaluable towards solving the mystery of the nanoparticle state during co-synthesis. There has been recent progress in the direction of enhanced time resolution, necessary for capturing such rapid processes. Key experiments have shown that electron pulses can be used to take "snapshot" diffraction patterns (15 nanoseconds) of phase transitions.[326]

The catalyst composition has also proven to play a significant role in the resulting morphology and structure of the VACNFs during co-synthesis. In addition, alloy nanoparticles are interesting in their own right for magnetic and metallurgical study. Both of these aspects were evaluated for three different alloy systems using a co-sputtering technique to deposit the metal thin films. Cu-Ni alloys, which are conventionally miscible at all concentrations of condensed phases, exhibited segregation in Cu-rich alloys due to the fact that Cu was essentially non-catalytic. For Fe-Co alloys, the morphology and magnetic properties of the nanoparticles was traced throughout the three synthesis stages for a range of compositions. The Fe-Co catalyst nanoparticles remained alloyed and ferromagnetic within the VACNFs, where the carbon coating effectively prevented oxidation. However, the saturation magnetization was depressed by several factors including oxidation of the initial films, loss of catalyst material due to plasma bombardment, and most interestingly the formation of superparamagnetic clusters during the synthesis process. Additionally, the Fe-Ni system was investigated near stoichiometric $FeNi_3$ compositions, though it was unable to be determined whether the ordered phase was formed. Here oxidation was also a factor as there was often an Fe_3O_4 particle that formed at the substrate-catalyst film interface. *In situ* heating up to 800˚C did not induce bulk melting or significantly change the crystal structure of the $FeNi_3$ nanoparticles. The presence of several asymmetric diffraction patterns warrants further investigation of the possibility of a large tensile strain in the $FeNi_3$ lattice along the growth direction.

Lastly, electron-beam-induced deposition is a useful technique for direct-writing of 3D dielectric, semiconductor, and metallic materials with nanoscale precision and resolution. The EBID process, however, has been limited in many cases because precursor byproducts (typically from organic precursors like $W(CO)_6$) are incorporated into the deposited material resulting in contaminated and amorphous structures. This dissertation has investigated the structure and composition of EBID tungsten nanostructures as-deposited from a tungsten hexafluoride (WF_6) precursor using a variety of electron beam scanning conditions. The evidence indicates that rapid, two-dimensional scanning results in high-purity (~90 at. %), polycrystalline tungsten deposits. In contrast, slow, one-dimensional lateral scanning produces textured β-tungsten

nanowire cores surrounded by an oxide secondary layer, while stationary vertical growth leads to single-crystal [100]-oriented W_3O nanowires. Furthermore, we have correlated how the growth kinetics affect the resultant nanowire structure and composition. Future work might involve the electronic characterization of the different nanofiber morphologies. In addition, *in situ* chemical and dimensional measurements in the SEM during growth would be useful to determine whether oxidation of the deposits happens during growth or after exposure to air.

References

[1] F. C. Meldrum, V. J. Wade, D. L. Nimmo, B. R. Heywood, and S. Mann, *Nature* **349,** 684 (1991).
[2] M. Young, DebbieWillits, M. Uchida, and T. Douglas, *Annual Review of Phytopathology* **46,** 361 (2008).
[3] K. H. Sandhage, M. B. Dickerson, P. M. Huseman, M. A. Caranna, J. D. Clifton, T. A. Bull, T. J. Heibel, W. R. Overton, and M. E. A. Schoenwaelder, *Advanced Materials* **14,** 429 (2002).
[4] M. Kerker, *Journal of Colloid and Interface Science* **105,** 297 (1985).
[5] C. Burda, X. B. Chen, R. Narayanan, and M. A. El-Sayed, *Chemical Reviews* **105,** 1025 (2005).
[6] © Trustees of the British Museum, www.britishmuseum.org, accessed on 9/19/2008.
[7] M. Reibold, P. Paufler, A. A. Levin, W. Kochmann, N. Patzke, and D. C. Meyer, *Nature* **444,** 286 (2006).
[8] L. E. Murr, J. J. Bang, E. V. Esquivel, P. A. Guerrero, and A. Lopez, *Journal of Nanoparticle Research* **6,** 241 (2004).
[9] M. Faraday, *Philos. Trans. Royal Soc. London* **147,** 145 (1857).
[10] *R&D Status and Trends in Nanoparticles, Nanostructured Materials, and Nanodevices in the United States*, WTEC Workshop, May 8-9, 1997.
[11] J. H. Sinfelt, *Bimetallic Catalysts* (Wiley, New York, 1983).
[12] V. Ponec, *Catalysis Reviews-Science and Engineering* **11,** 41 (1975).
[13] C. R. e. Martens, *Technology of Paints, Varnishes and Laquers* (Reinhold, New York, 1968).
[14] R. P. Feynman, "There's plenty of room at the bottom" in *Miniaturization*, edited by H. D. Gilbert (Reinhold Publishing Corporation, New York 1961).
[15] M. Pitkethly, *Nanotoday* **3,** 6 (2008).
[16] T. Suntola and J. Antson, Finnish Patent No. 52395 (1974).
[17] J. P. Borel, *Surface Science* **106,** 1 (1981).
[18] L. E. Brus, *Journal of Chemical Physics* **80,** 4403 (1984).
[19] H. W. Kroto, J. R. Heath, S. C. Obrien, R. F. Curl, and R. E. Smalley, *Nature* **318,** 162 (1985).
[20] S. Iijima, *Nature* **354,** 56 (1991).
[21] A. M. Thayer, *Chemical & Engineering News* **85,** 15 (2007).
[22] © National Nanotechnology Initiative, www.nano.gov, accessed on 9/19/2008.
[23] M. S. Daw, S. M. Foiles, and M. I. Baskes, *Materials Science Reports* **9,** 251 (1993).
[24] K. S. Kumar, H. Van Swygenhoven, and S. Suresh, *Acta Materialia* **51,** 5743 (2003).
[25] D. Q. Yang, J. N. Gillet, M. Meunier, and E. Sacher, *Journal of Applied Physics* **97,** Art. No. 024303 (2005).
[26] N. Lopez, T. V. W. Janssens, B. S. Clausen, Y. Xu, M. Mavrikakis, T. Bligaard, and J. K. Norskov, *Journal of Catalysis* **223,** 232 (2004).
[27] B. Hvolbaek, T. V. W. Janssens, B. S. Clausen, H. Falsig, C. H. Christensen, and J. K. Norskov, *Nano Today* **2,** 14 (2007).
[28] F. D. Fischer, T. Waitz, D. Vollath, and N. K. Simha, *Progress in Materials Science* **53,** 481 (2008).

[29] K. K. Nanda, A. Maisels, F. E. Kruis, H. Fissan, and S. Stappert, *Physical Review Letters* **91,** Art. No. 106102 (2003).
[30] J. Woltersdorf, A. S. Nepijko, and E. Pippel, *Surface Science* **106,** 64 (1981).
[31] A. S. Edelstein, *Nanomaterials: synthesis, properties, and applications*, online ed. (Institute of Physics Pub., Philadelphia, 1998).
[32] L. M. Liz-Marzan, *Materials Today* **7,** 26 (2004).
[33] M. N. Baibich, J. M. Broto, A. Fert, F. N. Vandau, F. Petroff, P. Eitenne, G. Creuzet, A. Friederich, and J. Chazelas, *Physical Review Letters* **61,** 2472 (1988).
[34] K. Koga, T. Ikeshoji, and K. Sugawara, *Physical Review Letters* **92,** Art. No. 115507 (2004).
[35] L. D. Marks, *Reports on Progress in Physics* **57,** 603 (1994).
[36] F. Baletto, C. Mottet, and R. Ferrando, *Physical Review B* **63,** Art. No. 155408 (2001).
[37] D. Zanchet, B. D. Hall, and D. Ugarte, *Journal of Physical Chemistry B* **104,** 11013 (2000).
[38] D. Reinhard, B. D. Hall, D. Ugarte, and R. Monot, *Physical Review B* **55,** 7868 (1997).
[39] K. L. Klein, A. V. Melechko, T. E. McKnight, S. T. Retterer, P. D. Rack, J. D. Fowlkes, D. C. Joy, and M. L. Simpson, *Journal of Applied Physics* **103,** Art. No. 061301 (2008).
[40] M. S. Dresselhaus, "Carbon: bonding" in *Encyclopedia of Materials: Science and Thechnology* (Elsevier Science Ltd., 2001).
[41] M. I. Katsnelson, *Materials Today* **10,** 20 (2006).
[42] A. Krishnan, E. Dujardin, M. M. J. Treacy, J. Hugdahl, S. Lynum, and T. W. Ebbesen, *Nature* **388,** 451 (1997).
[43] R. T. K. Baker, *Carbon* **27,** 315 (1989).
[44] A. V. Melechko, V. I. Merkulov, T. E. McKnight, M. A. Guillorn, K. L. Klein, D. H. Lowndes, and M. L. Simpson, *Journal of Applied Physics* **97,** Art. No. 041301 (2005).
[45] S. Iijima, *Physica B-Condensed Matter* **323,** 1 (2002).
[46] C. Dekker, *Physics Today* **52,** 22 (1999).
[47] A. Javey, J. Guo, Q. Wang, M. Lundstrom, and H. J. Dai, *Nature* **424,** 654 (2003).
[48] M. F. Yu, O. Lourie, M. J. Dyer, K. Moloni, T. F. Kelly, and R. S. Ruoff, *Science* **287,** 637 (2000).
[49] © Massachusets Institute of Technology, M. Bawendi, http://nanocluster.mit.edu/research.php, accessed on 7/16/2008.
[50] R. A. Farrer, F. L. Butterfield, V. W. Chen, and J. T. Fourkas, *Nano Letters* **5,** 1139 (2005).
[51] P. K. Jain, I. H. El-Sayed, and M. A. El-Sayed, *Nano Today* **2,** 18 (2007).
[52] G. Gundiah, N. S. John, P. J. Thomas, G. U. Kulkarni, C. N. R. Rao, and S. Heun, *Applied Physics Letters* **84,** 5341 (2004).
[53] R. D. Piner, J. Zhu, F. Xu, S. H. Hong, and C. A. Mirkin, *Science* **283,** 661 (1999).
[54] O. Masala, D. Hoffman, N. Sundaram, K. Page, T. Proffen, G. Lawes, and R. Seshadri, *Solid State Sciences* **8,** 1015 (2006).

[55] J. B. Tracy, D. N. Weiss, D. P. Dinega, and M. G. Bawendi, *Physical Review B* **72,** Art. No. 064404 (2005).
[56] V. Skumryev, S. Stoyanov, Y. Zhang, G. Hadjipanayis, D. Givord, and J. Nogues, *Nature* **423,** 850 (2003).
[57] N. Fukuda, J. Ishii, T. Tanaka, H. Fukuda, N. Ohnishi, and A. Kondo, *Biotechnology Progress* **24,** 352 (2008).
[58] M. Bettge, J. Chatterjee, and Y. Haik, *BioMagnetic Research and Technology* **2,** (2004).
[59] J. T. Hu, T. W. Odom, and C. M. Lieber, *Accounts of Chemical Research* **32,** 435 (1999).
[60] S. J. Tans, A. R. M. Verschueren, and C. Dekker, *Nature* **393,** 49 (1998).
[61] S. J. Tans, M. H. Devoret, H. J. Dai, A. Thess, R. E. Smalley, L. J. Geerligs, and C. Dekker, *Nature* **386,** 474 (1997).
[62] X. F. Duan, Y. Huang, Y. Cui, J. F. Wang, and C. M. Lieber, *Nature* **409,** 66 (2001).
[63] C. M. Lieber and Z. L. Wang, *Mrs Bulletin* **32,** 99 (2007).
[64] K. A. Dick, K. Deppert, M. W. Larsson, T. Martensson, W. Seifert, L. R. Wallenberg, and L. Samuelson, *Nature Materials* **3,** 380 (2004).
[65] M. Henny, S. Oberholzer, C. Strunk, and C. Schonenberger, *Physical Review B* **59,** 2871 (1999).
[66] O. Rabina, Y. M. Lin, and M. S. Dresselhaus, *Applied Physics Letters* **79,** 81 (2001).
[67] C. Durkan and M. E. Welland, *Physical Review B* **61,** 14215 (2000).
[68] C. Z. Li, H. X. He, A. Bogozi, J. S. Bunch, and N. J. Tao, *Applied Physics Letters* **76,** 1333 (2000).
[69] H. X. He and N. J. Tao, *Advanced Materials* **14,** 161 (2002).
[70] E. C. Walter, M. P. Zach, F. Favier, B. J. Murray, K. Inazu, J. C. Hemminger, and R. M. Penner, *Chemphyschem* **4,** 131 (2003).
[71] M. E. Toimil-Molares, A. G. Balogh, T. W. Cornelius, R. Neumann, and C. Trautmann, *Applied Physics Letters* **85,** 5337 (2004).
[72] M. A. Guillorn, X. Yang, A. V. Melechko, D. K. Hensley, M. D. Hale, V. I. Merkulov, M. L. Simpson, L. R. Baylor, W. L. Gardner, and D. H. Lowndes, *Journal of Vacuum Science & Technology B* **22,** 35 (2004).
[73] M. A. Guillorn, A. V. Melechko, and M. L. Simpson, United States Patent No. 7,151,256 (2005).
[74] J. Li, H. T. Ng, A. Cassell, W. Fan, H. Chen, Q. Ye, J. Koehne, J. Han, and M. Meyyappan, *Nano Letters* **3,** 597 (2003).
[75] J. Li, Q. Ye, A. Cassell, H. T. Ng, R. Stevens, J. Han, and M. Meyyappan, *Applied Physics Letters* **82,** 2491 (2003).
[76] T. E. McKnight, A. V. Melechko, D. W. Austin, T. Sims, M. A. Guillorn, and M. L. Simpson, *Journal of Physical Chemistry B* **108,** 7115 (2004).
[77] T. E. McKnight, A. V. Melechko, G. D. Griffin, M. A. Guillorn, V. I. Merkulov, F. Serna, D. K. Hensley, M. J. Doktycz, D. H. Lowndes, and M. L. Simpson, *Nanotechnology* **14,** 551 (2003).
[78] T. E. McKnight, A. V. Melechko, D. K. Hensley, D. G. J. Mann, G. D. Griffin, and M. L. Simpson, *Nano Letters* **4,** 1213 (2004).

[79] H. Cui, S. V. Kalinin, X. Yang, and D. H. Lowndes, *Nano Letters* **4,** 2157 (2004).
[80] B. L. Fletcher, E. D. Hullander, A. V. Melechko, T. E. McKnight, K. L. Klein, D. K. Hensley, J. L. Morrell, M. L. Simpson, and M. J. Doktycz, *Nano Letters* **4,** 1809 (2004).
[81] S. E. Baker, K. Y. Tse, C. S. Lee, and R. J. Hamers, *Diamond and Related Materials* **15,** 433 (2006).
[82] M. S. Dhindsa, N. R. Smith, J. Heikenfeld, P. D. Rack, J. D. Fowlkes, M. J. Doktycz, A. V. Melechko, and M. L. Simpson, *Langmuir* **22,** 9030 (2006).
[83] D. G. J. Mann, T. E. McKnight, A. V. Melechko, M. L. Simpson, and G. S. Sayler, *Biotechnology and Bioengineering* **97,** 680 (2007).
[84] A. V. Melechko, T. E. McKnight, M. A. Guillorn, V. I. Merkulov, B. Ilic, M. J. Doktycz, D. H. Lowndes, and M. L. Simpson, *Applied Physics Letters* **82,** 976 (2003).
[85] T. D. B. Nguyen-Vu, H. Chen, A. M. Cassell, R. J. Andrews, M. Meyyappan, and J. Li, *Ieee Transactions on Biomedical Engineering* **54,** 1121 (2007).
[86] Z. Yu, T. E. McKnight, M. N. Ericson, A. V. Melechko, M. L. Simpson, and B. Morrison, *Nano Letters* **7,** 2188 (2007).
[87] A. L. Elias, J. A. Rodriguez-Manzo, M. R. McCartney, D. Golberg, A. Zamudio, S. E. Baltazar, F. Lopez-Urias, E. Munoz-Sandoval, L. Gu, C. C. Tang, D. J. Smith, Y. Bando, H. Terrones, and M. Terrones, *Nano Letters* **5,** 467 (2005).
[88] D. Golberg, C. Z. Gu, Y. Bando, M. Mitome, and C. C. Tang, *Acta Materialia* **53,** 1583 (2005).
[89] D. Golberg, M. Mitome, C. Muller, C. Tang, A. Leonhardt, and Y. Bando, *Acta Materialia* **54,** 2567 (2006).
[90] S. Karmakar, S. M. Sharma, P. V. Teredesai, and A. K. Sood, *Physical Review B* **69,** Art. No. 165414 (2004).
[91] S. W. Liu, X. H. Tang, Y. Mastai, I. Felner, and A. Gedanken, *Journal of Materials Chemistry* **10,** 2502 (2000).
[92] S. J. Randolph, J. D. Fowlkes, and P. D. Rack, *Critical Reviews in Solid State and Materials Sciences* **31,** 55 (2006).
[93] H. W. P. Koops, C. Schossler, A. Kaya, and M. Weber, *Journal of Vacuum Science & Technology B* **14,** 4105 (1996).
[94] K. Murakami and M. Takai, *Journal of Vacuum Science & Technology B* **22,** 1266 (2004).
[95] J. Sellmair, K. Edinger, and H. W. P. Koops, *Journal of Vacuum Science & Technology B* **23,** 781 (2005).
[96] X. Yang, M. L. Simpson, S. J. Randolph, P. D. Rack, L. R. Baylor, H. Cui, and W. L. Gardner, *Applied Physics Letters* **86,** 183106 (2005).
[97] I. C. Chen, L. H. Chen, C. Orme, A. Quist, R. Lal, and S. H. Jin, *Nanotechnology* **17,** 4322 (2006).
[98] B. J. Rodriguez, S. Jesse, K. Seal, A. P. Baddorf, S. V. Kalinin, and P. D. Rack, *Applied Physics Letters* **91,** 093130 (2007).
[99] K. Edinger, H. Becht, J. Bihr, V. Boegli, M. Budach, T. Hofmann, H. W. P. Koops, P. Kuschnerus, J. Oster, P. Spies, and B. Weyrauch, *Journal of Vacuum Science & Technology B* **22,** 2902 (2004).
[100] S. J. Randolph, Thesis, University of Tennessee, 2005.

[101] M. Han, K. Mitsuishi, M. Shimojo, and K. Furuya, *Philosophical Magazine* **84,** 1281 (2004).
[102] C. C. Koch, *Nanostructured Materials* **9,** 13 (1997).
[103] S. G. Zhang, *Nature Biotechnology* **21,** 1171 (2003).
[104] R. S. Wagner and W. C. Ellis, *Appl. Phys. Lett.* **4,** 89 (1964).
[105] Y. N. Xia, P. D. Yang, Y. G. Sun, Y. Y. Wu, B. Mayers, B. Gates, Y. D. Yin, F. Kim, and Y. Q. Yan, *Advanced Materials* **15,** 353 (2003).
[106] S. Kodambaka, J. Tersoff, M. C. Reuter, and F. M. Ross, *Science* **316,** 729 (2007).
[107] A. I. Persson, M. W. Larsson, S. Stenstrom, B. J. Ohlsson, L. Samuelson, and L. R. Wallenberg, *Nature Materials* **3,** 677 (2004).
[108] K. B. K. Teo, C. Singh, M. Chhowalla, and W. I. Milne, "Catalystic Synthesis of Carbon Nanotubes and Nanofibers" in *Encyclopedia of Nanoscience and Nanotechnology*; Vol. X, edited by H. S. Nalwa (American Scientific Publishers, 2003).
[109] S. Helveg, C. Lopez-Cartes, J. Sehested, P. L. Hansen, B. S. Clausen, J. R. Rostrup-Nielsen, F. Abild-Pedersen, and J. K. Norskov, *Nature* **427,** 426 (2004).
[110] E. F. Kukovitsky, S. G. L'Vov, and N. A. Sainov, *Chemical Physics Letters* **317,** 65 (2000).
[111] K. M. Lee, B. Lukic, A. Magrez, J. W. Seo, G. A. D. Briggs, A. J. Kulik, and L. Forro, *Nano Letters* **7,** 1598 (2007).
[112] R. F. Bunshah, *Deposition and Technologies for Films and Coatings* (Noyes Publications, Park Ridge, NJ, 1982).
[113] M. Ohring, *Materials Science of Thin Films: Deposition and Structure*, 2 ed. (Academic Press, New York, 2002).
[114] Y. C. Choi, Y. M. Shin, S. C. Lim, D. J. Bae, Y. H. Lee, B. S. Lee, and D. C. Chung, *Journal of Applied Physics* **88,** 4898 (2000).
[115] P. A. Tesner and I. S. Rafalkes, *Doklady Akademii Nauk SSSR* **87,** 821 (1952).
[116] P. A. Tesner, Robinovi.Ey, I. S. Rafalkes, and E. F. Arefieva, *Carbon* **8,** 435 (1970).
[117] R. T. K. Baker, M. A. Barber, R. J. Waite, P. S. Harris, and F. S. Feates, *Journal of Catalysis* **26,** 51 (1972).
[118] W. Z. Li, S. S. Xie, L. X. Qian, B. H. Chang, B. S. Zou, W. Y. Zhou, R. A. Zhao, and G. Wang, *Science* **274,** 1701 (1996).
[119] A. M. Cassell, J. A. Raymakers, J. Kong, and H. J. Dai, *Journal of Physical Chemistry B* **103,** 6484 (1999).
[120] F. Jansen, *Plasma-Enhanced Chemical Vapor Deposition* (American Vacuum Society, New York, 1997).
[121] V. Merkulov, A. V. Melechko, M. A. Guillorn, D. H. Lowndes, and M. L. Simpson, *Chemical Physics Letters* **361,** 492 (2002).
[122] A. E. Ennos, *British Journal of Applied Physics* **4,** 101 (1953).
[123] K. M. Poole, *Proceedings of the Physical Society: Section B* **66,** 542 (1953).
[124] A. G. Baker and W. C. Morris, *Review of Scientific Instruments* **32,** 458 (1961).
[125] W. C. Oliver and G. M. Pharr, *Journal of Materials Research* **7,** 1564 (1992).
[126] P. E. Batson, N. Dellby, and O. L. Krivanek, *Nature* **418,** 617 (2002).

[127] J. Goldstein, D. Newbury, D. Joy, C. Lyman, P. Echlin, E. Lifshin, L. Sawyer, and J. Michael, *Scanning Electron Microscopy and X-ray Microanalysis*, 3 ed. (Springer, New York, 2003).
[128] B. Fultz and J. Howe, *Transmission Electron Microscopy and Diffractometry of Materials*, 2 ed. (Springer, New York, 2002).
[129] D. B. Williams and C. B. Carter, *Transmission Electron Microscopy* (Plenum Press, New York, 1996).
[130] Hitachi High Technologies America, in *Hitachi Scientific Instrument Technical Data: STEM Sheet No. 1*, File EX-E879-01 (printed in Japan, 1999).
[131] D. Brune, R. Hellborg, H. J. Whitlow, and O. Hunderi, *Surface Characterization* (Wiley-VCH, New York, 1997).
[132] D. P. Woodruff and T. A. Delchar, *Modern Techniques of Surface Science*, 2 ed. (Cambridge University Press, New York, 1994).
[133] B. D. Cullity, *Elements of X-ray Diffraction*, 2 ed. (Addison-Wesley Publishing Company, Inc., Reading, MA, 1978).
[134] H. E. Swanson and E. Tatge, *National Bureau of Standards* **539,** 1 (1953).
[135] D. N. Batchelder and R. O. Simmons, *Journal of Chemical Physics* **41,** 2324 (1964).
[136] F. Fultz and J. M. Howe, *Transmission Electron Microscopy and Diffractometry of Materials*, 3 ed. (Springer, New York, 2008).
[137] A. V. Melechko, K. L. Klein, J. D. Fowlkes, D. K. Hensley, I. A. Merkulov, T. E. McKnight, P. D. Rack, J. A. Horton, and M. L. Simpson, *Journal of Applied Physics* **102,** Art. No. 074314 (2007).
[138] L. R. Baylor, D. H. Lowndes, M. L. Simpson, C. E. Thomas, M. A. Guillorn, V. I. Merkulov, J. H. Whealton, E. D. Ellis, D. K. Hensley, and A. V. Melechko, *Journal of Vacuum Science & Technology B* **20,** 2646 (2002).
[139] M. A. Guillorn, M. L. Simpson, G. J. Bordonaro, V. I. Merkulov, L. R. Baylor, and D. H. Lowndes, *Journal of Vacuum Science & Technology B* **19,** 573 (2001).
[140] B. L. Fletcher, T. E. McKnight, J. D. Fowlkes, D. P. Allison, M. L. Simpson, and M. J. Doktycz, *Synthetic Metals* **157,** 282 (2007).
[141] S. E. Baker, K. Y. Tse, E. Hindin, B. M. Nichols, T. L. Clare, and R. J. Hamers, *Chemistry of Materials* **17,** 4971 (2005).
[142] S. E. Baker, P. E. Colavita, K. Y. Tse, and R. J. Hamers, *Chem. Mater.* **18,** 4415 (2006).
[143] L. Zhang, A. V. Melechko, V. I. Merkulov, M. A. Guillorn, M. L. Simpson, D. H. Lowndes, and M. J. Doktycz, *Applied Physics Letters* **81,** 135 (2002).
[144] M. A. Guillorn, T. E. McKnight, A. Melechko, V. I. Merkulov, P. F. Britt, D. W. Austin, D. H. Lowndes, and M. L. Simpson, *Journal of Applied Physics* **91,** 3824 (2002).
[145] T. E. McKnight, A. V. Melechko, M. A. Guillorn, V. I. Merkulov, M. J. Doktycz, C. T. Culbertson, S. C. Jacobson, D. H. Lowndes, and M. L. Simpson, *Journal of Physical Chemistry B* **107,** 10722 (2003).
[146] Q. Ye, A. Cassell, H. Liu, K.-J. Chao, J. Han, and M. Meyyappan, *Nano Letters* **4,** 1301 (2004).
[147] K. P. De Jong and J. W. Geus, *Catalysis Reviews-Science and Engineering* **42,** 481 (2000).

[148] M. Meyyappan, L. Delzeit, A. Cassell, and D. Hash, *Plasma Sources Science & Technology* **12,** 205 (2003).
[149] N. M. Rodriguez, A. Chambers, and R. T. K. Baker, *Langmuir* **11,** 3862 (1995).
[150] V. I. Merkulov, D. H. Lowndes, Y. Y. Wei, G. Eres, and E. Voelkl, *Applied Physics Letters* **76,** 3555 (2000).
[151] G. Eres, C. M. Rouleau, A. A. Puretzky, J. J. Jackson, and D. B. Goehegan**,** (to be published, 2009).
[152] A. V. Melechko, V. I. Merkulov, D. H. Lowndes, M. A. Guillorn, and M. L. Simpson, *Chemical Physics Letters* **356,** 527 (2002).
[153] I. Alstrup, *Journal of Catalysis* **109,** 241 (1988).
[154] A. Kock, P. K. Debokx, E. Boellaard, W. Klop, and J. W. Geus, *Journal of Catalysis* **96,** 468 (1985).
[155] J. R. Nielsen and D. L. Trimm, *Journal of Catalysis* **48,** 155 (1977).
[156] A. Sacco, P. Thacker, T. N. Chang, and A. T. S. Chiang, *Journal of Catalysis* **85,** 224 (1984).
[157] T. Baird, J. R. Fryer, and B. Grant, *Carbon* **12,** 591 (1974).
[158] A. Oberlin, M. Endo, and T. Koyama, *Journal of Crystal Growth* **32,** 335 (1976).
[159] G. G. Tibbetts, *Journal of Crystal Growth* **66,** 632 (1984).
[160] M. Chhowalla, K. B. K. Teo, C. Ducati, N. L. Rupesinghe, G. A. J. Amaratunga, A. C. Ferrari, D. Roy, J. Robertson, and W. I. Milne, *Journal of Applied Physics* **90,** 5308 (2001).
[161] Z. F. Ren, Z. P. Huang, D. Z. Wang, J. G. Wen, J. W. Xu, J. H. Wang, L. E. Calvet, J. Chen, J. F. Klemic, and M. A. Reed, *Applied Physics Letters* **75,** 1086 (1999).
[162] V. I. Merkulov, D. K. Hensley, A. V. Melechko, M. A. Guillorn, D. H. Lowndes, and M. L. Simpson, *Journal of Physical Chemistry B* **106,** 10570 (2002).
[163] S. Y. Zaginaichenko, D. V. Schur, and Z. A. Matysina, *Carbon* **41,** 1349 (2003).
[164] L. Delzeit, C. V. Nguyen, B. Chen, R. Stevens, A. Cassell, J. Han, and M. Meyyappan, *Journal of Physical Chemistry B* **106,** 5629 (2002).
[165] M. S. Kim, N. M. Rodriguez, and R. T. K. Baker, *Journal of Catalysis* **131,** 60 (1991).
[166] K. B. K. Teo, D. B. Hash, R. G. Lacerda, N. L. Rupesinghe, M. S. Bell, S. H. Dalal, D. Bose, T. R. Govindan, B. A. Cruden, M. Chhowalla, G. A. J. Amaratunga, J. M. Meyyappan, and W. I. Milne, *Nano Letters* **4,** 921 (2004).
[167] B. L. Fletcher, T. E. McKnight, A. V. Melechko, D. K. Hensley, D. K. Thomas, M. N. Ericson, and M. L. Simpson, *Advanced Materials* **18,** 1689 (2006).
[168] A. V. Melechko, T. E. McKnight, D. K. Hensley, M. A. Guillorn, A. Y. Borisevich, V. I. Merkulov, D. H. Lowndes, and M. L. Simpson, *Nanotechnology* **14,** 1029 (2003).
[169] H. T. Ng, B. Chen, J. E. Koehne, A. M. Cassell, J. Li, J. Han, and M. Meyyappan, *Journal of Physical Chemistry B* **107,** 8484 (2003).
[170] A. M. Cassell, Q. Ye, B. A. Cruden, J. Li, P. C. Sarrazin, H. T. Ng, J. Han, and M. Meyyappan, *Nanotechnology* **15,** 9 (2004).
[171] K. L. Klein, A. V. Melechko, P. D. Rack, J. D. Fowlkes, H. M. Meyer, and M. L. Simpson, *Carbon* **43,** 1857 (2005).

[172] K. D. Sorge, K. L. Klein, A. V. Melechko, C. L. Finkel, O. Malkina, T. Leventouri, J. D. Fowlkes, P. D. Rack, and M. L. Simpson, *Journal of Applied Physics* **104,** Art. No. 033909 (2008).
[173] V. I. Merkulov, A. V. Melechko, M. A. Guillorn, D. H. Lowndes, and M. L. Simpson, *Chemical Physics Letters* **350,** 381 (2001).
[174] C. Bower, O. Zhou, W. Zhu, D. J. Werder, and S. H. Jin, *Applied Physics Letters* **77,** 2767 (2000).
[175] V. I. Merkulov, A. V. Melechko, M. A. Guillorn, D. H. Lowndes, and M. L. Simpson, *Applied Physics Letters* **80,** 476 (2002).
[176] V. I. Merkulov, M. A. Guillorn, D. H. Lowndes, M. L. Simpson, and E. Voelkl, *Applied Physics Letters* **79,** 1178 (2001).
[177] K. B. K. Teo, M. Chhowalla, G. A. J. Amaratunga, W. I. Milne, G. Pirio, P. Legagneux, F. Wyczisk, J. Olivier, and D. Pribat, *Journal of Vacuum Science & Technology B* **20,** 116 (2002).
[178] X. J. Yang, M. A. Guillorn, D. Austin, A. V. Melechko, H. T. Cui, H. M. Meyer, V. I. Merkulov, J. B. O. Caughman, D. H. Lowndes, and M. L. Simpson, *Nano Letters* **3,** 1751 (2003).
[179] H. Cui, X. Yang, H. M. Meyer, L. R. Baylor, M. L. Simpson, W. L. Gardner, D. H. Lowndes, L. An, and J. Lui, *Journal of Materials Research* **20,** 850 (2005).
[180] S. S. Fan, M. G. Chapline, N. R. Franklin, T. W. Tombler, A. M. Cassell, and H. J. Dai, *Science* **283,** 512 (1999).
[181] V. I. Merkulov, A. V. Melechko, M. A. Guillorn, D. H. Lowndes, and M. L. Simpson, *Applied Physics Letters* **79,** 2970 (2001).
[182] V. I. Merkulov, A. V. Melechko, M. A. Guillorn, M. L. Simpson, D. H. Lowndes, J. H. Whealton, and R. J. Raridon, *Applied Physics Letters* **80,** 4816 (2002).
[183] J. Koehne, H. Chen, J. Li, A. M. Cassell, Q. Ye, H. T. Ng, J. Han, and M. Meyyappan, *Nanotechnology* **14,** 1239 (2003).
[184] J. Moser, R. Panepucci, Z. P. Huang, W. Z. Li, Z. F. Ren, A. Usheva, and M. J. Naughton, *Journal of Vacuum Science & Technology B* **21,** 1004 (2003).
[185] A. V. Melechko, T. E. McKnight, M. A. Guillorn, D. W. Austin, B. Ilic, V. I. Merkulov, M. J. Doktycz, D. H. Lowndes, and M. L. Simpson, *Journal of Vacuum Science & Technology B* **20,** 2730 (2002).
[186] B. McEnaney, "Mechanical properties of carbons and graphites" in *Encyclopedia of Materials: Science and Technology* (2001).
[187] B. G. Demczyk, Y. M. Wang, J. Cumings, M. Hetman, W. Han, A. Zettl, and R. O. Ritchie, *Materials Science and Engineering a-Structural Materials Properties Microstructure and Processing* **334,** 173 (2002).
[188] R. P. Gao, Z. L. Wang, Z. G. Bai, W. A. de Heer, L. M. Dai, and M. Gao, *Physical Review Letters* **85,** 622 (2000).
[189] H. Guo, A. Rasheed, M. L. Minus, and S. Kumar, *Journal of Materials Science* **43,** 4363 (2008).
[190] W. H. Zhong, J. Li, C. M. Lukehart, and L. Y. R. Xu, *Polymer Composites* **26,** 128 (2005).
[191] D. Golberg, P. M. Costa, M. Mitome, and Y. Bando, *Nano Research* **1,** 166 (2008).

[192] L. Zhang, D. Austin, V. I. Merkulov, A. V. Meleshko, K. L. Klein, M. A. Guillorn, D. H. Lowndes, and M. L. Simpson, *Applied Physics Letters* **84,** 3972 (2004).
[193] S. B. Lee, K. B. K. Teo, M. Chhowalla, D. G. Hasko, G. A. J. Amaratunga, W. I. Milne, and H. Ahmed, *Microelectronic Engineering* **61-2,** 475 (2002).
[194] M. Suzuki, Y. Ominami, Q. Ngo, C. Y. Yang, A. M. Cassell, and J. Li, *Journal of Applied Physics* **101,** Art. No. 114307 (2007).
[195] B. L. Fletcher, T. E. McKnight, A. V. Melechko, M. L. Simpson, and M. J. Doktycz, *Nanotechnology* **17,** 2032 (2006).
[196] T. E. McKnight, C. Peeraphatdit, S. W. Jones, J. D. Fowlkes, B. L. Fletcher, K. L. Klein, A. V. Melechko, M. J. Doktycz, and M. L. Simpson, *Chemistry of Materials* **18,** 3203 (2006).
[197] T. E. McKnight, A. V. Melechko, B. L. Fletcher, S. W. Jones, D. K. Hensley, D. B. Peckys, G. D. Griffin, M. L. Simpson, and M. N. Ericson, *J. Phys. Chem. B* **110,** 15317 (2006).
[198] R. J. Rice and R. L. McCreery, *Analytical Chemistry* **61,** 1637 (1989).
[199] M. Endo, Y. A. Kim, T. Hayashi, K. Nishimura, T. Matusita, K. Miyashita, and M. S. Dresselhaus, *Carbon* **39,** 1287 (2001).
[200] A. Chambers, C. Park, R. T. K. Baker, and N. M. Rodriguez, *Journal of Physical Chemistry B* **102,** 4253 (1998).
[201] J. Y. Howe, C. J. Rawn, L. E. Jones, and H. Ow, *Powder Diffraction* **18,** 150 (2003).
[202] N. A. Kiselev, J. L. Hutchison, A. P. Moravsky, E. V. Rakova, E. V. Dreval, C. J. D. Hetherington, D. N. Zakharov, J. Sloan, and R. O. Loutfy, *Carbon* **42,** 149 (2004).
[203] T. Ichihashi, J. Fujita, M. Ishida, and Y. Ochiai, *Physical Review Letters* **92,** Art. No. 215702 (2004).
[204] P. M. Ajayan, *Nature* **427,** 402 (2004).
[205] T. Bolse, H. Paulus, and W. Bolse, *Nuclear Instruments & Methods in Physics Research Section B-Beam Interactions with Materials and Atoms* **245,** 264 (2006).
[206] H. Cui, X. Yang, M. L. Simpson, D. H. Lowndes, and M. Varela, *Appl. Phys. Lett.* **84,** 4077 (2004).
[207] I. A. Merkulov, V. I. Merkulov, A. V. Melechko, K. L. Klein, D. H. Lowndes, and M. L. Simpson, *Physical Review B* **76,** Art. No. 014109 (2007).
[208] I. A. Merkulov, A. V. Meleshko, J. C. Wells, H. Cui, V. I. Merkulov, M. L. Simpson, and D. H. Lowndes, *Physical Review B* **72,** Art. No. 045409 (2005).
[209] I. A. Merkulov, K. L. Klein, and M. L. Simpson, *Journal of Applied Physics* **105,** Art. No. 064305 (2009).
[210] L. Dong, J. Jiao, C. Pan, and D. W. Tuggle, *Applied Physics a-Materials Science & Processing* **78,** 9 (2004).
[211] M. H. Kuang, Z. L. Wang, X. D. Bai, J. D. Guo, and E. G. Wang, *Applied Physics Letters* **76,** 1255 (2000).
[212] J. D. Fowlkes, A. V. Melechko, K. L. Klein, P. D. Rack, D. A. Smith, D. K. Hensley, M. J. Doktycz, and M. L. Simpson, *Carbon* **44,** 1503 (2006).
[213] S. J. Randolph, J. D. Fowlkes, A. V. Melechko, K. L. Klein, H. M. Meyer, M. L. Simpson, and P. D. Rack, *Nanotechnology* **18,** Art. No. 465304 (2007).

[214] G. Eres, A. A. Puretzky, D. B. Geohegan, and H. Cui, *Applied Physics Letters* **84,** 1759 (2004).
[215] *Phase Diagrams of Binary Iron Alloys*; Vol. 9, edited by H. Okamoto (ASM International, Materials Park, OH, 1993).
[216] P. D. Kichambare, D. Qian, E. C. Dickey, and C. A. Grimes, *Carbon* **40,** 1903 (2002).
[217] K. Kamada, T. Ikuno, S. Takahashi, T. Oyama, T. Yamamoto, M. Kamizono, S. Ohkura, S. Honda, M. Katayama, T. Hirao, and K. Oura, *Applied Surface Science* **212,** 383 (2003).
[218] A. Chambers, N. M. Rodriguez, and R. T. K. Baker, *Journal of Materials Research* **11,** 430 (1996).
[219] W. Z. Li, J. G. Wen, and Z. F. Ren, *Applied Physics Letters* **79,** 1879 (2001).
[220] D. Pradhan, M. Sharon, M. Kumar, and Y. Ando, *Journal of Nanoscience and Nanotechnology* **3,** 215 (2003).
[221] G. L. Zhang, F. Ambe, E. H. D. VanVoorthuysen, L. Niesen, and K. Szymanski, *Journal of Applied Physics* **80,** 579 (1996).
[222] D. Cai, J. M. Mataraza, Z. H. Qin, Z. P. Huang, J. Y. Huang, T. C. Chiles, D. Carnahan, K. Kempa, and Z. F. Ren, *Nature Methods* **2,** 449 (2005).
[223] X. C. Sun, A. Gutierrez, M. J. Yacaman, X. L. Dong, and S. Jin, *Materials Science and Engineering a-Structural Materials Properties Microstructure and Processing* **286,** 157 (2000).
[224] M. Z. Dang and D. G. Rancourt, *Physical Review B* **53,** 2291 (1996).
[225] K. L. Klein, A. V. Melechko, J. D. Fowlkes, P. D. Rack, D. K. Hensley, H. M. Meyer, L. F. Allard, T. E. McKnight, and M. L. Simpson, *Journal of Physical Chemistry B* **110,** 4766 (2006).
[226] T. Leventouri, A. V. Melechko, K. D. Sorge, K. L. Klein, J. D. Fowlkes, P. D. Rack, I. M. Anderson, J. R. Thompson, T. E. McKnight, and M. L. Simpson, *Metallurgical and Materials Transactions a-Physical Metallurgy and Materials Science* **37A,** 3423 (2006).
[227] K. L. Klein, A. V. Melechko, P. M. Costa, D. Golberg, P. D. Rack, and M. L. Simpson**,** (draft letter, 2009).
[228] W. D. Callister, Jr., *Materials Science and Engineering*, 6 ed. (John Wiley & Sons, Inc., New York, 2003).
[229] Y. Nishiyama and Y. Tamai, *Journal of Catalysis* **33,** 98 (1974).
[230] L. B. Avdeeva, O. V. Goncharova, D. I. Kochubey, V. I. Zaikovskii, L. M. Plyasova, B. N. Novgorodov, and S. K. Shaikhutdinov, *Applied Catalysis a-General* **141,** 117 (1996).
[231] C. A. Bernardo, I. Alstrup, and J. R. Rostrup-Nielsen, *Journal of Catalysis* **96,** 517 (1985).
[232] B. Gan, J. Ahn, Q. Zhang, S. F. Yoon, Rusli, Q. F. Huang, H. Yang, M. B. Yu, and W. Z. Li, *Diamond and Related Materials* **9,** 897 (2000).
[233] F. L. Deepak, A. Govindaraj, and C. N. R. Rao, *Chemical Physics Letters* **345,** 5 (2001).
[234] J. Li, C. Papadopoulos, and J. Xu, *Nature* **402,** 253 (1999).
[235] *Binary Alloy Phase Diagrams*; Vol. 1&2, edited by T. B. Massalski (ASM International, Materials Park, OH, 1990).

[236] V. I. Merkulov, A. V. Melechko, M. A. Guillorn, D. H. Lowndes, and M. L. Simpson, *Applied Physics Letters* **79,** 2970 (2001).
[237] A. A. Istratov and E. R. Weber, *Journal of the Electrochemical Society* **149,** G21 (2002).
[238] R. R. Chromik, W. K. Neils, and E. J. Cotts, *Journal of Applied Physics* **86,** 4273 (1999).
[239] C. S. Lee, H. Gong, R. Liu, A. T. S. Wee, C. L. Cha, A. See, and L. Chan, *Journal of Applied Physics* **90,** 3822 (2001).
[240] T. E. McKnight, A. V. Melechko, D. K. Hensley, D. G. J. Mann, G. D. Griffin, and M. L. Simpson, *Nano Letters* **4,** 1213 (2004).
[241] Y. Chen, Z. L. Wang, J. S. Yin, D. J. Johnson, and R. H. Prince, *Chemical Physics Letters* **272,** 178 (1997).
[242] Z. F. Ren, Z. P. Huang, J. W. Xu, J. H. Wang, P. Bush, M. P. Siegal, and P. N. Provencio, *Science* **282,** 1105 (1998).
[243] Y. Gogotsi, S. Dimovski, and J. A. Libera, *Carbon* **40,** 2263 (2002).
[244] Y. Gogotsi, J. A. Libera, N. Kalashnikov, and M. Yoshimura, *Science* **290,** 317 (2000).
[245] R. C. Mani, X. Li, M. K. Sunkara, and K. Rajan, *Nano Letters* **3,** 671 (2003).
[246] C. L. Tsai, C. F. Chen, and L. K. Wu, *Applied Physics Letters* **81,** 721 (2002).
[247] G. Y. Zhang, X. Jiang, and E. G. Wang, *Science* **300,** 472 (2003).
[248] M. Lin, K. P. Loh, C. Boothroyd, and A. Y. Du, *Applied Physics Letters* **85,** 5388 (2004).
[249] M. J. Vasile, C. Biddick, and H. Huggins, *Applied Physics Letters* **64,** 575 (1994).
[250] C. H. Hsu, H. C. Lo, C. F. Chen, C. T. Wu, J. S. Hwang, D. Das, J. Tsai, L. C. Chen, and K. H. Chen, *Nano Letters* **4,** 471 (2004).
[251] Y. Fujimoto, M. Nozu, and F. Okuyama, *Journal of Applied Physics* **77,** 2725 (1995).
[252] M. E. McHenry, M. A. Willard, and D. E. Laughlin, *Progress in Materials Science* **44,** 291 (1999).
[253] I. M. L. Billas, A. Chatelain, and W. A. Deheer, *Science* **265,** 1682 (1994).
[254] G. Herzer, *Journal of Magnetism and Magnetic Materials* **112,** 258 (1992).
[255] D. A. Eastham, P. M. Denby, A. Harrison, I. W. Kirkman, and A. G. Whittaker, *Journal of Physics-Condensed Matter* **14,** 605 (2002).
[256] S. V. Komogortsev, R. S. Iskhakov, A. D. Balaev, A. G. Kudashov, A. V. Okotrub, and S. I. Smirnov, *Physics of the Solid State* **49,** 734 (2007).
[257] C. Desvaux, C. Amiens, P. Fejes, P. Renaud, M. Respaud, P. Lecante, E. Snoeck, and B. Chaudret, *Nature Materials* **4,** 750 (2005).
[258] P. de la Presa, T. Rueda, A. Hernando, J. M. Ramallo-Lopez, L. J. Giovanetti, and F. G. Requejo, *Journal of Applied Physics* **103,** Art. No. 103909 (2008).
[259] Y. H. Lee, D. H. Kim, D. H. Kim, and B. K. Ju, *Applied Physics Letters* **89,** Art. No. 083113 (2006).
[260] M. E. McHenry, S. A. Majetich, J. O. Artman, M. Degraef, and S. W. Staley, *Physical Review B* **49,** 11358 (1994).
[261] X. C. Sun and X. L. Dong, *Materials Research Bulletin* **37,** 991 (2002).
[262] A. Diaz-Ortiz, R. Drautz, M. Fahnle, H. Dosch, and J. M. Sanchez, *Physical Review B* **73,** Art. No. 224208 (2006).

[263] M. Marella and M. Tomaselli, *Carbon* **44,** 1404 (2006).
[264] J. D. Fowlkes, J. M. Fitz-Gerald, and P. D. Rack, *Thin Solid Films* **510,** 68 (2006).
[265] K. Gallagher, F. Johnson, E. M. Kirkpatrick, J. H. Scott, S. Majetich, and M. E. McHenry, *Ieee Transactions on Magnetics* **32,** 4842 (1996).
[266] S. A. Majetich, J. H. Scott, E. M. Kirkpatrick, K. Chowdary, K. Gallagher, and M. E. McHenry, *Nanostructured Materials* **9,** 291 (1997).
[267] H. Q. Wu, P. S. Yuan, H. Y. Xu, D. M. Xu, B. Y. Geng, and X. W. Wei, *Journal of Materials Science* **41,** 6889 (2006).
[268] P. Bayliss, *Canadian Mineralogist* **28,** 751 (1990).
[269] R. Skomski and J. M. D. Coey, *Permanent Magnetism* (Institute of Physics, Philadelphia, PA, 1999).
[270] H. M. Choi, S. K. Choi, O. Anderson, and K. Bange, *Thin Solid Films* **358,** 202 (2000).
[271] Y. K. Kim and M. Oliveria, *Journal of Applied Physics* **74,** 1233 (1993).
[272] D. V. Berkov, P. Gornert, N. Buske, C. Gansau, J. Mueller, M. Giersig, W. Neumann, and D. Su, *Journal of Physics D-Applied Physics* **33,** 331 (2000).
[273] E. F. Ferrari, F. C. S. daSilva, and M. Knobel, *Physical Review B* **56,** 6086 (1997).
[274] S. H. Sun, C. B. Murray, D. Weller, L. Folks, and A. Moser, *Science* **287,** 1989 (2000).
[275] T. W. Huang, T. H. Tu, Y. H. Huang, C. H. Lee, and C. M. Lin, *Ieee Transactions on Magnetics* **41,** 941 (2005).
[276] J. H. J. Scott, K. Chowdary, Z. Turgut, S. A. Majetich, and M. E. McHenry, *Journal of Applied Physics* **85,** 4409 (1999).
[277] Z. Turgut, J. H. Scott, M. Q. Huang, S. A. Majetich, and M. E. McHenry, *Journal of Applied Physics* **83,** 6468 (1998).
[278] *Phase Diagrams of Binary Nickel Alloys*; Vol. 6, edited by P. Nash (ASM International, Metals Park, OH, 1991).
[279] R. J. Wakelin and E. L. Yates, *Proc. Phys. Soc., London* **221,** (1953).
[280] M. Endo, K. Takeuchi, T. Hiraoka, T. Furuta, T. Kasai, X. Sun, C. H. Kiang, and M. S. Dresselhaus, *Journal of Physics and Chemistry of Solids* **58,** 1707 (1997).
[281] H. E. Swanson and E. Tatge, *National Bureau of Standards* **539,** 1 (1955).
[282] Z. S. Basinski, W. Hume-Rothery, and A. L. Sutton, *Proceedings of the Royal Society of London, Series A: Mathematical and Physical Sciences* **229,** 459 (1955).
[283] T. Onozuka, Yamaguch.S, Hirabaya.M, and T. Wakiyama, *Journal of the Physical Society of Japan* **37,** 687 (1974).
[284] M. Singh, M. Barkei, G. Inden, and S. Bhan, *Phys. Status Solidi A* **87,** 165 (1985).
[285] K. L. Klein, S. J. Randolph, J. D. Fowlkes, L. F. Allard, H. M. M. III, M. L. Simpson, and P. D. Rack, *Nanotechnology* **19,** Art. No. 345705 (2008).
[286] W. F. van Dorp, B. van Someren, C. W. Hagen, P. Kruit, and P. A. Crozier, *Nano Letters* **5,** 1303 (2005).
[287] K. S. Kim, S. C. Lim, I. B. Lee, K. H. An, D. J. Bae, S. Choi, J. E. Yoo, and Y. H. Lee, *Review of Scientific Instruments* **74,** 4021 (2003).
[288] J. D. Fowlkes, S. J. Randolph, and P. D. Rack, *Journal of Vacuum Science & Technology B* **23,** 2825 (2005).

[289] A. Perentes and P. Hoffmann, *Chemical Vapor Deposition* **13,** 176 (2007).
[290] K. Molhave, D. N. Madsen, A. M. Rasmussen, A. Carlsson, C. C. Appel, M. Brorson, C. J. H. Jacobsen, and P. Boggild, *Nano Letters* **3,** 1499 (2003).
[291] M. Weber, H. W. P. Koops, M. Rudolph, J. Kretz, and G. Schmidt, *Journal of Vacuum Science & Technology B* **13,** 1364 (1995).
[292] I. Utke, T. Bret, D. Laub, P. A. Buffat, L. Scandella, and P. Hoffmann, *Microelectronic Engineering* **73-74,** 553 (2004).
[293] I. Utke, J. Michler, P. Gasser, C. Santschi, D. Laub, M. Cantoni, P. A. Buffat, C. Jiao, and P. Hoffmann, *Advanced Engineering Materials* **7,** 323 (2005).
[294] I. Utke, A. Luisier, P. Hoffmann, D. Laub, and P. A. Buffat, *Applied Physics Letters* **81,** 3245 (2002).
[295] P. D. Rack, S. Randolph, Y. Deng, J. Fowlkes, Y. Choi, and D. C. Joy, *Applied Physics Letters* **82,** 2326 (2003).
[296] H. W. P. Koops, R. Weiel, D. P. Kern, and T. H. Baum, *Journal of Vacuum Science & Technology B* **6,** 477 (1988).
[297] Y. R. Choi, P. D. Rack, S. J. Randolph, D. A. Smith, and D. C. Joy, *Scanning* **28,** 311 (2006).
[298] W. Li and D. C. Joy, *Journal of Vacuum Science & Technology A* **24,** 431 (2006).
[299] S. Matsui, T. Ichihashi, and M. Mito, *Journal of Vacuum Science & Technology B* **7,** 1182 (1989).
[300] S. Minghui, K. Mitsuishi, and K. Furuya, *Crystallization under 1 MeV electron beam irradiation of nanometer-sized W-dendrites fabricated on alumina substrates with electron-beam-induced deposition*, Beijing, China, 2005 (Trans Tech Publications).
[301] G. Q. Xie, M. H. Song, K. Mitsuishi, and K. Furuya, *Physica E-Low-Dimensional Systems & Nanostructures* **29,** 564 (2005).
[302] N. A. Kislov, I. I. Khodos, E. D. Ivanov, and J. Barthel, *Scanning* **18,** 114 (1996).
[303] K. T. Kohlmann von Platen and W. H. Bruenger, *Journal of Vacuum Science & Technology B* **14,** 4262 (1996).
[304] F. Rugamas, D. Roundy, G. Mikaelian, G. Vitug, M. Rudner, J. Shih, D. Smith, J. Segura, and M. A. Khakoo, *Measurement Science & Technology* **11,** 1750 (2000).
[305] J. Fujita, M. Ishida, T. Ichihashi, Y. Ochiai, T. Kaito, and S. Matsui, *Journal of Vacuum Science & Technology B* **21,** 2990 (2003).
[306] A. Katagiri, M. Suzuki, and Z. Takehara, *Journal of the Electrochemical Society* **138,** 767 (1991).
[307] O. Yamaguchi, D. Tomihisa, H. Kawabata, and K. Shimizu, *Journal of the American Ceramic Society* **70,** C94 (1987).
[308] H. Hartmann, F. Ebert, and O. Bretschneider, *Zeitschrift Fur Anorganische Und Allgemeine Chemie* **198,** 116 (1931).
[309] P. Petroff, T. T. Sheng, A. K. Sinha, G. A. Rozgonyi, and Alexande.Fb, *Journal of Applied Physics* **44,** 2545 (1973).
[310] R. L. Moss and I. Woodward, *Acta Crystallographica* **12,** 255 (1959).
[311] S. Basavaia and S. R. Pollack, *Applied Physics Letters* **12,** 259 (1968).
[312] Y. G. Shen, Y. W. Mai, Q. C. Zhang, D. R. McKenzie, W. D. McFall, and W. E. McBride, *Journal of Applied Physics* **87,** 177 (2000).

[313] W. R. Morcom, W. L. Worrell, H. G. Sell, and H. I. Kaplan, *Metallurgical Transactions* **5,** 155 (1974).
[314] P. M. Petroff and W. A. Reed, *Thin Solid Films* **21,** 73 (1974).
[315] M. Arita and I. Nishida, *Japanese Journal of Applied Physics: Part 1* **32,** 1759 (1993).
[316] T. Kizuka, T. Sakamoto, and N. Tanaka, *Journal of Crystal Growth* **131,** 439 (1993).
[317] M. G. Charlton, *Nature* **169,** 109 (1952).
[318] G. Hagg and N. Schonberg, *Acta Crystallographica* **7,** 351 (1954).
[319] M. G. Charlton and G. L. Davis, *Nature* **175,** 131 (1955).
[320] G. Mannella and J. O. Hougen, *Journal of Physical Chemistry* **60,** 1148 (1956).
[321] T. Millner, A. J. Hegedus, K. Sasvari, and J. Neugebauer, *Zeitschrift Fur Anorganische Und Allgemeine Chemie* **289,** 288 (1957).
[322] V. J. Neugebauer, A. J. Hegedus, and T. Millner, *Z. Anorg. Allg. Chem.* **293,** 241 (1958).
[323] D. G. Bhat and R. A. Holzl, *Thin Solid Films* **95,** 105 (1982).
[324] N. J. Archer and K. K. Yee, *Wear* **48,** 237 (1978).
[325] N. N. Matiushenko, L. N. Yefimenko, and D. P. Solopikhin, *The Physics of Metals and Metallography* **8,** 67 (1959).
[326] J. S. Kim, T. La Grange, B. W. Reed, M. L. Taheri, M. R. Armstrong, W. E. King, N. D. Browning, and G. H. Campbell, *Science* **321,** 1472 (2008).

Appendix

Phase Diagram of Fe-C

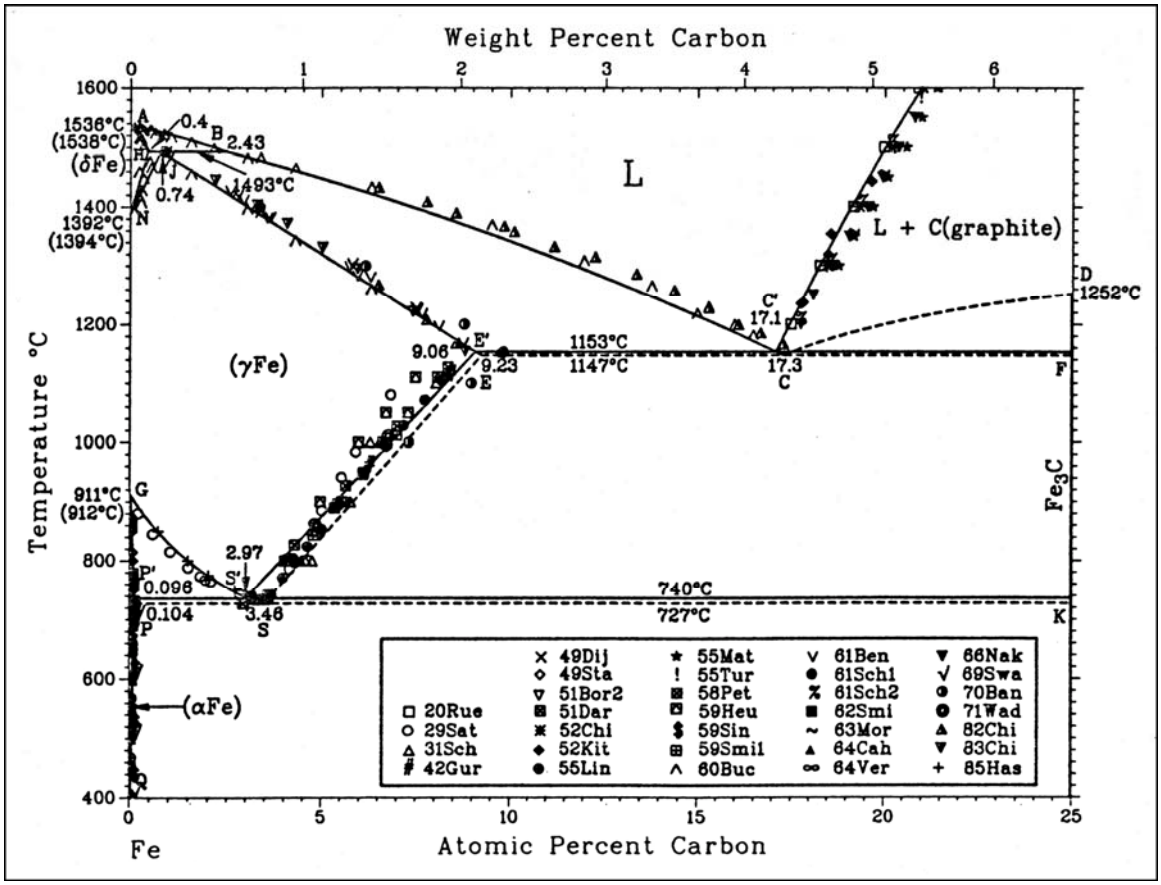

Reprinted from [215].

Phase Diagram of Co-C

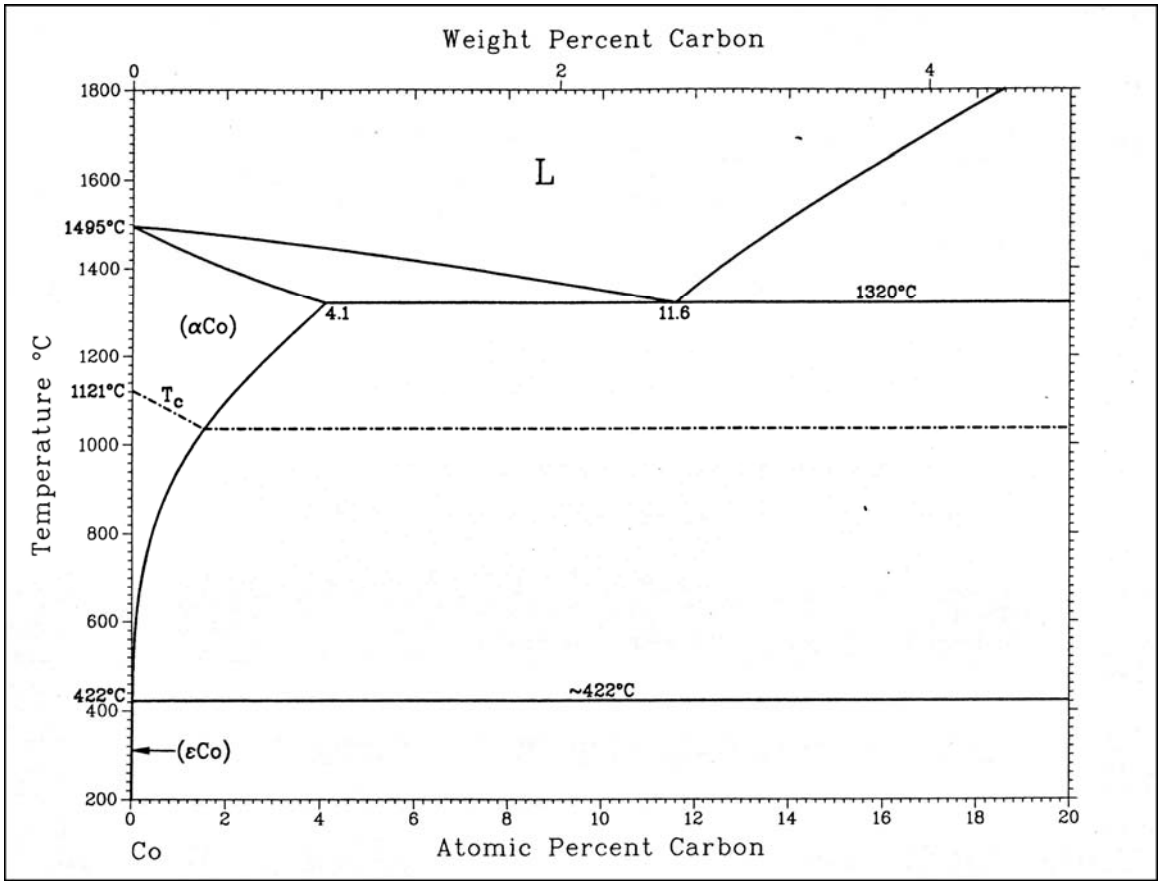

Reprinted from [235].

Phase Diagram of Ni-C

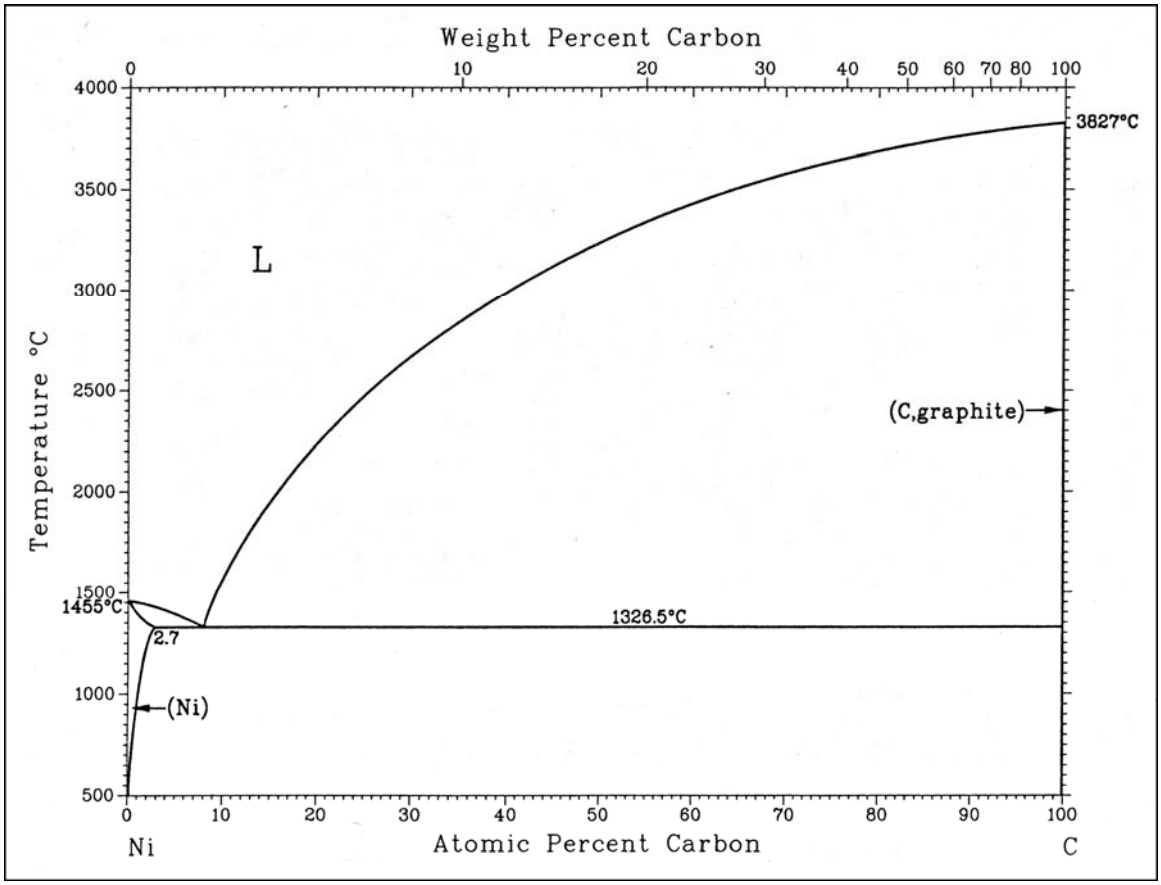

Reprinted from [235].

Phase Diagram of Cu-C

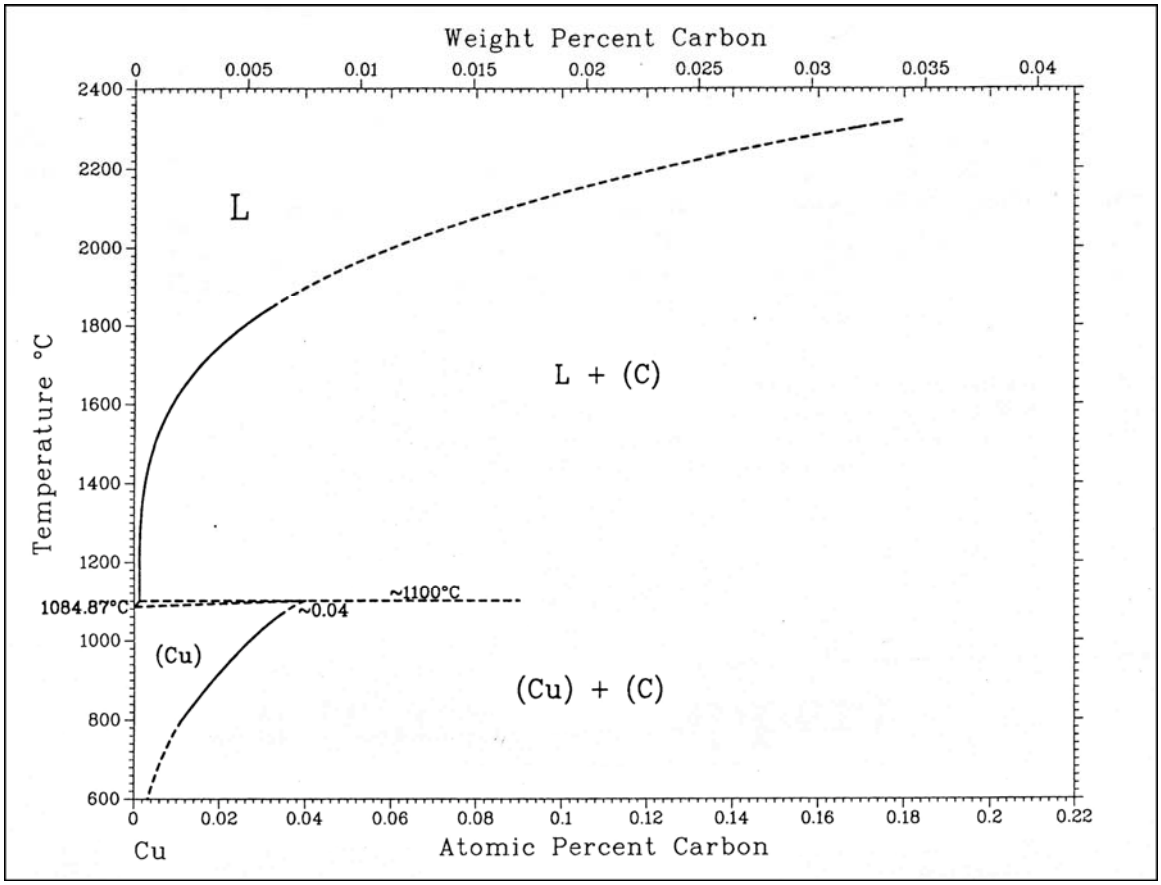

Reprinted from [235].

Phase Diagram of Cu-Ni

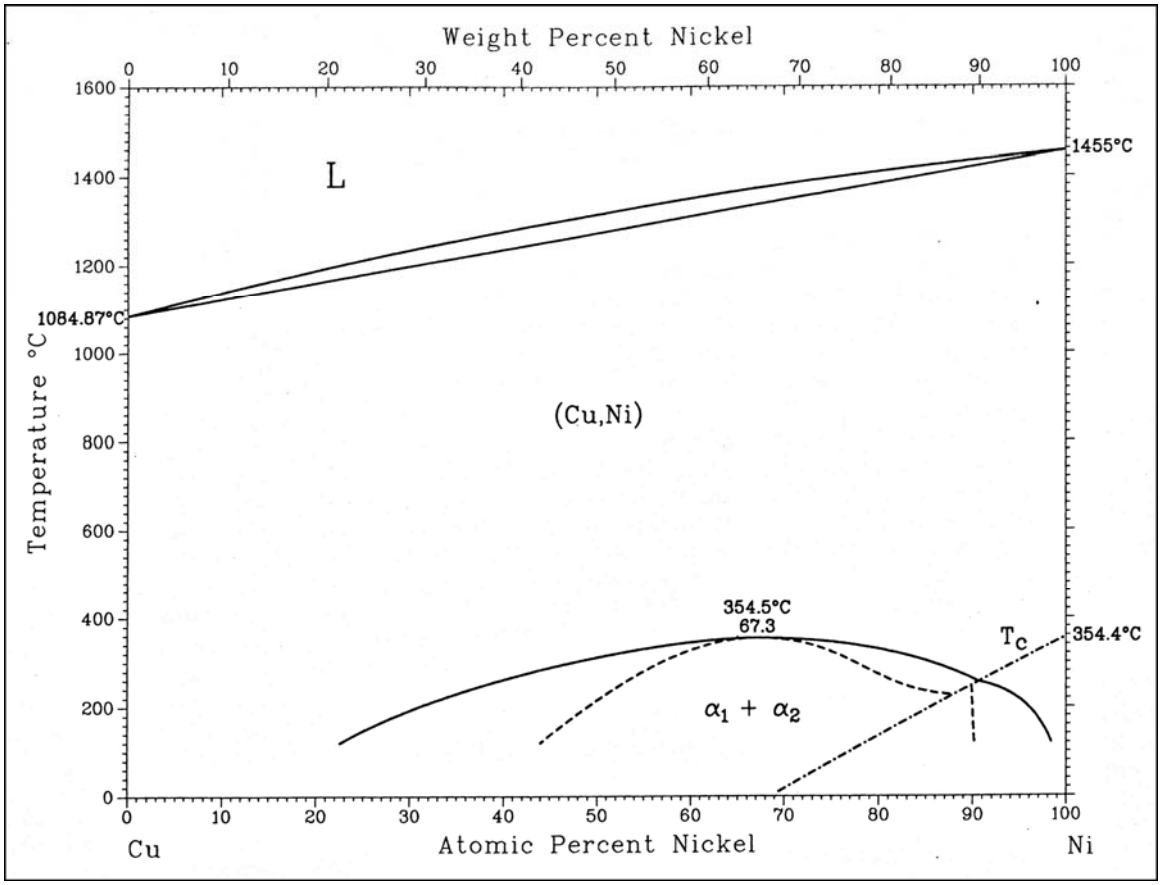

Reprinted from [235].

Phase Diagram of Fe-Ni

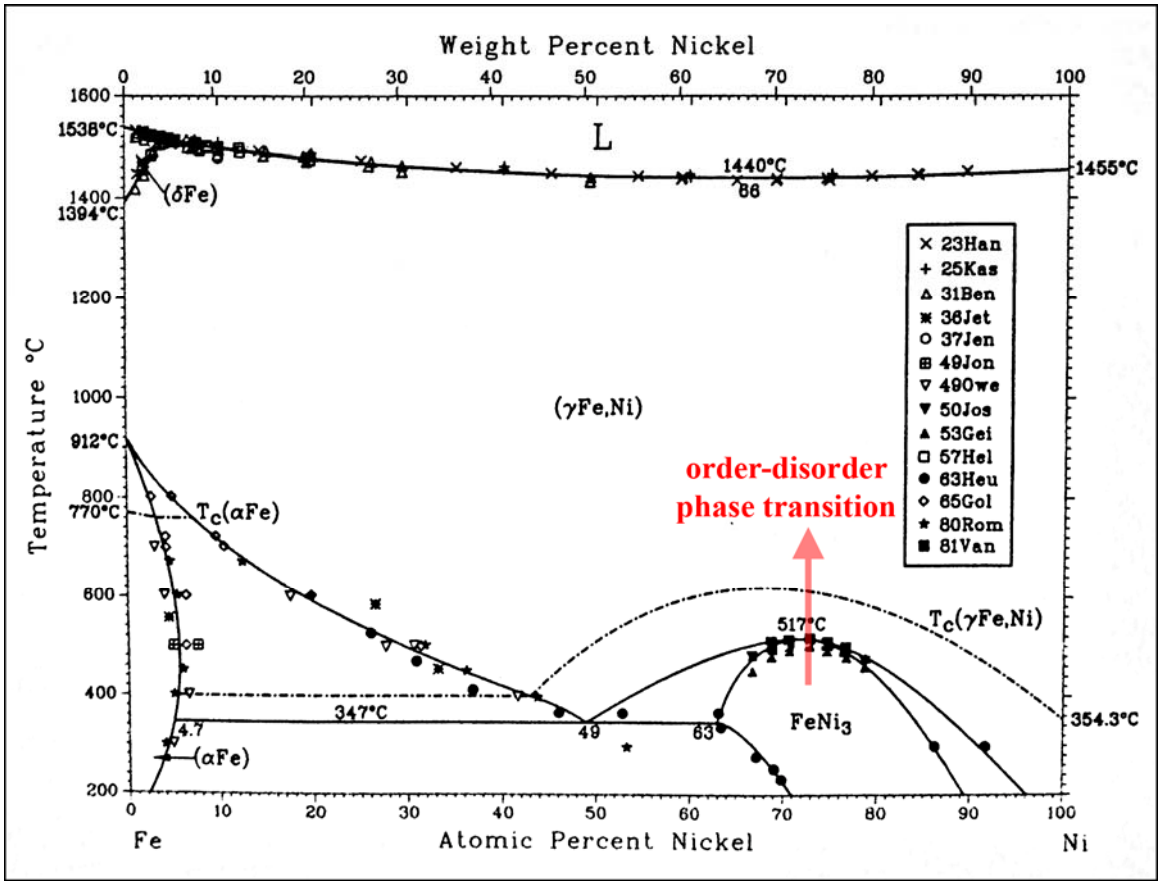

Reprinted from [278].

Phase Diagram of Fe-Co

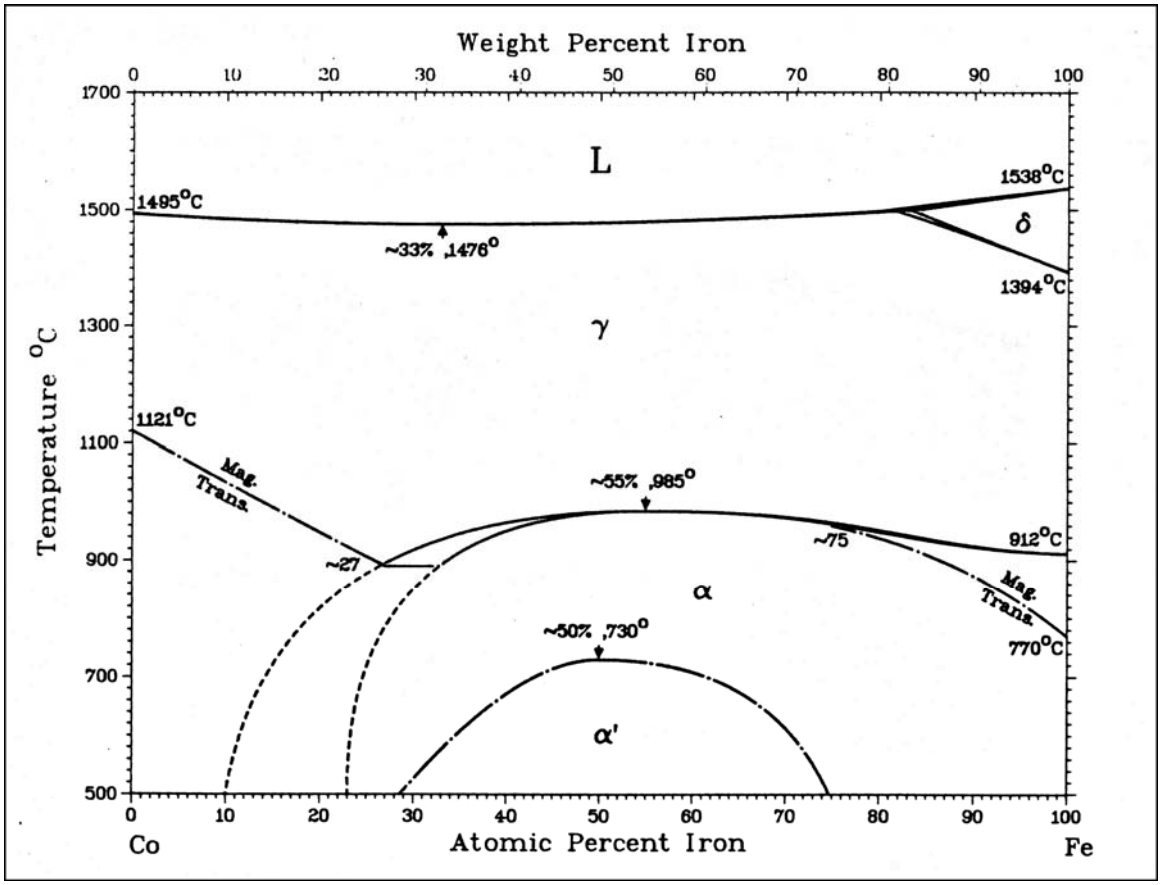

Reprinted from [215].

Vita

Kate Klein was born on November 21, 1980 and grew up in the rural town of Huntington, Vermont. She graduated from Mount Mansfield Union High School in 1998. From there Kate spent a year abroad as a foreign exchange student in Guayaquil, Ecuador. Upon returning she enrolled in undergraduate study at Trinity College in Hartford, Connecticut to pursue a Bachelor of Science in Engineering. At Trinity she spent four years as a varsity athlete on the Trinity cross-country and track and field teams, earning recognition as a member of the All-NESCAC Academic Team as well as receiving the Trinity Scholar Athlete of the Year Award in 2002. During her undergraduate summers she was afforded research fellowships at Stanford University under the National Science Foundation NNUN REU program and at Oak Ridge National Laboratory with the Department of Energy's ERULF program. The latter summer experience was instrumental in determining the course of her career in Materials Science and her return to the same research group after attaining her degree. In the fall of 2003, Kate rejoined the Molecular-Scale Engineering and Nanoscale Technologies (MENT) research group as a research associate at the University of Tennessee (UT). The following year, under the direction of Dr. Michael L. Simpson, she enrolled full-time in a doctoral program in Materials Science and Engineering at UT, Knoxville. Presently, Kate looks forward to a postdoctoral National Research Council appointment at the National Institute of Standards and Technology in Gaithersburg, Maryland. In what little spare time she may have, Kate enjoys traveling, cooking, hiking, and gardening.